Development of a Primary Standard for the Measurement of Nano-Flow Rates of Liquids

Abir Boudaoud

▶ **To cite this version:**

Abir Boudaoud. Development of a Primary Standard for the Measurement of Nano-Flow Rates of Liquids. Fluid mechanics [physics.class-ph]. Université Paris sciences et lettres, 2022. English. ⟨NNT : 2022UPSLS073⟩. ⟨tel-04187912⟩

HAL Id: tel-04187912

https://pastel.hal.science/tel-04187912v1

Submitted on 25 Aug 2023

HAL is a multi-disciplinary open access archive for the deposit and dissemination of scientific research documents, whether they are published or not. The documents may come from teaching and research institutions in France or abroad, or from public or private research centers.

L'archive ouverte pluridisciplinaire **HAL**, est destinée au dépôt et à la diffusion de documents scientifiques de niveau recherche, publiés ou non, émanant des établissements d'enseignement et de recherche français ou étrangers, des laboratoires publics ou privés.

HAL Authorization

PSL
UNIVERSITÉ PARIS

THÈSE DE DOCTORAT
DE L'UNIVERSITÉ PSL

Préparée à ESPCI Paris et CETIAT

Development of a Primary Standard for the Measurement of Nano-flow Rates of Liquids

Développement d'un système primaire de mesure de nano-débits de liquides

Soutenue par
Abir-Wissam BOUDAOUD
Le 16 décembre 2022

École doctorale n°564
Physique en Île-de-France

Spécialité
Physique

Laboratoire
UMR 7083 - GULLIVER

Composition du jury :

Jean-Luc AIDER Research Director, ESPCI Paris	*Président*
Jacques FATTACCIOLI A. Professor, Sorbonne Université	*Rapporteur*
Stéphane COLIN Professeur, INSA Toulouse	*Rapporteur*
Christine BARROT LATTES Assistant Professor,IUT Paul Sabatier	*Examinatrice*
Vania SILVERIO Assistant Researcher, INESC MN	*Examinatrice*
Teresa LOPEZ-LEON Chargée de Recherche, ESPCI Paris	*Directrice de thèse*
Florestan OGHEARD Chargé d'affaires, CETIAT	*Co-encadrant*
Joshua D. MCGRAW Chargé de Recherche, ESPCI Paris	*Co-encadrant*

ESPCI PARIS | PSL

Contents

Introduction **1**

1 Project and Context **4**
1.1 Brief History of Flow Measurement 4
1.2 Metrology for Drug Delivery Projects 13
1.3 Low Flow Rate Applications 15
1.3.1 Drug Delivery 15
1.3.2 Microfluidics 16
1.3.3 Inkjet Printing 19
1.3.4 Nano-liquid Chromatography 20
1.4 Metrology Vocabulary and Concepts 21
1.4.1 Definitions Related to Measurements and Standards 21
1.4.2 Definitions Related to Measurement Uncertainty 23
1.4.3 Interlaboratory Comparisons 25

2 Nano-flow Rate Measurement Methods **27**
2.1 Primary Measurement Methods 27
2.1.1 Gravimetric Method 27
2.1.2 Particle Image Velocimetry (PIV) 33
2.1.3 Interferometric Method 35
2.1.4 Pendant Drop Method 36
2.1.5 Front Tracking Method 36
2.2 Secondary Measurement Methods 39
2.2.1 Coriolis Mass Flow Meters 39
2.2.2 Thermal Mass Flow Meters 41

3 Methods and Materials **44**
3.1 Description of the Measurement System 44
3.2 Working Principle 50
3.2.1 Template Matching 50
3.2.2 Measurement of the Interface's Displacements 52
3.2.3 Template Update 54
3.2.4 Region of Interest 56
3.2.5 Computer Program 58
3.2.6 Flowcharts 61
3.3 Calibration Procedure for a Flow Generator or Meter 66
3.3.1 Preparation of the System 66
3.3.2 System Configuration 68
3.3.3 Measurements 69

4 Traceability and Uncertainty Budget **71**
4.1 Camera and Timestamps' Calibration 71
4.1.1 Measurement of the Pixel Size 71
4.1.2 Quantification of Optical Distortions 78
4.1.3 Edge Detection Errors Management 81
4.1.4 Flowcharts 81
4.1.5 Timestamps' Traceability 83
4.2 Uncertainty Components 84
4.2.1 Interface Displacement 84
4.2.2 Time 87
4.2.3 Other Components 88
4.3 Measurement of the Inner Diameter of Glass Capillary Tubes 90
4.3.1 Existing Methods 90
4.3.2 Measurement of the Inner Diameter by Confocal Microscopy 97

5 Preliminary Results **106**
5.1 Stick-Slip Effect 106
5.2 Calibration of a Coriolis Flow Meter 110

6 Validation by Interlaboratory Comparison **114**
6.1 Comparison Protocol 114
6.2 Results and Discussion 115

7 Application and Perspectives **124**
7.1 Calibration of Treprostinil Infusion Pump 124
7.2 Pendant Drop Method 127
7.2.1 Description of the Method 127
7.2.2 Image Processing Algorithm 129
7.2.3 Uncertainty Budget 131
7.2.4 Discussion of the Pendant Drop Method 132

Conclusion **134**

A Edge Detection **136**

B Results of the Interlaboratory Comparison **141**

Acknowledgement

I realize today that I never had the chance to properly thank my parents, Houria and Mohamed (a.k.a Lhawla and Mha), for all they did for me. So I will start with that.

Mom, I want to thank you for being such a great woman and my first role model ever. For being the number one reason I value my freedom and independence as a woman more than anything else. For your constant generosity which inspires me and guides me every day. For all the times you shared with me and my sister, collecting seashells and painting them, teaching us how to sew dresses and do embroidery, and so much more. You may not realize it, but those moments are the ones that make me resilient today and allow me to fight for my own happiness. Maybe I'm constantly searching for those happy, safe times I knew as a child, thanks to you.

Dad, the fact that I thank you in second place doesn't make me any less grateful to you. Thank you for all the discussions we had from an early age that opened my mind to things beyond what my society taught me. For always encouraging me to explore new things and go beyond my abilities. For always insisting that we get out into nature even when we just wanted to stay home and play on the computer. You knew we'd regret it one day and I'm happy that you pushed us to go out, because the moments spent in the forest and especially at the sea are the best moments of my life.

I want you both to know how much I admire you for all the effort you put into making my sister and I have a great childhood. For giving us what you did not receive. Thank you for understanding and accepting my choices even when they are radically different from yours. Je vous aime.

Rim (a.k.a. Rimouch), my one and only sister, I thank you from the bottom of my heart for always being there for me. I have learnt so much from your constant empathy and kindness. I wish you all the happiness you and your family. I love you.

Houssem, thank you for being the brother I never had and for being the father of my amazing little nephew, Adib (a.k.a. Debdoub) that I love so much.

I would like to thank my love Pierre (a.k.a. Bisounours) who has shared with me the last months of my thesis. Thank you for all the support, affection and love you have given me. For the wonderful times we spent together and will spend together in the future. Thank you for cooking everyday. I love you.

A special thanks to my amazing friends and colleagues in CETIAT, who brought so much joy to my life at and outside of work. I want to thank in particular Bayan because she asked me explicitely to thank her here and for being the best office colleague and such a good friend

to me. Bayan, I wish you all the best especially for your thesis. I want to thank my friend and first intern Sana for doing such a good job at transforming the ugly GUI I developed to a beautiful and functionnal one. Many thanks to Nessrine who shared for months the same office as me, Bayan and Sana. Together, we broke the record for the noisiest office in CETIAT and we are proud of it. I am grateful to my best childhood friend, Nawel (a.k.a. Nounou) for being part of my life for more than 20 years. For all my friends, thank you. I love you all.

I would like to express my deepest and warmest thanks to my thesis directors: Florestan Ogheard, Joshua D. McGraw and Teresa Lopez-Leon. Thank you Florestan for your constant support, guidance and all the time you devoted to teaching me metrology, a field that I was not familiar with before this thesis. Thank you for explaining to me 1000 times the difference between precision and accuracy, for your constant presence and care in order to make the thesis as pleasant as possible for everyone and for believing in my work and doing your best to ensure its continuity.

Thank you Josh for all the discussions we had which always lead to new ideas and insights. I look back and I realize that all the improvements in the interface tracking algorithm would not have been possible without your precious collaboration. Above all, thank you for all the "JDMRN" and "JDMUDC" without which I would have the caption "Image of an objective micrometer as seen by a camera" almost in every figure of the manuscript.

Thank you Teresa for your involvement in the project, your constant support even from afar, and for your valuable feedback over the past three years. Thank you also for working so hard and being committed to achieve equality in the workplace. This means a lot for us.

I would like to express my deepest gratitude to my committee members, Eric Georgin and Kristina Davitt, for their valuable support and advice. Thank you Eric for everything you have done for me to be in the best working conditions at CETIAT, for always listening, for your precious help and encouragement, and for being simply the best "Parrain" one can have.

A special thanks to Florian Courage who carried out the calibration of the Treprostinil infusion pump, to Bertrand Cinquin for his precious training and help regarding the measurement of the capillaries' inner diameter using confocal microscopy and to all my colleagues in CETIAT and Gulliver laboratory.

Acronyms

BHT Bronkhorst High-Tech BV. 31, 32

BIPM International Bureau of Weights and Measures (Bureau International des Poids et Mesures). 21

CETIAT Centre Technique des Industries Aérauliques et Thermiques. 13, 28, 29, 83

CMI Cesky Metrologicky Institut. 13, 32, 33

DTI Teknologisk Institut. 13, 31

GUM Guide to the Expression of Uncertainty in Measurement. 21

HS Hahn-Schickard-Gesellschaft für angewandte Forschung e.V.. 33, 34

IPQ Instituto Português da Qualidade, I.P.. 13, 30, 31, 35, 36, 38

ISO International Organization for Standardization. 21

JCGM Joint Committee for Guides in Metrology. 21

METAS Eidgenössisches Institut für Metrologie METAS. 13, 29, 30

NEL TÜV SÜD National Engineering Laboratory. 34, 35

NMI National Metrology Institute. 44

THL Technische Hochschule Lübeck. 13, 37, 38

TÜBİTAK The Scientific and Thecnological Research Council of Türkiye. 13

UMC Teknologisk Institut. 13

VIM International Vocabulary of Metrology (Vocabulaire International de Metrologie). 21

VSL Netherlands' National Metrology Institute. 13

Introduction

Liquid flows have always been an important part of our daily lives and the interest in measuring them began as early as 3000 years ago, in the ancient Egyptian civilization. Egyptians used to measure the flood of the Nile river in order to ensure the irrigation of their agricultural lands. Moreover, they were behind the invention of the waterclock, which they used to measure time. Centuries later, the ancient Romans were able to regulate and measure the water distributed to households, using what can be considered as the early ancestor of orifice plates. It took centuries to properly understand the volumetric flow rate as a volume that passes per unit of time. This would not have been possible without the work and discoveries in fluid mechanics made by prominent scientists such as Leonardo da Vinci, Daniel Bernoulli and long before that, Heron of Alexandria.

In the modern times, liquid flows have reached all sorts of application areas, from residential water distribution, wastewater treatment processes to food industry. Many of these applications tend to involve increasingly low flow rates with a constant need for flow generators and measurement techniques, in order to ensure the accuracy of the small volumes handled. To meet this constant need, various types of flow meters were developed and commercialized, covering flow rates from 10^7 L/h down to 10 nL/min.

In this thesis, we are interested in liquid nano-flow rates, which range from 1 nL/min to 1000 nL/min. Nano-flow rates are important mainly in the medical field and microfluidics, the latter which involves the manipulation of liquid flows and emulsions inside micrometric channels. In droplet microfluidics, the flow rate is an important parameter to control the size, frequency and monodispersity of the generated droplets. In organs-on-chip, low flows ensure the continuous perfusion of cell cultures and the control of their biochemical and physical environment. In the medical field, drug delivery devices such as syringe pumps and infusion pumps are used to deliver drugs at flow rates as low as 10 nL/min. These drugs include for example painkillers, insulin, anesthetics, and vasoactive drugs, some of which are used in intensive care and must be given in controlled doses. The dose delivered to a patient depends on the flow rate generated by the device. As a result, any flow rate error can lead to an excess or a reduction in the necessary dose, thus endangering the patient' health. It is then important before using flow devices, to evaluate their performances through calibrations that are traceable to primary standards.

Calibrating a flow device allows us to evaluate the deviation of the flow rates that it generates or measures from reference values that are measured by a secondary or primary system. The latter ensures a link between the measurements and S.I. units and provides the best uncertainties for the measured quantity. However, before this thesis, the traceability of devices operating at nano-flow rates could not be ensured, as no primary standard existed. In fact, the French national standard at CETIAT, the institute at which the work presented in this thesis was carried out, ensured COFRAC-certified (ISO 17025) calibrations for liquid flow rates going down to 16 μL/min. COFRAC accreditation, being an official recognition of the calibration competences of CETIAT. Below the limit of 16 μL/min, traceable calibrations were not possible in France or even in Europe.

Most of the primary standards that existed by then were based on the gravimetric method. This method consists in measuring the mass over time of a collected liquid. As can be imagined, gravimetry is limited by the resolution of the weighing scales which cannot be better than 0.1 μg. In fact, at 1 nL/min, one needs to wait around 10 s in order to measure a mass change equal to the resolution of the best micro-balance. This method is then not adapted to the measurement of fluctuating flow rates such as those generated by drug delivery devices.

The metrological gap caused by the lack of primary standards for liquid nano-flow rates was the reason behind the creation of this doctoral project, which is part of the "Metrology for Drug Delivery II (MeDD II)" European joint research project. The latter gathered national metrology institutes, academia and hospitals with the same objective: developing a new metrological infrastructure to ensure the traceability to the S.I. of Units of flow generators and meters, for flow rates going down to 5 nL/min and with a best expanded uncertainty (k=2) of 2 %.

In the context of this thesis and the MeDD II project, we developed a primary system based on the interface tracking method. This optical method consists in the tracking of a water/air interface moving inside a glass capillary tube. The volumetric flow rate is determined from the interface displacements over time, which are measured using a template matching algorithm, and the cross sectional area of the capillary which is obtained from the measurement of the capillary's inner diameter.

We dedicate this manuscript to the description of the interface tracking method developed in the framework of this thesis and its validation through the MeDD II interlaboratory comparison. The work is organized as follows.

In the **first chapter**, we go through the historical milestones that led to the understanding and definition of liquid flow rates and briefly describe the evolution of their measurement methods. Then, we present the two MeDD projects that set the context of this thesis, and describe several applications that show the growing interest for the measurement of nano-flow rates, in the health and research fields. At the end of the chapter, we define the metrological concepts used in the development, evaluation and validation of our measurement method.

In the **second chapter**, we present the current state-of-the-art of primary and secondary flow measurement methods. The primary methods presented were developed in the context of the MeDD projects. As for the secondary methods, we focus on Coriolis and thermal mass flow meters which are largely used to measure nano-flow rates.

In the **third chapter**, we present in detail the experimental setup and operating principle of the interface tracking method that we developed, after which we describe the procedure used to calibrate a flow generator or meter using this method.

We devote **chapter four** to the metrological aspect of our system. First, we describe the different methods developed to ensure its traceability to the S.I. of Units, then we present the associated uncertainty budget with a detailed explanation of every source of uncertainty. Finally, we present a confocal fluorescent method used for the measurement of the capillaries' inner diameter, which constitutes an important part of the system's traceability.

In **chapter five**, we move on to the first flow measurement results, which served as a first evaluation of the system's performance. First, we discuss the stick-slip phenomenon and how it affects the stability of the flow rates and propose a simple method to reduce its

effect. Then, we present preliminary results obtained for the calibration of a Coriolis flow meter.

Chapter six is devoted to the interlaboratory comparison that was carried out within the framework of the MeDD II project, with the aim of validating the primary methods developed by the different participating laboratories. We start by describing the comparison protocol, after which we present the results obtained.

In the **seventh and last chapter**, we present a direct application of our system in the medical field. This application consisted in the calibration of an infusion pump, in order to evaluate its performance before use by patients. We conclude the chapter by presenting a different configuration of the interface tracking system which allows the measurement of flow rates from the increasing volume of a pendant drop.

We dedicate the end of the manuscript to a general conclusion of the work done in this thesis. We also provide additional details on the edge detection algorithm used in camera calibration and the results of the interlaboratory comparison, in the appendices.

Chapter 1

Project and General Context

In this chapter, we briefly describe the evolution of liquid flow measurement methods. In the first section, we give the historical milestones leading to the understanding and definition of liquid flow rates. Traveling from ancient civilizations to modern times, we describe the most significant scientific discoveries that led to a better understanding of flow rate, and later on, to the development of methods to measure it. From liquid flows as high as 10^{10} L/h down to 1 mL/h, we make stopovers to explain succinctly the flow meters developed, their operating principle and provide, when possible, their date of commercialisation. At the end of this section, we summarize the main events in the history of liquid flow measurement by a timeline diagram (Fig. 1.11). After this chronological overview, we move on to the scale of liquid nano-flows on which we will focus throughout this thesis.

In the second section, we present the two European research projects "Metrology for Drug Delivery (MeDD I)" and "MeDD II", which are behind the development of new reference methods for the measurement of very low flow rates. These projects were created to meet a growing need for the evaluation of drug delivery devices such as infusion pumps and syringe pumps, which operate at increasingly low flow rates. The need for new measurement and calibration techniques is manifested by the increase in applications where low flow rates constitute an important parameter. In section three, we precisely give examples of the main applications, in microfluidics and the medical field, where nano-flow rates are encountered.

To conclude this chapter, we define the metrological concepts used in the development, evaluation and validation of our measurement methods. These concepts are crucial to understand the objectives of this project and the reasons why it was initially created.

1.1 Brief History of Flow Measurement

This section is highly inspired by the work of Furio Cascetta [32] in the presentation of historical events, citations, and the classification of the different flow meters. Information is reinforced each time with other references to provide additional details, especially when we explain the working principle of a measurement method. When possible, we also cite the source where a scientific work was originally published.

The first water meter for open channels was probably a rough form of weir used by ancient Egyptians, 3000 years ago. These weirs were used to measure the flood levels of the Nile river, which allowed them to predict annual agricultural production and plan the planting season [32, 29]. The water levels of the river were measured by an instrument known as a Nilometer (Fig. 1.15(left)). Besides their interest in flood levels, ancient Egyptians' understanding of the relationship between time and flow was also reflected by their development of the oldest water clock, around 1300 BC [142]. This instrument was used to measure time by the

Figure 1.1: Photograph of a Nilometer in Elephantine Islands(left) [109] and a reconstruction of an Egyptian Clepsydra from the Temple of Karnak (right)[165]

.

regulated flow of water into or out of a marked container where the level of water indicated the elapsed time (Fig. 1.15(right)).

Centuries after Egyptians, Romans used to distribute water from sources to houses by means of stone piping systems, as seen in Fig. 1.2. The flow rate of the distributed water was regulated and measured using what can be considered as the early ancestor of orifice plates. For the Romans, only the dimensions of the pipe or the orifice determined the flow rate. In fact, each consumer was paying for a continuously running discharge of water. It appears that some dishonest householders were installing larger pipes at their discharge to receive more flow [152, 100]. The Greek engineer Heron of Alexandria (1st century A.D.) on the other hand, completely understood the flow rate's dependence on the pipe's cross-sectional area as well as the flow's velocity. In his book Dioptra, he studied the flow of water from springs and concluded that it is necessary to know both the wetted area of an open channel and the water's speed in order to determine the amount of water supplied by the spring. He also understood that by digging a reservoir under the stream of the spring and measuring with the help of a sundial the amount of water that flows into it during an hour, one can determine how much water will be furnished in a day [114]. Quoting Heron of Alexandria:

> *"Observe always that it does not suffice to determine the section of flow to know the quantity of water furnished by the spring .... it is necessary to find the velocity of the current .... for this reason, after having dug a reservoir under the stream, examine by means of a sundial how much water flow into it in an hour and from that deduce the quantity furnished in a day [92]."*

From Roman times to around 1500 AD, not much information about flow measurement is available. In fact, Heron's work went unnoticed for about 1500 years, until Leonardo da Vinci discovered it. It is worth noting that the city of Milan tried in the 12th century to regulate the irrigation activity and control the delivered flow by defining a unit for the measurement of the flow rate, known as "*oncia d'acqua milanese*". However, this unit was defined as the amount of water discharged by a rectangular orifice of given dimensions without taking into consideration the dependence of the discharge on the flow velocity [152, 31].

From the 16th to the 18th century, many distinguished scientists studied fluid-dynamics

Figure 1.2: Photograph of a stone pipe of Patara's aqueduct, in Turkey [87].

concepts such as Leonardo da Vinci, Daniel Bernoulli and Giovanni Battista Venturi, for example. These studies led to the development of different flow measurement instruments such as pressure differential, positive and inferential flow meters[10].

In his study about the flow of rivers, Leonardo da Vinci (1452-1519) correctly described the flow rate as the volume of water flowing through a particular cross section of the river in a given time interval and concluded that in steady flow :

> *"The river transports in every section of its length in the same time the same quantity of water[31]."*

He also realized that, in a steady flow, the river's cross sections and average velocity are inversely proportionnal :

> *"A river of uniform depth will have a more rapid flow at the narrower width than at the greater, to the extent that the greater width surpasses the narrower[31]."*

Leonardo was the first to take an interest in turbulent flows. As a chief engineer in a large area of Italy, he focused his studies on vortices produced by bluff bodies and succeeded to identify several types of these which he often represented with accurate drawings (Fig. 1.3(left)). However, his discoveries remained unpublished until the 19th century and flow rates continued to be measured in terms of "*Oncia Milanese*". Leonardo's work on water vortices was exploited commercially for flow measurement only in the 20th century by the release of the first vortex shedding flow meter (1970s)[32]. The latter consists of a bluff bar (shedder bar) that sheds vortices from both sides in an alternate way (Fig. 1.3(right)). Two signal detectors are placed on both sides and are used to measure the frequency of vortices which is proportional to flow rate. The frequency of the signal is then converted by a software to velocity and flow rate readings [164].

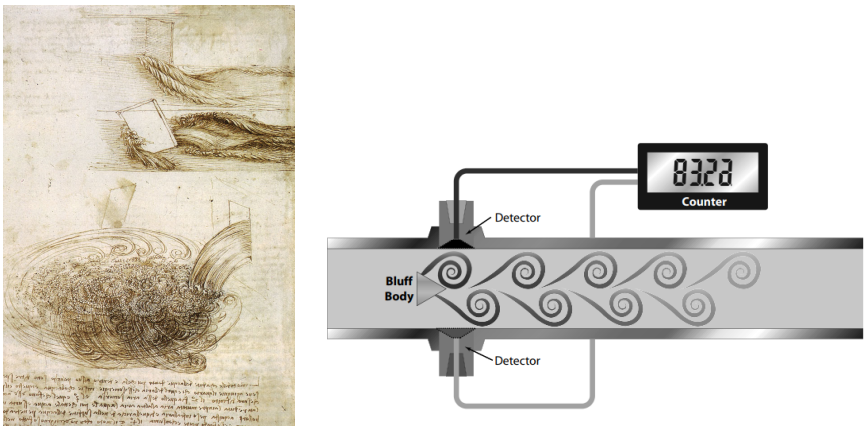

Figure 1.3: Elementary vortices of different scales drawn by Leonardo da Vinci (left)[11]. Schematic illustration of the working principle of a Vortex flow meter (right)[153].

Benedetto Castelli (1578-1643) student of Galileo Galilei, also understood the dependence of flow rate on flow velocity in addition to the cross section of the channel which he expressed in his book "Delia misura dell'acque correnti" in 1628[35]. In addition, Castelli studied the link between velocity and head in a flow through an orifice, but only came up with a defective unsatisfactory proof. His work was however carried on by his student Evangelista Torricelli (1608-1647) who demonstrated that the flow through an orifice was proportional to the square root of the head [49], which is known as Toriccelli's Law :

> *"Liquids which issue with violence have at the point of issue the same velocity which any heavy body would have, or any drop of the same liquid if it were to fall from the upper surfaces of the liquid to the orifice from which it issues [32, 97]."*

In his "Traité du Mouvemement des Eaux et des Autres Corps" published in 1686 [94], Edme Marriotte (1620-1684) showed the proportionality between the force exerted by a jet of liquid and the square of its velocity, the principle on which are based modern target flow

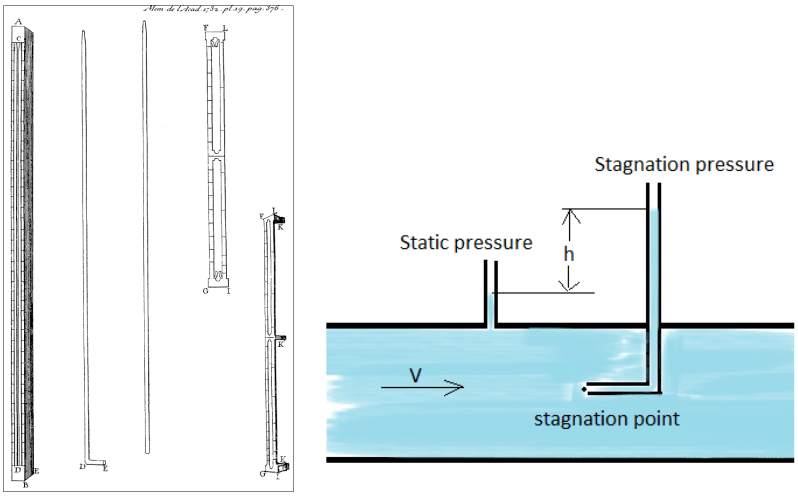

Figure 1.4: Original design of a Pitot tube drawn by Henri Pitot's [27] (left). Schematic illustration of the working principle of a Pitot flow meter [172] (right).

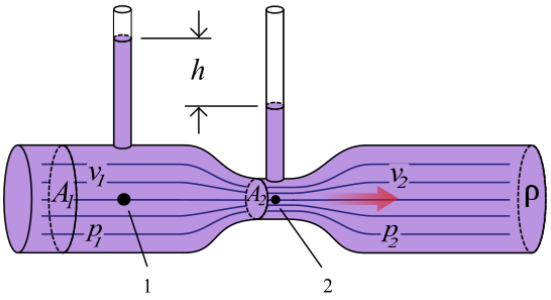

Figure 1.5: Schematic illustration of the working principle of a Venturi flow meter: The static pressure p_1 in tube 1 is higher than p_2, and the fluid speed v_1 is lower than v_2, as the cross-sectional area of tube 1 is larger than that of tube 2 [66].

meters [26, 9]. Using a similar force-velocity relation, the first device for the measurement of a river's flow velocity was invented by Domenico Guglielmini (1655-1710) in the 17th century [32]. The device consisted of a pendulum ball suspended from a quadrant gauge that is calibrated in velocity units. The initially vertical string attached the ball was deflected by the flow and the resulted deflection was measured using the quadrant [49].

In 1732, Henri Pitot (1695-1771) invented an instrument to measure water's velocity and the speed of ships, known as the Pitot tube. Pitot's device consisted of two bore tubes, one straight and the other right angled. The tubes were inserted in parallel into water so that the end of the bent tube faced the flow (Fig. 1.4). The velocity and rate of flow were determined by measuring the differences between the static pressure (measured by the straight tube) and the stagnation pressure (measured by the right angled tube) [116].

In his book Hydrodynamica published in 1738, Daniel Bernoulli (1700-1782) stated that [20]:

> *"An increase in the speed of a fluid occurs simultaneously with a decrease in static pressure or a decrease in the fluid's potential energy."*

However, it was Leonhard Euler (1702-1783) who, starting from Newton's laws, derived

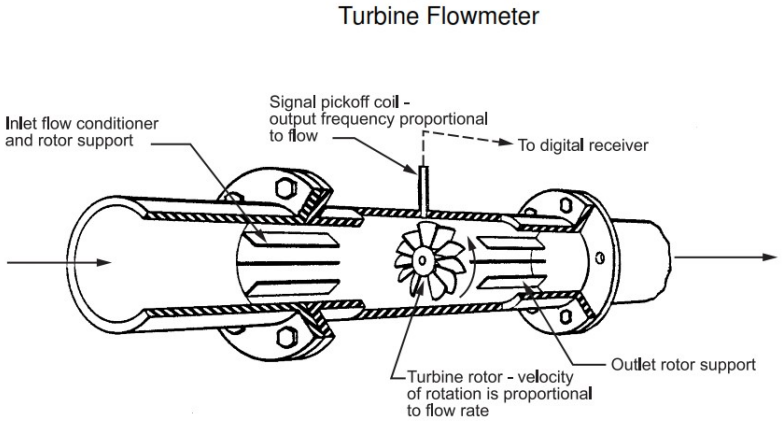

Figure 1.6: Schematic illustration showing the working principle of a turbine flow meter [159].

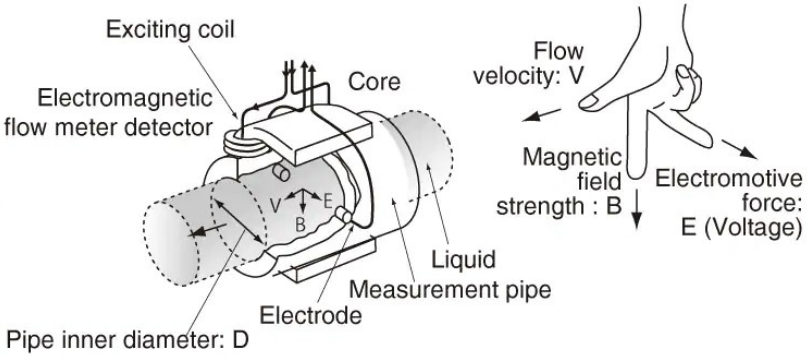

Figure 1.7: Schematic illustration showing the working principle of an electromagnetic flow meter [120].

the equation bearing his name. Based on Bernoulli's principle, Giovanni Battista Venturi (1746-1822) discovered in the 18th century the phenomenon named after him, *i.e.* Venturi effect. In his book "Recherches Experimentales sur le Principe de la Communication Latérale du Mouvement dans les Fluides Appliqué à l'explication de Differents Phénomenes Hydrauliques" published in (1797) [163], Venturi stated that the velocity of a fluid passing through a constricted section of a pipe increases while its static pressure decreases (Fig. 1.5). Based on his work, Clemens Herschel (1842-1930) developed in 1887 the commercial Venturi tube used to measure flow rate [68].

During the same decade in which Venturi published his work, Reinhard Woltman (1757-1837) developed in 1790 another type of flow measuring devices, known as turbine flow meters. As shown in Fig. 1.6, these meters consist of a multi-bladed rotor angled in such a way to transform the energy of the flow into rotational energy. The flow rate is determined from the angular velocity of the rotating rotor to which it is directly proportional [9, 26].

Flow measurement techniques were further developed in the 19th century. One can mention the pioneering work of Michael Faraday (1791-1867) who carried out in 1832 experiments in which he attempted to measure the flow rate of the river Thames, using his laws of electromagnetic induction[53]. The idea behind his experiments, which turned out to be unsuccessful, was to measure the voltage generated by the river's flowing water through earth's magnetic field. Later on, in 1851, Charlton Wollaston carried out similar experiments

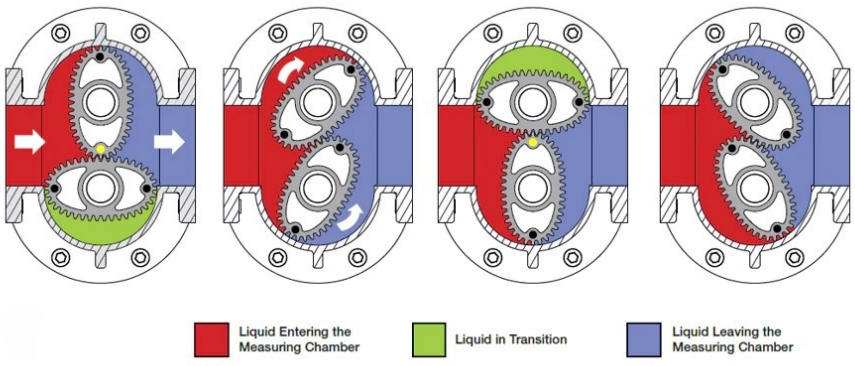

Figure 1.8: Schematic illustration showing the working principle of a positive displacement flow meter [127].

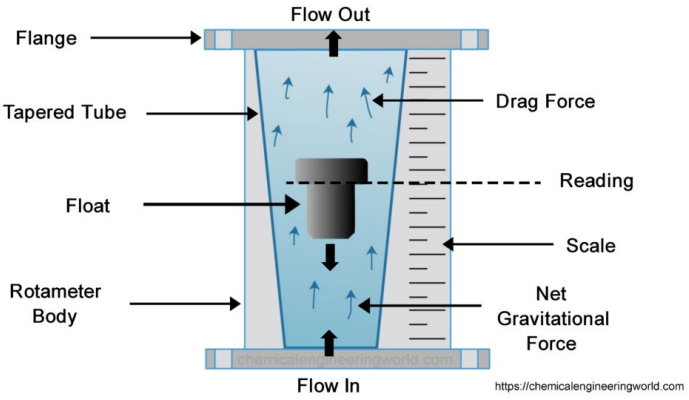

Figure 1.9: Schematic illustration showing the working principle of Variable area flow meters ("Rotameter") [131].

with success[91]. The operating principle behind electromagnetic flow meters (Fig. 1.7) is based on Faraday's law, according to which a conductive liquid flowing inside a pipe through a magnetic field, generates an electromotive force that is proportional to the strength of the magnetic field, the pipe's inner diameter and flow velocity [9, 26]. The first commercial electromagnetic flow meter was introduced in 1952 by the Dutch Tobi-meter Company.

During the same century, positive-displacement flow meters appeared through Samuel Clegg's invention of the gas meter in 1815 [155]. Positive-displacement flow meters are widely used as residential water meters. They operate by passing the fluid through rotating components of a chamber with a fixed volume. Each rotation of the components, translating the passage of a known discrete volume, produces an electronic pulse to record the passing volume. The flow rate is measured by counting the number of times the chamber fills, which is deduced from the number of rotations (Fig. 1.8).

The 20th century saw the development and commercialisation of several new flow meters. In 1908, Karl Kueppers (1874–1933) invented and patented the first variable area flow meter (German patent 215225). This type of meters consists of a tapered metering tube containing a float that is pushed up by the flow and pulled down by gravity. When the flow rate increases the float rises in the tube to increase the area for the passage of the fluid (Fig. 1.9). The flow rate is then measured according to the height of the float.

In 1959, Shigeo Satomura developed the first ultrasonic flow meter based on Doppler effect, for blood analysis [132]. Doppler ultrasonic flow meters are not suitable for clean liquids and require the presence of sonically reflective materials such as solid particles and air bubbles in the flowing liquid. These Doppler flow meters operate by measuring the frequency shift of ultrasound waves that are transmitted then received by a sensor after

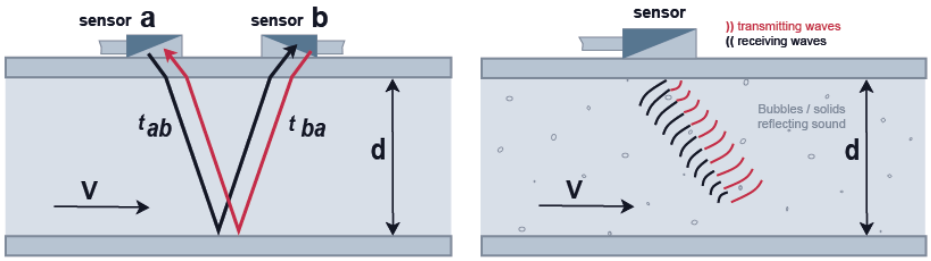

Figure 1.10: Schematic illustration showing the working principle of transit time difference (left) and Doppler (right) ultrasonic flow meters [160].

being reflected by the moving particles (Fig. 1.10(right)). The measured frequency shift is directly proportional to the flow velocity from which the flow rate is determined [9]. In the 1990s, Transit time (time of flight) ultrasonic flow meters were developed[125]. This type of technology measures the time it takes for an ultrasonic wave to reach the other side of a pipe wall in the two cases where it propagates in the same direction of flow and in the opposite direction (Fig. 1.10(left)). The time difference is proportional to flow velocity of the fluid in the pipe.

Mass flow meters appeared in the market in the second half of 20th century. In 1979, the company "Micro Motion Inc." [17] introduced the first Coriolis mass flow meter based on Coriolis effect which was described in an 1835 paper published by Gaspard-Gustave de Coriolis (1792-1843)[41]. Thermal mass flow meters emerged in the 1960s and 1970s. They operate according to King's law, published by L.V. King in 1914 [81], which describes mathematically the heat transfer in flows and the velocity at a point in the flow. The working principle of thermal and Coriolis flow meters is described with details in Section 2.2. The significant events that contributed to the evolution of flow measurement methods and which we described above, are summarized in the timeline diagram shown in Fig. 1.11.

Towards Nano-flow Rates

In this thesis we are interested in the measurement of a range of liquid flow rates that cannot be covered by most of the above mentioned flow meters. These flow rates range from 1 nL/min to 1000 nL/min and are defined as nano-flow rates. In order to give an idea on how low are these rates, we determine the time necessary to form an average drop of water at a flow rate of 1 nL/min. The equation that gives the volumetric flow rate Q_V is written as the time derivative of the liquid's volume V:

$$Q_V = \frac{dV}{dt} \tag{1.1}$$

The average volume of a water drop is roughly equal to 50 μL which corresponds to a diameter of about 4.5 mm. The time needed to form this volume is given by:

$$t = \frac{V_{\text{drop}}}{Q_V} = \frac{5 \times 10^4[\text{nL}]}{1[\text{nL/min}]} \simeq 35 \text{ days} \tag{1.2}$$

This means that one needs to wait more than a month to get a drop of water with a diameter of about 4.5 mm. Even more remarkable, one needs to wait more than 300 000 years to fill a bathtub of 160 L, at 1 nL/min.

After having defined the concept of flow rate and described the methods and devices traditionally used to the measurement of a wide range of them, we focus on the scale of nano-flow rates. In the following section, we present two projects that have brought together national metrology institutes, universities and even hospitals with the same objective: filling the void caused by the lack of measurement and calibration techniques for extremely low flow rates.

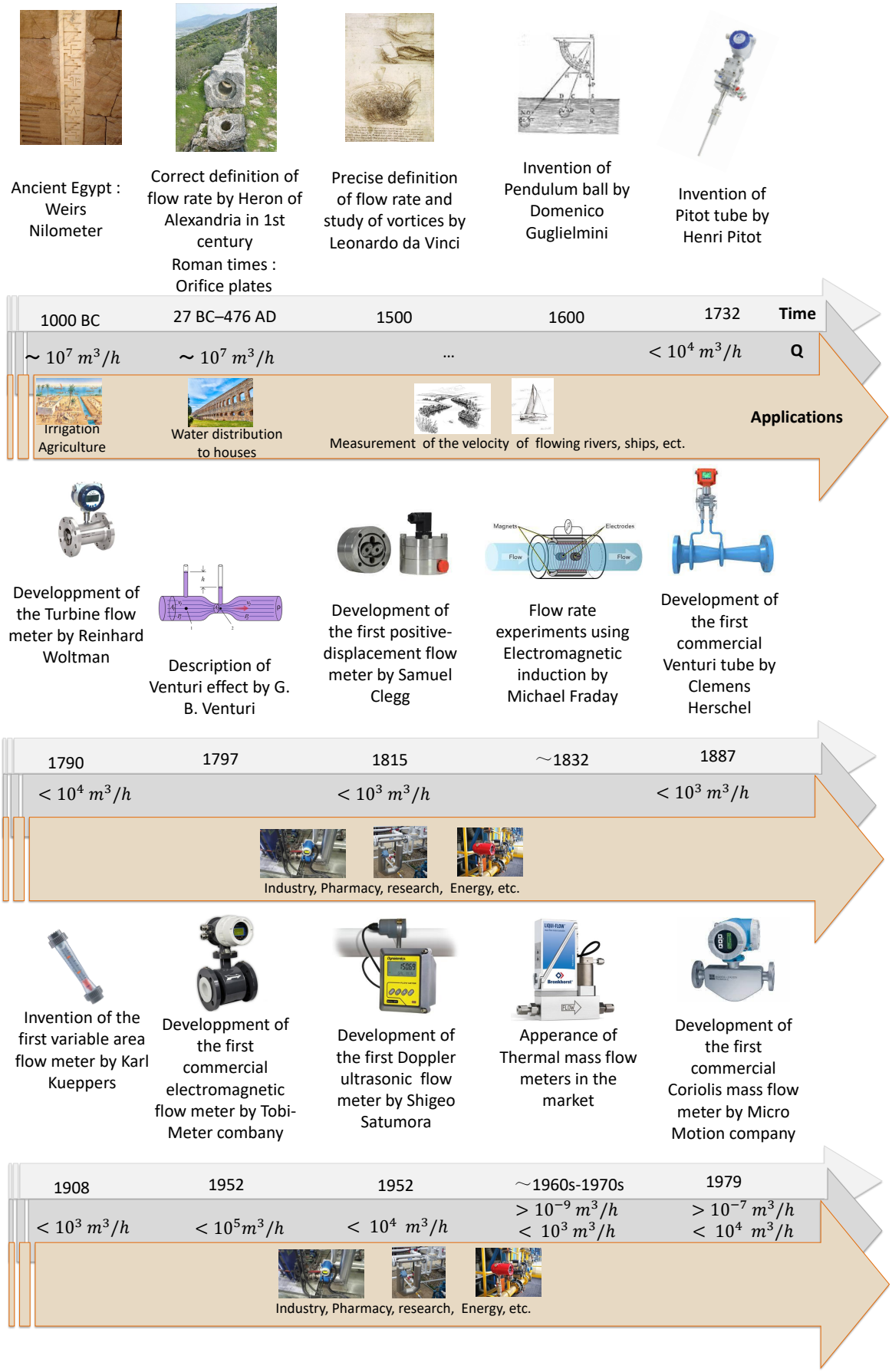

Figure 1.11: Timeline diagram describing the history of flow measurement methods.

1.2 Metrology for Drug Delivery Projects

This thesis was carried out in the context of the "Metrology for Drug Delivery II" (MeDD II) European project. This project is the following up of a previous project, "Metrology for Drug Delivery I" (MeDD I), in which flow rates down to 2 μL/min were calibrated [25]. In the following, we present the first MeDD project and briefly recall its main results. After that, we move on to the MeDD II project of which we specify the main objectives and the participating institutes. The results of this project are part of the work carried out in this thesis and will be presented in Chapter 6.

Metrology for Drug Delivery (JRP HLT07 MeDD) is a European joint research project that was carried out with funding by EMRP as part of the 2011 call in the "Health, SI Broader Scope and New Technologies" field. This project aimed to improve the metrological infrastructure for pharmaceutical drug delivery in order to ensure accurate and efficient treatments, and improve patient safety. This goal was to be achieved by the development of primary standards for flow rate measurements down to 1 nL/min. The project was started in 2012 and finalized in 2015. It involved metrology institutes, academia and hospitals such as: the French Technical Center CETIAT, VSL (Germany, the coordinator of this project), CMI (Czech Republic), DTI (Danemark), IPQ (Portugal), METAS (Switzerland), TÜBİTAK (Turkey), THL (Germany) and UMC (Netherlands). The specific MeDD I project objectives were the following:

1. Development and characterisation of primary standards for liquid flow rates ranging from 10 ml/min down to 1 nL/min with a target uncertainty better than 0.5 %.

2. Characterisation of commercially available flow meters by investigating flow fluctuations and the influence of various physical parameters and connectors.

3. Metrological assessment and characterisation of drug delivery systems. This included the delivery systems as well as the tubing and needles used to deliver the drugs.

In order to realise the required metrological infrastructure, several primary standards have been developed. The associated working principles were mainly based on the gravimetric method. For flow rates lower than roughly 5 μL/min, the front tracking and volume expansion methods were used. These systems will be described in detail in Section 2.1.

In order to validate the developed standards, interlaboratory comparisons were organised. These intercomparisons were based on the calibration of several flow meters and a syringe pump by the different partners. The table in Fig. 1.12 shows the flow rate range and the associated expanded uncertainty measured by each laboratory. The comparison results showed that all standards are consistent with each other within the claimed uncertainties and for a flow range of 3 μL/h to 600 mL/h (equivalent to 3 mg/h to 600 g/h),

Organisation	Mass flow rate range	Volumetric flow rate range	Uncertainty (k=2)
CETIAT	1 g/h – 8000 g/h	1 ml/h – 2 l/h	0.6 % - 0.1 %
DTI	1 g/h – 6000 g/h	1 ml/h1 – 6l/h	5 % - 0.05 %
IPQ	0.12 g/h – 600 g/h	120 µl/min – 0.6 l/h	6 % - 0.15 %
METAS	0.006 g/h – 60 g/h	6 µl/h – 60 ml/h	0.6 % – 0.1 %
VSL	0.25 g/h – 600 g/h	0.25 ml/h – 0.6 l/h	1 % – 0.1 %

Figure 1.12: Flow ranges and the associated relative expanded uncertainties of the developed standards. The given mass flow rates were divided by the density of water at the calibration temperature to obtain the volumetric flow rates [24].

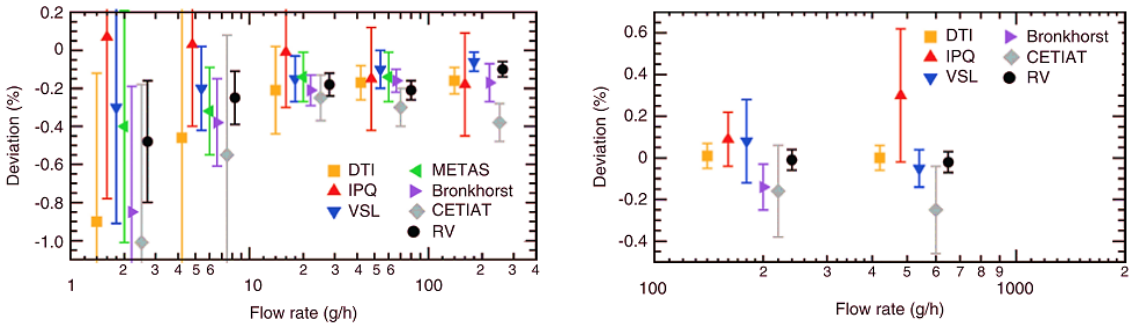

Figure 1.13: Relatives measurement errors for different mass flow rates, obtained by the calibration of a flow meter against the standards developed, in the context of the intercomparison [25].

see Fig. 1.13. Following these intercomparisons, three project partners (VSL, METAS and IPQ) have claimed Calibration and Measurement Capability (CMC) entries at the BIPM or country-specific accreditation. The uncertainties obtained range from 0.6% for the lowest flow rate, *i.e.* 6 μL/h to 0.05% for the highest flow rate, *i.e.* 6 L/h [25, 24].

As a continuation to the first MeDD project, MeDD II (18HLT08) was created in 2019 (Fig. 1.14). The main goal of this project was to ensure the traceability to S.I. of Units of volume, flow and pressure measurements and improve the accuracy of drug delivery devices for flow rates of at least an order of magnitude lower than those measured in MeDD. This was to be accomplished through the development of new primary standards and calibration methods that would expand the existing metrological infrastructure. The project also aimed to study fluctuating flow rates, the physical properties of mixtures and occlusion phenomena in multi-infusion systems, allowing a complete characterization of drug delivery devices.

More specifically, the main objectives of the project are the following [121, 13] :

1. Development of new primary methods for the measurement of flow rates going down to 5 nL/min with a measurement uncertainty of 1 % (k=2) for steady flows and 2 % (k=2) for fluctuating flow rates. These methods will allow the study of the response or delay time of medical flow devices (e.g. infusion pumps, pain controllers and infusion pump analysers).

2. Upgrade of the existing flow facilities of the participating NMIs in order to enable traceable measurements of the dynamic viscosity of Newtonian liquids as a function of the flow rate and pressure difference, with a target uncertainty of 2 % (k=2).

3. Development of a proof-of-concept on-chip microfluidic pump that generates flow rates lower than 100 nL/min and can be used as a transfer standard in microfluidics applications e.g. drug discovery and organs-on-a-chip.

The developed primary systems are based on different methods namely: the gravimetric (METAS, DTI, RISE), interface or front tracking (CETIAT, THL), interferometric (IPQ) and micro-PIV methods (NEL, HS). These will be described in detail in Section 2.1. In order to validate the different methods, an interlaboratory comparison was carried out for flow rates ranging from 5 nL/min to 1500 nL/min. The comparison's protocol and results are presented in Chapter 6.

The presented projects were created to develop new techniques that cover lower flow rates. From this, questions arise as to why we are interested in the measurement of nano-flow rates and where we can encounter them. To answer these questions, we present in the following

Figure 1.14: Photograph of MeDD II participants at the project meeting hosted by METAS, Switzerland.

section the main applications where low flow rates play an important role. Contrary to what one may think, nano-flow rates can be encountered in a large range of fields. For this reason, we decided to focus only on the medical field, as it is at the heart of the project MeDD II, and microfluidics which generally involves flows within small channels, at low rates.

1.3 Low Flow Rate Applications

We devote this section to the presentation of various applications involving nano-flows. In doing so, we want to demonstrate the important role that nano-flows play in scientific research applications but also in the health sector, where patient safety is at the center.

1.3.1 Drug Delivery

In the medical field, drugs are delivered using different devices such as syringe pumps, and portable and implantable infusion pumps. The most common used portable infusion devices are most likely insulin pumps. According to HAS ("Haute Autorité de Santé") there are about 62500 patients using insulin pumps in France, during the year 2020 [118]. For some patients, insulin is delivered continuously at very low basal rates. The latter is defined as the specific amount of insulin that the pump continuously delivers each hour. As an example, "Medtronic MiniMed" pump can deliver a minimal basal rate of 0.025 units/h for U-300 insulin (300 units of 1 mL total volume), which is equivalent to a continuous insulin flow rate of about 1 nL/min [98]. The use of portable infusion pumps is also common in Pulmonary Arterial Hypertension treatment by the administration of Treprostinil [12, 140].

Implanted infusion pumps are small devices placed under the skin for intravenous, intra-arterial, subcutaneous, etc. drug delivery. Contrary to other methods, they can provide targeted and consistent medicine by sending medications through a catheter to a specific part of the patient's body. They are generally used for the treatment of chronic pain by the administration of pain killers at very low and controlled infusion rates. As an example, "Medtronic SynchroMed" implantable pump nominally delivers a minimal programmable flow rate of 0.048 mL/day which is equivalent to about 33 nL/min [1].

In hospitals, the most used drug delivery devices are syringe pumps. Applications such as critical care, anesthesia and pediatrics require the administration of drugs at precise and

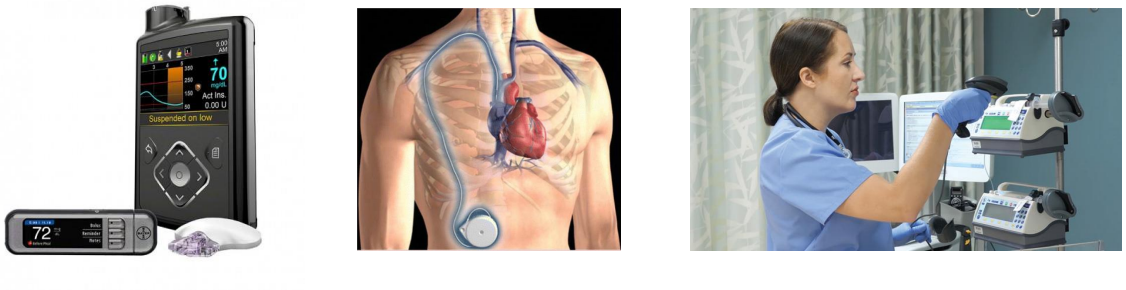

Figure 1.15: Picture of a Medtronic MiniMed infusion pump (left). Illustration of the Medtronic Synchromed pump implanted on the skin of a patient (middle). Photograph showing the Medfusion syringe pumps implemented in a hospital for drug delivery (right) [98, 1, 95].

controllable flow rates. As an example, the "Medfusion" syringe system, which is trusted in many US hospitals and is the most widely indicated syringe pump on the market, can deliver nominal flow rates going down to 0.01 mL/h, *i.e.* 167 nL/min, with a 2 % accuracy and high continuity[95].

1.3.2 Microfluidics

Flow rate is an important parameter in microfluidics applications, especially those involving droplet generation and Organs-on-a-chip [144]. Droplet-based microfluidics is employed for example in polymerase chain reaction (PCR) analyses [174], enzyme kinetics studies [149], cell cultures [96], functional component encapsulation [64], polymeric particle synthesis [89], etc. Hong *et al.* [71] investigated numerically the effect of flow rate on droplet formation in a co-flow geometry. They showed that by changing the flow rate ratio Q_d/Q_c of the dispersed and continuous phases, the generated droplets transit from a state where their size and frequency are strongly dependent on the flow rate ratio to a state where they are almost independent of the ratio. More specifically, they showed that when $Q_d/Q_c \geq 1$ droplets' size control was easier since it depended weakly on the generated flow rates and instead depended on the capillary number. In addition, the frequency of the droplets was shown to

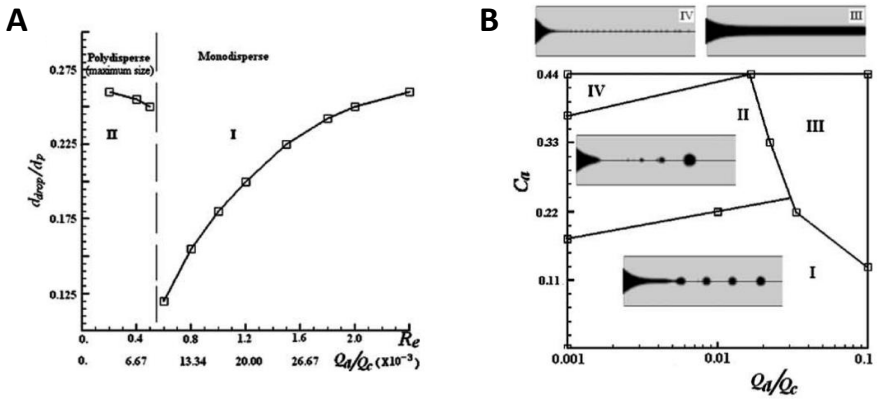

Figure 1.16: (A) Images of four drop patterns, produced in a co-flow geometry, for a flow rate ratio $Q_d/Q_c < 0.1$. (B) Diameters of the generated droplets as a function of Reynolds number R_e and the ratio Q_d/Q_c at a Capillary number $C_a = 0.221$ [71]

be proportional to the flow rate of the dispersed phase Q_d in the same range of flow ratios. In the case where $Q_d/Q_c < 1$, the droplets' size and pattern were changed by adjusting the input flow rates (Fig. 1.16).

Zhu *et al.* [181] studied droplet generation in a co-flow geometry under fluctuating flow rates of the dispersed phase. The flow was perturbed by applying mechanical vibrations, of specific frequencies and amplitudes to the microfluidics channel containing the inner fluid. They showed that for frequencies lower than the natural generation frequency of droplets f_d, the formation of these was perturbed resulting in a polydisperse size distribution. By subjecting the tubing to vibrations with a frequency in the range of f_d to a critical value the droplets were monodisperse and generated with the same frequency as that of the applied vibrations. In this synchronization region droplet size can be modulated in a wide range. Above the critical value the generation frequency and droplet size were weakly affected by the frequency of vibrations. The droplet size and uniformity in this region was rather affected by the vibrations' amplitude which at high values causes important flow rate fluctuations that can be negative in some cases. The induced flow rate fluctuations change the local force balance where the droplets break up and as a consequence, can be exploited to modulate the droplets' size, uniformity and generation frequency (Fig. 1.17).

Costa *et al.* [43] studied the formation regimes of water-in-oil droplets, generated in a flow-focusing device, under the influence of flow rate and flow rate ratio of the dispersed and continuous phases. The flows were generated by syringe pumps with flow rates ranging from 500 nL/min to 6 μL/min. For a flow rate ratio lower than 0.5, droplets were generated in dripping regime, the latter corresponding to a droplet formation mode in which the droplets detach at the orifice. For a ratio between 0.5 and 1 the squeezing regime and larger droplet sizes were observed. Droplets were not able to form when the flow rate of the dispersed

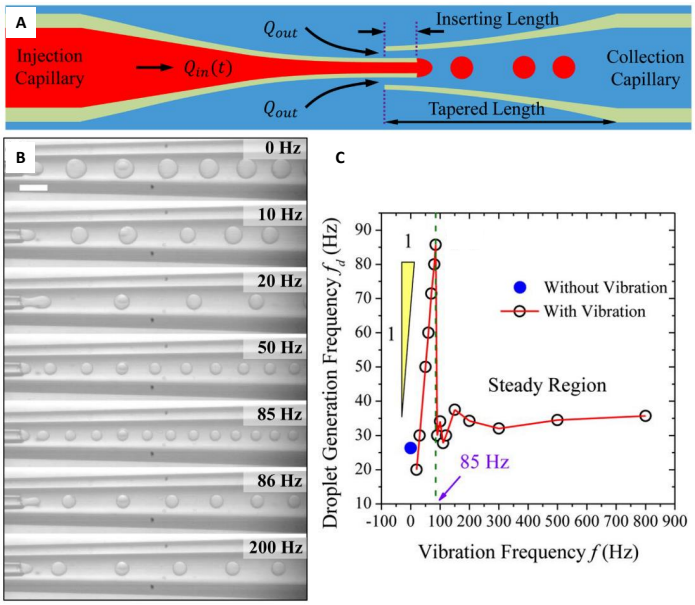

Figure 1.17: Effects of vibration frequency on droplet generation, in a co-flow geometry. (a) Schematic of the microfluidics channel's geometry. $Q_{in}(t)$ is the fluctuating flow rate of the inner phase, due to the generated vibrations. Q_{out} is the flow rate of the outer phase. (b) Images of droplet generation with increasing vibration frequencies, at the flow rates $Q_{in} = 80$ μL/h and $Q_{out} = 1$ mL/h. The frequency of the generated vibrations is marked on the upper right corner of each image. (c) Plots of droplet generation frequency f_d versus vibration frequency f at the same conditions as (b) [181].

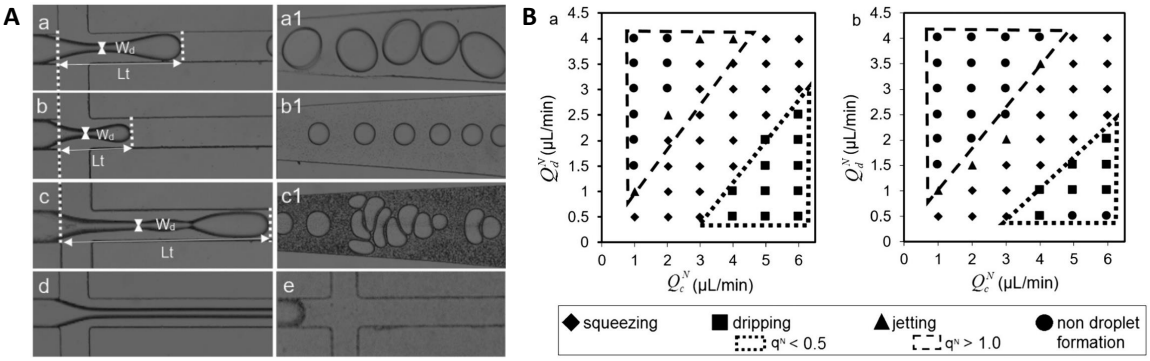

Figure 1.18: Droplet formation regimes. (A) Microscope images of Gellan droplets produced using a flow-focusing geometry at the beginning and end of the process. The flow rate of the dispersed phase $Q_d^N = 0.5$ µL/min and continuous phase Q_c^N : (a and a1) 1.0 µL/min (squeezing regime), (b and b1) 4.0 µL/min (dripping regime) and (d) 1.0 µL/min (non droplet formation). For $Q_d^N = 1.5$ µL/min: (c and c1) $Q_c^N = 2.0$ µL/min (jetting regime) and (e) $Q_c^N = 1.0$ µL/min (non droplet formation). (B) Droplets formation regimes as a function of nominal flow rate of the phases. The dispersed phase in (a) is water and (b) aqueous solution of gellan [43].

phase exceeded that of the continuous phase. The jetting regime was observed at flow ratios greater than 1 and represented a transition between the formation and non-formation regimes (Fig. 1.18). Jetting occurs when the inner phase forms a jet that breaks, away from the orifice, to form droplets. The droplets' size and monodispercity also was affected by the flow rate of the continuous phase which, increasing, led to smaller and more uniform droplets.

Low flow rates are also present in Organ-on-chip applications that generally include cell cultures, whose physiological and chemical environment is controlled by the injection of nutrients at low flow rates. In their studies of drug toxicity on human hepatocytes, Lee *et*

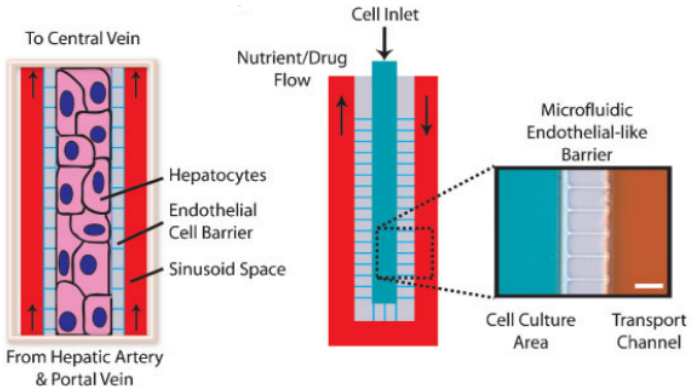

Figure 1.19: Schematic illustration of the microfluidic liver sinusoid. The hepatocyte culture area (blue) is separated from the nutrient transport channel (red) by parallel microfluidic channels with small cross-sections. This creates a high fluidic resistance into the cell culture which concentrates the cells in the culture area and minimizes convective flow through the cell culture region while allowing diffusive transport [88].

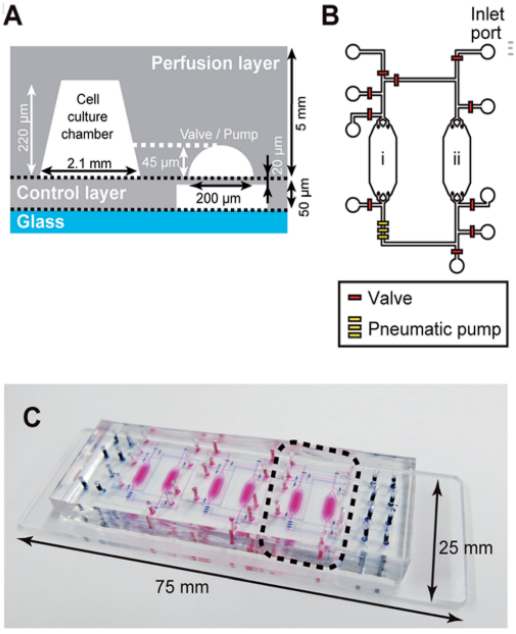

Figure 1.20: Design of the microfluidic chip used for iHCC. (A) Illustration of the side view of the chip. (B) Circulation loop that mimics the blood circulatory system and interconnects the different cell tissues.(C) Photograph of an actual iHCC chip [80].

al. [88] created an artificial liver sinusoid on a microfluidics chip with an endothelial-like barrier represented by a set of parallel channels (Fig. 1.19). The hepatocytes culture was fed by the passage of nutrients through the endothelial-like barrier at controlled flow rate of 10 nL/min, necessary for maintaining cell survival within the microfluidic chip.

In their study of the side effects of the anti-cancer drug doxorubicin, Kamei *et al.* [80] developed an integrated Heart/Cancer on a Chip (iHCC) using human healthy heart cells and liver cancer cells. The microfluidic chip included an artificial blood circulatory system in the form of a closed circulation loop in order to connect the different cell tissues (Fig. 1.20). Pneumatic valves and a peristaltic micropump were microfabricated and integrated in the chip for precision flow control. The drugs and metabolites were moved from a chamber to another through the loop at a generated flow rate of 26 nL/min.

1.3.3 Inkjet Printing

Electrohydrodynamic jet (e-jet) printing is a high resolution (down to 50 nm) printing technology where the printed liquid is driven by an electric field [101]. More specifically, the ink is pulled from a nozzle tip by imposing a voltage between the nozzle and an opposing conducting support. Different jetting modes are possible depending on the strength of the electric field and the flow rate (Fig. 1.21). The pulsating mode (characterized by the ejection of distinct droplets) and the cone-jet mode (characterized by a continuous stream of liquid) are favored in patterning processes as they allow the deposition of individual droplets and lines with micro- and nano-metric sizes, as noted above. In these modes, the flow rate plays an important role in setting the frequency of the ejected droplets and the diameter and stability of the jet [110]. For instance, in the cone-jet mode and for flow rates ranging from 300 nL/min and 1300 nL/min, the pattern's width is directly proportional to the flow rate, however the length of the jet decreases with increasing in the flow rates due to instabilities [38].

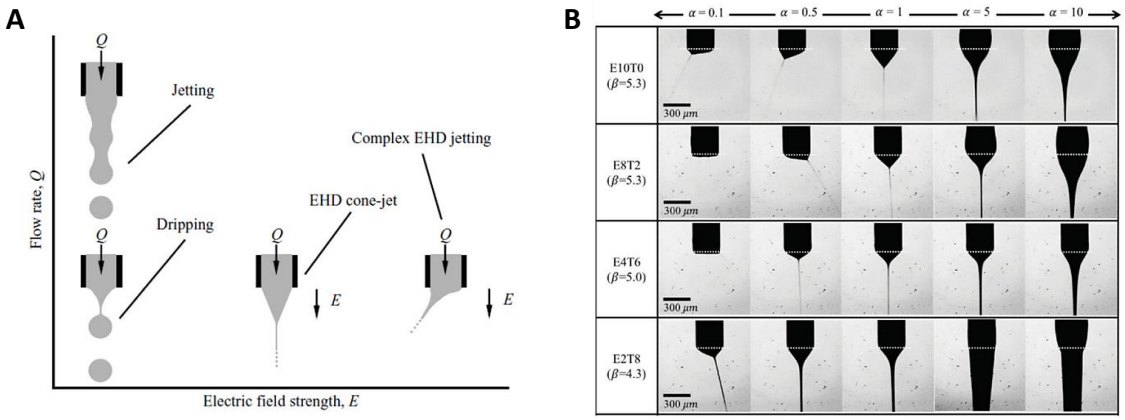

Figure 1.21: Formation of electrohydrodynamically produced jets. (A) Modes of jetting depending on the flow rate and applied electric tension [40]. (B) Produced Jets of mixtures (ethanol and terpineol) depending on the values of the dimensionless parameters: β for flow rate and α for voltage [110].

1.3.4 Nano-liquid Chromatography

Liquid chromatography is an analytical separation technique based on the separation of compounds that are carried by a liquid through a solid, depending on the interactions between the compounds and the liquid and solid phases (Fig. 1.22). In the case of Nano-Liquid Chromatography (Nano-LC) the separations are performed using columns of 10–100 μm internal diameter and mobile phase flow rates of the order of 10-1000 nL/min [37]. Nano-LC is applied in many pharmaceutical and biomedical applications such as the analyses of proteins and peptides (50 nL/min) [93], biomarkers (350 nL/min) [141], drugs (190 nL/min) [47] and forensic analyses (0.4 nL/min) [180]. Nano-flow rates have permitted to achieve better mass and concentration sensitivity compared to the conventional LC [37]. It is extremely important during the analyses to maintain the flow rate at the required value. As a matter of fact, flow rates higher than required may affect the quality of the separation, as the compounds do not have enough time to interact with the stationary phase. Likewise, a lower flow rate than the required one expands analyses' time and causes delays in the appearance of the peak [138, 129, 60]. As a consequence a special care was given to the choice of the flow generating pump [60, 37].

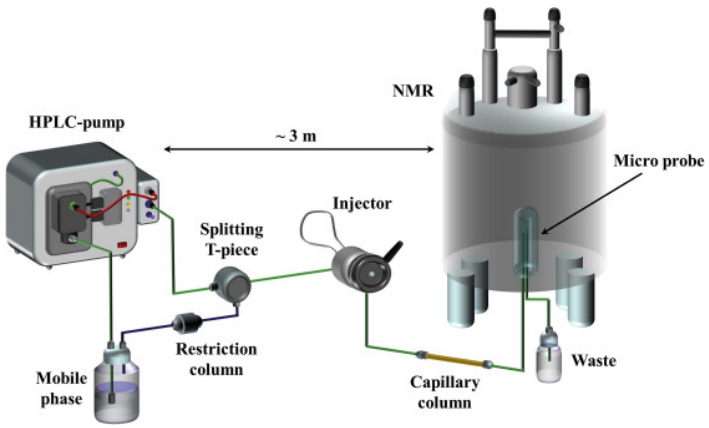

Figure 1.22: Schematic illustration of the experimental setup for nano-liquid chromatography [52].

In the last sections, we defined liquid nano-flow rates and outlined the main applications where they play an important role. We also presented two european projects in the context of which national primary standards were developed. We recall here the main objective of this thesis that is part of the project MeDD II:

> *"Development of a primary standard for the calibration of devices which operate at nano-flow rates, in order to ensure the measurements' traceability to the S.I. of Units."*

In this statement only, one can notice the intensive use of a particular vocabulary which refers to various metrological concepts, placing metrology at the very center of this thesis. Thus, before moving on to the next chapter, we believe that it is essential to recall the definitions of the main metrological concepts that are important for understanding the structure and purpose of this thesis work.

1.4 Metrology Vocabulary and Concepts

We devote this section to the definition of the metrological concepts necessary for the understanding of this thesis, after which we briefly explain the procedure of interlaboratory comparisons that we used for the external validation of our system. The information provided here correspond to the official definitions given in the VIM [22] and GUM [79]. These two guides were established by the JCGM which is formed by 7 international organisations such as BIPM and ISO, for example.

1.4.1 Definitions Related to Measurements and Standards

Measurement standard: Realization of the definition of a given quantity, with stated quantity value and associated measurement uncertainty, used as a reference.

Primary Standard: Measurement standard established using a primary reference measurement procedure, or created as an artifact, chosen by convention.

Secondary Standard : Measurement standard established through calibration with respect to a primary measurement standard for a quantity of the same kind.

Calibration: Operation that, under specified conditions, in a first step, establishes a relation between the quantity values with measurement uncertainties provided by measurement standards and corresponding indications with associated measurement uncertainties and, in a second step, uses this information to establish a relation for obtaining a measurement result from an indication.

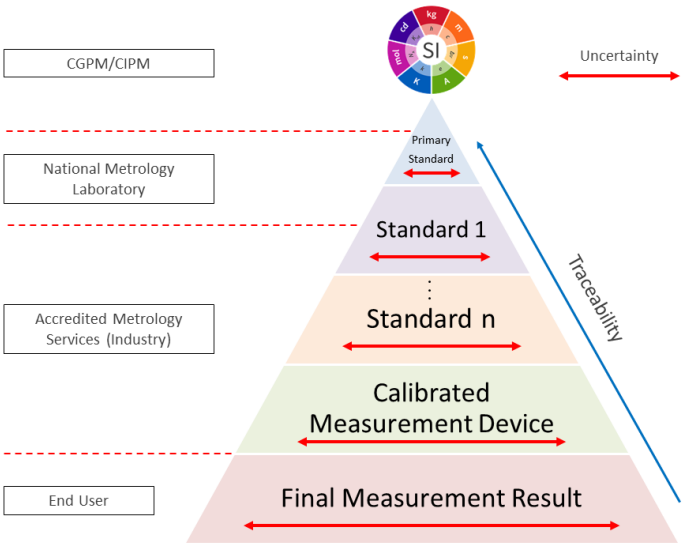

Figure 1.23: Schematic illustration explaining the traceability chain to the I.S. of Units [171].

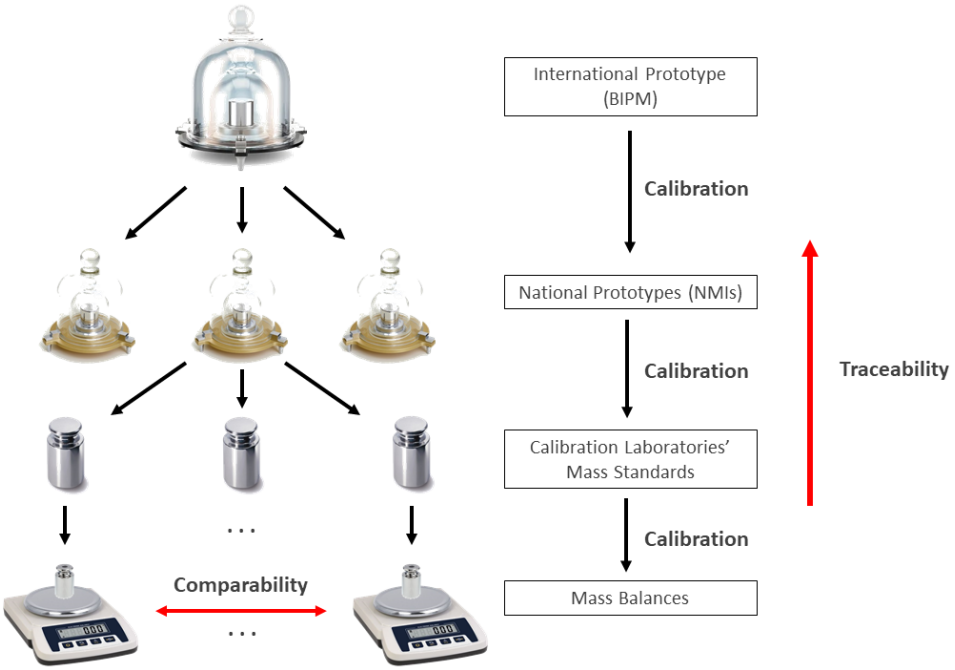

Figure 1.24: Schematic illustration showing the mass calibration chain using the International Prototype of the Kilogram. This artefact is not a primary standard anymore since 2019. [105].

Traceability: property of a measurement result whereby the result can be related to a reference through a documented unbroken chain of calibrations, each contributing to the measurement uncertainty.

1.4.2 Definitions Related to Measurement Uncertainty

Standard uncertainty: uncertainty of the result of a measurement expressed as a standard deviation.

Expanded uncertainty: quantity defining an interval about the result of a measurement that may be expected to encompass a large fraction of the distribution of values that could reasonably be attributed to the measurand.

Coverage Factor k: number larger than one by which a combined standard measurement uncertainty is multiplied to obtain an expanded measurement uncertainty. The value of k is chosen depending on the level of confidence required for the interval y-U to $y + U$.

Repeatability: measurement precision under a set of repeatability conditions of measurement. A repeatability condition being condition of measurement, out of a set of conditions that includes the same measurement procedure, same operators, same measuring system, same operating conditions and same location, and replicate measurements on the same or similar objects over a short period of time.

Reproductibility: measurement precision under reproducibility conditions of measurement. A reproducibility condition being a condition of measurement, out of a set of conditions that includes different locations, operators, measuring systems, and replicate measurements on the same or similar objects.

Combined Uncertainty: the standard uncertainty of the result of a measurement when that result is obtained from the values of a number of other quantities, equal to the positive square root of a sum of terms, the terms being the variances or covariances of these other quantities weighted according to how the measurement result varies with changes in these quantities.

Generally, a measurand Y is not measured directly, but is determined from N other quantities $X_1, X_2, ..., X_N$ through a function $f = (X_1, X_2, ..., X_N)$ relating these quantities. By taking y as the measurement result of Y, and given that all input quantities are independent, the standard uncertainty of y, denoted $u_c(y)$, is obtained by combining the standard uncertainties of each quantity estimate as follows:

Type	Normal	Uniform (Rectangular)	Triangular
Graphical Distribution	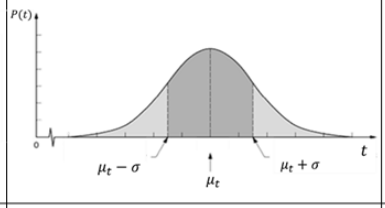	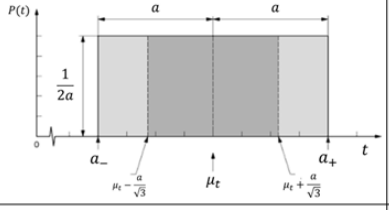	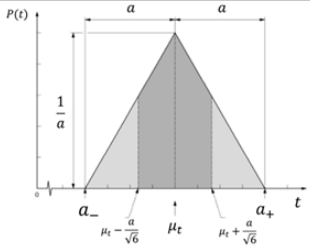
Probability density function	$p(t) = \frac{1}{\sigma\sqrt{2\pi}} e^{-\frac{1}{2}\left(\frac{t-\mu_t}{\sigma}\right)^2}$	$p(t) = \frac{1}{2a}$, $a_- \le t \le a_+$ $p(t) = 0$, *otherwise*	$p(t) = \frac{t-a_-}{a^2}$, $a_- \le t \le \frac{a_- + a_+}{2}$ $p(t) = \frac{a_+ - t}{a^2}$, $\frac{a_- + a_+}{2} \le t \le a_+$ $p(t) = 0$, *otherwise*
Use	When the values of the quantity t that are obtained from reapeated measurements are shown to follow a normal distribution with expectation μ_t and standard deviation σ	When the variation limits of the quantity t are known but little information is available about its distribution. What is done is to suppose that t is described by a symmetric, uniform probability distribution of lower limit a_- and upper limit a_+. The best estimate of t is its expectation $\mu_t = \frac{a_+ + a_-}{2}$	When the variation limits of the quantity t and its most likely value are known but little information is available about its distribution. What is done is to suppose that t is described by a symmetric, triangular probability distribution of lower limit a_- and upper limit a_+. The best estimate of t is its expectation $\mu_t = \frac{a_+ + a_-}{2}$
Standard Uncertainty	$u(\mu_t) = \sigma$	$u(\mu_t) = \frac{a}{\sqrt{3}}$	$u(\mu_t) = \frac{a}{\sqrt{6}}$
Example	Uncertainty from a calibration certificate	Resolution of a degital readout	Uncertainty associated with temperature variation in a temperature-controlled room

Figure 1.25: Uncertainty distributions and the associated standard uncertainties, with examples of where they can be used.

$$u_c^2(y) = \sum_{i=1}^{N} \left(\frac{\partial f}{\partial x_i} \right)^2 u^2(x_i) \tag{1.3}$$

Where $f = (x_1, x_2, ..., x_N)$ is the functional relationship relating the quantity estimates $x_1, x_2, ..., x_N$.

The measurement error is defined as the measured quantity value minus a reference quantity value (Equation (1.4)). For example, measurement error is used for the comparison of the measurement values, given by an instrument under calibration, with reference values that are measured by a primary system.

$$e_{\text{absolute}} = x_{\text{measured}} - x_{\text{reference}} \tag{1.4}$$

It is sometimes called absolute error to distinguish it from the relative error which is defined as the error of measurement divided by a reference value of the measurand, as given in the equation below:

$$e_{\text{relative}}(\%) = \frac{x_{\text{measured}} - x_{\text{reference}}}{x_{\text{reference}}} \tag{1.5}$$

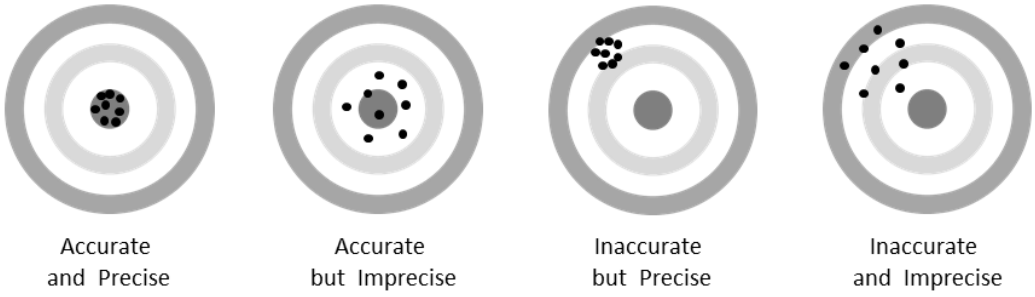

Figure 1.26: Schematic illustration explaining the difference between accuracy and precision

In order to determine the mean flow velocity or flow rate using our method (Chapter 3.2), we perform a linear regression on the measured positions of the meniscus y with respect to time x. The line that best fits our data is determined using the least squared method and is expressed by:

$$\hat{y} = \beta_0 + \beta_1 x \tag{1.6}$$

Where β_1 is the slope, which is equal to the flow velocity, and β_0 is the intercept.

In order to estimate the measurement uncertainty associated with the mean flow velocity we calculate what is known as the residual standard error (RSE). If the fit line was determined using n independent data points, in our case these are the positions of the meniscus and the associated timestamps, the degrees of freedom of their respective standard uncertainties is $d_f = n - 2$. The measurement uncertainty is, in this case, expressed by [79, 78]:

$$RSE = \sqrt{\frac{RSS}{d_f}} = \sqrt{\frac{\sum_{i=1}^{n} (y_i - \hat{y}_i)^2}{d_f}} \tag{1.7}$$

Where $RSS = \sum_{i=1}^{n} (y_i - \hat{y}_i)^2$ is the residual sum of squares, y_i the measured position, $\hat{y}_i$ the predicted position by the linear regression and $d_f = n - 2$ the degrees of freedom. n is the number of measured positions and $\bar{y} = \frac{\sum_{i=1}^{n} y_i}{n}$ the mean of the measured positions.

1.4.3 Interlaboratory Comparisons

An interlaboratory comparison (ILC) is the organization, performance and evaluation of measurements or tests on the same or similar items by two or more laboratories in accordance with predetermined conditions, as defined in the ISO/IEC 17043:2010 [76]. An ILC comparison can be organised in many different ways. The one adopted in our project is explained below and illustrated in Fig. 1.27. A detailed description of the testing procedure, conditions and tested items is presented in Chapter 6.

1. The test item is initially sent by the coordinating body to the first laboratory which tests the item under given conditions that are in accordance with the established comparison protocol.

2. The first laboratory forwards the item to the next laboratory which tests it under the same conditions, then forwards it to the following laboratory and so on.

3. The last laboratory to receive and test again the item is the first one.

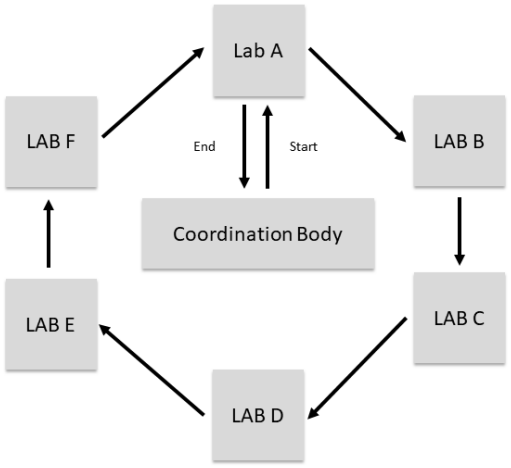

Figure 1.27: Schematic illustration of the organisation of an interlaboratory comparison

4. Each participant laboratory sends their test results to the coordinating body which evaluates the results and issues a comparison report.

In order to assess the quality and comparability of the measurements we determine for each laboratory the degree of equivalence [76, 18] which is calculated from the measurement errors, the associated uncertainties, the weighted mean value and the weighted uncertainty as shown in the equations below:

$$E_{n_i} = \frac{x_i - x_{REF}}{\sqrt{u(x_i)^2 - u(x_{REF})^2}} \tag{1.8}$$

$$x_{REF} = \frac{\sum x_i / u(x_i)^2}{\sqrt{\sum 1/u(x_i)^2}} \tag{1.9}$$

$$u(x_{REF}) = \frac{1}{\sqrt{\sum 1/u(x_i)^2}} \tag{1.10}$$

Where $x_i$is the relative measurement error of lab i at given flow rate, $u(x_i)$ is the measurement uncertainty of lab i at given flow rate, x_{REF} is the weighted mean value and $u(x_{REF})$ is the weighted uncertainty.

According to E_n's value, the measurement systems are validated or excluded as follows:

- $E_n \leq 1$ the results are considered satisfactory.
- $E_n > 1$ The results are considered unsatisfactory.

Chapter 2

Nano-flow Rate Measurement Methods

In the previous chapter, we described the evolution of liquid flow measurement methods starting from ancient egyptian times until the 20th century. We presented the working principle of various flow meters which operate at flow rates ranging from 10^{10}L/h down to 1 mL/h. Furthermore, we presented two projects and several applications that show the growing interest, mainly in the health and research sectors, for the measurement of nano-flow rates. At the end of the chapter, we defined the metrological concepts necessary to understand the purpose of this thesis.

In this chapter, we present the current state-of-the-art of primary flow measurement methods. These methods were developed by national metrology institutes in different European countries, in the framework of the "Metrology for Drug Delivery" projects. To conclude the chapter, we describe the thermal mass and Coriolis methods on which are based most of the flow meters that operate at low flow rates.

2.1 Primary Measurement Methods

2.1.1 Gravimetric Method

Most micro-flow calibration facilities in Europe are based on the gravimetric method. CETIAT[108, 56, 25], METAS[25, 23], IPQ[25, 16] and many other national metrology institutes possess their own national primary standard that is based on gravimetry. The calibration facilities of the NMIs may be different, but they are all based on the same principle: measuring the change in the mass of a collected liquid over time, under the effect of a generated flow [75, 25]. Fig 2.1 illustrates the most simple measurement setup for the gravimetric method. The mass flow rate Q_m writes as:

$$Q_m = \frac{\Delta m}{\Delta t} \tag{2.1}$$

where Δm is the change in the mass of the collected liquid and Δt is the time interval over which the mass change is measured.

In the remainder of this chapter, we describe the existing facilities developed by different NMIs based on the gravimetric method, starting by CETIAT. These facilities were mainly developed for the measurement of liquid micro- and milli-flow rates, as part of the project MeDD. Most of the developed calibration systems were adapted and improved during the project MeDD II, for the standardization of lower flow rates.

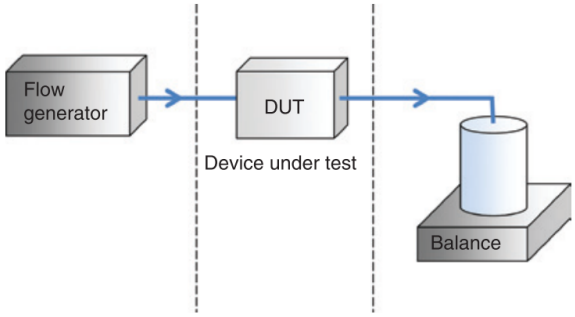

Figure 2.1: Illustration of the working principle of the gravimetric method [25].

CETIAT's Facility

The French national standard for liquid (water) flow is held by CETIAT, which is the French designated institute for liquid water flow, humidity, and air speed. For liquid flow, a new facility has been inaugurated and accredited in 2012 to extend the national standard down to micro-flow rates. CETIAT's facility consists of three main parts, shown in Fig. 2.2. In the first part, water is filtered, degassed and demineralised using a purification system. The ultra-pure water flows into a tank placed in a thermostatic chamber. In order to generate a flow rate, the pressure of the tank is regulated using a metal bellow. The temperature of the chamber can be adjusted from 10 °C to 50 °C in order to perform the measurements in the working conditions under consideration by the calibration. Under the generated pressure, water leaves the tank and flows towards another thermostatic chamber, through a thermally insulated tubing. The device to be calibrated lies on this second part of the facility. Naturally, the temperature of the second chamber is adjusted so as to maintain the same conditions in the whole system. Leaving the second chamber, water flows until it reaches a beaker in which it is collected. The beaker is placed on a weighing scale in order to measure the mass changes produced by the collected water. Water flows inside the beaker through a vertical stainless steel capillary with an inner diameter in the range of 100 μm to 500 μm.

In order to reduce water evaporation, the beaker is covered by leaving a hole around

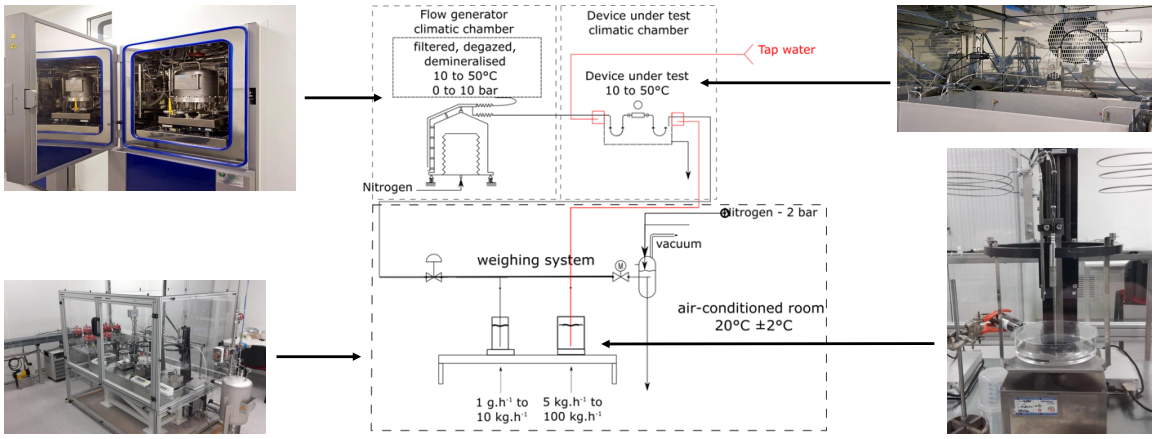

Figure 2.2: Schematic illustration with real photographs of CETIAT's gravimetric facility [25].

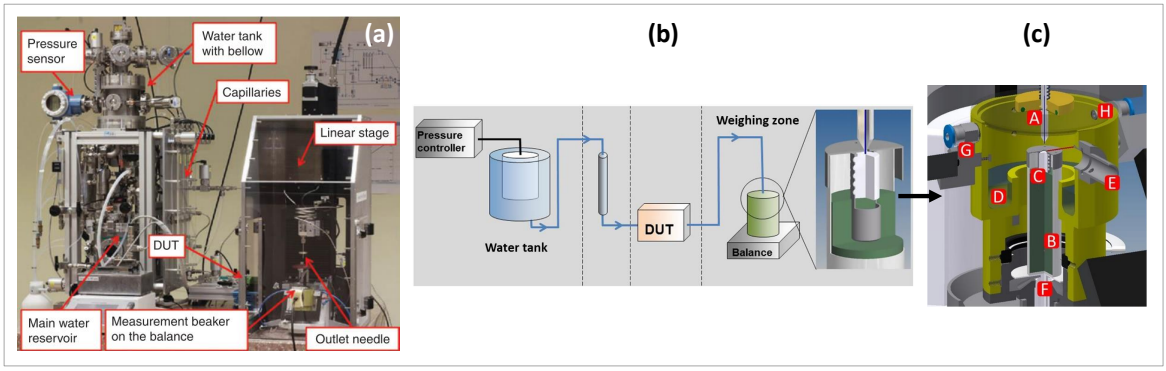

Figure 2.3: METAS' gravimetric primary system. (a) Photograph of the calibration facility. (b) Schematic Illustration of the experimental setup. (c) Schematic illustration of the beaker. A: outlet needle. B: measurement beaker. C: glass filter,D: water in evaporation trap. E: mount for temperture and humidity sensor. F: balance. G: tubing for humidity exchanger. H: cover [25].

the capillary, to avoid air saturation. Nevertheless, evaporation is measured before and after every calibration and used to correct the measured flow rate. As the capillary tube is immersed in water, other phenomena arise, creating new sources of uncertainty. These come essentially from buoyancy and capillary forces. In a move towards more accurate calibrations, CETIAT implemented new measurement procedures to quantify the encountered physical phenomena and to systematically correct the reported flow rate values [56].

In order to ensure the traceability of the measured masses to the S.I. of Units, the weighing scale is calibrated against mass standards which are previously calibrated in the national standard laboratory for mass (LNE) . The traceability of the timestamps recorded by the computer is ensured by the calibration of the computer's clock against CETIAT's Rubidium atomic clock that is calibrated against the French national standard for time and frequency, at LNE-SYRTE (Section 4.1.5). CETIAT's micro-flow facility covers static and dynamic (fluctuating) flow rates from 1 g/h to 100 Kg/h with a best expanded measurement uncertainty of 0.1 % (k=2) [25].

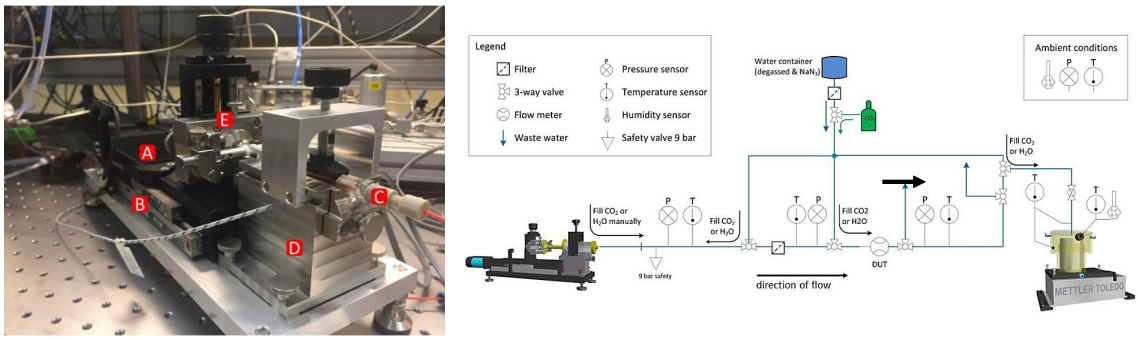

Figure 2.4: Photograph (left) and schematic illustration (right) of METAS' gravimetric bench [104].

METAS' Facility

The generation of a stable flow rate in METAS' micro-flow facility, is carried out in a similar way as in CETIAT. Mainly, a constant pressure drop is created between the water in the tank and the tip of a capillary tube, the latter which is connected to the collecting beaker. The inner diameter of the capillary and the imposed pressure drop determine the flow rate, according to Hagen-Poiseuille law. Special care is taken regarding the water's quality. To stop the growth of bacteria, water is treated with UV light or sodium azide which, if added in small amounts, does not affect water's density appreciably. In addition, the liquid is continuously degassed as it brought to flow in a closed loop, going from the water tank, through the tubing and back to the tank. In order to avoid air bubbles, the system is flushed with CO_2 and then with ultra pure water before the calibrations.

The beaker where water is collected is placed inside an evaporation trap within the weighing zone housing (Fig 2.3). To avoid condensation around the capillary tube because of the saturated air, the humidity is regulated by two holes that are located in the upper part of the housing and act as a humidity exchanger. Contrary to CETIAT's facility, the tip of the capillary is not immersed in water. Instead, it is placed at 50 μm above a glass filter that sucks by capillarity the water and avoids droplet formation at the tip. Passing through the glass filter, water flows into a foam where it is absorbed. The glass filter and absorbing foam are important to avoid surface tension effects that need to be corrected.

METAS' primary standard covers steady flow rates going from 0.1 μL/min to 1 mL/min with expanded measurement uncertainties (K=2) in the range of 0.6% to 0.1%. The measurement times vary between 240 min for the lowest flow rate to 1 min for the highest one. Calibrations of pulsating flow rates can be performed from 1 μl/min to 1 ml/min, with expanded measurement uncertainties in the range of 2.7% to 0.2%.

In a more recent version of the facility, the flow rate is generated using a homemade piston prover (Fig 2.4). The latter is used to push the plunger of a filled syringe, in a similar way as a syringe pump. By measuring the positions of the piston over time, the generated flow rate can be deduced from the cross sectional area of the piston multiplied by its speed. The piston is moved using a high precision linear stage. Its positions are determined from the number of pulses sent by a linear measuring system and recorded using a software. The latter pairs the measured positions with timestamps used to determine the piston's speed. The device under test (DUT) is placed between the piston prover system and the beaker that collects water. The flow rate is measured in the weighing zone following the same method as for the oldest version of the facility [104, 103, 25, 23].

IPQ's Facility

IPQ's gravimetric facility (Fig. 2.5) includes four precision balances with measurement capacities in the range of 500 g down to 0.5 g. To reduce evaporation, the weighing beaker is placed inside an evaporation trap. Droplet formation at the capillary's tip is avoided by immersing the capillary in water inside the beaker. In order to avoid the formation of bubbles, a vacuum membrane is integrated in the system to degas water before filling the flow generator. To generate flow rates IPQ use a high precision syringe pump. As the mass changes are very small at low flow rates, a balance with a resolution of 0.001 mg and maximum capacity of 20 g is used. IPQ's system enables calibrations with measurement times from 15 to 20 min. The flow rates covered are in the range of 50 nL/min to 10 mL/min with measurement uncertainties from 0.6% to 0.15%, respectively [25].

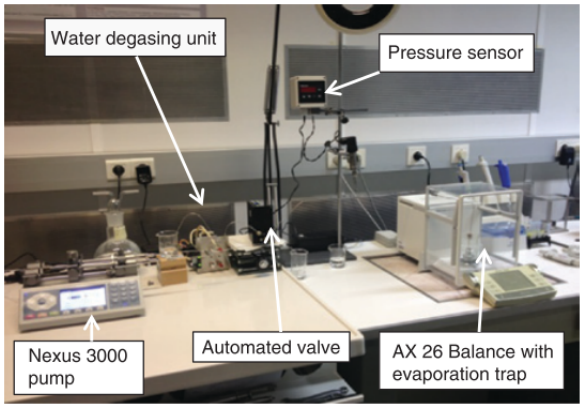

Figure 2.5: Photograph of IPQ' gravimetric bench [25].

DTI's Facility

The system developed by DTI' includes the main components of a typical gravimetric setup (Fig. 2.6). In addition to covering the water's surface with oil to reduce evaporation, the latter is measured in order to minimize its correction uncertainty. As the volume of the beaker is limited, the setup includes a system to empty automatically the beaker when it is full. The whole setup is placed inside an isolation chamber made of metal with an isolation layer, in order to stabilize the temperature and minimize convection effects. During a calibration of a flow meter, water flows from the reservoir to the syringe pump, passing by the degasser. The degassed water is used to fill the syringe. When a flow rate is generated using the syringe pump water flows through the flow meter and ends in the weighing beaker. The main uncertainty component in this system is the capillary forces from the rise in the water and oil's level along the needle. DTI's primary system covers a flow range of 83 nL/min to 1 mL/min, with measurement times from 10 min up to 75 min, for the lowest flow rates [104, 25].

BHT's Facility

BHT's measurement system consists of a pressurized water tank to generate the flow, filter (0.5 μm pore size) and degasser to produce extra pure water, pressure sensor, a Bronkhorst flow meter with a piezoelectric valve, a weighing scale and valves (Fig. 2.7). In order to reduce

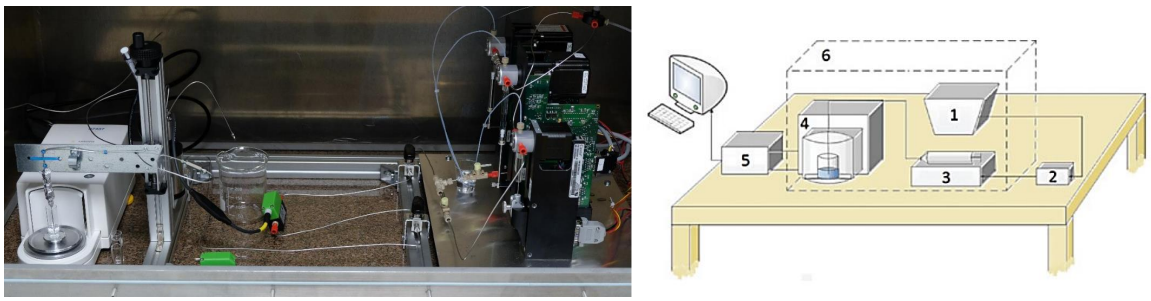

Figure 2.6: DTI' gravimetric facility. (left) photograph of the experimental setup. (right) schematic illustration of the setup. (1): reservoir. (2): degasser. (3) syringe pump. (4): balance. (5): balance electronics. (6): isolating chamber [25].

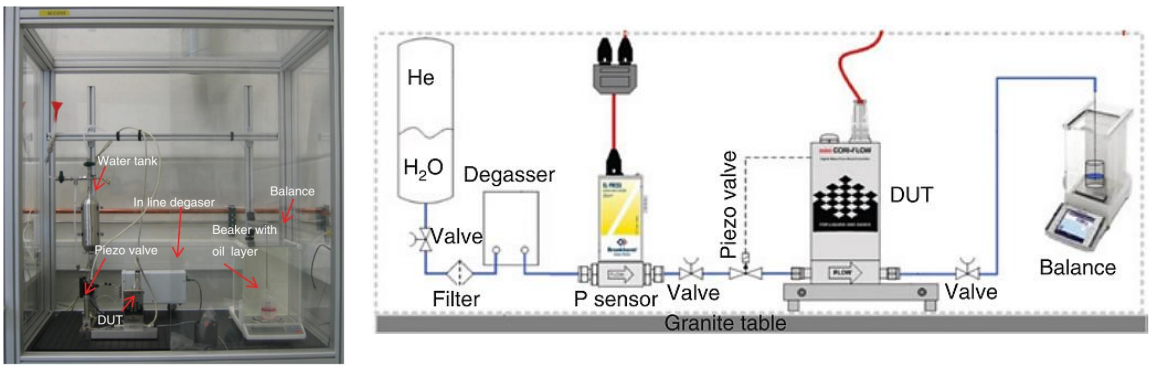

Figure 2.7: Photograph (left) and schematic illustration (right) showing BHT' facility [117].

vibrations, the whole setup is placed on a granite table. Evaporation is reduced significantly by covering the water's surface with a layer of oil. The fast temperature changes are reduced by putting the setup in a box. The particularity of BHT's system is that the flow's stability is ensured by the flow meter which controls the piezoelectric valve. In fact, the flow meter measures continuously the flow rate and as a response to fluctuations, controls the valve to keep the flow rate constant. The mass flow rate values that are measured using the balance are filtered with a sliding average window of 60 s. BHT's facility cover two ranges of flow rates. The first corresponds to 1–2000 mg/h which is equivalent to 20 nL/min – 33.3 μL/min. The corresponding measurement uncertainties vary between 8.8 % and 0.25 % (k=2) with measurement times ranging from 2 hours to 2 minutes. The second range corresponds to lower flow rates going from 0.3 mg/h to 1.2 mg/h, *i.e.* from 5 nL/min to 20 nL/min. The associated uncertainties vary between 29.2 % and 8.8 % (k=2), with measurement times of 2 hours [25, 117, 104].

CMI's Facility

CMI's gravimetric system is based on a special beaker with the purpose of eliminating systematic errors due to buoyancy and capillary forces. The beaker includes three parts schematically shown in Fig. 2.8. Water flows through the needle to part (A) where water is collected and the needle immersed. The inner beaker is placed inside a glass capillary and both are covered on the top by a plexiglass lid. The space between the inner beaker and cover allows the water to flow from part A to the collecting beaker (C) in order to keep the water's level constant in part (A). Oil is added on the surface of water in part (A) and

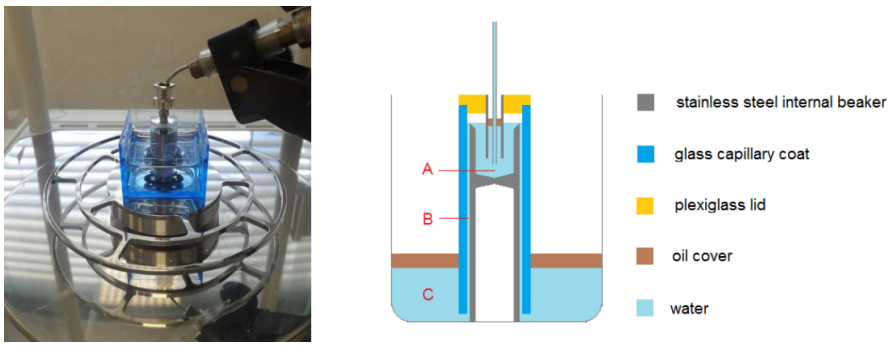

Figure 2.8: Schematic illustration of CMI' gravimetric setup [104].

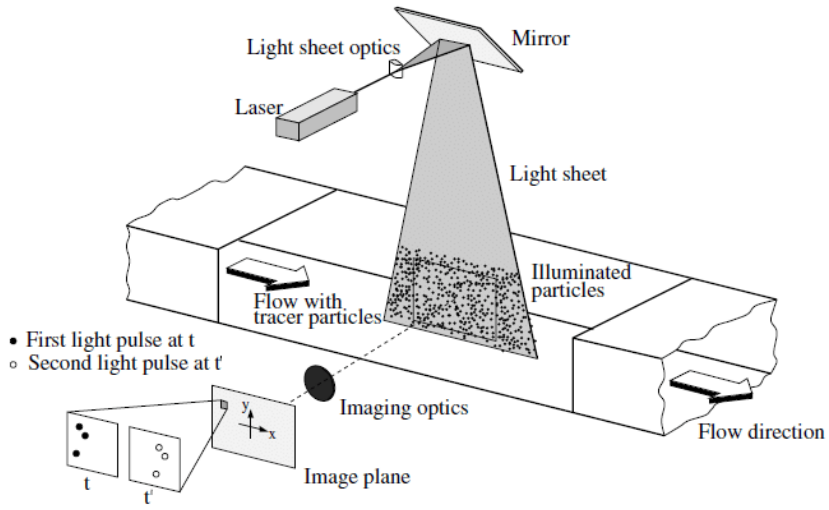

Figure 2.9: Schematic illustration of a typical PIV setup [124].

(C) to reduce its evaporation. The uncertainty due to buoyancy correction is reduced since the buoyancy force between a needle and a weighing scale is kept constant. In addition, the fluctuations in mass readings are reduced as the water level is kept constant, *i.e.* the slip-stick motion of the water surface along the needle due to the increasing in water's level, is suppressed. CMI's facility was developed to measure flow rates going down to 1 mg/h, which is equivalent to about 17 nL/min [104].

2.1.2 Particle Image Velocimetry (PIV)

PIV is an optical method used to measure the instantaneous velocities in a flowing fluid. A PIV setup consists essentially of a CCD camera for image acquisition, a laser unit, optics to produce the light sheet, seeding particles and a synchronizer to synchronise the camera with the laser pulses Fig. 2.9. This method consists on the seeding of the fluid under investigation with tracer particles that are small enough to faithfully follow the flow dynamics. The tracer particles within a given plane of the fluid are illuminated with a laser light sheet at short exposure times to avoid motion blur. Images of the moving particles are acquired at different instants, from which the displacements of the particles are measured by cross-correlation. The fluid's velocity profile is deduced from the measured particle displacements [2, 173].

HS' Facility

For the measurement of flow rates using PIV method, HS use two different setups. For small channels (with a height smaller than 50 μm), they use a standard microscopy with transmitted light. Flow rates are generated using a high precision syringe pump. The flow is visualized in a channel of a microfluidics chip, which is placed below the camera and lens (Fig. 2.10). The magnifications of the lens used vary from 10x to 50x. The fluid is seeded with Polystyrene beads having a diameter of 20 μm. The fluid is a mixture of deionized water and heavy water (50 % v/v) which leads to a medium and beads density of 1.05 g/cm^3.

For channels larger than 50 μm, a holographic setup is used. This setup consists of a laser diode, a hole, and a CMOS sensor for image acquisition (Fig. 2.11 (left)). The main advantage of this method is that multiple flow planes can be reconstructed from a single image of the particles' interference pattern. Fig. 2.11 (right) shows the steps of holographic analysis: The acquired holograms are reconstructed then edited to obtain an images from which the

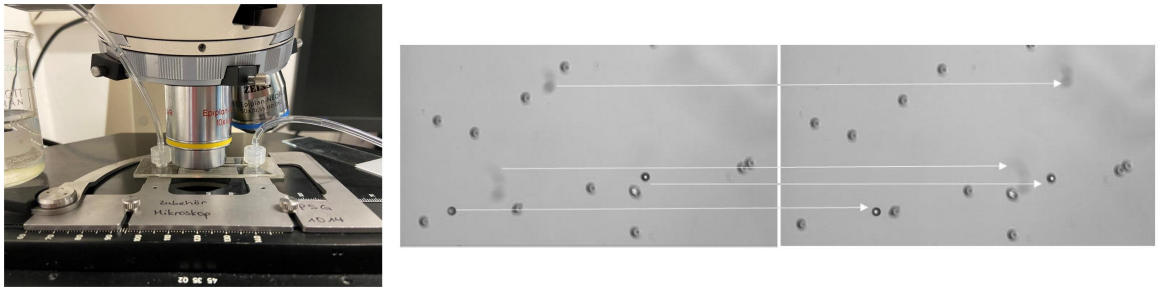

Figure 2.10: HS's experimental setup used for flow rate measurements using PIV method. On the left is shown a photograph of the measurement system. The dimensions of the microfluidics channel are equal to 50x5x0.85 mm (LxWxH). The seeding beads used have a diameter of 20 μm. On the right are shown 2 images acquired by the microscope at different instants. The white arrows show the beads that moved between the two instants. The beads that didn't move are sedimented at the bottom of the channel [104].

particle's displacements are measured by cross-correlation. Unwanted artifacts are removed from images by thresholding. However, when using the holographic method, small channels appear dark as the outer surface of the channel diffracts a lot of light. As a consequence, the interference pattern of the tracer particles is hidden by that of the channel's surface. As mentioned above, this limitation can be overcome by the use of standard microscopy. HS's PIV system covers flow rates ranging from 60 to 6000 μL/min with possible improvements to go down to 5 nL/min [104].

NEL's Facility

NEL's system is based on the tracking of fluorescent seeding particles. The measurement setup consists essentially of a epifluorescent microscope, a microfluidics chip and a pressure system to generate flow rates (Fig. 2.12). The microfluidics chip includes a serpentine channel with a rectangular cross section. In order to measure the different flow rates with

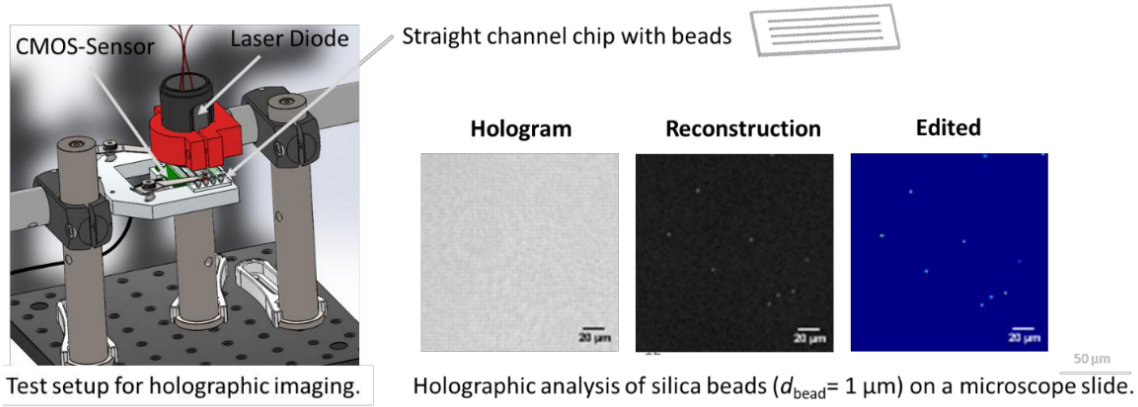

Figure 2.11: HS's experimental setup used for flow rate measurements using the Holographic PIV method. On the left is shown a schematic illustration of the measurement system. On the right are shown three images explaining the steps of holographic processing performed on the acquired images [104].

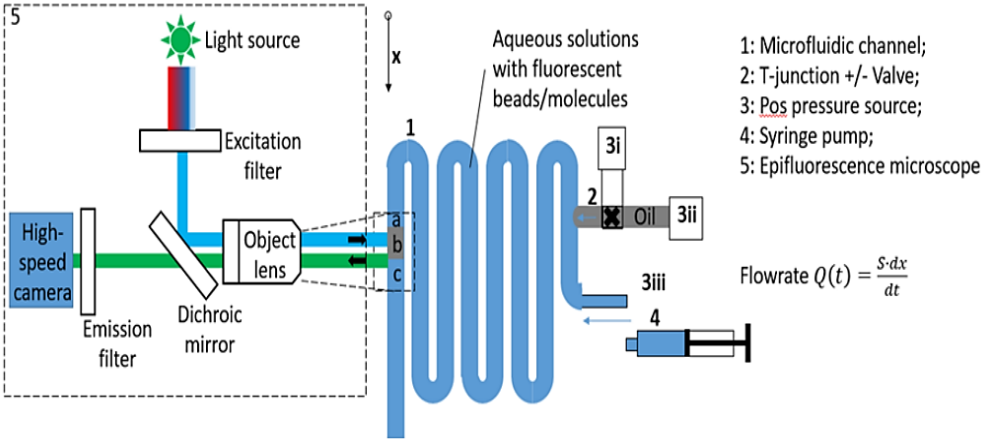

Figure 2.12: NEL's experimental setup used for flow rate measurements using PIV and front tracking methods [104].

approximately the same flow velocities, the channel's width and length are varied. The height, however, is always kept constant. Changing the dimensions of the channel leads to a change in the fluidic resistance which is derived each time from Hagen-Poiseuille's law. The latter is used to determine the generated flow rate from the fluidic resistance and applied pressure. Notice, when using a syringe pump, the generated flow rate corresponds to the target flow rate at which the pump is set. Flow rate in the channel is measured from the velocity of the beads multiplied by the cross sectional area of the channel. In addition to PIV measurements, it is possible to measure the flow rate using front tracking method. This is achieved by introducing in the channel a small volume of an immiscible liquid and measuring the displacement of the moving interface. As the cross sectional area of the channel is an important parameter to determine the flow rate, the channel is characterized using a scanning electron microscope and a surface profiler. NEL's facility was designed to measure a maximum flow rate of 100 nL/min [104].

2.1.3 Interferometric Method

The interferometric method was developed by IPQ in the context of MeDD II. In this method an interferometer is used to measure the distances travelled by the pusher block which pushes the piston of a syringe pump. The corresponding experimental setup (Fig. 2.13) consists of

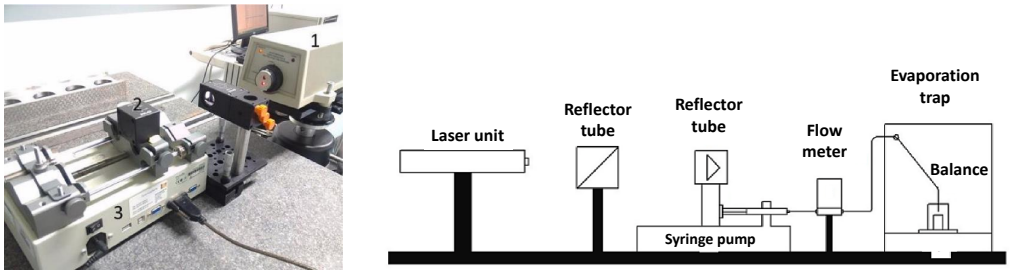

Figure 2.13: Schematic illustration showing IPQ's experimental setup used for flow rate measurements using interferometry [104, 15].

a syringe pump, laser unit with an incorporated detector, two retroreflector cubes (one with an attached beam splitter that has a partially reflective surface and the other placed on top of the pusher block) and a Control Unit. Flow rates are generated by moving the pusher block using the stepper motor with which it is connected. When a laser beam achieves the reflector cube with the beam splitter, it splits into two sub-beams, one is received by the reflector cube that is placed on top of the pusher block, and the other is reflected back to the detector. The interference pattern formed at the detector depends on the shift between the two beams. If this shift is a multiple of the wavelength the pattern formed corresponds to that in the case of no shift. This allows the measurement of distances with the resolution of a a laser wavelength. The flow rate is determined by multiplying the measured distances with cross sectional area of the syringe. IPQ's system covers flow rates in the range of 1 mL/h to 0.0001 mL/h with expanded measurement uncertainties from 2 % to 3 %, respectively [104, 15].

2.1.4 Pendant Drop Method

Pendant drop method consists on the tracking of the volume of a droplet that is suspended at the end of a vertical capillary. This method will be discussed in more details in Section 7.2. The volumetric flow rate is defined as the change in the droplet's volume with respect to time. As part of the project MeDD II, IPQ developed a measurement system based on this method, with a setup that is very similar to that of the front tracking method (Fig. 2.14). In order to reduce evaporation, the droplet is placed inside an evaporation trap with saturated air. The droplet's volume is measured by image processing by slicing the total volume into cylindrical subvolumes. IPQ's system covers flow rates in the range of 1 mL/h down to 0,01 mL/h with expanded measurement uncertainties of 4 % to 30 %, respectively [104].

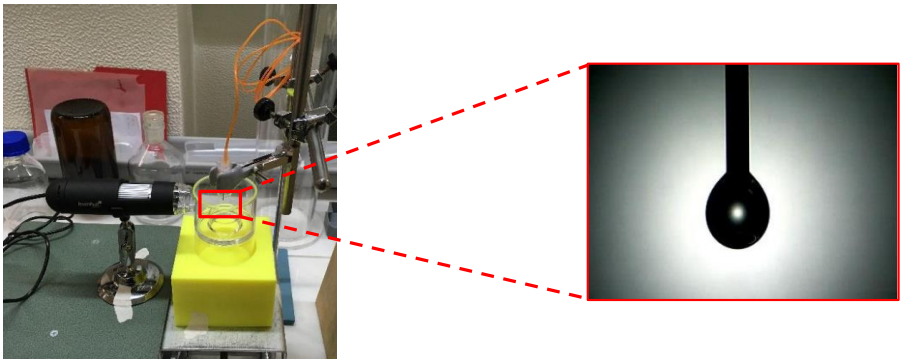

Figure 2.14: Schematic illustration showing IPQ's experimental setup used for flow rate measurements using pendant drop method [104].

2.1.5 Front Tracking Method

The interface tracking method consists of measuring the displacement over time of a water/air interface moving inside a glass capillary tube (Fig. 2.15). The volumetric flow rate is obtained by multiplying the mean flow velocity by the cross sectional area of the capillary tube:

$$Q_V = v.\pi R^2 = \frac{x}{t}.\pi\frac{d^2}{4} \tag{2.2}$$

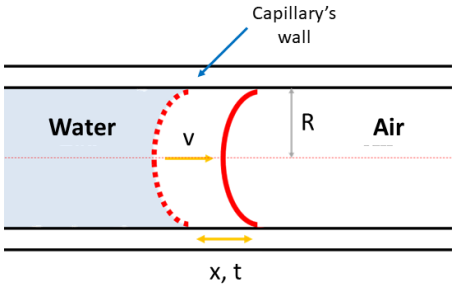

Figure 2.15: Schematic illustration showing the working principle of the interface/front tracking method.

where v is the mean flow velocity, R is the capillary's inner radius and d its inner diameter $d = R/2$, and x is the displacement of the interface during the time interval t.

Because of its simplicity, the interface/front tracking method has been largely used. In 1991, Pfahler *et al.* [115] used this method to measure the flow rate of N-propanol in microchannels with rectangular cross section. The objective of their study being the measurement of the friction factor and evaluation of the predictions of flow behaviour by Navier-Stockes equations.

As part of their research to investigate the temperature dependence of Poiseuille number in microchannel flow, Urbanek *et al.* [161] used the front tracking method to measure the flow rate in the microchannel, from which the poiseuille number was determined.

Richter *et al.* [128] used this method to develop a theoretical model relating flow rates and pressure differences, in channels with different geometries. The model developed was then used to assess geometrical and physical influences in laminar flows.

Interface tracking method was employed in the context of other studies [63, 8, 145, 126, 6, 59], but also for the calibration of flow meters and drug delivery devices [3, 4, 134, 14]. In the following sections, we describe the two main institutes using interface tracking as a calibration system.

THL's Facility

THL's front tracking measurement system consists of a high speed camera combined with a magnifying lens, glass capillary tubes with inner diameters ranging from 0.15 mm to 1 mm and a white light source (LED), as shown in Fig. 2.16. A telecentric lens is placed between the camera and the capillary tube in order to collimate the emitted light. The camera is

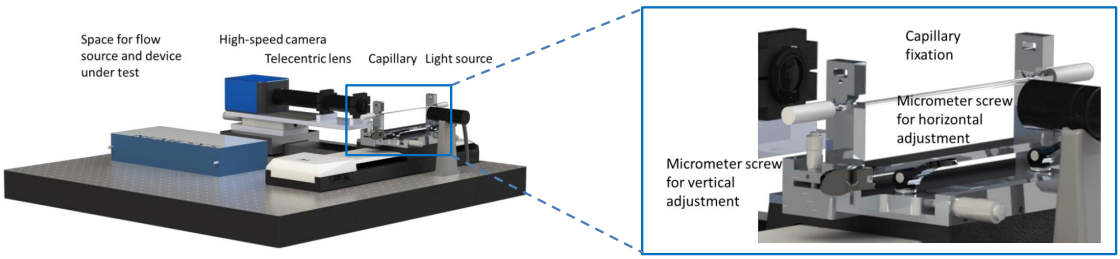

Figure 2.16: Schematic illustration showing THL's experimental setup used for flow rate measurements using front tracking method [104].

placed on a high precision translation stage which is used to track the meniscus along the capillary. In order to determine the pixel size, the camera is calibrated using a glass scale from Leica. Flow rates are generated using a syringe pump. Once the meniscus arrives in the capillary, its displacements over time are measured in real time using a homemade software which constantly detects the front's edges. As the stage holding the camera moves, its displacement is included automatically in the measurement of the front's positions. The acquisition times for this system vary between 2 and 60 s. This time can be adjusted along with the distance resolution by changing the capillary's diameter, the camera's magnification and the recording frequency. The inner diameters of the capillaries are measured at both their ends, using a Keyence digital microscope. The system covers flow rates ranging from 50 nL/min to 500 μL/min with an expanded uncertainty of 4% for flow rates higher than 50 nL/min, as declared by THL [3, 4, 134, 104].

IPQ's Facility

IPQ's measurement system is similar to the previous one, with the capillary tube placed vertically and a translucent paper placed between the light source and capillary tube to diffuse light (Fig. 2.17(left)). In order to determine the pixel size in images, the camera is calibrated using as a reference the external diameter of the capillary. First, the diameter is measured in meters using a caliper. Then, it is measured from the image in pixels using the function selectROI of OpenCV. This function allows to select a region of interest and save its coordinates. Thus, by selecting the whole height of the capillary in the image, one obtains the external diameter in pixels and compare it with the one in meters to determine the pixel size. The front's positions are determined by measuring the coordinates of a single point (The blue point in Fig. 2.17 (right). This point is taken as the intersection between the outer edge of the meniscus and the capillary's axis. IPQ's system covers flow rates in the range of 1000 L/h down to 1 L/h with measurement uncertainties going from 2% to 7% (k = 2) [14, 104].

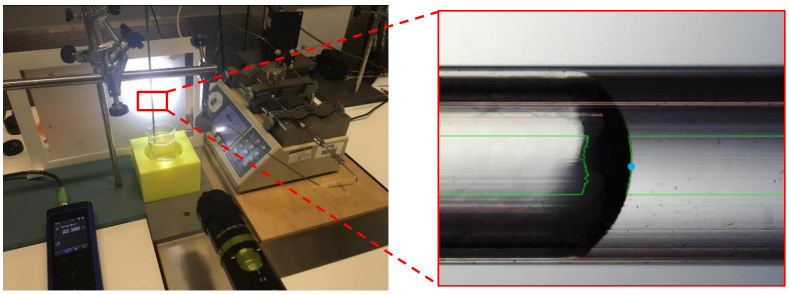

Figure 2.17: Schematic illustration showing IPQ's experimental setup used for flow rate measurements using front tracking method [104].

2.2 Secondary Measurement Methods

In this section, we present the working principle of the two main techniques that are used for low flow meters. These techniques allow to measure a mass flow rate instead of the volumetric one. The first is based on Coriolis effect and the second on heat dissipation as explained below.

2.2.1 Coriolis Mass Flow Meters

Typical Coriolis flow meters consist of one or two vibrating tubes, with a fixed inlet and outlet, through which the liquid passes (Fig. 2.18). Different tube geometries are possible (U-shaped, rectangular, triangular, etc.) depending on the required measurement sensitivity. The tube is vibrated using an electromagnetic, piezoelectric or capacitive drive, resulting in a predictable vibration profile in the case of no flow. When a flow is generated, the tube twists due to Coriolis force, causing a phase shift in the predictable profile (Fig. 2.19) [10, 169].

In the first half of the tube the fluid gains an acceleration by traveling from the fixed axis to the position with maximum vibration. On the other hand, it decelerates in the second half by moving away from the maximum vibration point towards the outlet. The acceleration of the fluid on the inlet side causes the tube to lag behind its no-flow position. On the outlet side, the deceleration force causes the tube to lead ahead of the no-flow position. This results in a twisting motion of the tube (Fig. 2.20). The vibration of the tube at any point represents a sine wave. Due to the mass flow, a phase shift of the sine wave occurs between the inlet and outlet sides. This phase shift is proportional to the flow rate of the fluid. Coriolis flow meters also enable the measurement of the fluid's density. As a matter of fact, the mass flow rate is proportional to the fluid's density which determines the tube's resonant frequency. Therefore, monitoring the resonant frequency of the tube allows to precisely determine the fluid's density [10, 169].

The Coriolis force induced by flow is given by Equation (2.3) which is equivalent to Newton's second law for rotational motion [10]:

$$F_c = 2m(\Omega \times \mathbf{v}) \tag{2.3}$$

where F_c is Coriolis force, m is the mass to be applied to a known point at a distance L from the fixed axis, Ω is a vector representing angular velocity and $\mathbf{v}$ is the average velocity vector.

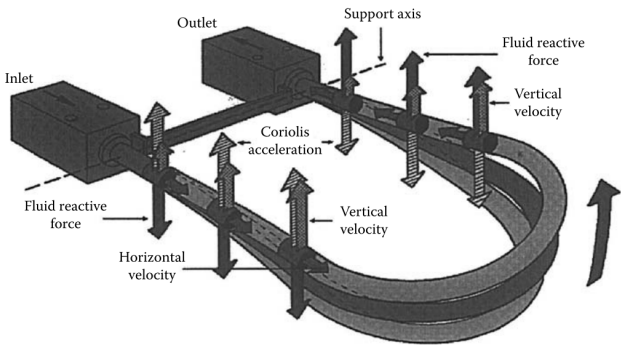

Figure 2.18: Schematic illustration showing the Working principle of a Coriolis flow meter with a U shaped tube [169].

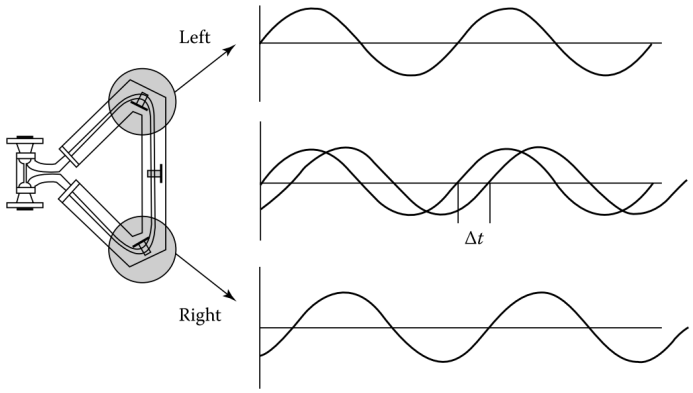

Figure 2.19: Phase shift in the vibration frequency of the Coriolis tube, between the inlet and outlet, due to the fluid's flow [169].

For the special case of a U-shaped tube, the mass flow rate Q_m is related to the measured shift τ in the transit time of the two sides, as follows [10]:

$$Q_m = \frac{K_s(1-\omega^2/\omega_s^2)}{2Kd^2}\tau \tag{2.4}$$

where K is an integration constant, K_s is the spring constant of the U-tube in twisting oscillation, ω is the driving frequency, ω_s is the frequency in twisting and d is the width of the U-tube.

Coriolis flow meters have the advantage of being highly accurate. Besides, they are not sensibly affected by fluid parameters such as viscosity, pressure, temperature, and density thus, in general, they do not have to be calibrated for different fluids [10, 169].

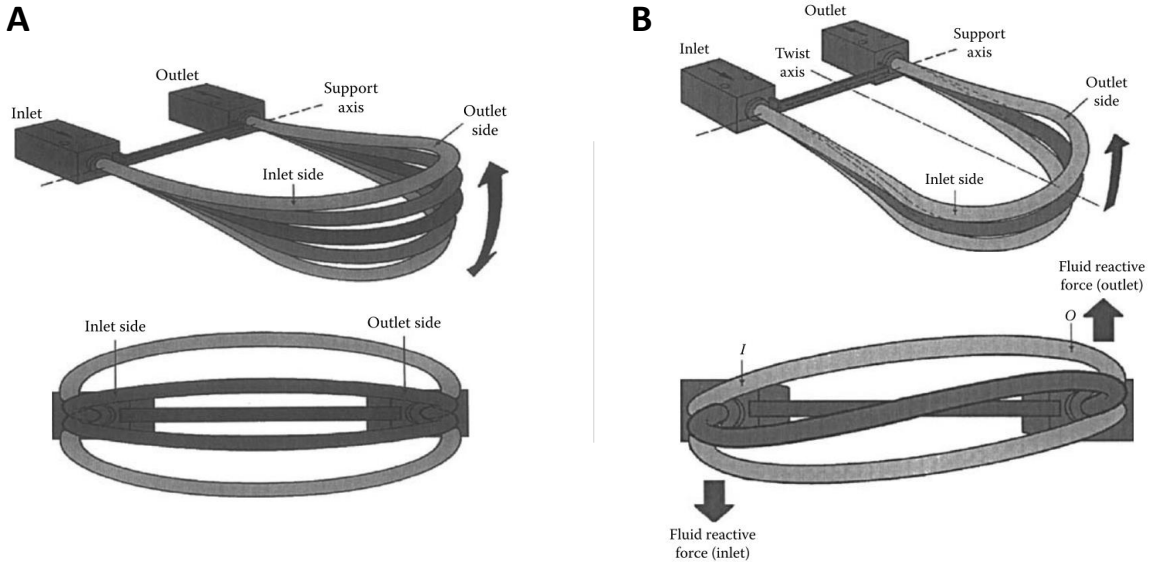

Figure 2.20: Schematic illustration showing the different forces and vibrations of the U tube in the case of no flow (A) and when a flow is generated (B) [169].

2.2.2 Thermal Mass Flow Meters

Thermal mass flow meters can be divided into three types according to their operating principle: The Anemometric, Time-of-Flight and Calorimetric type.

Anemometric

In the Anemometric type the heat dissipated by the flowing fluid from a heated temperature sensor is correlated with the flowing velocity. The flow meter uses either a resistive wire (Hot Wire Anemometer) or a thin film resistive element (Hot Film Anemometer). The heat transfer coefficient is given by King's law as follows [81]:

$$h = a + b\sqrt{v} \tag{2.5}$$

where a and b are calibration constants and v is the flow velocity.

The flow cools down the heater/sensor and changes its resistance R which varies with temperature as follows [10, 57]:

$$R(T) = R(T_{ref})[1 + \alpha(T - T_{ref})] \tag{2.6}$$

where $R(T)$ is the resistance of the heater at the temperature T, $R(T_{ref})$ is the resistance of the heater at the reference temperature T_{ref} and α is the temperature coefficient of resistance.

At equilibrium the supplied electric power is equal to the lost thermal power :

$$RI^2 = hA(T - T_f) = A(a + b\sqrt{v})(T - T_f) \tag{2.7}$$

where I is the intensity of the input current, R is the resistance of the heater/sensor, T and T_f are the temperatures of the heater and fluid respectively and A is the heat transfer area.

Two measurement modes are possible, the constant temperature mode (CTA) and the constant current mode (CCA), as shown in Fig. 2.22. In the first mode, the heater/sensor is heated so as to create a temperature difference ΔT with the fluid. The mass flow rate of the flowing fluid is then calculated by measuring the power required to maintain constant the temperature difference. In the second mode, a constant current is generated. Due to heat dissipation the temperature decreases causing a change in the resistance of the heater. The mass flow rate is determined from voltage or resistance measurements.

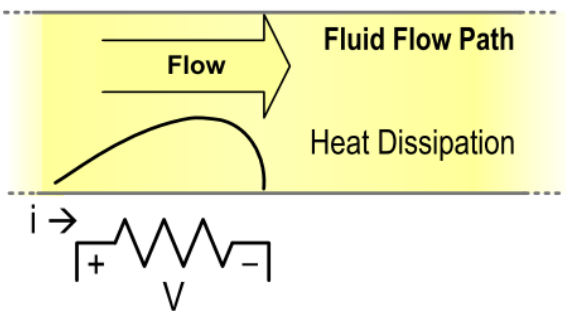

Figure 2.21: Schematic illustration of the working principle of Hot-Wire/ Hot-Film Anemometer [166].

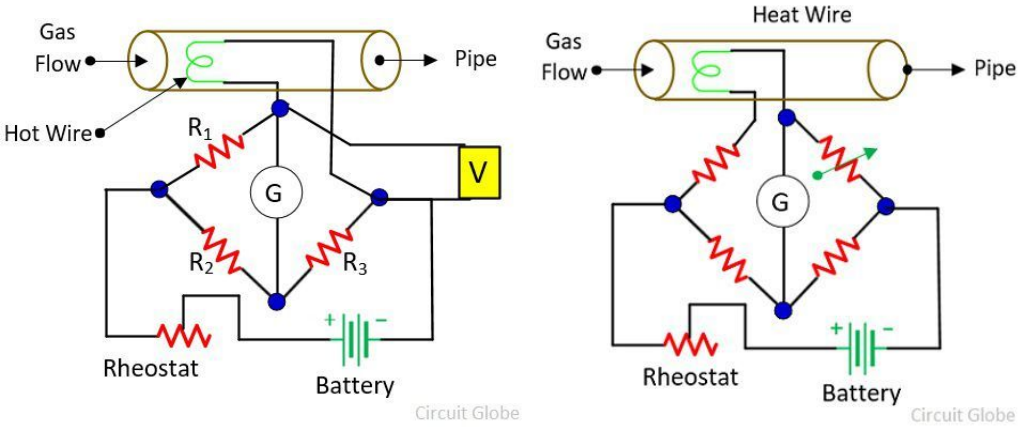

Figure 2.22: Hot-Wire anemometer's modes. (left) Constant Current (CCA). (right) Constant temperature (CTA) [72].

Time-of-Flight Flow Meters

Time-of-Flight flow meters consist of at least one heater and one downstream temperature sensor (Fig. 2.23). The heater generates a short thermal pulse that travels with the flow until it is detected by the sensor. The transit time between the generation of the heat pulse and its detection depends on many parameters: the thermal conductivity and diffusivity of the fluid, the distance between the heater and sensor, and flow velocity. At relatively high flow rates the transit time tends to [10, 85]:

$$t = \frac{d}{v} \tag{2.8}$$

where d is the sensor-heater distance and v is the average flow velocity of the fluid. However, for low flow rates the transit time depends mainly on thermal diffusion.

Calorimetric Flow Meters

Calorimetric flow meters use generally a heater and two temperature sensors placed at equidistant positions on both sides of the heater (downstream and upstream), see Fig .2.24. In the absence of flow the temperature profile produced by the heating element is symmetric. Fluid flow through the channel cools the upstream sensor while heating the downstream one

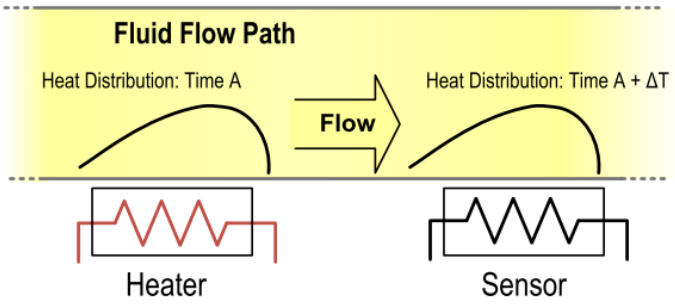

Figure 2.23: Schematic illustration showing the Working principle of Time-of-Flight thermal mass flow meter [166].

causing an asymmetry in the heat distribution. This asymmetry is detected by the sensors in terms of a temperature difference, expressed in Equation (2.9), which is correlated with the mass flow rate of the fluid. The sensors also allow to determine the direction of flow [50].

$$\Delta T = T(e^{x_1 d_1} - e^{x_2 d_2}) \tag{2.9}$$

where T is the temperature of the heater; d_1 and d_2 are the distances between the heater and the two sensors, and x_1 and x_2 are parameters depending on the fluid's characteristics such as velocity, thermal diffusivity and boundary layer thickness.

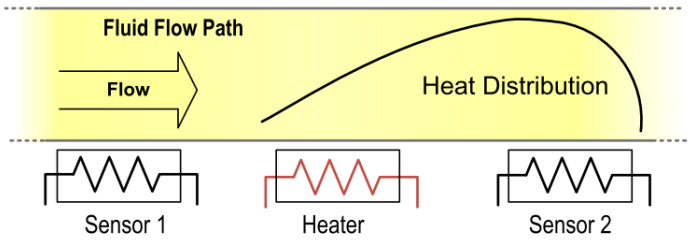

Figure 2.24: Schematic illustration showing the working principle of Calorimetric thermal mass flow meter [166].

Chapter 3

Methods and Materials

In the previous chapter, we presented the primary methods that were developed by European NMIs in the context of the MeDD II project to measure flow rates, and we briefly explained the working principle of the front/interface tracking method on which is based our primary system. At the end of the chapter, we presented the thermal mass and Coriolis methods which constitute the two main secondary methods on which are based most of the flow meters that operate at low flow rates.

In this chapter, we start by describing in detail our experimental setup, after which we explain the method we developed to measure the displacements of the interface inside the capillary. The image processing algorithm behind this method, allows measurements for any shape of the meniscus whether this latter is static or changes with time due to physical effects, such as stick-slip for example. To conclude this chapter, we explain the procedure used for the calibration of a flow generator or flow meter.

3.1 Description of the Measurement System

In this section, we provide a detailed description of the measurement system shown in Fig. 3.1. The various devices and the associated software as well as the tubing and connectors are described with the associated characteristics and references, allowing the construction of a complete functional system by any user.

In short, the system consists of a high resolution/high speed camera with a motorised zoom for image acquisition, a high intensity light source, 4 translation stages and 1 rotary

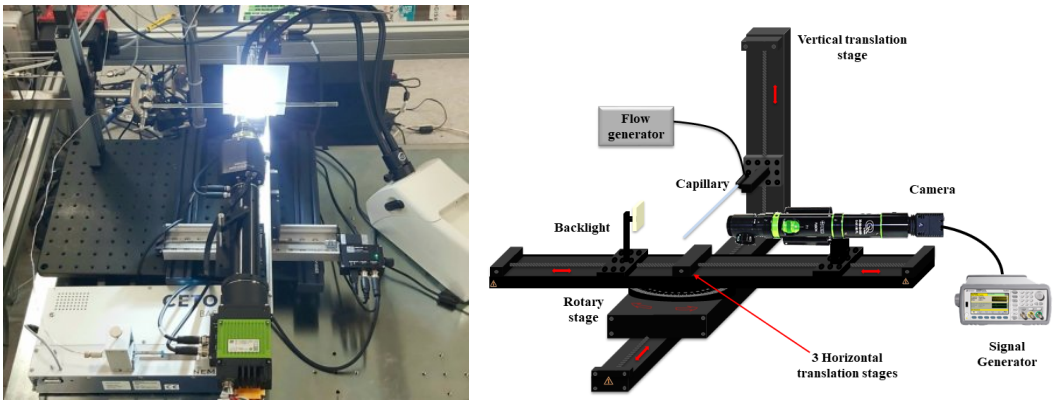

Figure 3.1: Picture (left) and schematic illustration (right) of the "interface tracking" measurement system.

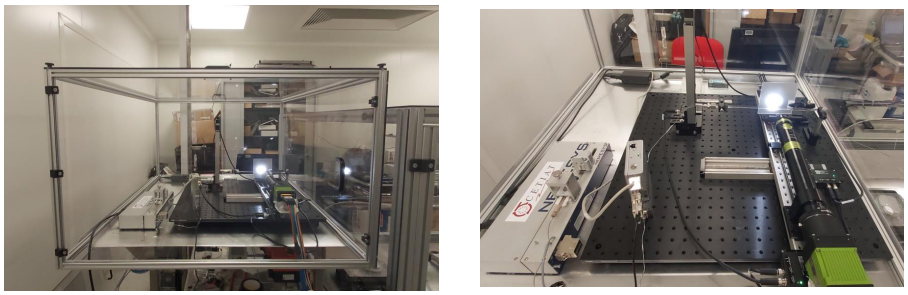

Figure 3.2: Outside (left) and inside (right) view photographs of the new interface tracking measurement set up.

stage for motion along the 3 axes and rotation about the vertical axis, a glass capillary tube inside of which the liquid flows, a translucent plate to diffuse the light, and a frequency generator to trigger image acquisition by the camera. The setup is mounted on an aluminum optical breadboard plate with sorbothane isolating feet. For the calibration of the camera two targets are used, one for the measurement of the pixel size and the other for the quantification of the optical distortion. The calibration of the frequency generator is realised using a Rubidium atomic clock that is calibrated against the French national standard for time and frequency at LNE-SYRTE (Paris Observatory).

The camera used was a matrix monochrome 12-Megapixel JAI SP-12000M-CXP4-F from the Spark series with a resolution of 4096 (H) x 3072 (V), of a pixel size 5,5 µm and a frame rate of 189 fps at full resolution. The camera was connected to a lens system from Optem®Fusion (Fig. 3.3). The latter included a camera mount (F, 25-60-24-000) used to connect the camera to a camera tube (Mini 3x 600 FL, 35-08-16-000). The latter provides the final magnification and image size for the optical system and is connected to a motorized zoom 7:1 (35-31-60-000) with a field of view between 2.3 mm x 1.7 mm and 0.4 mm x 0.3 mm, a depth of field varying between 42 and 450 μm and a work distance of 50 mm. The motorized zoom is controlled using a stepper controller (35-05-20-000) and is connected to a final lens (3.0X / 67FL, 35-00-01-000) through a diaphragm (Aperture set 35-07-20-000) and a mount (Basic lower function module, 35-01-00-000). The camera was mounted on one

Figure 3.3: Components of the lens system used with the JAI spark camera [111].

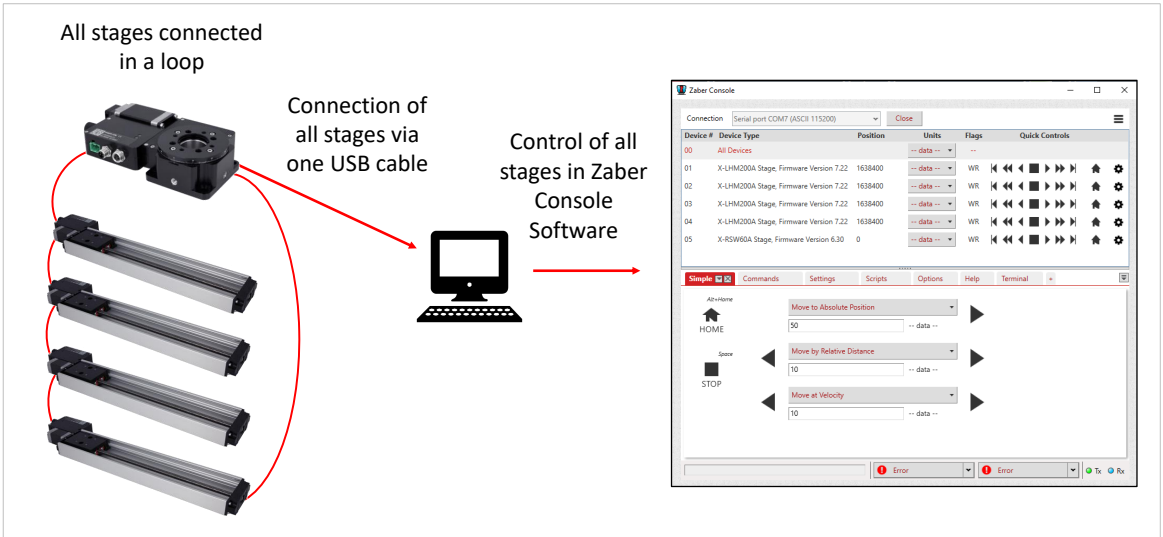

Figure 3.4: Schematic illustration showing the connection of the different rotary and linear stages and the associated software, *i.e.* Zaber Console

of the translation tables using a universal base plate from Thorlabs (UBP2/M, 65 mm (L) x 65 mm (W) x 10 mm (H)) and a camera tube clamp from Optem Fusion.

The 4 motorized linear tables (X-LHM200A-KX13AF) and the rotary stage (X-RSW60A - KX13AF) are from Zaber. One of the linear stages is placed vertically to hold the capillary tube. Two other linear stages, one holding the camera and the other the diffuser plate and light guides, are aligned on the same axis and fixed on the rotary stage which itself is fixed on the fourth linear stage. The latter is placed perpendicularly to the two aligned stages and is used to move the camera and backlight on the x axis, *i.e.* along the capillary. The rotary stage is used to align the capillary perpendicularly with the camera's axis. The rotary stage was placed under the table holding the capillary in order to have a stable system (Fig. 3.2). All five stages are connected to one another so as to form a closed loop. They are controlled either manually or remotely using Zaber Console software, by connecting one of the stages to the computer via a USB cable. The detailed specifications of the stages are given in Table 3.1.

The system uses a cold light source (Schott KL 2500 LED) with bifurcated flexible gooseneck light guides (SCHOTT Flexible Lightguides 155 204 2 Branch). The LED provides a light intensity going up to 1100 lm. A large, translucent plate (100 mm x 100 mm N-BK7 Ground Glass Diffuser 1500 Grit, DG100X100-1500) is used to diffuse the light coming from the LED and illuminate the capillary homogeneously. The Light guides and diffusion plate are fixed on the translation table which is in the same axis of the camera's and perpendicular

Table 3.1: Specifications of the rotary and translation stages [90].

Specifications	Linear stage	Rotary stage
Maximum travelling distance	203.2 mm	360 °
Microstep size (Default Resolution)	0.124023437 μm	0.000234375 °
Unidirectional accuracy	225 μm	0.08 °
Maximum speed	65 mm/s	115 °/s
Minimum Speed	0.000076 mm/s	0.000143 °/s
Maximum centered mass	2.5 kg	20 kg

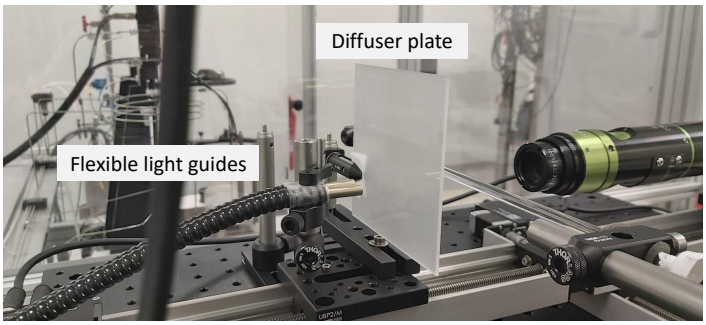

Figure 3.5: Image of the Optem Fusion camera tube used in interface tracking measurement system in front of the diffuser plate and the flexible light guides

to the capillary tube (Fig. 3.5).

The setup is mounted on an aluminum optical breadboard plate (600 mm (L) x 600 mm (W) x 12.7 mm (H), MB6060/M) and sorbothane feet (AV6/M) from Thorlabs. The feet are used to isolate the optical plate from vibrations. The whole system is placed inside a custom made transparent enclosure in order to reduce temperature and ambient pressure variations (Fig. 3.6).

Various glass capillary tubes were used depending on the targeted flow rate. In general, for low flow rates where small inner diameter ($\leq$500 μm) capillaries are necessary, we chose to use heavy wall capillaries from VitroCom, made of borosilicate (Schott Duran) with a length of 30 cm and an external diameter of 6.2 mm. These capillaries are easier to connect than the thin-walled capillaries which are fragile and hard to manipulate. For relatively higher inner diameters, we used thin-walled capillaries made of quartz (GE Type 214 CFQ) with lengths of 10 cm to 20 cm.

The flow rates were generated using a CETONI neMESYS syringe pump with SETonic glass syringes. Two syringe volumes were used depending on the generated flow rate, 10 μL (SYR 10 μL PTFE PEEK – 1/4"-28UNF, 2624415) and 100 μL (SYR 100 μL PTFE PEEK – 1/4"-28UNF, 2624715). The plunger's seal was made of PTFE and the syringes were connected to tubing through a PEEK connector. The syringe pump was controlled using neMESYS UserInterface software which allowed to configure a virtual syringe according to the one used by specifying its internal volume, inner diameter and the length of the graduated part. These input values were used by the software to calculate the displacement of the plunger required for the generation of the target flow rate. In general, this software allows the generation of a constant flow as well as a dynamic flow profile consisting of different flow stages, each lasting for an initially specified time interval.

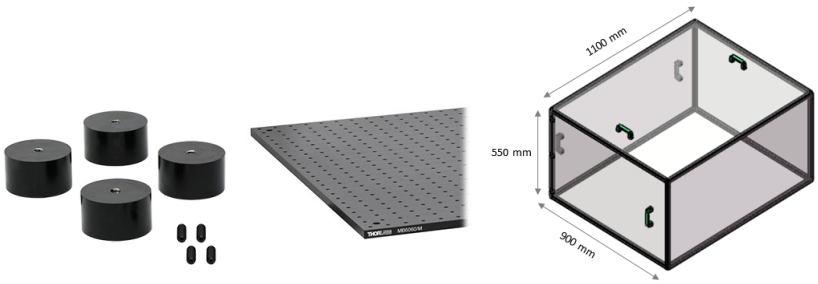

Figure 3.6: Support and enclosure of the setup. From left to right: sorbothane isolating feet, Aluminum breadboard plate and enclosure to reduce the variations of temperature and pressure.[156].

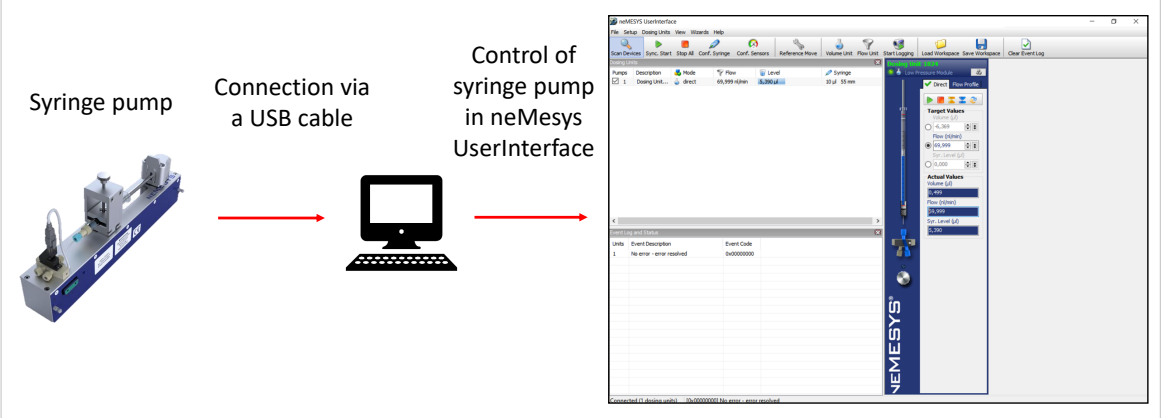

Figure 3.7: Schematic illustration showing the connection of the syringe pump and the associated software.

NorPix StreamPix 8 software was used to control the camera and image acquisition (Fig. 3.8). This software allows mainly:

1. The configuration of the camera's parameters such as exposure time, trigger mode, ROI, etc.

2. The possibility to record directly to the RAM which is important if the frame rate is high or, as in our case, the size of images is very large (12 MO).

3. Saving images as a single sequence or separately in format TIFF, BMP, etc.

4. Saving the timestamps associated with images.

The capillary is fixed on the vertical translation stage and connected to the flow generator by means of stainless steel tube of inner diameter equal to 100 μm and length as short as possible. Image acquisition is triggered by a Keysight 33510B signal generator which is connected to the camera via a DC IN/ trigger IN cable (Fig. 3.9).

As the size of images that are transferred and saved is very large (about 12 Mb per image, at up to 189 fps), the choice of the adequate hardware is essential. The computer used has an Intel Core i9 9900K (3.6 GHz) processor and a RAM 4x 16GB DD4 (64GB). The camera was connected to a CoaXPress frame grabber (Euresys Coaxlink Quad G3 PCIe 3.0), integrated in the computer, by means of a CoaXPress cable (COAX-CX-34-1-34-3M

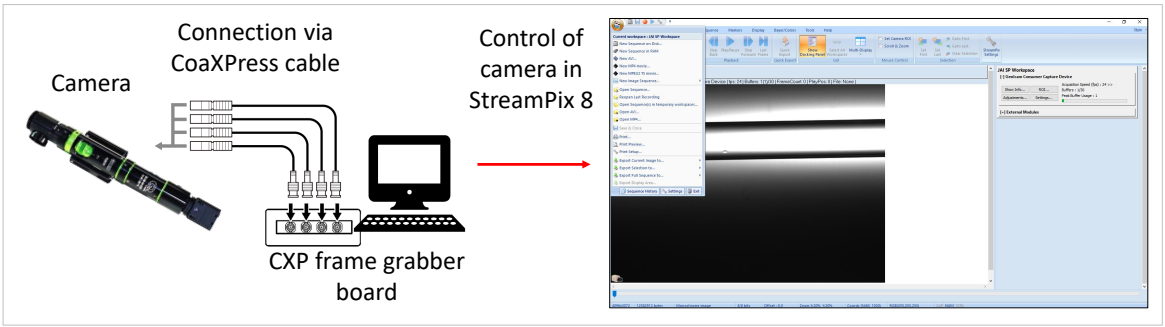

Figure 3.8: Schematic illustration showing the connection of the camera with the computer's frame grabber and the software used for images acquisition (StreamPix 8).

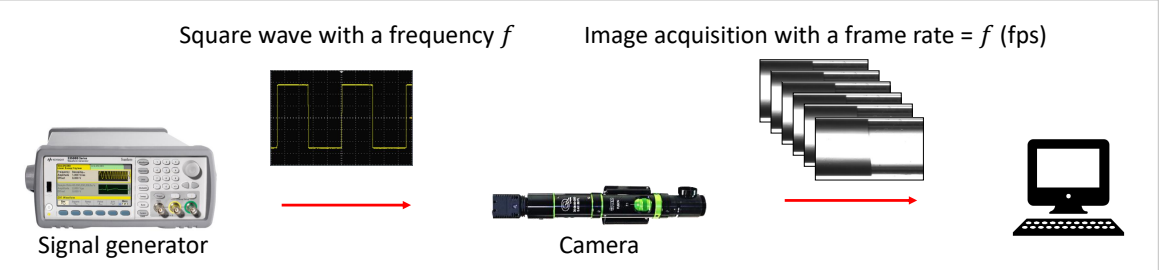

Figure 3.9: Schematic illustration showing camera triggering using a signal generator: the frequency of the generated signal is equal to the acquisition frame rate.

four-connection). The cable allows the transfer of up to 12 Gb/s data and the frame grabber has a bandwidth of 25 Gb/s from camera to host PC memory.

Two calibration targets were used to calibrate the camera. The first is a transmitted light objective micrometer from Olympus (OB-M) with a scale of 1 mm length and 0.01 mm divisions. The second is a multi-frequency distortion target from Thorlabs (R1L3S3P) including 4 grid arrays with grid spacings of 10 μm, 50 μm, 100 μm and 500 μm, respectively. Both calibration targets were previously calibrated at LNE ISO17025 (COFRAC) accredited laboratory (Section 4.1). During calibration the targets are held in front of the camera using a one-axis translation mount from Thorlabs (XF100/M) with a length of 100 mm and which is compatible with rectangular optics from 12.7 mm to 126.2 mm long and up to 4 mm thick.

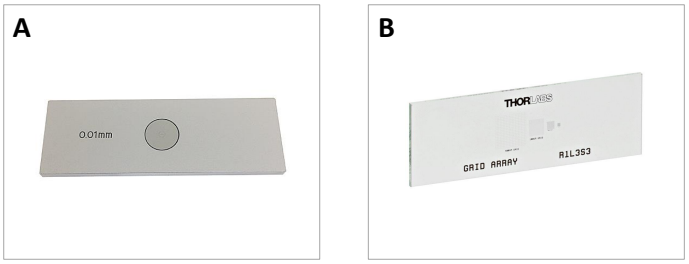

Figure 3.10: Calibration targets. (A): Objective micrometer. (B): Distortion target [107, 123].

3.2 Working Principle

In this section, we explain the working principle of the interface tracking method developed in this thesis and in particular the image processing algorithm which allows us to determine the flow rate from the acquired images. We explain the different methods used in the algorithm and represent them with detailed flowcharts.

The general operating principle of the interface tracking method was explained in Section 2.1.5. In short, the volumetric flow rate is obtained by multiplying the mean flow velocity $v = \frac{dx}{dt}$, with x the meniscus' displacements over time t, by the cross sectional area $\frac{\pi}{4}d^2$ of the capillary tube, as given in Equation (2.2) that we remind here:

$$Q_V = \frac{x}{t}.\pi\frac{d^2}{4} \tag{3.1}$$

Due to the different refractive indices of water and air, the interface moving inside the capillary tube appears as a separation between two regions, a dark (air) and a light one (water). The contrast between the two regions is what allows to detect and track the interface. Fig. 3.11 shows an example of images of an interface, moving inside a thick-walled capillary with an inner diameter of 500 μm, at different times.

The displacements of the interface were measured by image processing using a homemade computer program that was written in Python language. The method's algorithm is based on template matching, which is used to search and find the location of a template image in a larger image. The operating principle of this method is explained in the next subsection.

3.2.1 Template Matching

The template matching method is available in OpenCV library as the function cv.matchTemplate() [106]. The latter operates by sliding the template over the large image, pixel by pixel as in 2D convolution, and comparing the template's pixel levels with those of the overlapped region in the large image (Fig. 3.13). Several comparison modes are implemented in the function and are mainly based on a correlation comparison (TM_CCORR or TM_CCOEFF) of the sum of squared differences SSD (TM_SQDIFF). The function returns a grayscale image where each pixel has an intensity that conveys how closely its neighbors match the template. The method we chose to apply is the SSD since it is suitable for discrete signals like images [69]. Besides, Trucco and Verri demonstrated in their book [158] that SSD works better than cross-correlation for template matching.

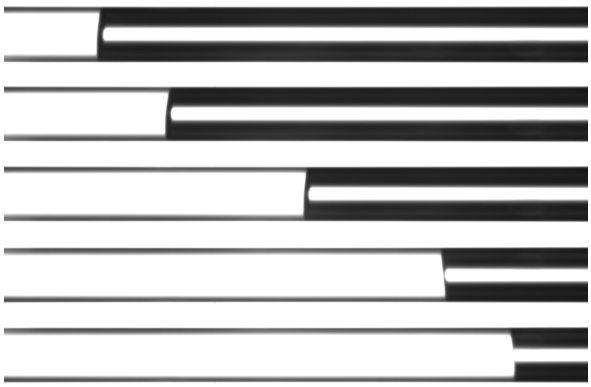

Figure 3.11: Images of an advancing water/air interface acquired by the JAI Spark camera at different instants, for a generated flow rate of 50 nL/min. The dark side is the part with air.

Figure 3.12: Input image of size $W \times H$ (left) and template of size $w \times h$ (right) on which template matching function is applied.

.

If the input image is of size $(W \times H)$ and the template of size $(w \times h)$, the output image will have a size of $(W - w + 1, H - h + 1)$ (Fig. 3.12). The function slides the template through image and calculates the sum of squared differences according to:

$$R(x,y) = \sum_{x',y'} (T(x',y') - I(x+x',y+y'))^2 \tag{3.2}$$

where $T(x',y')$ is the intensity of the pixel at position (x',y') in the template $(x' = 0...w - 1, y' = 0...h - 1)$, $I(x+x',y+y')$ is the intensity of the pixel at position $(x+x',y+y')$ in the large image, (x,y) being the position of the upper left corner of template $(x = 0...W - w + 1, y = 0...H - h + 1)$, $R(x,y)$ is the summation value at the position (x,y).

The position of the template at which the SSD is calculated is given by the coordinates of the template's upper left corner (Fig. 3.13). The minimum SSD value in the output image represents the situation where the differences between the template pixels and those of the overlapped region are the smallest, thus the best matching. The minimal value the SSD can take is zero. This occurs when the template is perfectly identical to a region of the input image.

In order to find the position of the template, the location of the minimum $R(x,y)$ value

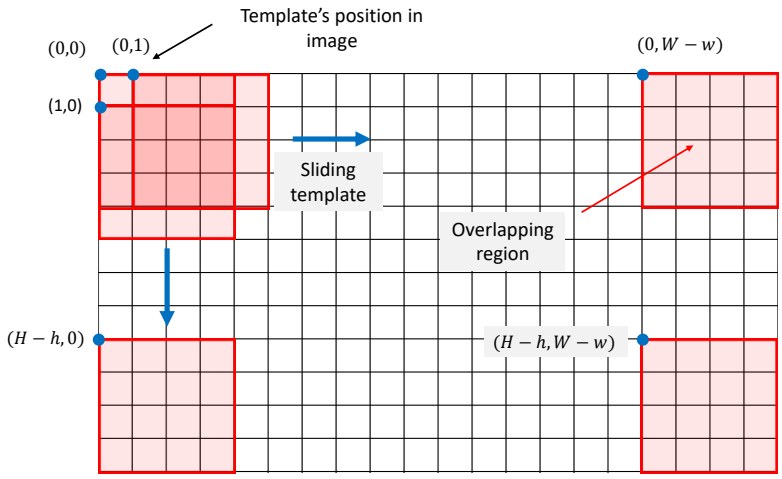

Figure 3.13: Schematic illustration of the positions in image where the SSD between the latter and the template is computed. The pixel size is exaggerated for illustration.

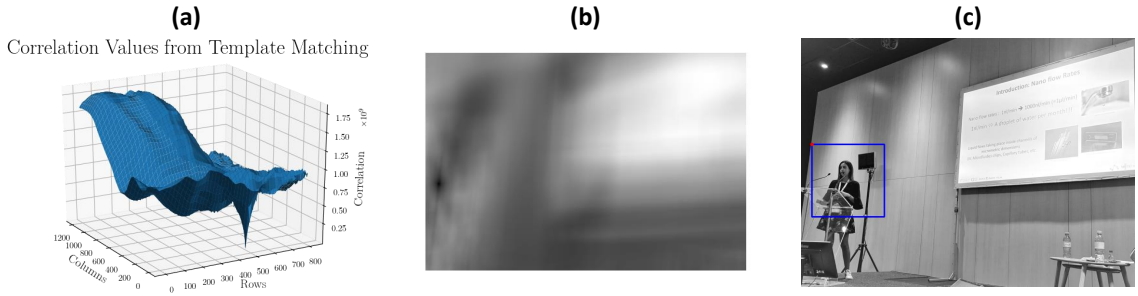

Figure 3.14: Results of the template matching applied on the input image and template of Fig. 3.12. (a) Curve of the obtained SSD function in 3D. (b): Grayscale image with pixel intensities equal to SSD values. (c): Template displayed on the input image at the position where the SSD function has a minimum.

is determined using *cv.minMaxLoc()* function which takes as an input the output grayscale image (Fig. 3.14 (b)). The obtained results are displayed on the input image in (Fig. 3.14 (c))

3.2.2 Measurement of the Interface's Displacements

The method described above can be applied to measure the distance traveled by the meniscus interface between two instants t_1 and t_2 from the images acquired at these instants. The template is extracted from image 1 in such a way that its width is large enough to include the interface and a part from both its sides. Its height should be equal to that of the interface. The front is placed in the center of the template so that the light (liquid) and dark (air) parts each occupy half of the template. The match template function is then applied on the template and image 2 (Fig. 3.15).

By taking (x_1, y_1) as the coordinates of the upper left corner of the template in image 1 and (x_2, y_2) as the location of the SSD's minimum, *i.e.* the position of the template in image 2, the displacement of the template, thus that of the interface is given by the difference $\Delta x = x_2 - x_1$. As the interface moves only on the x axis, $y_2 = y_1$. Yet, small vertical displacements were observed due to occasional vibrations in the system. In order to avoid the measurement of displacements along the y axis, the template is taken in such a way that

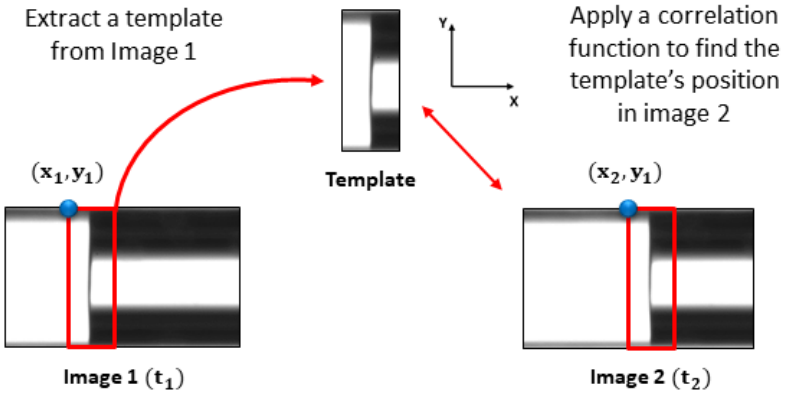

Figure 3.15: Schematic illustration showing how template matching is performed on images of the moving interface.

it occupies the whole image's height. The sliding of the template in image 2 is performed only along the x axis, resulting in a 2-dimensional SSD function and a reduction in the processing time.

A simple way to employ this method would be to measure the displacements of the interface with respect to the origin $(x = 0, t = 0)$, *i.e.* the first image. In this case, only one template that is taken from the initial image is matched with every other image. The measured displacements represent directly the positions of the interface (Fig. 3.16). The instant t_i at which an image i was acquired, *i.e.* its timestamp is determined from the camera's frame rate f according to: $t_i = i \times \frac{1}{f}$. In order to determine the mean flow velocity v during a given time interval, a linear regression is performed on the measured positions. The equation of the regression line is written as: $x(t) = v \times t + c$. With t the timestamp and c the line's intercept. The algorithm for this initial version of the method is summarized in the flow chart of Fig. 3.25.

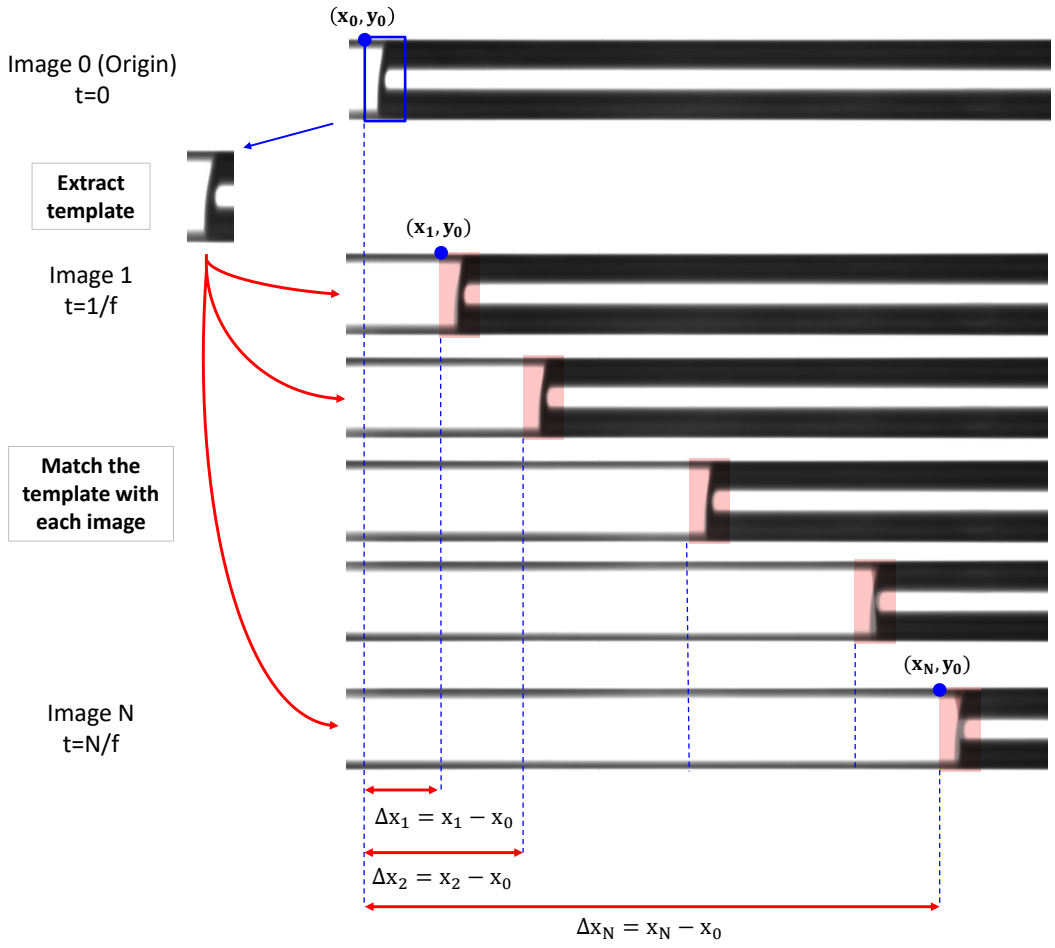

Figure 3.16: Measurement of the meniscus' displacements by matching a template that is extracted from the initial image with all the remaining images.

3.2.3 Template Update

It is important to specify that the procedure described above is applied with the assumption that in each image we look for the same object. However, the liquid/air interface is not static over time as shown in Fig. 3.16, in which the template (in red) is placed each time at the position of the SSD's minimum. In the bottom images, we can see clearly that the interface in the template does not match entirely the one in the image. These changes are mainly due to the stick-slip effect which is detailed in Section 5.1. This phenomenon was reduced considerably by coating the capillary's inner wall with a commercially available glass treatment, resulting in a more stable interface (Section 3.3.1). However, some changes are still observed when the template and the image with which it was matched are separated by a long time interval. As a consequence, the distances travelled by the interface, which in some cases are of the order of the camera's resolution, are strongly affected. In order to assess the effect of changes in meniscus' shape, we compare the matching results of a single template with images separated from it by increasing time intervals.

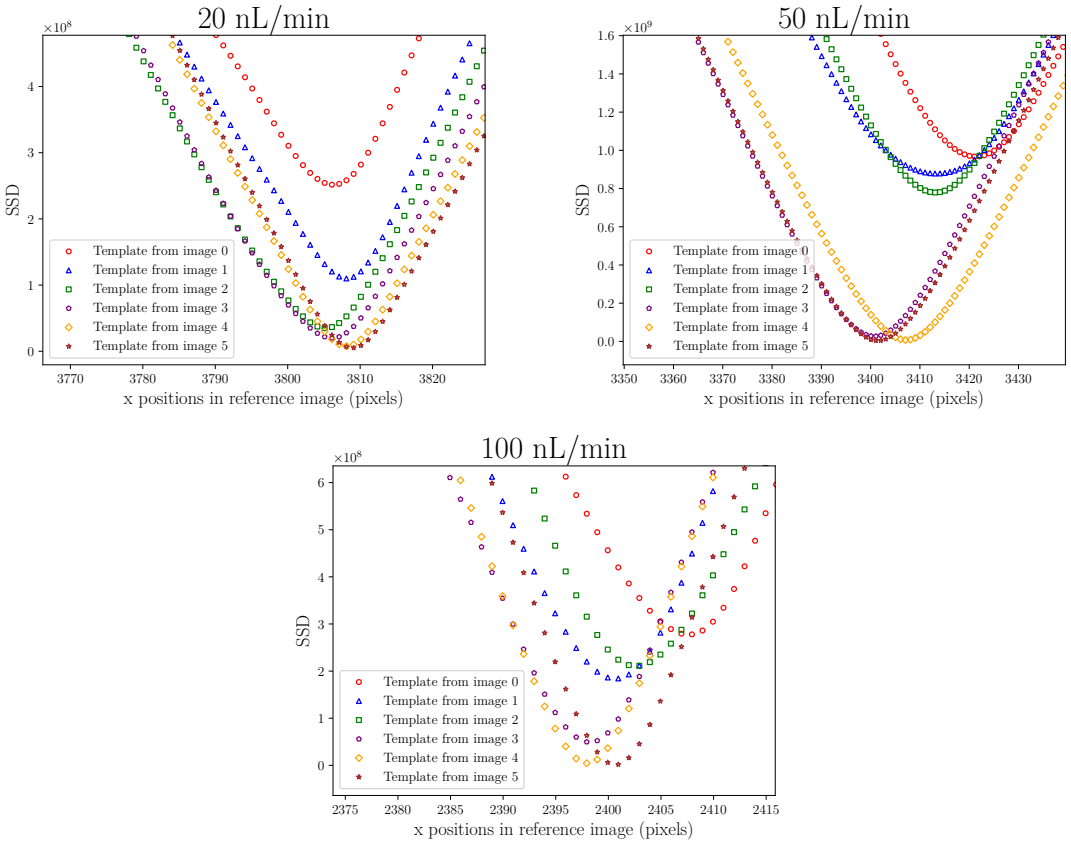

Figure 3.17: SSD values for different templates matched with the same input image, computed for three image sequences. The different symbols represent the matching results between a template that was extracted from an image separated from the input image by a given time interval. The template from image 0 is the furthest from the input image and the template from image 5 is the closest to it. The differences in the position of the SSD's minimum are due to the fact that the interface does not necessarily have the same position inside the extracted template.

Fig. 3.17 shows the obtained results. As can be seen from SSD values, the larger the time interval separating the template and image, the further the SSD's minimum from zero, *i.e.* the less the template matches the image. Even if the SSD function has a minimum in all cases, the location of the latter cannot be interpreted only as the position of the interface since the minimum's value also includes the differences in pixel intensities due to changes in the meniscus' shape. In general the further the minimum gets from zero the less sure we can be about its interpretation, as the displacement and deformation of the interface cannot be decorrelated. As a consequence, we decided to update the template for each measured displacement. By doing so, we make the assumption that due to the short acquisition times, the interface does not change considerably between 2 successive images or changes only slightly in such a way that the minimum of the SSD is not affected.

Template updating is explained in Fig. 3.18. To start, an initial template is selected from image 0 and matched with image 1, resulting in the first measured displacement. In order to measure the next displacement, a template is selected from image 1 this time with updated coordinates that are equal to the sum of the old coordinates with the previously measured displacement. This template is then matched with image 2, resulting in the measurement of

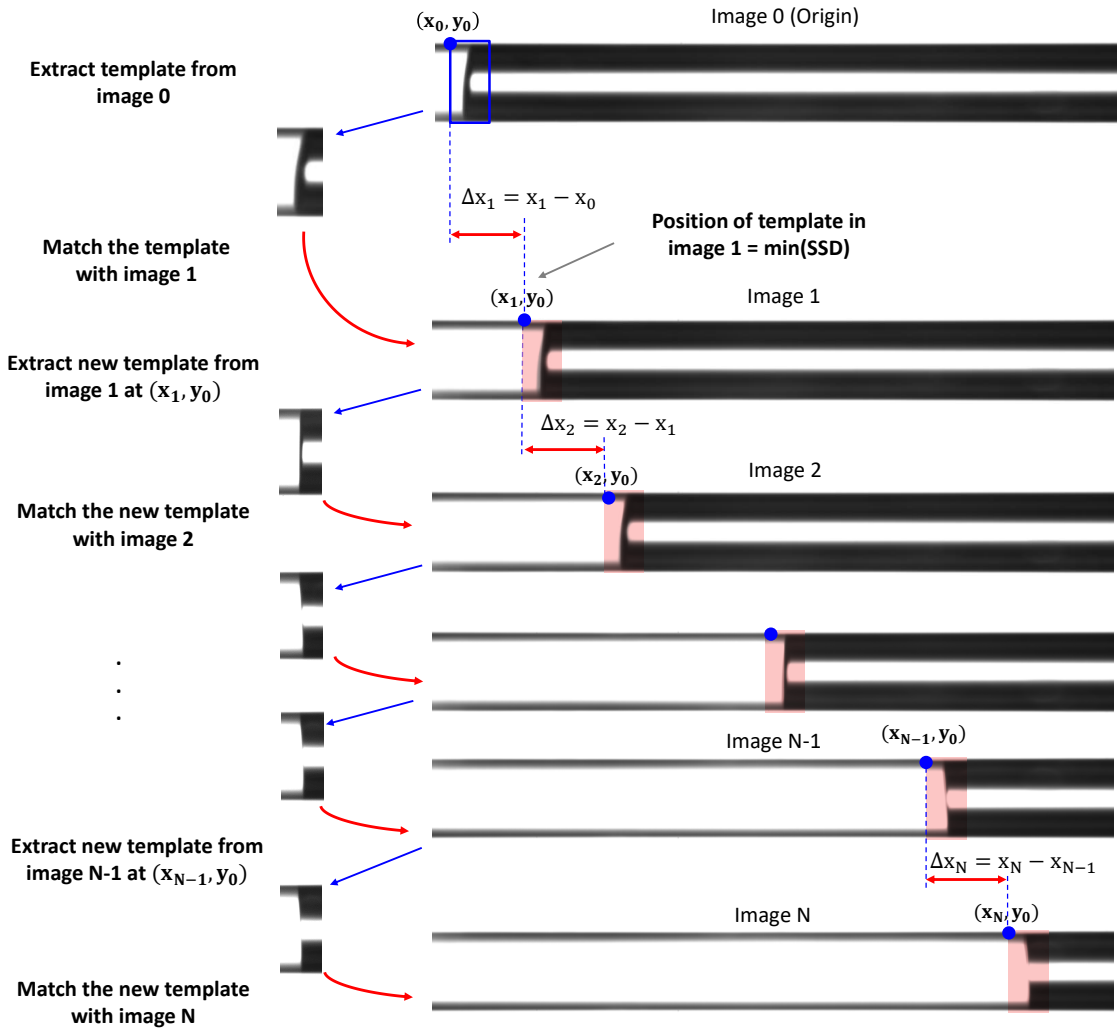

Figure 3.18: Measurement of the meniscus' displacements by matching every two successive images and updating each time the coordinates of the template.

the second displacement and so on. These operations are performed inside a loop that goes through all the images two by two. The general expression of the updated coordinates of the ith template is given by:

$$x^{i}_{template} = x^{0}_{template} + \sum_{j=0}^{i-1} \Delta x_j \tag{3.3}$$

Where $x^{0}_{template}$ is the position of the template in the initial image and Δx_j is the displacement of the template (the interface) between image j and $j+1$. The algorithm for this version of the procedure is summarized in the flowchart of Fig. 3.26.

3.2.4 Region of Interest

The acquired images have a width of around 4096 pixels (full resolution of the JAI camera). When the match template function is applied on the template and the whole image, the calculation of the SSD values at every position along the image's width takes a considerable time. In addition, some positions in the large image are not important because far from the interface (Fig. 3.19 (left)). For these reasons, we cropped the images, defining regions of interest (ROI). The ROI must be small enough to reduce measurement time, but large enough to contain the template and leave a distance on both its sides to allow it to slide (Fig. 3.19 (right)).

Table. 3.2 is an example of the processing time of template matching function when it is performed on the original image and on a ROI extracted from the image. The processing

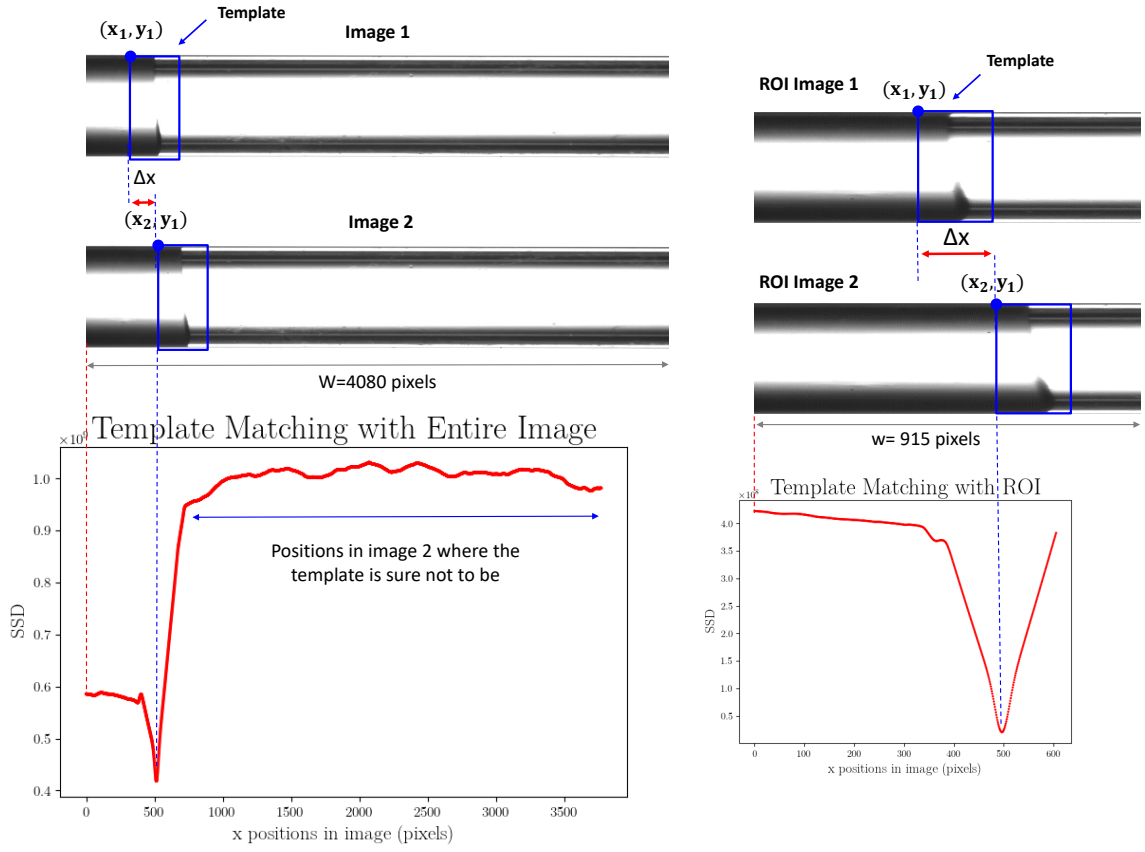

Figure 3.19: SSD values when a template is matched with the entire image (left) and with a ROI extracted from the input image.

Table 3.2: Processing time of the template matching function when when applied to an entire image and on an ROI.

	Original image	ROI
Size (Height x Width)	(892 x 4080)	(231 x 832)
Processing time for template matching function (ms)	322.65	18.27

time in the case of a ROI that is about 19 times smaller than the image, is about 18 times lower.

As the interface travels the full width of the image, it eventually goes out of the initially selected ROI if the latter is not updated. For this reason, the ROI is taken in each image at a different position that depends on the displacement of the interface. The initial ROI is extracted from image 0 and image 1. From the ROI of image 0 is extracted the initial template which is matched with the ROI of image 1, resulting in the first measured displacement. For the second displacement, the ROI's position is updated by adding the previously measured displacement to its initial position. A new ROI, having the same dimensions as the old one, is extracted from image 1 and 2 and the template selected from image 1. Contrary to the previous version of the algorithm, the coordinates of the template are not updated. The template occupies the same position in the ROI which is moved each time following the interface. The general expression of the ROI's position, *i.e.* the coordinates of its upper left corner are given by Equation (3.3). Note, the ROI is taken in such a way that it occupies the whole height of the image thus, it moves only along the x axis. Nevertheless, if its height is chosen differently the coordinates along the y axis are chosen initially and kept constant. The template on the other hand should always occupy the full height of the ROI.

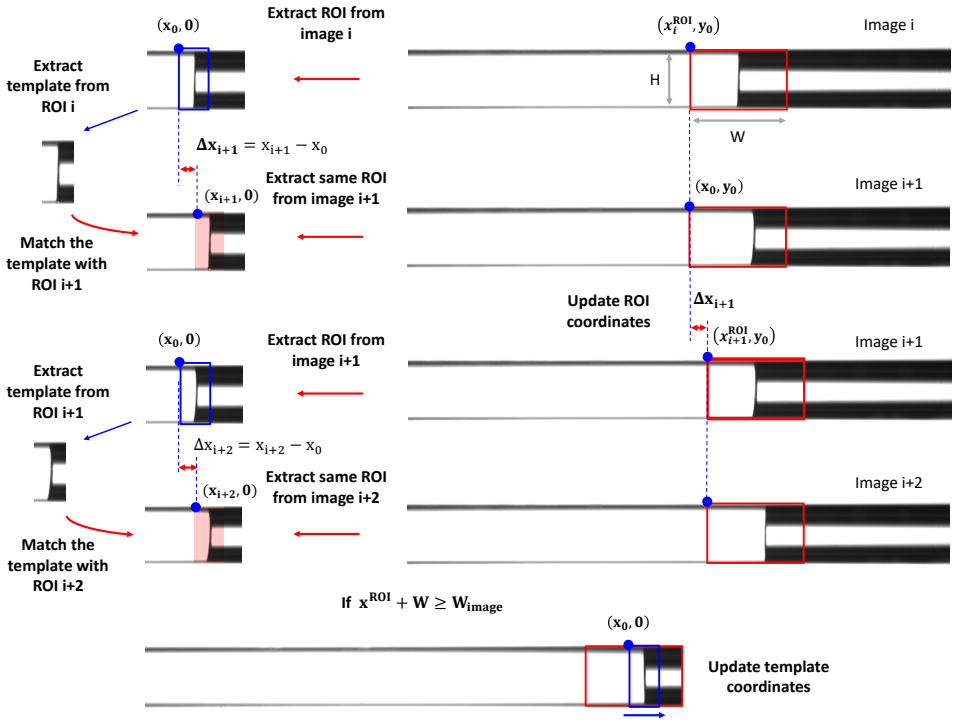

Figure 3.20: Measurement of the meniscus' displacements by matching the ROIs of every two successive images and updating each time the coordinates of the ROI.

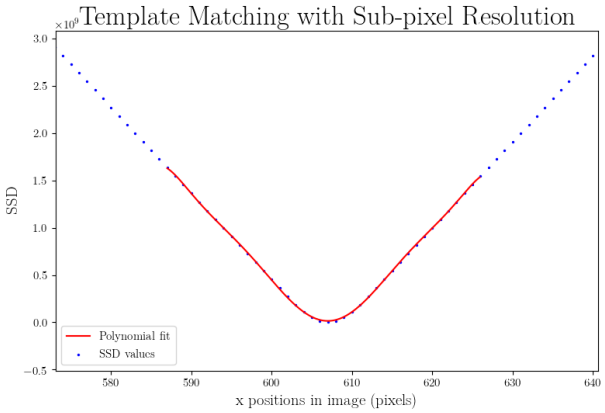

Figure 3.21: Polynomial fit performed on the SSD function near its minimum in order to determine template positions with a sub-pixel resolution.

It is important to note that, when the ROI arrives to the right edge of the image its position cannot be updated as it is impossible to select it outside of the image. In this situation, we keep it in the position where it stopped and let the template move by updating its coordinates. The updated coordinates of the template are expressed by Equation (3.3) where $x^0_{template}$ is the template's initial position which wasn't updated and i is a kind of a counter for the number of measured distances starting from the moment when the ROI stops moving. The template's position is updated until it reaches the edge of the ROI. In this situation, the SSD's values only decrease as the interface is too close to the edge. The right side of the interface being not accessible, the values doesn't increase and a minimum cannot be determined. For this reason, the measurements are stopped when the template's right edge arrives at a distance of 50 pixels from the ROI's edge. This version of the algorithm is represented by the flowchart in Fig. 3.27.

As the template matching function gives the SSD values for each pixel position, the location of the minimum is given with a pixel resolution. This means that all interface displacements that are smaller than a pixel are not measured. In order to overcome this limitation, a polynomial fit is performed on the SSD values around the minimum. The location of the minimum of the polynomial function can be determined with sub-pixel resolution. However, one must keep in mind that the better the resolution, the more calculated x positions (from the polynomial) and the larger is the processing time. The table below shows the time necessary to determine the location of the minimum at different precisions.

Table 3.3: Processing time necessary to determine the position of the polynomial fit's minimum with different resolutions.

Resolution of polyfit function	0.1	0.01	0.001	0.0001
Necessary time to determine the minimum (ms)	1.04	1.78	9.84	116.33

3.2.5 Computer Program

The different operations are carried out using a home made python script with a Graphical User Interface (GUI) made using TKinter (GUI framework integrated in the standard library of Python). (Fig. 3.22) is a general view of the GUI when an image is opened. As can be seen, four sections are implemented. The "Images and ROI" section allows to select an image directly from a folder and display it in a separate window, enter the path of the rest of images

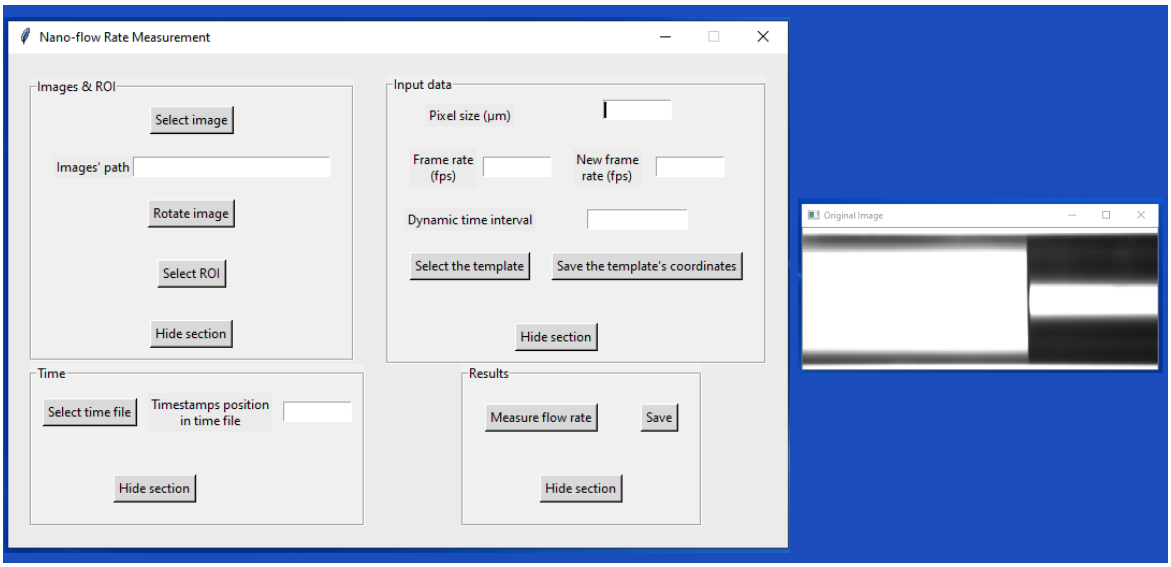

Figure 3.22: GUI associated with the interface tracking algorithm.

to be processed, rotate the image to have an interface that moves from left to right and select a ROI directly on the image (Fig. 3.23 (Left)) to display it in the same window. The initially selected image must be the first in the sequence as the program always reads the images by order. Therefore, if the initial ROI is extracted from a random image, the interface would not be centered in the template because its position will change inside the ROI. The ROI's coordinates and dimensions are saved in the program as input parameters.

The section "Time" allows to select a file that contains the timestamps of images. These can also be determined from the frame rate that is specified in the section "Input data" as an input parameter. In general, the input section allows to enter the different parameters necessary for the calculation of the flow rate such as the pixel size, the number of position points used to calculate each value of the dynamic flow rate, and the selection of the template directly on the displayed ROI (Fig. 3.23 (Right)). The coordinates of the template are saved in the program by clicking on the associated saving button. In case of choosing to measure the displacement between images that are separated by longer time intervals, one can use a lower frame rate. The new timestamps are calculated in the program from the new frame rate, which must be a divisor of the old one. In addition, only the images corresponding to the new timestamps are taken into account for the flow rate calculation. Note, the new frame rate does not change the initial timestamps, instead the corresponding values and the associated images are skipped in the loop.

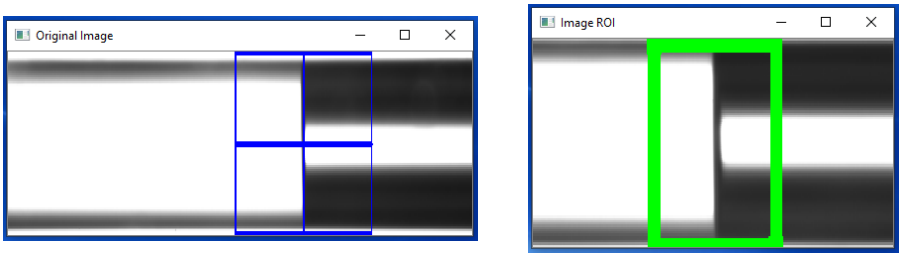

Figure 3.23: Example of operations that can be performed on an image within the GUI. (left): selection of an ROI. (right): selection of a template from the ROI.

Table 3.4: Notifications displayed in the terminal when performing operations on the image.

Operation	Displayed notification
ROI selection	Select a ROI and then press SPACE or ENTER button! Cancel the selection process by pressing c button!
ROI validation	"The coordinates and dimensions of the ROI"
Template selection by drawing a rectangle	CLICK RIGHT if you wish to stop drawing (after right clicking, the current coordinates can be saved by clicking on Save button)
Right click to stop the selection	Coordinates ready to be saved, click on the SAVE button
Click on the saving button of the template	"Coordinates of the saved template"

The section "Results" allows to launch the program by clicking on the button "Measure flow rate". When the calculations are finished, the graphs of the different calculated variables are displayed one after the other in a separate window. The input parameters and the measurement results are all saved automatically in text files. In order to guide the user in the realisation of the different operations and to easily identify the errors, explicit notifications are displayed in the terminal. Examples of guiding and error notifications are given in Tables 3.4 and 3.5, respectively.

Table 3.5: Notifications displayed in the terminal in case errors are made.

Error	Displayed notification
Wrong or missing path of images	Error while loading images! No images found
Click on "Select ROI" button without openning an image	You need to select an image first!
Click on "Select the template" button without openning an image	You need to select an image or ROI first!
Click on "Save the template's coordinates" button without selecting a template	Error: No coordinates to save!
Wrong format or missing input parameters	Error: Verify data typing or selection!

Another version of the existing GUI was made by our intern student, Sana Hassen (Fig. 3.24). The new software allows to display the images, make all the operations and display the results all in the same window. The measurement uncertainty is also calculated in this software, whereas before it was determined separately using Microsoft Excel software.

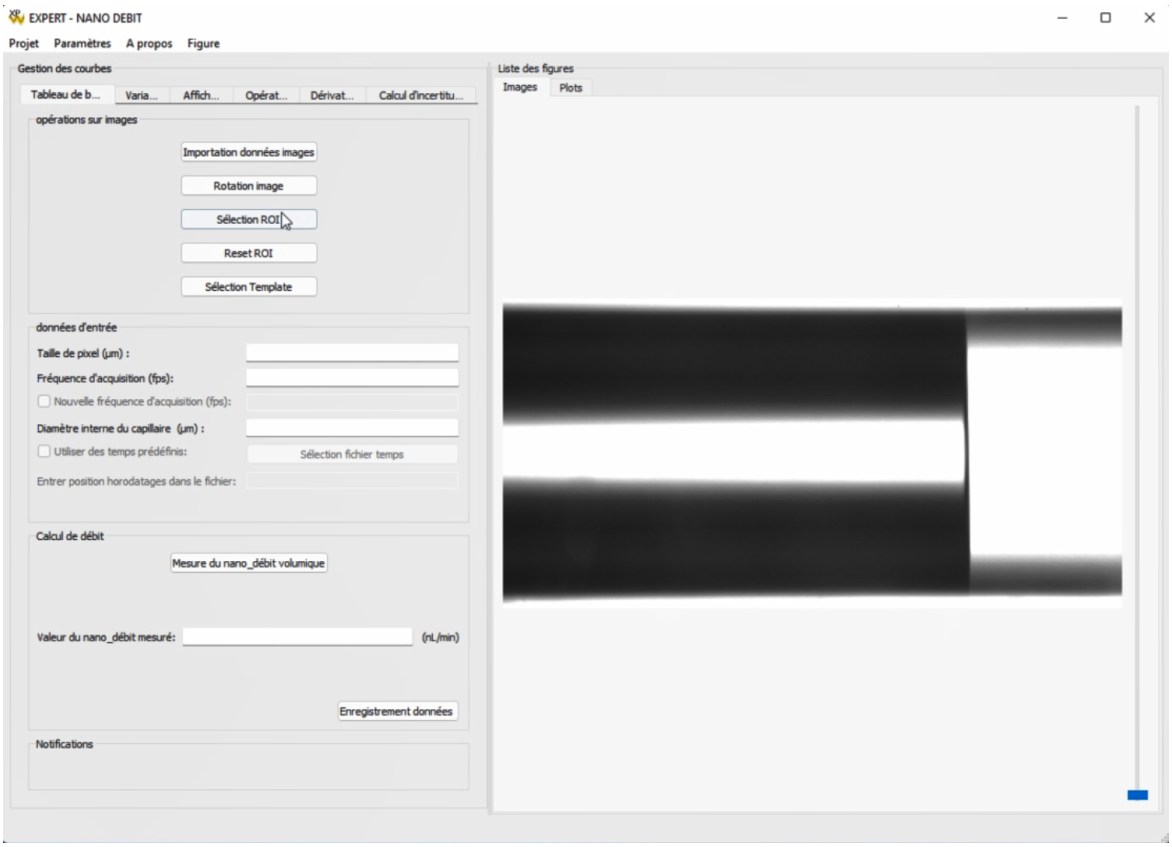

Figure 3.24: Image of the new GUI for the interface tracking.

3.2.6 Flowcharts

The algorithms presented in Section 3.2 are described below, in the form of flowcharts. The first flowchart (Fig.3.25) represents the most simple way in which template matching can be applied. This simple version is based on the matching of one template extracted from the initial image with all the remaining images. The flowchart of Fig. 3.26 corresponds to the case where the coordinates of the template are updated but the matching is performed on the entire images. Fig. 3.27 shows the case where the images are cropped and the matching is applied on the ROIs which are each time updated. The final version of the algorithm is shown in Fig. 3.28. This version includes the case where the ROI reaches the image's end and cannot be updated, so only the template's coordinates are updated.

After presenting the experimental setup for the interface tracking method and explaining its working principle, we move on to the calibration procedure of flow generators and meters using our primary system.

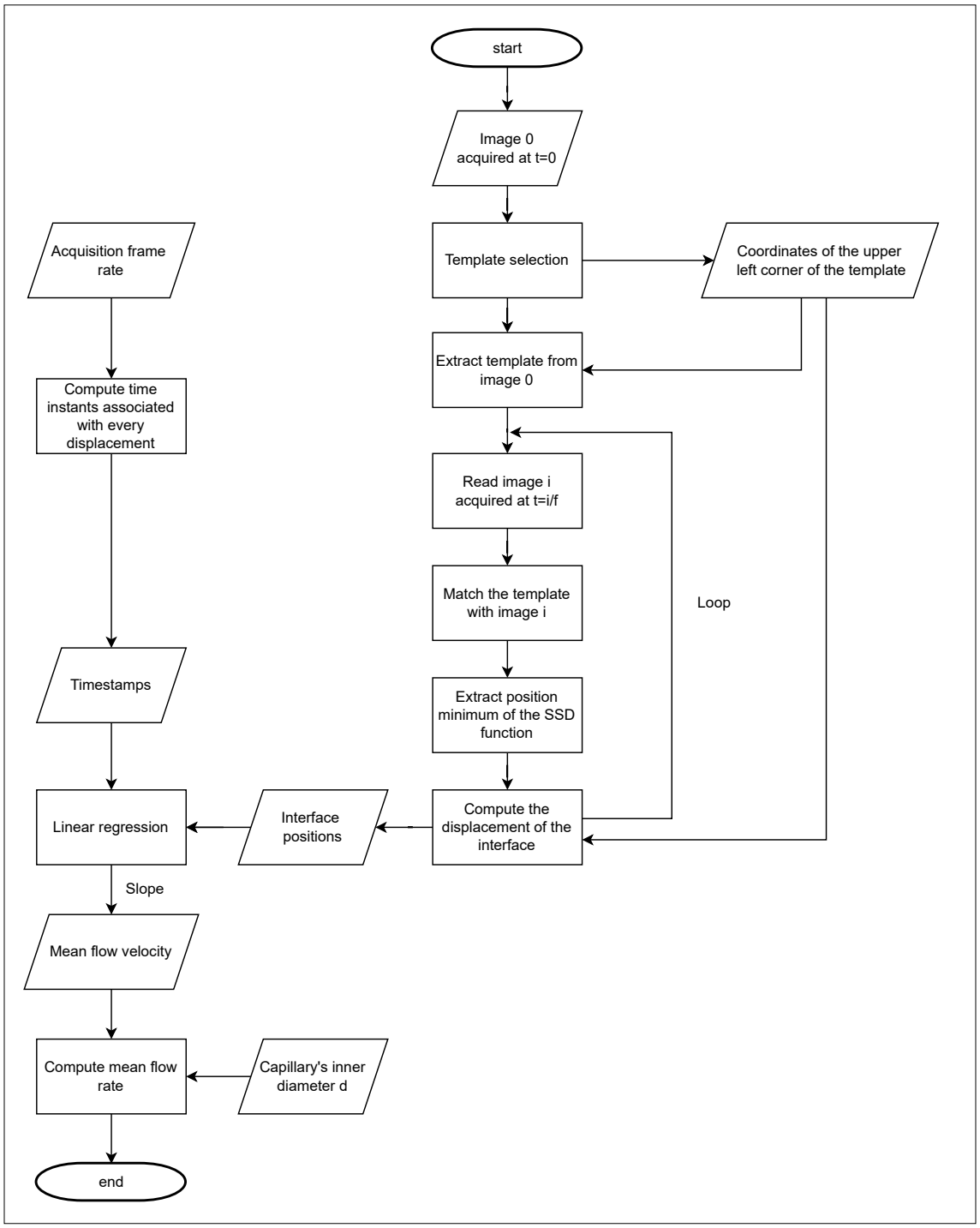

Figure 3.25: Interface tracking algorithm corresponding to the case where one template is matched with all images.

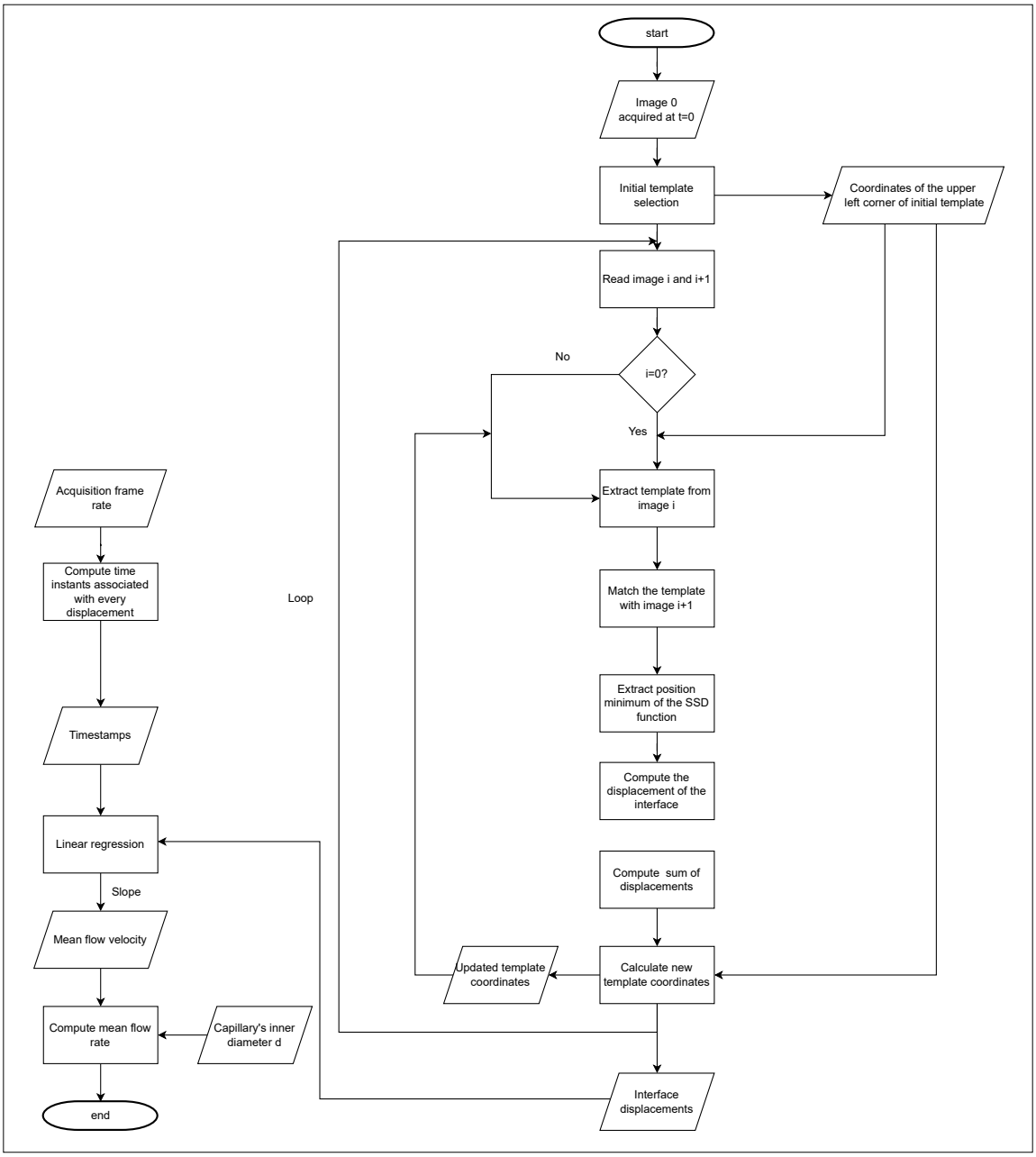

Figure 3.26: Interface tracking algorithm corresponding to the case where the template is updated.

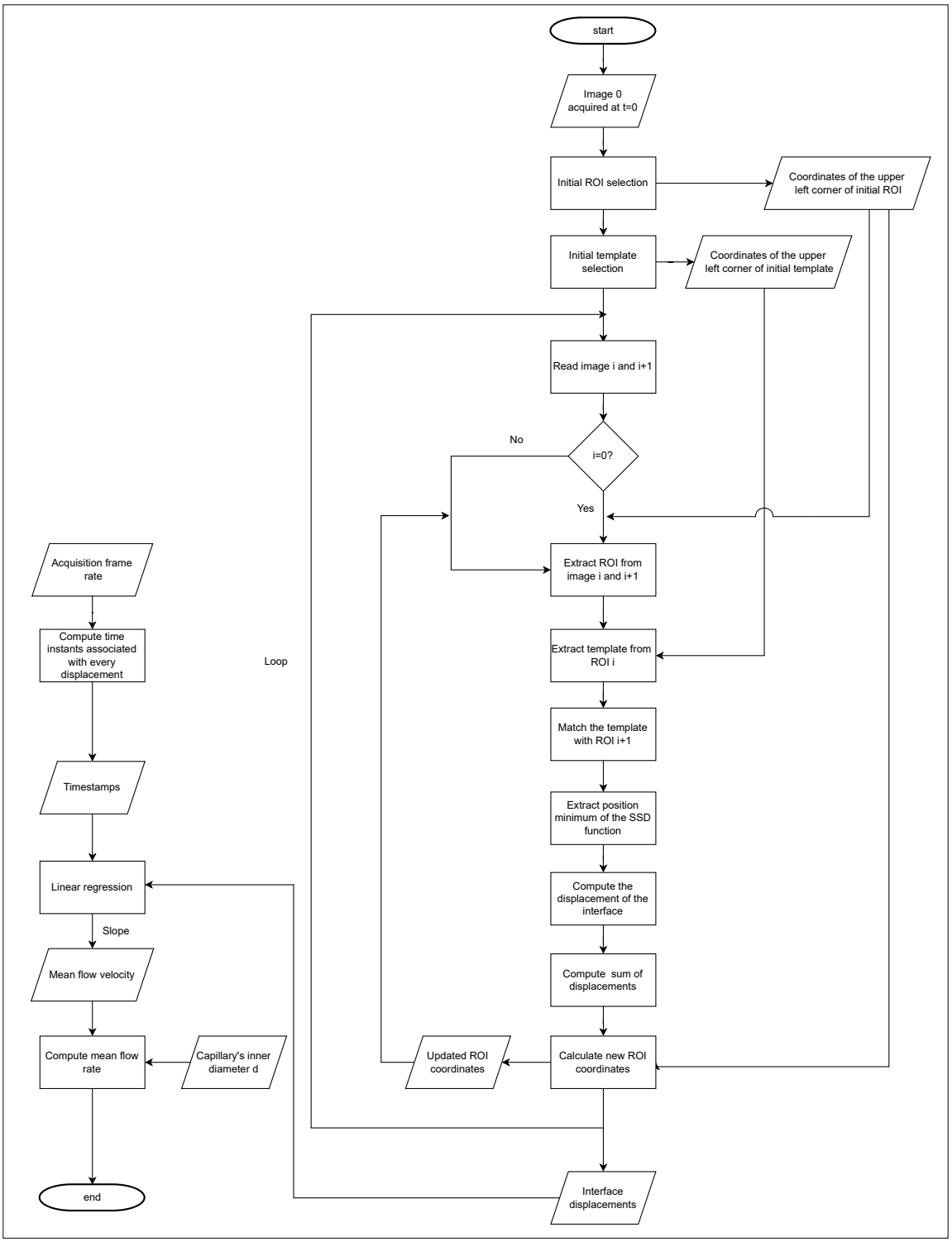

Figure 3.27: Interface tracking algorithm corresponding to the case where images are cropped to ROIs.

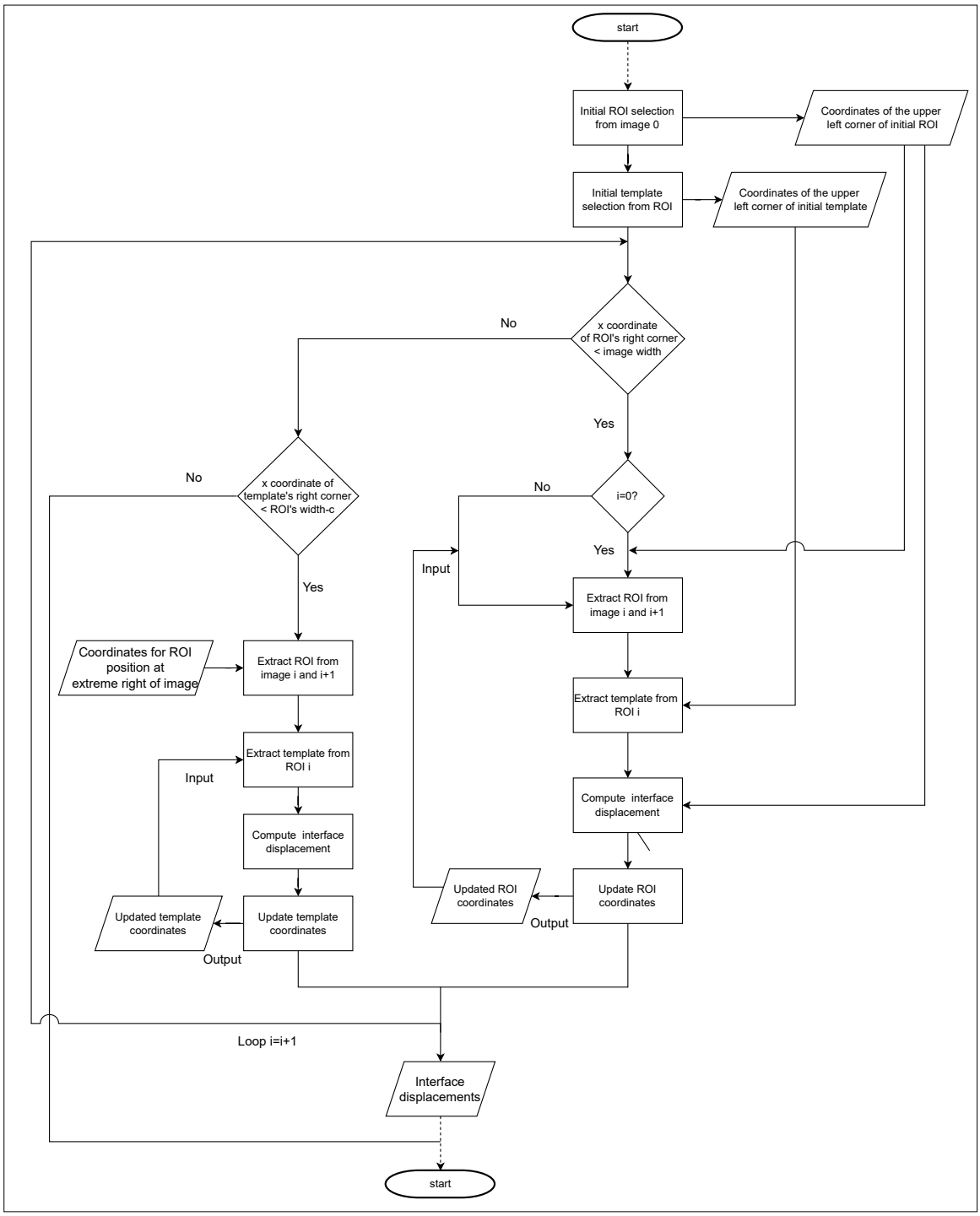

Figure 3.28: Final Interface tracking algorithm which includes the use of ROIs instead of images, updating of the ROI's coordinates and the updating of template's coordinates when the ROI reaches the image's end.

3.3 Calibration Procedure for a Flow Generator or Meter

In this section we present the procedure for the calibration of a flow meter or flow generator. We start by a brief description of the calibration setup. Then, we explain in details the steps of the system's preparation including the cleaning, treatment of the capillaries and the adjusting of the different devices. Finally, we present with practical examples, the method to determine the most adapted configuration of the system for a given flow rate, *i.e.* the choice of parameters such as camera resolution, measurement time, etc.

3.3.1 Preparation of the System

The experimental setup for the calibration of low-flow-rate devices is explained in detail at the beginning of this chapter. In short, for the calibration of a flow meter, the latter must be connected between our flow generator and the capillary tube (Fig. 3.29 (A)). In the case of the calibration of a flow generator, ours is replaced by the one to be calibrated as shown in Fig. 3.29 (B).

In order to facilitate water handling inside the capillary and reduce the stick-slip effect during measurements, the capillaries' inner surface was coated by a hydrophobic and oleophobic glass repellency solution from Aculon® (Section 5.1). This solution is a nano-scale treatment product resulting in a contact angle of around 115° for water and a coating thickness of 2 to 20 nm. The thickness being way thinner than the capillary, it can be neglected. The coating procedure is explained below.

The capillaries must be cleaned and dried in a proper way before the coating. Isopropyl alcohol is used for the cleaning after which the capillaries are left to dry in ambient air. There are several application techniques for the coating: wiping, dipping, flow coating and spraying. The adapted technique for the capillaries is the flow coating which consists in dispensing the solution over the surface to be coated and let the excess drain. In our case, the coating must flow inside of the capillary. For this, a syringe is filled with the treatment solution that is introduced inside the capillary tube by pushing the piston slowly (Fig. 3.30). After making sure that the solution covered all the inner walls of the capillary, this latter is held vertical to allow the excess material to drain. The capillary is then left for 24 hours to cure at ambient temperature. The capillaries may also be cured for 2 hours at 150 °C knowing that higher temperatures create coatings with increased durability.

Once the capillaries were dry we started to prepare the system for the measurement. The different connecting pipes were cleaned separately using isopropanol then connected to the flow meter and capillary tube. The capillary was not cleaned with alcohol to avoid that the

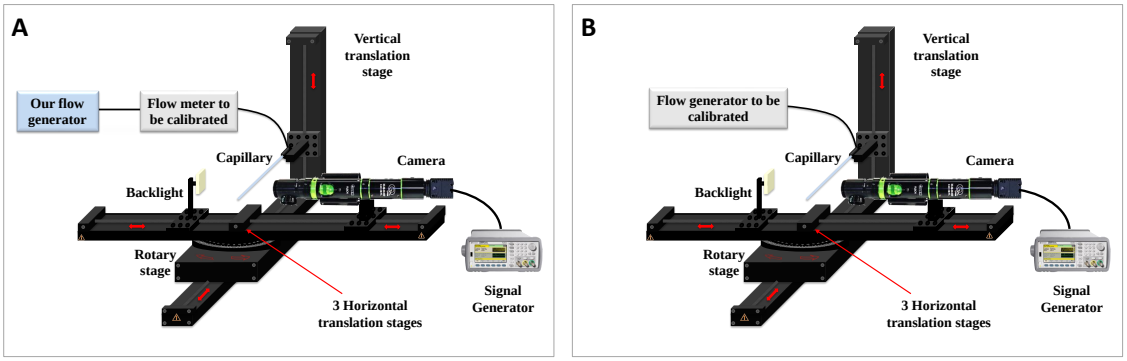

Figure 3.29: Configuration of the experimental setup for the calibration of a flow meter (A) and flow generator (B).

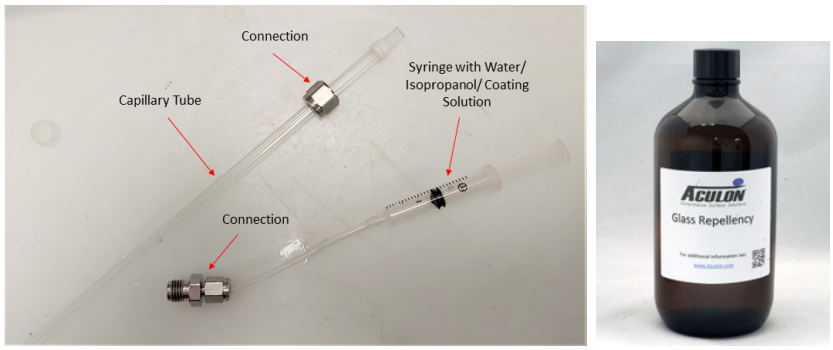

Figure 3.30: Syringe and tubing used for the coating of the capillary (left) and Aculon's glass repellency solution (right) [73].

coating comes off. The whole system was then purged with ultrapure water during several minutes by means of a large syringe. After disconnecting the syringe, the pipe was held slightly at a lower level than the capillary's in such a way that water flows outside of it.

The syringe was filled with ultra-pure water then, connected to the tube. Small volume syringes ($< 100\mu L$) are very hard to fill by drawing out water, instead they were filled directly from the ultra-pure water system or by another syringe with the plunger removed. During the connection, water was left to flow out of the tube in a way that the interface moved backwards in the capillary. At the same time, the syringe's plunger was pushed slowly to make sure its entrance contained water. This avoided introducing air bubbles in the system. The interface was moved at least half of the capillary's length in order to prevent it from reaching the capillary's end after successive measurements and to have a smaller rate of evaporation.

After illuminating the capillary and moving the interface in the camera's field of view, the interface needed to stay static as the system was closed at one side by the syringe and no flow was generated yet. Since water is an incompressible liquid and evaporation is so low to be seen in the live images, a motion of the interface was interpreted either as a leak or air bubbles in the system. The focus was adjusted with respect to the center of the meniscus, not the inner or outer diameter of the capillary, a good focus corresponded to the situation where the meniscus' outer edge was sharp and as far as possible from the inner one (Fig. 3.31).

Most of the capillary tubes used had an outer diameter of 6.2 mm and a few millimeters thick wall, which made them easy to manipulate compared to thin-walled capillaries that break easily. Besides, as the camera's depth of field is smaller than the capillaries' outer diameter, all the dust that deposited on the surface of the capillary was out of focus. Additionally, the contrast between the parts containing water and the one with air was higher in thick wall capillaries than that in thin ones.

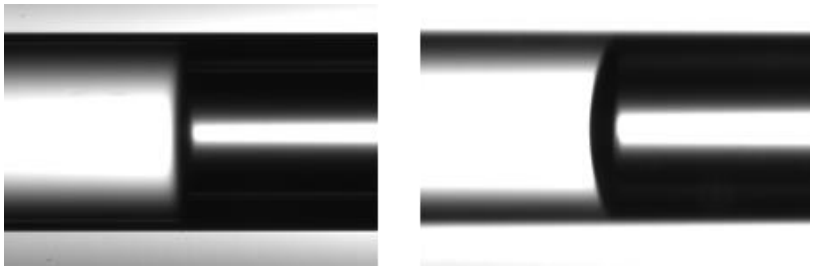

Figure 3.31: Images showing a bad (left) and good (right) focus.

Image illumination was adjusted in such a way that the contrast between the part containing the water and the one with air was high. The illumination pattern along the capillary in a given part needed to be the same to ensure that every two successive image ROIs that were used to measure the interface's displacement by template matching, had the same background.

As images were acquired only when the interface was in the camera's field of view, it was important, before starting a measuring point, to move back the interface either by generating a negative flow rate or by simply moving the camera forward along the x axis. The position at which the interface needed to be placed had to allow about 10 minutes of flow stabilization before the interface entered in the camera's FOV and measurements started. The method to determine system parameters such as the proper frame rate, camera resolution, etc. is explained in the following section.

3.3.2 System Configuration

The displacement of the interface between two successive images depends on several parameters including the capillary's inner diameter, acquisition frame rate and the pixel size at a given zoom. It is then important to choose, for each flow rate, the right parameters that allow from one hand a measurable distance, *i.e.* a distance superior than the camera's resolution, and from the other hand, a measurement time sufficient for the characterisation of the device under calibration. In this section, we explain how these parameters are determined.

In Table 3.6, we give system configurations for flow rates ranging from 1 to 1500 nL/min. Starting from a flow rate Q_V, an inner diameter d_{inner} and camera zoom are chosen. The latter sets the values of the pixel size p and the horizontal field of view W:

$$W(\mu m) = W(pixels) \times p(\mu m) \tag{3.4}$$

This information is enough to determine the nominal flow velocity:

$$v = \frac{4Q_V}{\pi d_{inner}^2} \tag{3.5}$$

as well as the transit time $t_{transit}$ which is defined as the time needed by the interface to cross the entire distance W, *i.e.* the time spent by the interface in the camera's FOV:

$$t_{transit} = \frac{W}{v} \tag{3.6}$$

If the flow velocity was high enough so as to be able to detect the meniscus' displacements at the given resolution, and if the transit time was large enough, then the adapted acquisition

Table 3.6: Examples of system configurations at different flow rates.

Q_V (nL/min)	d_{inner} (µm)	Zoom (%)	p (µm)	W (µm)	v (µm/s)	v_p (pixels/s)	$t_{transit}$ (min)	t_{meas} (min)	f (fps)	N_{images}
1500	2000	0	1,35	5530	8,0	5,9	11,6	11,6	5	3474
1000	2000	0	1,35	5530	5,3	3,9	17,4	17,4	3	3127
500	1000	0	1,35	5530	10,6	7,9	8,7	8,7	5	2606
100	500	0	1,35	5530	8,49	6,3	10,9	10,9	5	2792
70	500	0	1,35	5530	5,94	4,4	15,5	15,5	4	2606
50	500	0	1,35	5530	4,24	3,1	21,7	21,7	3	2400
20	500	25	0,855	3502	1,70	2,0	34,4	34,4	2	2063
5	250	50	0,546	2236	1,70	3,1	22,0	22,0	2	2635
1	250	50	0,546	2236	0,34	0,6	109,8	45,0	1	2700

Table 3.7: Values of the delivered volumes at the configurations defined in Table 3.6 and the adapted syringe volumes.

Q_V **(nL/min)**	$V_{delivered}$ **(µl)**	$V_{syringe}$ **(µl)**
1500	58,1	100
1000	43,1	100
500	28,0	100
100	6,3	10
70	5,4	10
50	4,8	10
20	1,8	10
5	0,5	10
1	0,2	10

frame rate f was chosen. The choice was made in such a way that $\frac{v}{f} \geq 1$, *i.e.* the displacement between two successive images was equal or larger than the pixel size. This condition allowed to have measurable distances. If the transit time was too long, a shorter measurement time t_{meas} was defined instead. The frame rate and measurement time were used to compute the number of images $N_{images} = f \times t_{meas}$ that would be acquired, in that configuration.

In Table 3.7, we give the liquid volumes that would be delivered at each configuration. This volume is defined as the total volume delivered by the syringe after 3 successive measurements, at the same generated flow rate:

$$V_{delivered} = 3 \times Q_V(t_{meas} + t_{stability}) \tag{3.7}$$

where $t_{stability}$ is the time necessary for the flow to stabilize. Calculating the nominal delivered volume allows to choose an adapted syringe volume $V_{syringe}$, the latter being chosen in such a way that $V_{syringe} > V_{delivered}$.

3.3.3 Measurements

The interface needed to be placed at a distance $d_{stability}$ before the camera's FOV, in order to allow the flow to stabilize for a duration of $t_{stability}$. This distance depended on the interface's velocity v at the targeted flow rate and for a given camera zoom:

$$d_{stability} = t_{stability} * v \tag{3.8}$$

Before starting any series of measuring points, evaporation was measured during at least 10 minutes, following the procedure explained in Section 4.2. Before generating a flow, the flow rate measured by the flow meter was recorded during three minutes after which the flow was generated. When the interface entered the camera's FOV after a time interval that was approximately equal to the calculated stability time, image acquisition was started. When the interface reached the FOV's right edge, acquisition was stopped and after around 20 seconds the flow was stopped too. The recording of the flow rates measured by the flow meters continued for approximately three minutes in order to measure the flow meter's zero. The time instants associated with each of the above mentioned actions were noted from the time recorded by the flow meter. The calibration procedure is shown schematically in Fig. 3.32.

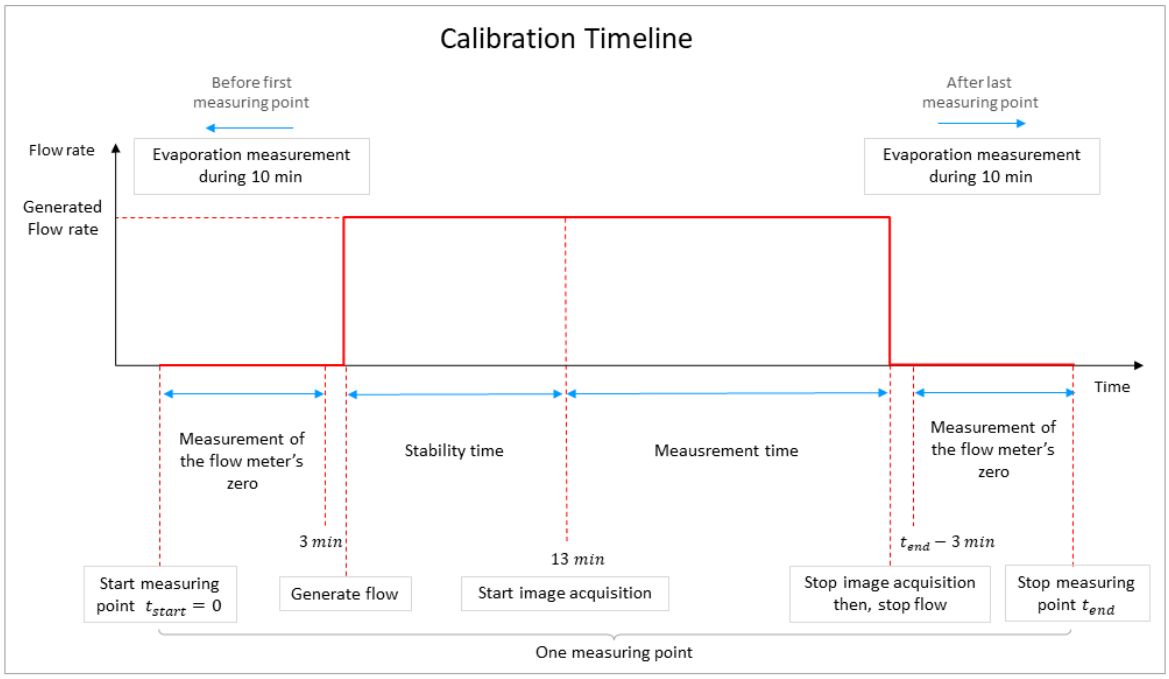

Figure 3.32: Timeline of one flow meter calibration point. Evaporation is measured during 10 minutes at the beginning and end of a series of measurement points of the same calibration.

Our interface tracking method is based on a robust template matching algorithm which can be employed with the only condition of having contrast on both sides of the interface. As the algorithm takes into account the general shape of the interface and the template is always updated, no constraint is imposed on the meniscus, which can change over time. It is this quality that constitutes the strength of our method compared to other ones, which are based on edge detection of the meniscus. In these methods, the displacements can be affected considerably by the change in the shape of the meniscus or when the latter does not appear entirely.

Chapter 4

Traceability to the S.I. of Units and Uncertainty Budget of the System

After describing the operating principle of our method and how it is employed to calibrate flow generators and meters, we move on to the metrological features of the measurement system. As the displacements of the interface are measured in pixels by image processing, they need to be converted to metric units. This is achieved by calibrating the camera using a transfer standard, in order to determine the pixel size in metric units and use it to convert the distances. The first section is dedicated to the procedure used to measure the pixel size using a transfer standard which ensures the traceability of the pixel size, thus that of the measured distances. In addition, a quantification of the optical distortions is carried out and used to estimate the uncertainty associated with the measurement of the pixel size. At the end of this section, we describe the traceability of the images' timestamps which is ensured by triggering the camera using a frequency generator, itself traceable to the French primary standard for time and frequency.

In the second section, we present the uncertainty budget associated with our system. We start by giving the general expression of the total measurement uncertainty, then we describe in detail every component.

To conclude this chapter, we discuss the traceability of the system through the measurement of the capillary's inner diameter. First, we describe existing methods based on various working principles. Then, we present a new method that we developed in the context of this thesis.

4.1 Camera and Timestamps' Calibration

This section is devoted to the traceability of the measured flow velocities which includes the traceability of the distances and that of the timestamps.

4.1.1 Measurement of the Pixel Size

In order to determine the pixel size at a given zoom, we use a length transfer standard that is an objective micrometer (OM). The latter is a rectangular slide on which is etched a 1 mm scale that allows the passage of light from a backlight to the camera (Fig. 4.1). An image of this light transmitting scale is taken at different zooms and, the different interline distances are measured in pixels by image processing. The experimental setup used is shown in Fig. 4.2 (a). The calibration of the micrometer in a COFRAC (ISO 17025:2017) accredited laboratory allows to have the previously measured distances in real units. The pixel size is determined by dividing calibration distances (in metric units) by the associated

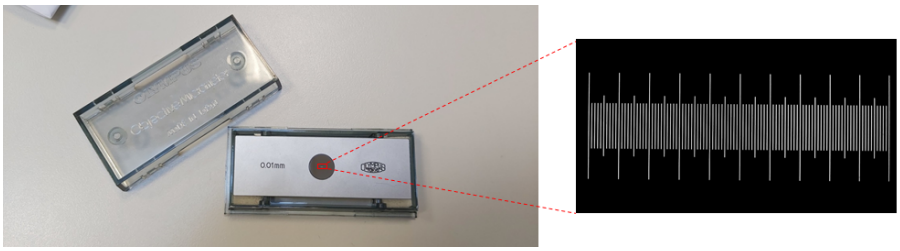

Figure 4.1: Image of the objective micrometer (left) as seen by a camera or microscope (right).

measured ones (in pixels). The detailed steps for the determination of the micrometer's inter-line distances in pixels and the associated uncertainty are explained below.

Alignment of the Objective Micrometer In spite of the efforts to visually align the micrometer with the camera's axis during measurements, it is important to check the obtained images in order to detect any misalignment before image processing. In the following, we explain the procedure to correct misalignment which can occur in different planes compared to the camera's axis.

When the micrometer is not aligned perfectly in the (oyz) plane, it appears rotated in the images (Fig. 4.2 (b)). The distance between the image's edge and the lines varies from top to bottom. These changing distances can be used to determine the angle of rotation of the micrometer and rotate images before the measurements.

The distances are measured from the left and right edges of the image to the closest large lines as follows. First, the original image is cropped so that the large lines occupy the whole image's height as shown in Fig. 4.3 (a). Then, a Gaussian blur filter with a window size of 3x3 is applied on the image to reduce noise. Next, the lines' edges are detected by applying a Canny edge detection filter from OpenCV Python library. This filter takes as inputs the image to be processed and two threshold values. The first one is the gradient intensity under which the edges are eliminated and the second one the gradient intensity above which all edges are sure to be real edges. The threshold values are determined by applying Otsu's method on the gradient image which is obtained using a Sobel filter (Appendix A). The maximum threshold for Canny method is taken as $t_{\max} = t_{\text{Otsu}}$ and the minimum one as $t_{\min} = \frac{t_{\text{Otsu}}}{2}$ where t_{Otsu} is the threshold given by Otsu's method. The output is a

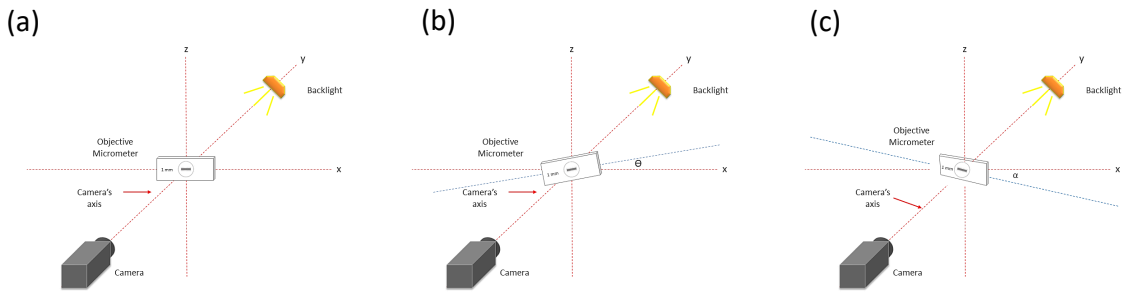

Figure 4.2: Camera calibration setup using an objective micrometer. (a): Micrometer perfectly perpendicular the the camera's axis. (b): misalignment of the micrometer with respect to the camera's axis in the plane (oyz). (c): misalignment in the plane (oxy).

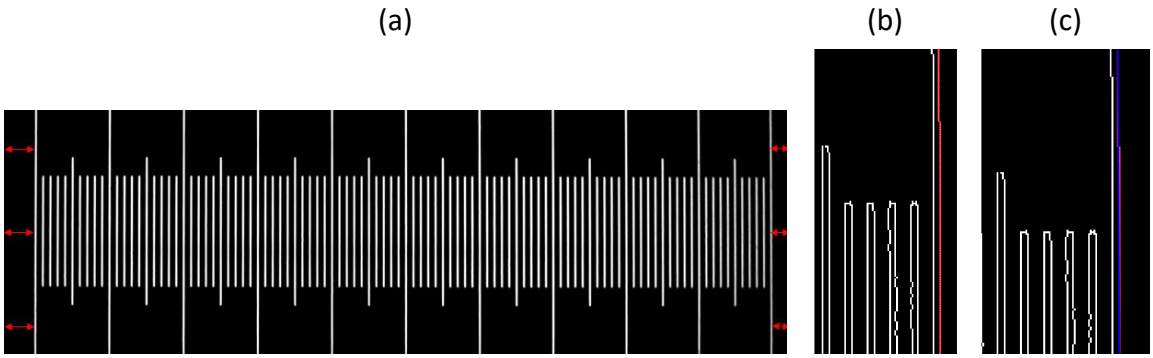

Figure 4.3: Image of the objective micrometer's scale. (a): the red arrows represents the distances measured to determine the mean angle of misalignment. (b): zoom into a part of one of the micrometer's ends, after edge detection. the red points are the detected external edges which are fitted linearly. (c): results of the fitting represented as a blue line.

binary image with white (255) pixels corresponding to the detected edges and a black (0) background. From this binary image, the coordinates of the rightmost and leftmost external line edges are determined by detecting the white pixels in the binary image (Fig. 4.3 (b)). A linear fit is then performed on the two sets of detected edges, from which the 2 angles of rotation are determined:

$$\Theta(^\circ) = arctan(A) \times \frac{360}{\pi} \tag{4.1}$$

where A is the slope of a fitting line. The original image is rotated by the average of the the two rotation angles, if the absolute value of this latter is larger than a threshold.

The other possible misalignments occur when the target's surface is not perfectly perpendicular to the camera's axis (Fig. 4.2 (c)). This creates distortions in the target's lines that result in pixel size variations from left to right and/or top to bottom. These distortions are not corrected, but included in the uncertainty budget as explained in the coming paragraphs. The flowcharts summarizing the procedure described above are given in Fig. 4.19 of Section 4.1.4.

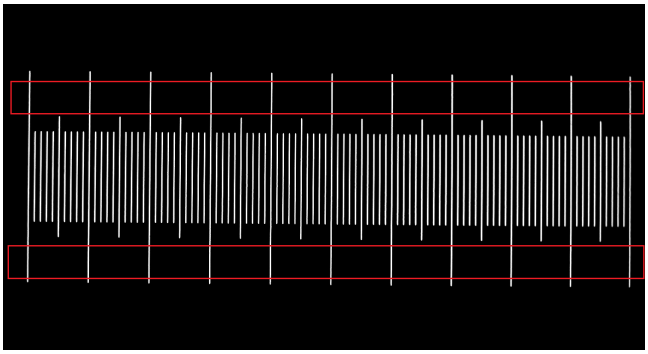

Figure 4.4: Image of the objective micrometer with the selected upper and lower parts to be cropped (red).

Figure 4.5: Distances measured between the lines of the micrometer to determine the pixel size

Measurement of Inter-line Distances In this part, the steps for the measurement of the mean pixel size, *i.e.* the resolution of the camera are shown. The idea is to measure the distances (in pixels) between the lines of the micrometer and compare them with the associated distances given in metric units, in the calibration certificate. The distances are measured as follows. First, the original image is cropped into two parts, one containing the upper long lines and the other including the lower ones (Fig. 4.4). The objective micrometer consists of 11 long lines (10 large divisions). The distances d_{meas} are measured between the center of each line and that of the origin line, similarly in the upper and lower parts of the calibration target (Fig. 4.5). A Gaussian blur filter with a window size of 3x3 is applied to reduce noise, after which the pixel intensities are averaged vertically. This is achieved by computing for every column of the image the mean pixel intensity and replace all the column's pixels with new mean value (Fig. 4.6).

Using Canny edge detection method, the lines' edges are detected. The threshold values are determined using Otsu's method. The edges' coordinates are determined by detecting the white pixels in the binary image. A zoom into a line before and after edge detection is shown in Fig. 4.7.

One edge is detected on each side of a given line. Since the image was vertically averaged before edge detection, Each edge is a perfectly vertical line that we can represent only by a horizontal coordinate x (Fig. 4.8). By taking x_{left} and x_{right} as the respective coordinates of a given line's edges, the center of each line:

$$x_{center} = \frac{x_{left} + x_{right}}{2} \tag{4.2}$$

The distance in pixels, d_{meas}, between the center of a line i, x^i_{center}, and that of the origin, x^0_{center}, is written as:

$$d_{meas}(pixels) = x^i_{center} - x^0_{center} \tag{4.3}$$

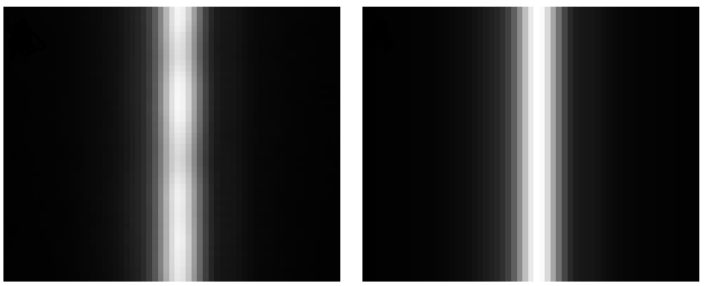

Figure 4.6: Micrometer line before (left) and after (right) vertical averaging of pixel intensities

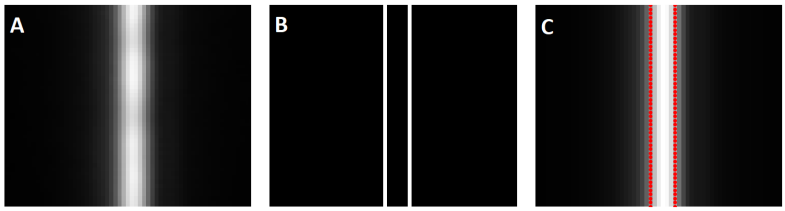

Figure 4.7: Edge detection of a micrometer's line. (A) initial image. (B) detected edges obtained from the vertically averaged image. (C) detected edges displayed (in red) on the initial image of the line.

The pixel size p is determined using each measured distance d_{meas} (pixels) and the associated calibration distance d_{calib} (μm):

$$p = \frac{d_{calib}}{d_{meas}} \tag{4.4}$$

For N measured pixel sizes at the top and bottom parts of the micrometer, the average pixel size is given by:

$$p_{mean} = \frac{\sum_{i=1}^{N} p_i}{N} \tag{4.5}$$

The next step after the measurement of the pixel size is the estimation of the associated uncertainty. The latter comes essentially from the detection of the line's edges from which the position of the centers and the distances between the different lines are deduced. When passing from the background to a given line, the pixel levels change gradually (Fig. 4.9). Canny edge detection method selects pixels representing local maximum gradients (Appendix A). The final position of the edges is affected by many parameters such as the contrast between the background and the micrometer's lines, the choice of the minimum and maximum thresholds, etc. In addition, the positions coordinates are given with a resolution of one pixel.

One way to assess the maximum uncertainty associated with the position of an edge would be to determine the widest range of positions where the edge is likely to be. To do so, we suggest to calculate the variance of the lines. Applying a variance filter to an image using a sliding window of size w amounts to replace each pixel with the variance of the intensities of the pixels included in the window, in which the replaced pixel is centered (Appendix A).

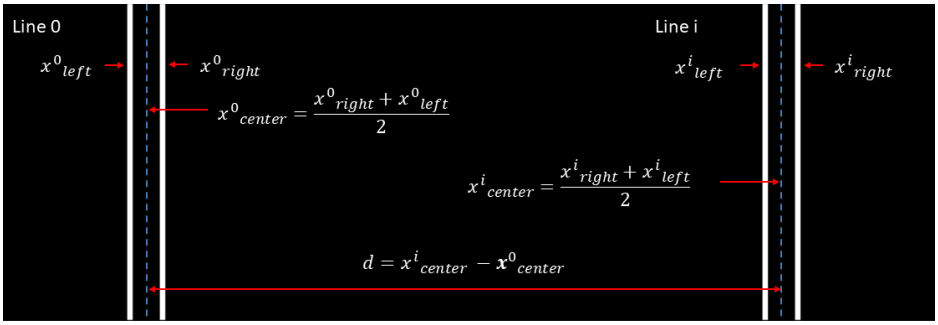

Figure 4.8: Schematic illustration showing the coordinates of two lines' edges and those of the lines' centers from which the interline distance is deduced

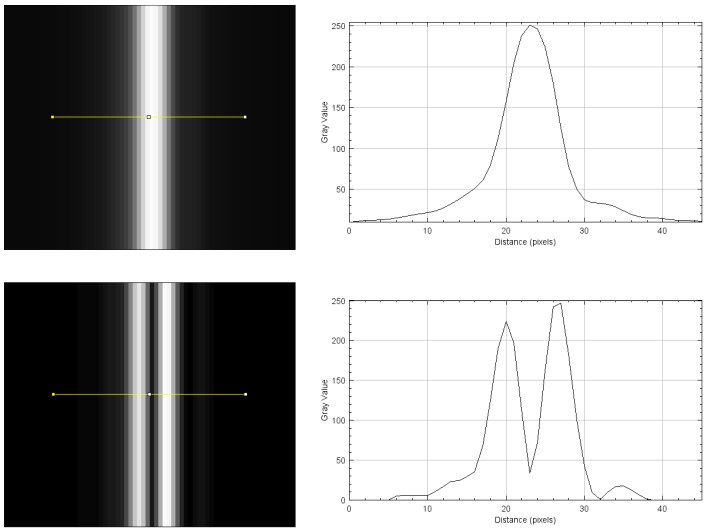

Figure 4.9: Pixel intensity profile across a line from the micrometer before (top) and after (bottom) application of a variance filter

A low variance reflects pixel levels that are close to the mean intensity and a high variance, pixel levels that are far from the mean. For example if all pixels at a given position of the sliding window have the same intensity, the variance is zero. Therefore, variance is a good way to detect the regions in an image where pixel intensities change. These regions can correspond to a passage from the background to the visualized object, in our case the edges of the micrometer's lines.

The maximum range for edge positions is determined as follows. First, a variance filter with a window size of 3x3 is applied on the vertically averaged image (Fig. 4.10). The variance filter exists in SciPy library as the function *numpy.var* or *numpy.std* for standard deviation (Appendix A). Next, the edges are detected in the variance image, resulting in two edges on each side of a line (Fig. 4.10). Since the image was vertically averaged before edge detection, each edge is a perfectly vertical line that can be represented only by its horizontal coordinate x.

In order to find the center x_{center} of each line, the 4 coordinates of the previously detected edges, *i.e.* the edges obtained after the application of the variance filter are taken into account additionally to x_{left} and x_{right} that were detected initially in the original image. Including the 4 possible extreme positions of the line's edges results in 6 different edges (Fig. 4.11), 9 possible centers per line and $9 \times 9 = 81$ distances' combinations between every 2 lines, thus 81 pixel size values. Fig. 4.12 shows a schematic illustration of two lines with all their

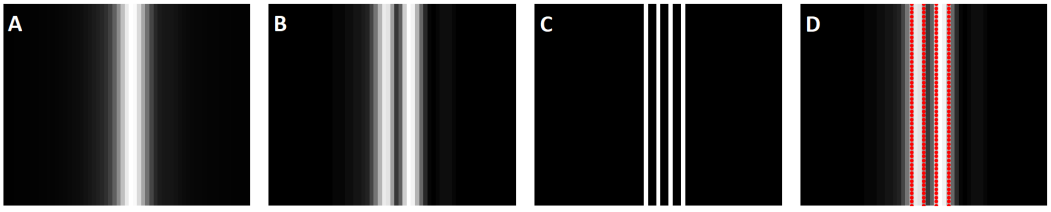

Figure 4.10: Results of filters' application on a micrometer line. (A) initial image. (B) variance filter. (C) detected edges using Canny method. (D) detected line edges displayed on the variance image.

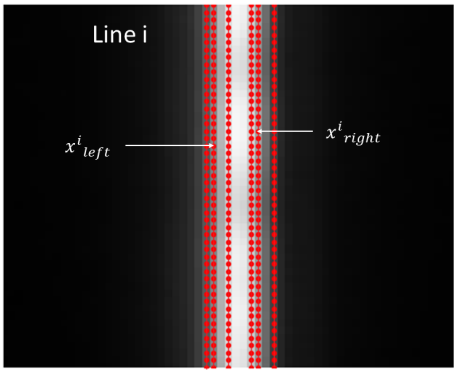

Figure 4.11: Micrometer line with all detected edges (red), *i.e.* initial and extreme edge positions

detected edges and the possible combinations of line centers that give distances in the range of $d_{\min}$ to $d_{\max}$.

The coordinate of a line's center are given by Equation (4.2) and the distance between two possible line centers by Equation (4.3). The pixel sizes are determined from each measured distance (pixels) and the associated calibration distance (μm) using Equation (4.4). The obtained pixel sizes include the most probable ones, *i.e.* the ones deduced from the initially detected edges in the original image, but also the least probable ones which have been deduced from the extreme positions where the edges are not likely to be. The differences in the pixel size values are used to quantify the maximum measurement uncertainty associated with edge detection. The method by which these differences are exploited depends on the distribution of the pixel sizes. As the micrometer contains in total 20 divisions, it is interesting to apply the previous steps on all the divisions, *i.e.* each couple of lines. This results in a large number of pixel sizes that follow principally a Gaussian distribution (Fig. 4.13).

The final pixel size is taken as the mean of all measured values following Equation (4.5). N in this case is equal to the total number of the micrometer's divisions multiplied by the number of distance combinations between every line and the origin one. A normality test is performed on the pixel size values. In case their distribution is normal, the uncertainty associated with edge detection and the possible differences along the micrometer, due to misalignments of the target relative to the camera's axis, is given by the standard deviation on the pixel sizes:

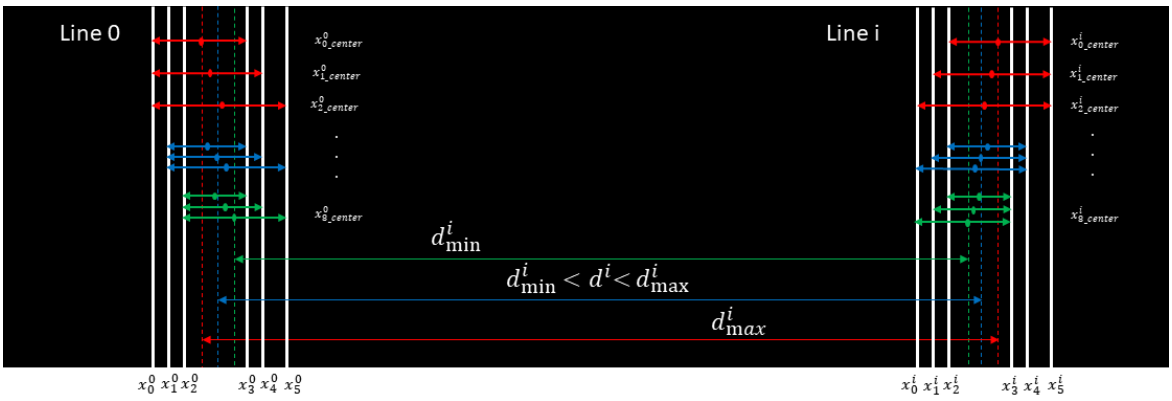

Figure 4.12: Schematic illustration showing the possible centers for one line and the associated interline distance combinations

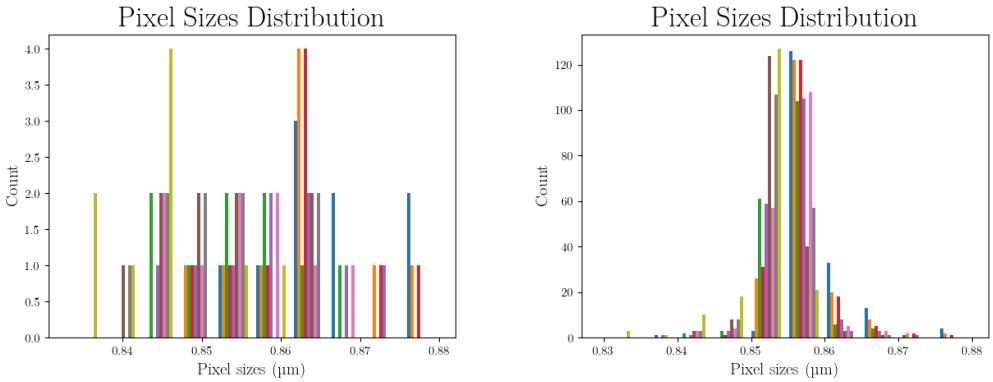

Figure 4.13: Histogram of the pixel sizes deduced from the distances between only two lines (left) and from all the interline distances along the micrometer (right)

$$u_{edges}(p) = \sigma = \sqrt{\frac{\sum_{i=1}^{N} (p_i - \bar{p})^2}{N}}, \tag{4.6}$$

where $\bar{p}$ is the mean pixel size defined as:

$$\bar{p} = \frac{\sum_{i=1}^{N} p_i}{N} \tag{4.7}$$

If the distribution is not normal, we consider a uniform (rectangular) distribution which maximizes the uncertainty. The latter writes as:

$$u_{edges}(p) = \frac{p_{max} - p_{min}}{2\sqrt{3}}, \tag{4.8}$$

where p_{max} and p_{min} are the maximum and minimum pixel size values, respectively.

In this part, we presented the method used to determine the pixel size using a micrometer objective. In addition, we defined its measurement uncertainty which results mostly from the detection of the micrometer's edges. However, the measurement of the pixel size can be affected by other factors, such as optical distortions. In the following part, we describe the method used to quantify this uncertainty source, using a transfer standard.

4.1.2 Quantification of Optical Distortions

Due to lens distortions, the pixel size may vary depending on the position where it is measured. The differences in pixel size values within the camera's field of view (FOV) are

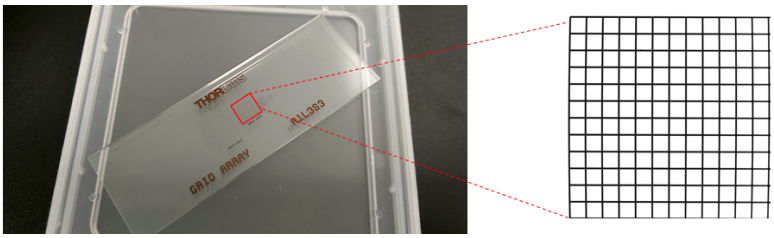

Figure 4.14: Image of the distortion target's grid as seen by a camera/microscope objective

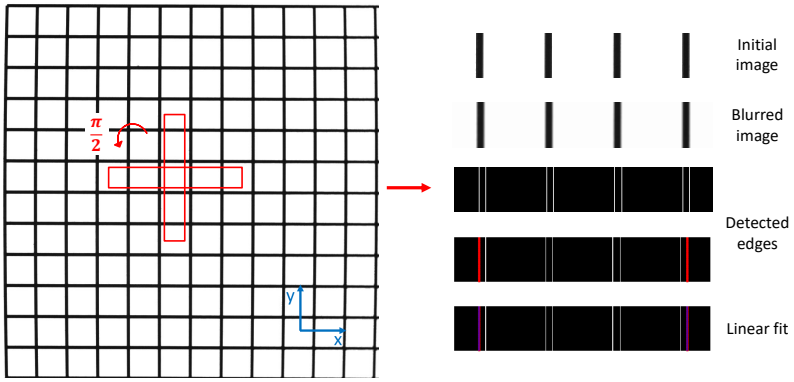

Figure 4.15: Parts of the target's grid that are used to measure the angle of rotation in the image

measured using a distortion calibration target. This latter is a rectangular glass slide on which is etched 4 square grids with different sizes (Fig. 4.14). For each camera zoom or microscope objective an image of the appropriate grid is taken and, the inter-line distances along all the raws and columns are measured in pixels by image processing. A calibration of the distortion target in a COFRAC (ISO 17025:2017) accredited laboratory allows to have the previously measured distances in metric units. The pixel size is determined by dividing the calibration distances (in metric units) by the associated measured ones (in number of pixels). The relative variations of the pixel size values within the cameras FOV are computed and included in the uncertainty budget as the uncertainty source associated with lens distortions.

Before starting image processing for the measurement of the inter-line distances, it is important to ensure the alignment of the grid. The angle of rotation is measured following the same steps as for the micrometer objective, from a part of the image that includes row or column lines located around the center where the distortions are the weakest (Fig. 4.15 (left)). In case column lines are used, the associated image should be initially rotated by an angle of $\pi/2$. In short, the edges of the lines are detected using Canny edge detection method and the coordinates of the leftmost and rightmost edges are fit linearly. From the slopes of the two linear fits, the mean angle of rotation is determined using Equation (4.1). The results of each image processing step are shown in Fig. 4.15 (right).

In order to measure the inter-line distance, the original image is initially cropped into

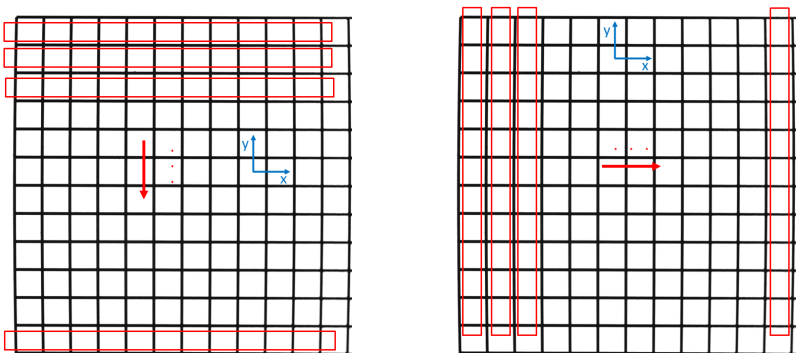

Figure 4.16: Parts of the distortion target's grid that are used to measure inter-line distances and the pixel sizes over the grid.

Figure 4.17: Measured inter-line distances along a column/row from the target's grid.

many parts. Each part contains either a row or column from the grid, selected in such a way that the lines occupy the whole image's height (Fig. 4.16). The distances are measured between the centers of every two lines, similarly for rows and columns (Fig. 4.17).

The image processing steps are practically the same as for the micrometer objective. Each image representing the lines of a given row or column is rotated by an angle θ_{mean}, blurred using a Gaussian blur filter and averaged vertically for uniform pixel intensities. The lines' edges are detected using Canny edge detection method for which the threshold values are determined previously using Otsu's method, applied on the gradient image. A standard deviation filter is applied on the vertically averaged image and the edges of the obtained line sides are detected using Canny method. The thresholds for Canny method are determined by applying Otsu's method on the gradient of the standard deviation image.

Similarly as for the objective micrometer, the possible centers of each line are computed from the different detected edges and used to determine all the inter-line distance combinations. The pixel sizes are computed by dividing every distance obtained by the calibration of the distortion target in real units, by the associated one measured by image processing in pixels, following Equation (4.4). The mean pixel size is given by Equation (4.5), where N is the total number of measured inter-line distances over the grid multiplied by the number of inter-line distance combinations. The differences in pixel size values come mainly from lens distortions, as the grid squares are located at different positions in the camera/microscope's field of view. The uncertainty associated with lens distortions is calculated from Equation (4.6) or Equation (4.8) depending on the distribution of the pixel sizes. This uncertainty includes the one associated with lines' edge detection since extreme edge positions were taken into account and from a possible non-perpendicularity between the target slide and the camera or microscope objective's axis.

The total uncertainty which corresponds to the measurement of the pixel size, including lens' distortions, is discussed in Section 4.2. Nevertheless, to illustrate the differences in the

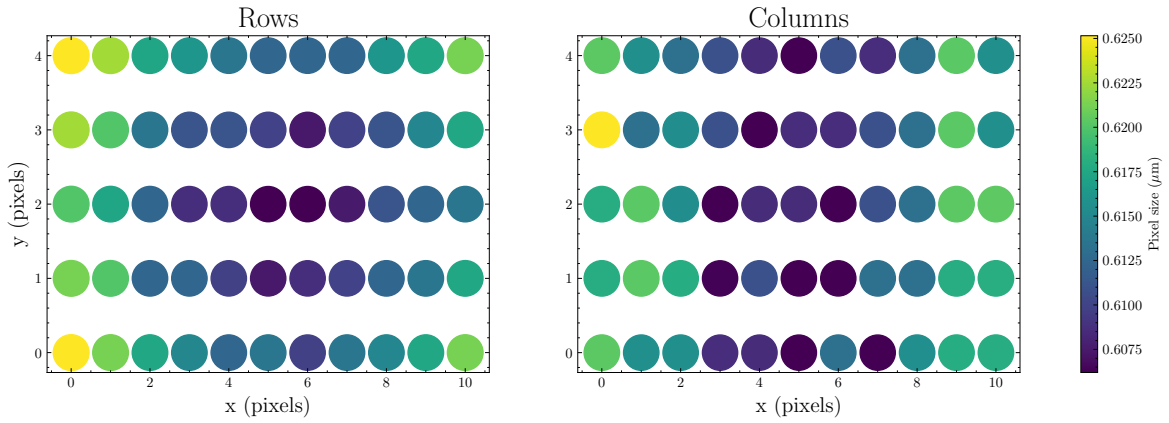

Figure 4.18: Colormap of the pixel sizes when these are measured along rows (left) and along columns (right).

pixel size depending on the position where it is measured, we show in Fig. 4.18 the calibration results of the confocal microscope LEICA DMi 8. The results clearly show the tendency of pixel size to increase away from the center. For this example the relative standard deviation of the pixel sizes, whether measured along rows or columns, is equal to 1.8 % for a mean pixel size of 0.612 μm.

4.1.3 Edge Detection Errors Management

During image acquisition, it is very important to make sure to have a good contrast between the illuminated lines and the background, and a homogeneous illumination of the lines. In case these two conditions are not respected, errors may occur during image processing. This section deals with the management of these errors that can affect the measurement of the pixel size.

Errors occur mainly during edge detection of the lines after the application of the variance filter. In some cases, instead of detecting four edges for each line, less or more edges are detected. As a consequence the measurement of the different lines' centers and inter-line distances are affected. This kind of errors is not corrected as they depend on the conditions in which the image was acquired. Instead, a condition was added in the algorithm to check the number of detected edges per line and filter all those for which more or less than 4 edges were detected. The distances, *i.e.* pixel sizes are measured only using lines that were correctly detected. Since the distances are measured with reference to the origin line, if this latter is not correctly detected, the measurements are done with reference to the first correctly detected line. The distances given by the calibration certificate and which are entered in the program as input parameters, should be modified accordingly.

The image processing methods described in this section are presented in the form of flowcharts, in the following part.

4.1.4 Flowcharts

In this section, we give the different flowcharts corresponding to the algorithms developed for camera calibration. The flowchart in Fig. 4.19 describes the image processing steps to

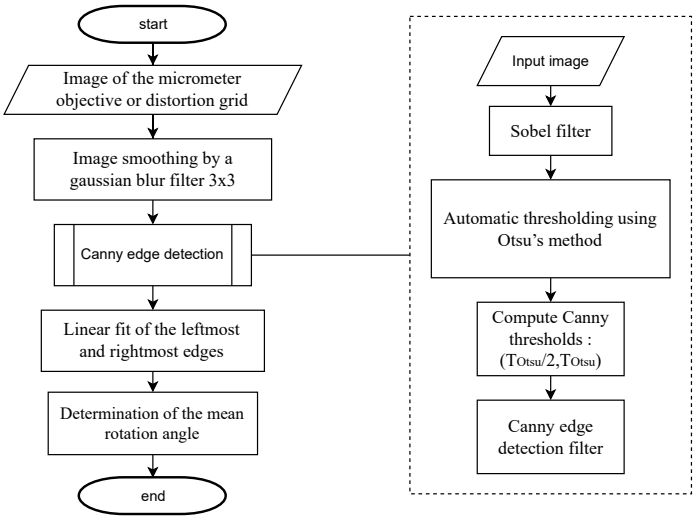

Figure 4.19: Flowchart of the algorithm used to determine the mean rotation angle of a micrometer scale or distortion grid in an image.

measure the misalignment angle of an objective micrometer or distortion target, the latter which is used to adjust the images before analysis. The flowchart in Fig. 4.20 shows the steps of the pixel size's measurement and the associated uncertainty, using one of the two calibration targets.

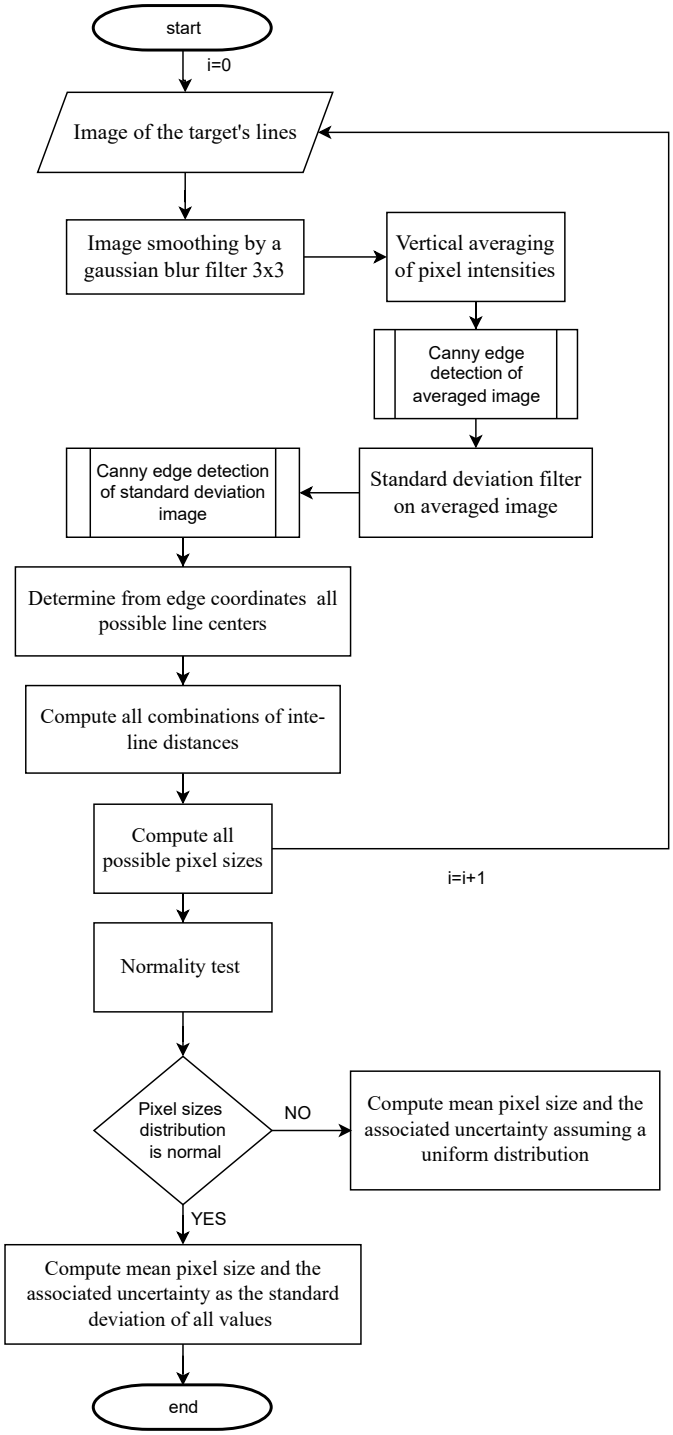

Figure 4.20: Algorithm used to measure the pixel size and the associated uncertainty.

4.1.5 Timestamps' Traceability

As was explained in the previous sections, the traceability of the measured displacements to dimensional units is ensured by the calibration of the camera against transfer standards that are calibrated in a COFRAC accredited laboratory, traceable to the national primary standard. In order to ensure the traceability of the flow velocity, that of the timestamps must also be ensured. These timestamps are determined from the acquisition frame rate which is equal to the frequency of the signal generator. Therefore, the traceability of time can only be ensured by that of the signal's frequency, *i.e.* by the calibration of the signal generator against a primary standard.

The calibration procedure is the following. First, the signal sent by a satellite is received by the GNSS antenna at CETIAT then, transmitted and timestamped by the GNSS receptor. This latter is clocked by a rubidium atomic clock at a frequency of 10 MHz. The timestamps of the signal received by CETIAT are saved. In parallel, The GNSS antenna of LNE-SYRTE at Paris Observatory receives the same signals which are timestamped by the LNE-SYRTE receptor. The latter which is clocked by the French national standard for time and frequency, in Paris Observatory (Fig. 4.21). Since both CETIAT and Paris observatory record the time for the same signal, the timestamps recorded by CETIAT are continuously compared to those of the reference, which ensures their metrological traceability.

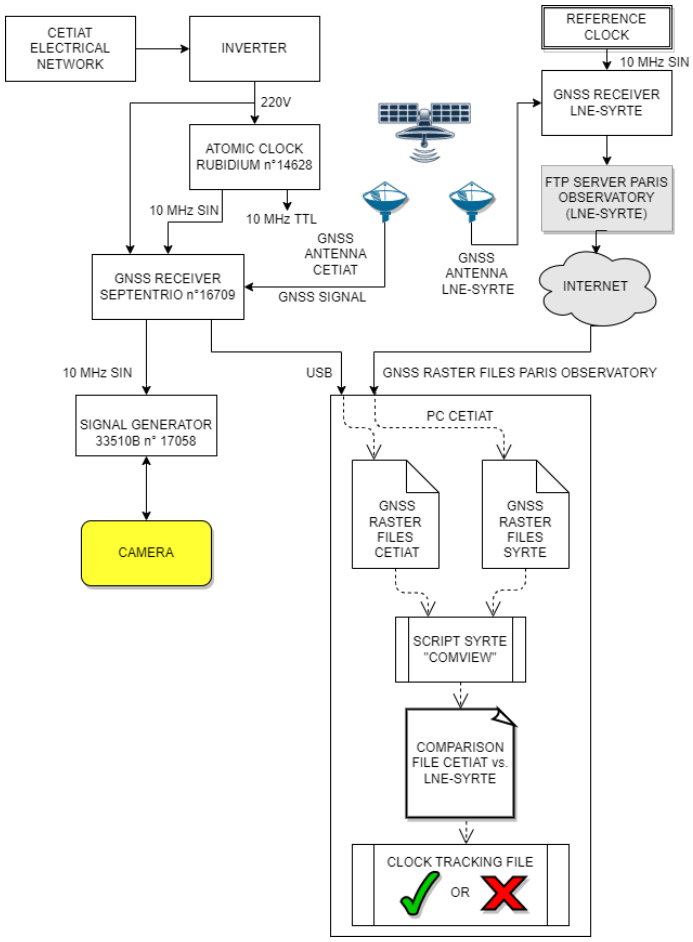

Figure 4.21: Flowchart explaining the calibration procedure of the signal generator

4.2 Uncertainty Components

In this section we present the uncertainty budget of our nano-flows' measurement system. The volumetric flow rate is expressed as a function of the front's displacements x, timestamps t and the inner diameter of the capillary tube d. The measurement of each of these quantities represents a source of uncertainty. Besides these components, we take into account the physical phenomena that can affect the measurement of the displacements. The two main phenomena are water evaporation, as the meniscus is in contact with air, and thermal expansion caused by temperature variations. As the mean flow rate during the measurement time is determined from a linear regression of the displacements over time, the standard deviation of the fluctuating values is also included in the total budget. The flow rate's relationship with the measured quantities is given by Equation (2.2), which we remind here:

$$Q_V = \frac{x}{t}.\pi\frac{d^2}{4} \tag{4.9}$$

As the different measured quantities are independent, the total uncertainty is determined from Equation (4.10) which is the general equation for a combined standard uncertainty [79]:

$$u_c^2(Q_V) = \sum_{i=1}^{N} \left(\frac{\partial f}{\partial x_i}\right)^2 u^2(x_i) \tag{4.10}$$

where f is the functional relationship giving the volumetric flow rate Q_v, from the different measured quantities x_i. The measurement uncertainty ($K = 1$) writes as:

$$u_c(Q_V) = \sqrt{\left(\frac{\partial Q_V}{\partial x}\right)^2 u^2(x) + \left(\frac{\partial Q_V}{\partial t}\right)^2 u^2(t) + \left(\frac{\partial Q_V}{\partial d}\right)^2 u^2(d) + u_{\text{thermal}}^2 + u_{\text{evap}}^2 + u_{\text{fit}}^2} \tag{4.11}$$

where u_{thermal} , u_{evap} and u_{fit} are the uncertainties associated with thermal expansion, evaporation and the linear fit, respectively. The partial derivatives of the flow rate Q_V with respect to the different quantities are sensitivity coefficients:

$$\frac{\partial Q_V}{\partial x} = \frac{1}{t}\pi\frac{d^2}{4} \tag{4.12}$$

$$\frac{\partial Q_V}{\partial t} = -\frac{x}{t^2}\pi\frac{d^2}{4} \tag{4.13}$$

$$\frac{\partial Q_V}{\partial d} = \frac{x}{t}\pi\frac{d}{2} \tag{4.14}$$

The uncertainty components are explained separately with details, in the following sections.

4.2.1 Interface Displacement

This section is devoted to the uncertainty associated with the measurement of the front's displacements. This uncertainty itself includes other components. Briefly, the measured distances are affected by the pixel size which ensures the conversion from pixels to metric units. As was discussed in Section 4.1, the pixel size's uncertainty u_{pixel} includes the measurement of the micrometer's inter-line distances, and the quantified distortions. To these two components, we add the calibration uncertainties of the transfer targets, which are provided in their respective calibration certificates. In addition to the pixel size, the measurement

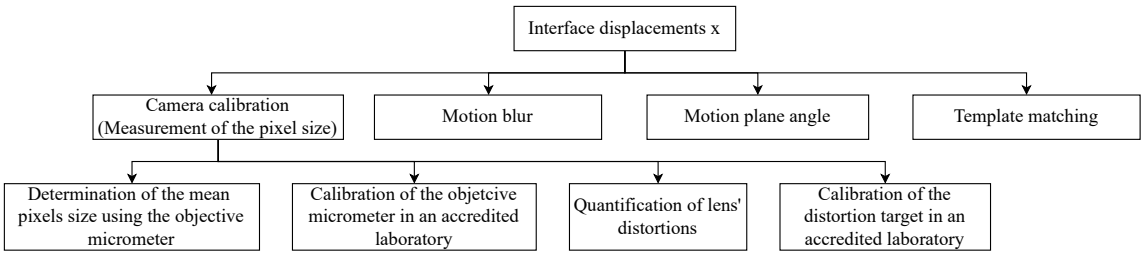

Figure 4.22: Uncertainty components associated with the measurement of the front's displacements.

of the displacements is affected by motion blur effect u_{blur}. The latter which is caused by the motion of the interface during exposure time, *i.e.* during the acquisition of an image. Errors can also be introduced if the motion axis is not perfectly perpendicular to that of the camera, in such a way that the measured displacements are projections of the real ones. This uncertainty is noted u_{angle}. The last component includes the limitations of the template matching function u_{matching} due to its pixel resolution. The total displacement uncertainty is given by:

$$u(x) = \sqrt{u_{\text{pixel}}^2 + u_{\text{blur}}^2 + u_{\text{angle}}^2 + u_{\text{matching}}^2} \tag{4.15}$$

The uncertainty sources presented above are illustrated in Fig.4.22 and explained in detail, in the following sections.

Camera Calibration

The pixel size is obtained from the calibration of the camera as explained in Section 4.1. The associated uncertainty u_{pixel} results from the determination of the pixel size using a micrometer objective u_{edges} and the quantification of the camera's distortions using a distortion target $u_{\text{distortion}}$:

$$u_{\text{pixel}} = \sqrt{u_{\text{edges}}^2 + u_{\text{OM}}^2 + u_{\text{distortion}}^2 + u_{\text{DT}}^2} \tag{4.16}$$

Where u_{OM} and u_{DT} are the uncertainties associated with the calibration of the micrometer and distortion target, respectively. These values were provided by the accredited laboratory:

$$u_{\text{OM}}(K = 1) = 7.510^{-8} m \tag{4.17}$$

$$u_{\text{DT}}(K = 1) = 7.510^{-7} m \tag{4.18}$$

The components u_{edges} and $u_{\text{distortion}}$ are determined from Equation (4.6) or Equation (4.8) depending on the distribution of the measured pixel sizes (Section 4.1).

Motion Blur

Image acquisition in not instantaneous but is carried out over a time interval known as exposure time, the latter which is necessary to form the image. When a flow is generated, the liquid/air interface keeps moving during this time interval resulting in a blurry meniscus. This phenomenon is called motion blur which, in general, is caused by the motion of the

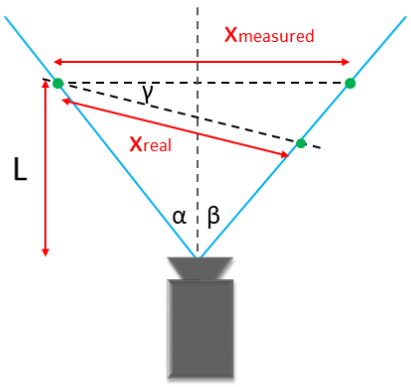

Figure 4.23: Schematic of the real and measured distances when the object moves in a plane making an angle γ with the perpendicular to the camera's axis (adapted from [130].

visualised object while the image is forming [130]. Considering a uniform distribution, the standard uncertainty associated with motion blur is determined from the distance traveled by the interface D during exposure time $t_{exposure}$, at the generated flow rate:

$$u_{\text{blur}} = \frac{D}{2\sqrt{3}} = \frac{v.t_{exposure}}{2\sqrt{3}}, \tag{4.19}$$

where v is the interface's mean flow velocity.

Motion Plane Angle

When the capillary tube is not perfectly perpendicular to the camera's axis, the interface moving inside the capillary travels apparent distances which are projections of the real distances (Fig.4.23). The real distance x_{real} traveled by the interface is given by [130]:

$$x_{real} = \frac{x_{\text{measured}}}{(cos\gamma + tan\beta sin\gamma)} \tag{4.20}$$

where x_{measured} is the apparent distance traveled by the interface , γ the angle between the capillary tube and the orthogonal plane and, α and β are the angles between the camera's axis and the starting and ending points of motion of the interface, respectively (Fig. 4.23). The uncertainty due to motion plane angle is given by:

$$u_{\text{angle}} = \frac{x_{measured} - x_{real}}{2\sqrt{3}} = \frac{x_{measured}}{2\sqrt{3}} \left(1 - \frac{1}{cos\gamma + tan\beta sin\gamma}\right) \tag{4.21}$$

The angle γ is taken as the minimum step of the rotary stage which is equal to 0.1°. The value of $tan\beta$ is determined from the case where the interface travels the whole camera's field of view (FOV). L being the working distance of the camera, $tan\beta$ can be written as:

$$\tan_{\beta} = \frac{\text{FOV}}{2.L}, \tag{4.22}$$

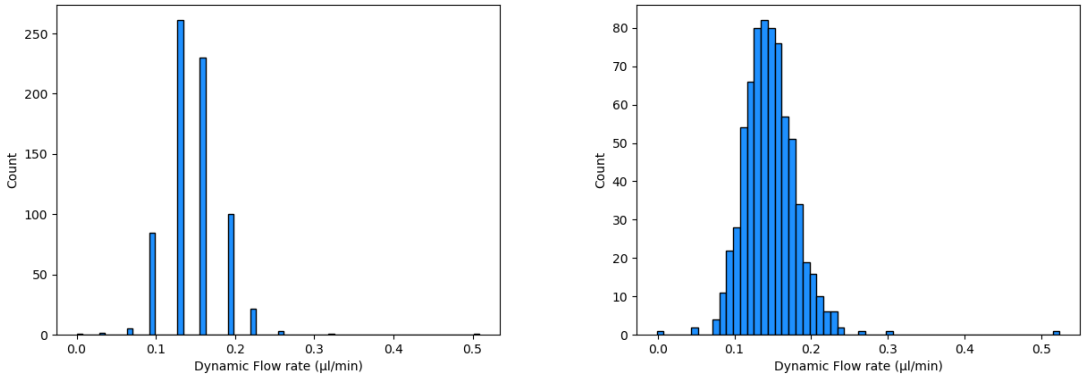

Figure 4.24: Histogram of the measured flow rates without (left) and with (right) the fit of SSD function.

which is replaced in Equation (4.21):

$$u_{\text{angle}} = \frac{x_{measured} - x_{real}}{2\sqrt{3}} = \frac{x_{measured}}{2\sqrt{3}} \left(1 - \frac{1}{cos\gamma + \frac{FOV}{2.L} sin\gamma}\right) \tag{4.23}$$

Template Matching Resolution

The displacement of the interface between 2 successive images is measured by image processing using template matching function. As was explained in Section 3.2.1, this function returns SSD values found at each position in the input image. The minimum SSD value corresponds to the location of the template which is given in terms of pixel coordinates. As a consequence, the measured distances are limited by the pixel size, *i.e.* the camera's resolution. For this reason, we apply a polynomial fit on the SSD values from which we determine the minimum's position and the front's displacement, with a sub-pixel resolution (Fig. 4.24). The uncertainty associated with the matching function is estimated considering a uniform distribution and the full pixel size p:

$$u_{\text{matching}} = \frac{p}{2\sqrt{3}} \tag{4.24}$$

4.2.2 Time

This section is dedicated to the uncertainty associated with timestamps. This uncertainty includes the calibration of the signal generator u_{freq} which ensures the timestamps' traceability, the effect of exposure time on the recorded timestamp u_{expt} and synchronisation between the signal's frequency and frame rate u_{synchro} (Fig. 4.25). The total timestamps' uncertainty is given by:

$$u(t) = \sqrt{u_{\text{freq}}^2 + u_{\text{expt}}^2 + u_{\text{synchro}}^2} \tag{4.25}$$

The uncertainty due to the calibration of the signal generator is given by:

$$u_{\text{freq}} = 6,5 \times 10^{-8} s \tag{4.26}$$

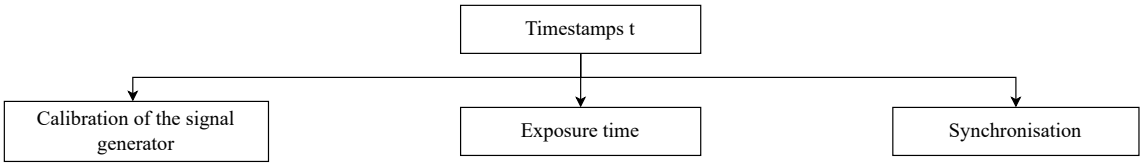

Figure 4.25: Uncertainty components associated with the measurement of the timestamps.

Exposure Time

When the camera receives the acquisition order from the signal generator, the shutter protecting the camera's sensor opens to collect light during exposure time, *i.e.* the time interval necessary for forming one image. As we cannot be sure about the exact instant at which the interface was at the measured position, we include this time interval $t_{exposure}$ as an uncertainty component that follows a uniform distribution:

$$u_{\text{expt}} = \frac{t_{exposure}}{2\sqrt{3}} \tag{4.27}$$

Synchronisation

Image acquisition using the camera is triggered by a signal generator that is clocked by a rubidium atomic clock. Since the camera's frame rate is equal to the frequency of the generated signal, the timestamp t_i of an images i can be written by:

$$t_i = i \times \frac{1}{\text{Framerate}} \tag{4.28}$$

It is however possible to have delays between the instant at which the camera receives the signal and the one at which the image is acquired. These possible delays are included in the uncertainty budget. In order to estimate this uncertainty component, we compare the camera's timestamps that are recorded in the software, with the timestamps deduced from the signal's frequency:

$$u_{\text{synchro}} = \sqrt{\frac{\sum_{i=1}^{N} \left(\Delta t_i - \bar{\Delta} t\right)^2}{N}}, \tag{4.29}$$

where $\Delta t_i = t_{\text{camera}} - t_{\text{signal}}$ is the difference between a timestamp saved by the software and the one deduced from the signal's frequency and $\bar{\Delta} t$ is the mean of all timestamp differences: $\bar{\Delta} t = \frac{\sum_{i=1}^{N} \Delta t_i}{N}$ for N images. This uncertainty has a zero value if the timestamps are perfectly synchronised with the signal's frequency or if they are all shifted by the same time interval.

4.2.3 Other Components

Thermal Expansion The temperature in the system is regulated at 20°C with an uncertainty of 1 °C. Fluctuations of the temperature lead to changes in the density of water, thus an expansion or contraction of the water's volume. The relative change in water's volume inside the capillary, is calculated for a temperature difference of $T_{\max} - T_{\min}$, *i.e.* the minimum and maximum measured temperatures in the system.

In order to determine $T_{\min}$ and $T_{\max}$, a temperature sensor is used to measure the temperature at different positions inside the enclosure. The relative change in the water's volume is written as:

$$\Delta V = \frac{V(T_{\max}) - V(T_{\min})}{V_{\text{mean}}}, \tag{4.30}$$

where V_{mean} is the mean water's volume from $T_{\min}$ to $T_{\max}$. By replacing V_{mean} in Equation (4.30) we find:

$$\Delta V = 2\frac{V(T_{max}) - V(T_{min})}{V(T_{max}) + V(T_{min})} = 2\frac{1 - \frac{V(T_{min})}{V(T_{max})}}{1 + \frac{V(T_{min})}{V(T_{max})}} \tag{4.31}$$

Since the density of a liquid is given by $\rho = \frac{m}{V}$, with V the volume occupied by a mass m of the liquid, The relative volume change can be written as:

$$\Delta V = 2\frac{1 - \frac{\rho(T_{max})}{\rho(T_{min})}}{1 + \frac{\rho(T_{max})}{\rho(T_{min})}} \tag{4.32}$$

The densities of ultra-pure water at the temperatures T_{min} and T_{max} are determined using Tanaka's formula [154]:

$$\rho_{Tanaka}(T_{min,max}) = a_5 \left[1 - \frac{(T_{min,max} + a_1)^2 (T_{min,max} + a_2)}{a_3 (T_{min,max} + a_4)}\right] \tag{4.33}$$

where $a_1 = -3.983035\ K$, $a_2 = 301.797\ K$, $a_3 = 522528.9\ K^2$, $a_4 = 69.34881\ K$ and $a_5 = 999.974950\ Kg.m^{-3}$. The standard uncertainty associated with thermal expansion, considering a uniform distribution, is given by:

$$u_{\text{thermal}} = \frac{\Delta V}{2\sqrt{3}} Q_V \tag{4.34}$$

Evaporation When no flow is generated, evaporation causes the interface to move backwards. By measuring the negative displacements of the interface using interface tracking method, evaporation rate can be determined and included in the total uncertainty budget. This rate is measured before and after a flow rate calibration, for about 10 min. The associated uncertainty is given by:

$$u_{\text{evap}} = v.\pi \frac{d^2}{4\sqrt{3}} \tag{4.35}$$

Linear Regression Residuals The mean flow velocity v during a measurement time t is obtained by performing a linear regression on the measured positions. The relative uncertainty associated with the linear fit is deduced from Equation (1.7):

$$u_{\text{fit}} = \sqrt{\frac{\sum_{i=1}^{n} (x_i - \hat{x}_i)^2}{n-2}} \frac{Q_V}{\bar{x}} \tag{4.36}$$

where x_i is the measured position, $\hat{x}_i$ is the predicted position by the linear regression, $d_f = n - 2$ is the degrees of freedom for n measured positions and $\bar{x}$ is the mean of the measured positions.

In the previous sections, we described the traceability of our measurement system to dimensional and temporal units. We have shown that traceability is ensured by calibrating

the camera using transfer standards, in order to convert the measured distances into metric units, and calibrating the trigger system against a traceable atomic clock. These calibrations against national primary standards provide traceability of flow velocity only. However, the volumetric flow rate also depends on the inner diameter of the capillary, the traceability of which must also be ensured. In the next section, we focus on this part of the system's traceability.

4.3 Measurement of the Inner Diameter of Glass Capillary Tubes

This section is dedicated to the traceability of the interface tracking system through the traceable measurement of the capillary's inner diameter. We start by presenting existing measurement methods based on various operating principles, such as gravimetry and optical techniques. Then, we describe a new measurement method based on fluorescence confocal microscopy, that we developed as part of this thesis.

4.3.1 Existing Methods

In this section we present various methods for the measurement of the inner diameter of glass capillaries. The first part is dedicated to the gravimetric method which is based on weighing a liquid volume that fills completely or partially the capillary tube, then relating its mass to other physical quantities. In the second part, we describe methods based on the measurement of the electric resistance of Mercury-filled capillaries. We conclude this section with optical methods such as classical microscopy, X-ray tomography, scanning electron microscopy, *etc.*

Gravimetric

Weighing a thread of mercury inside a capillary and measuring its length to determine the inner diameter of the capillary is a method that has existed for a long time. H. Schultze [135] suggested this method in 1901 in the context of his research on Argon's viscosity at different temperatures. The method he presented consisted on running a mercury thread of 2 cm length along the capillary, with steps of about 2 cm. At each position the temperature, length and mass of the thread were measured, from which the average radius R was deduced:

$$R = \sqrt{\frac{1}{\pi[l - \frac{1}{2}(h + h')]}\left[m(1 + 0.000181T)0.07355 - \pi\frac{h^3 - h'^3}{6}\right]} \tag{4.37}$$

where l is the length of the thread and m its mass at the temperature T. h and h' are the height of the threads menisci.

In 1906, W. J. Fisher [55] adapted this method for the measurement of smaller inner diameters, for which the mass of the mercury thread cannot be measured accurately. His method consisted on weighing longer mercury threads and relate them with a formula to the volume and length of a smaller thread. Schultze's technique was also employed by C. T. Collett *et al.* in 1950 [39], to measure the inner diameter of metallic tubes with the help of X-ray imaging.

As part of their study to determine the surface tension of water and benzene using capillary rise method, W. D. Harkins *et al.* (1918) [67] measured the inner radius of capillary tubes using mercury, as shown in Fig. 4.26. First, they introduced a short column of mercury inside a tube and measured its length (L_1) using a micrometer, then weighed the capillary which contains the mercury (m_1). Next, they filled the same capillary with a longer column of mercury and likewise, measured its length (L_2) and weighed the capillary (m_2). Subtracting

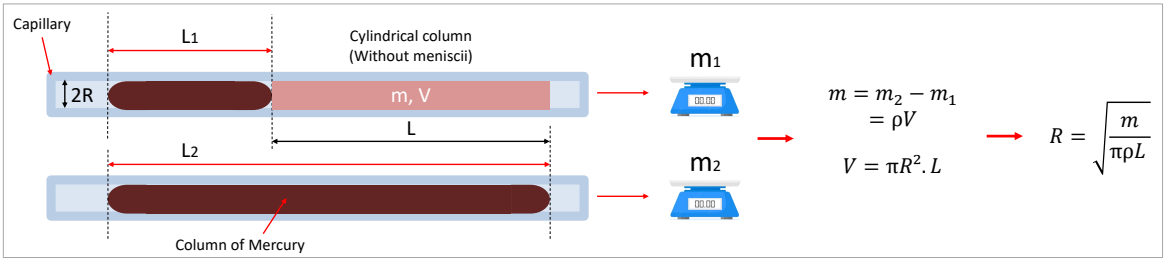

Figure 4.26: Schematic illustration showing the method used to determine a capillary's inner radius by the gravimetric method.

the mass (m_1) from (m_2) gives the mass m of a cylindrical column of length $L = L_2 - L_1$ and volume $V = \pi R^2 L = m/\rho$, where ρ is the density of mercury. The obtained volume does not include that of the menisci since they were eliminated by subtracting the short column's menisci from those of the long column. Finally, the inner radius of the capillary was deduced as follows:

$$R = \sqrt{\frac{m}{\pi \rho L}} \tag{4.38}$$

In their study to determine the absolute viscosity of water at 20 °C, J.F. Swindells *et al.* [150] measured the inner diameter of the viscometer's glass capillary tubes using two methods. The first one consisted on weighing the amount of mercury that completely fills the tube at a given temperature and the second one, on mercury resistance as explained in the next part. The inner diameters of the capillaries varied between 0.5 mm and 50 mm. In the Swindells method, the capillary tube was filled under vacuum with double distilled-mercury, then placed vertically in a temperature-controlled water bath with 4 mm of the capillary above the water's level. A glass optical flat (an extremely flat glass piece used to test the flatness of a surface) was placed horizontally at the end of the capillary which was illuminated and observed by a magnifying glass. The temperature of the bath was increased until the thermally expanding mercury reached the optical flat. The exact temperature θ at which the mercury filled completely the capillary, *i.e.* when the contact area between the mercury and the flat was equal to the cross sectional area of the capillary, was determined by observing the interference fringes between the flat and the surface of the capillary's end. The temperature of the bath was then decreased until the flat and mercury were no longer in contact. The capillary was taken out of the bath and the mercury weighed. The inner radius of the capillary was determined for 20 °C, the temperature at which they were to be used. The mass of mercury m_θ that fills the capillary at the temperature θ is given by:

$$m_\theta = \pi r_{20}^2 (1 + \alpha \Delta\theta)^2 l_{20} (1 + \alpha \Delta\theta) D_{20} (1 + \beta \Delta\theta) \tag{4.39}$$

where r_{20} is the inner radius of the capillary tube at 20 °C and l_{20} its length, α is the temperature coefficient of the linear expansion of glass,β is the temperature coefficient of density of mercury and $\Delta\theta = \theta - 20$.

$$m_{20} = \pi r_{20}^2 l_{20} D_{20} \tag{4.40}$$

The inner radius was deduced from the measured mass and temperature as follows:

$$r_{20} = \sqrt{\frac{m_\theta}{\pi l_{20} D_{20} [1 + (3\alpha - \beta)(\theta - 20)]}} \tag{4.41}$$

In order to measure the diffusion coefficient of small and large molecules inside thin capillary tubes, M. S. Bello *et al.* [19] employed Taylor-Aris dispersion theory. According to this theory, the apparent diffusion coefficient $D*$ (which is experimentally measured) is written as a function of the molecular diffusion coefficient D, the fluid's mean velocity inside the capillary U and the inner radius of the capillary tube R [7]:

$$D* = D + \frac{R^2U^2}{48D} \tag{4.42}$$

The inner diameters of the fused-silica capillaries used, which varied from 50 to 100 μm, were measured by weighing a drop of mercury occupying a given length in the capillary. The mass of the drop was converted to a volume using the density of mercury. From this cylindrical volume and the measured length the inner diameter was measured and used to determine the molecular diffusion coefficient.

The gravimetric method has also been used with other liquids than mercury. For example, J. Kohr *et al.* [83] used this method in the context of their study on the optical and surface properties of commercial quartz capillaries. These capillaries were used in electrophoresis, the detection sensitivity of which depends on the capillary's inner diameter. The capillaries (having nominal diameters of about 75 μm) were weighed empty then filled with water. The obtained mass difference was converted to a volume using water's density. By taking into account this volume and measuring the length of the capillary the inner diameter was determined with a maximum uncertainty of 1 %.

Electric Resistance

As mentioned above, J.F. Swindells *et al.* [150] also determined the mean inner radius of a viscometer's capillaries, by measuring the electric resistance of the capillaries when filled with mercury. The resistance of a cylindrical conductor, which in our case is mercury, is given by:

$$R = \frac{\rho l}{\pi r^2} \tag{4.43}$$

where ρ is the specific resistivity of mercury that is known accurately, L is the column's length and r is the inner radius of the capillary. Fig. 4.27 shows the experimental setup they have used. This setup consisted essentially of 4 capillary tubes brought up from glass bulbs. In order to measure the resistance of mercury, the entire apparatus was filled with double-distilled mercury. A distance of 1 cm was left at the tops of the four capillaries at which electric connectors were placed, and the resistance was determined using a Muller bridge. The final value of the capillary's radius at 20 °C was obtained from Equation (4.44) after including the thermal expansion of glass and a correction that accounts for the flow of electricity at the ends of the capillary:

$$r_{20}^2 = \frac{\rho_\theta}{R_\theta}\left[\frac{l_{20} + 1.64r_{20}}{\pi(1 + \alpha\Delta\theta)}\right] \tag{4.44}$$

This equation was then solved by replacing r_{20} in the second term by an approximate value.

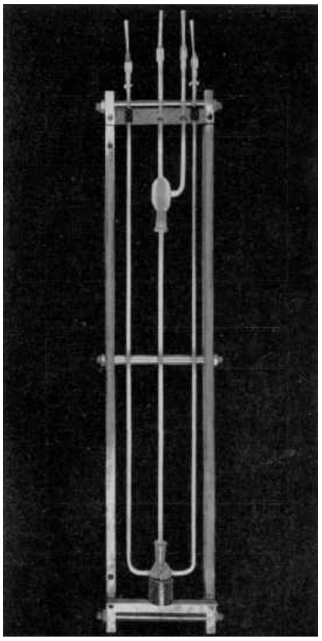

Figure 4.27: Photograph of the experimental setup used to measure the inner diameter of capillary tubes using electric Resistance method [150].

In their research to develop an on-column electrochemical detector for open-tubular capillary columns that are used in liquid chromatography, L. Knecht *et al.* [82] used Mercury's electric resistance to measure the inner diameter of the capillary columns. First, they filled entirely a column with mercury and measured its electric resistance. Then, they weighed the mercury which was pushed outside of the capillary. The resistance of mercury R is given by Equation (4.43) and its mass by:

$$m = d_{Hg}V = d_{Hg}l\pi r^2 \tag{4.45}$$

where d_{Hg} is the density of mercury. Using literature values for ρ and d_{Hg} and the measured resistance and mass of mercury, the length of the capillary as well as its inner radius are determined. By this method columns diameters down to 14.86 pm were measured.

The electric resistance method was also used by D. M. Dohmeier *et al.* [51] in their study of the efficiency of etched borosilicate capillary columns, used in liquid chromatography. The measured diameters varied between 6.5 and 14.6 pm. As a last example, we can mention C. T. Culbertson *et al.* [44] who developed a new method to increase the resolving power of separation in capillary electrophoresis. The resistance measurements were performed on fused-silica columns with nominal inner diameters from 5 to 10 μm.

Optical Methods

The most largely used optical method is end-on microscopy. This method consists on measuring the capillary's inner diameter at both ends from images acquired by an optical microscope or by scanning electron microscopy (SEM) (Fig. 4.28) [54, 84, 36, 5, 61]. By extracting the pixel profile along the capillary's cross section and assuming the diameter to be uniform along the capillary, the value of the inner diameter can be deduced. Evidently, the capillary tube needs to be perfectly parallel with the objective's axis.

Another optical method has been proposed by W. A. Wakeham *et al.* [167] which consists in filling the capillary tube with mercury and immersing it in a liquid having a refractive index similar to that of the capillary (Fig. 4.29). The immersion liquid avoids the refraction of light passing through the cylindrical capillary which deforms the internal diameter.

S. Kwon *et al.* [86] employed an X-ray projection imaging technique in which monocapillary X-ray glass optics with inner diameters of around 108 μm were scanned, using a high intensity synchrotron radiation beamline (Fig. 4.30). The inner diameters at different positions were determined with an accuracy of 1.32 μm. However, this method requires synchrotron radiation which is difficult to access regularly. Besides, it does not allow analysing the inner surface of the capillaries. In order to overcome these limitations and in the context of studying the monocapillary performance under the effect of inner radius variations, S.

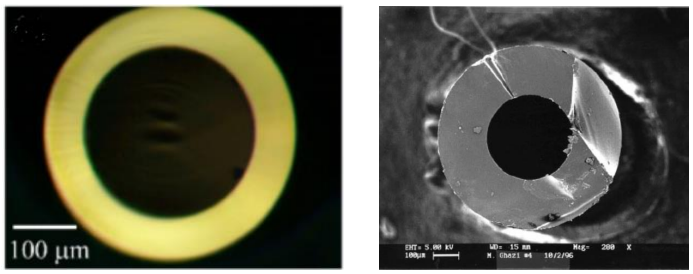

Figure 4.28: Images of capillary tubes' cross-section obtained using optical microscopy (left) [36] and SEM (right) [61]. The inner diameters of the capillaries are about 200 and 300 μm, respectively.

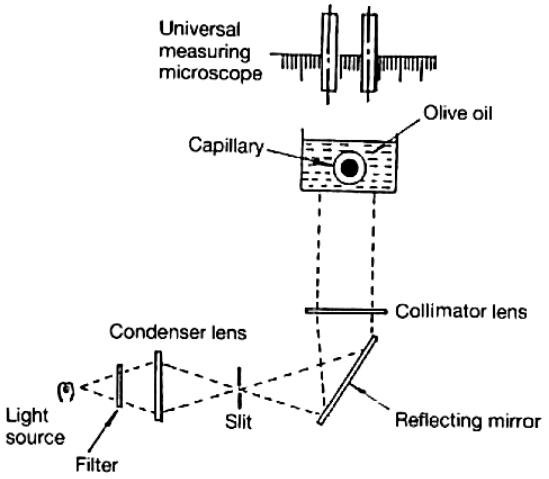

Figure 4.29: Experimental setup for the measurement of the inner diameter of a capillary tube using optical microscopy and an immersion liquid [167].

Zhang *et al.* [175] applied a contrast-enhanced micro-CT (micro-Computer Tomography) to reconstruct in 3D the inner surface of the monocapillaries and analyse their roundness. However, this method is limited by the spatial resolution of the projection images. This method was improved by Z. Wang *et al.* [168] by accelerating the scanning process and 3D image Reconstruction. X. Zhang *et al.* [177, 176] proposed in 2019 another X-ray technique based on confocal X-ray fluorescence. This method consists in filling the monocapillary optics with a zinc chlorine solution and, from the scanning it into the confocal micro-volume.

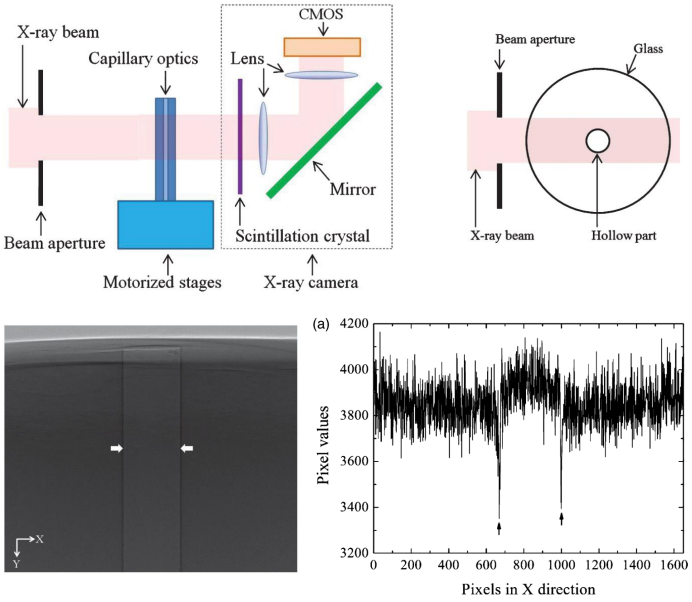

Figure 4.30: Measuremnt of the inner dimater using X-ray imaging. (a): schematic of the experimental setup. (b): X-rays beam trajectory across the monocapillary. (c): X-ray image near the end of the monocapillary. (d): Pixel intensity profile extracted from the X-ray image [86].

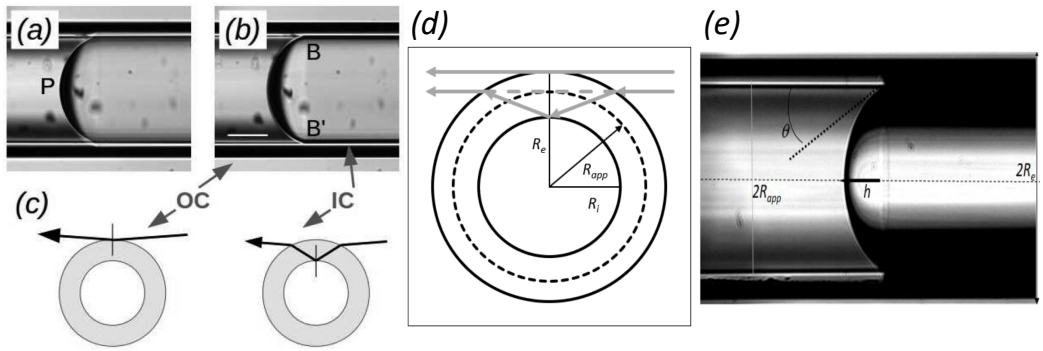

Figure 4.31: Formation of the white cusp in the capillary. (a) and (b) are transmission images of a pure water/CO2 meniscus with a focus on (P) and (BB'), respectively. (c) Light rays that produce inner and outer cusps. (d) Schematic illustration showing the light refraction across the capillary which results in an apparent diameter R_{app}. (e) Transmission image of a meniscus formed at the interface of water with cyclopentane and the white cusp on the water's side. The capillaries have an inner and outer diameter equal to 200µm and 330µm, respectively [70, 179].

Then, from the X-ray fluorescent spectra of Zn the boundary between the solution and capillary's wall is detected. Using this, nominal inner diameters of about 300 μm were measured non-destructively with a relative uncertainty of 4.1 %.

N. Hobeika *et al.* [70, 179] proposed an optical method which takes advantage of the refraction of light through capillaries in order to study the contact angle of immiscible fluids and detect thin films on the inner wall of the capillary. In their paper, they proposed a mathematical equation relating the inner diameter of the capillary with an apparent diameter that appears, in images of the capillaries and under certain focus conditions, as two white lines (cusps) (Fig. 4.31). The adjustment of the focus in order to make the white lines appear is however difficult and the associated uncertainty wasn't evaluated in their paper.

$$\frac{R_i}{R_e} = \frac{R_{app}/R_e}{n_g\sqrt{1-(R_{app}/R_e)^2}\sqrt{1-(R_{app}/R_e)^2/n_g^2}+(R_{app}/R_e)^2} \tag{4.46}$$

In connection with their research on two-phase laminar flows inside round capillary tubes, K. Mishima *et al.* [99] determined the inner diameters analytically from the friction factor for a laminar Hagen-Poiseuille flow:

$$\lambda = \frac{64}{R_e} \tag{4.47}$$

where $R_e = \frac{\rho v D}{\mu}$ is Reynolds number, written as a function of the fluid's density ρ and dynamic viscosity μ, and the capillary's inner diameter. The latter was determined by first assuming a guess value. After that, the diameter for which the friction factor and Reynolds number are correlated was computed iteratively. With this methods measurements of capillary's with nominal diameters of 1 and 4 mm was performed with a relative uncertainty of 2 %.

In addition to the methods presented above, other techniques exist such as confocal reflectance microscopy [42], coherance scanning interferometry [162] and the method using Jurin's law, from the capillary rise of a liquid within the capillary tube [178].

Discussion

In this section, we described multiple techniques for the measurement of the inner diameter of glass capillary tubes. For flow rate calibrations using our interface tracking system, the inner diameters of the capillaries used were determined using end-on microscopy or, in some cases, the gravimetric method. For practical reasons, the optical measurements were carried out using our high resolution camera instead of an optical microscope. The capillary tubes were placed either in the same axis as that of the camera or with an angle θ from the axis. In fact, the camera operates only with transmitted light. As the light source cannot be placed directly in front of the capillary's entrance, the latter appears dark in images (this problem does not exist if a reflective light microscope is used). In order to ensure a maximum illumination of the capillary's entrance wall the light source and the camera were placed on both sides and at the same angle from the capillary's axis (Fig. 4.32 (a)). The capillary had to be placed in the same horizontal plane as the camera. In this case, the entrance appeared as an ellipse with a large axis that corresponds to the inner diameter of the capillary (Fig. 4.32 (b)). The inner diameter was measured by image processing by detecting the hollow's edges using Canny edge detection method. In order to estimate the uncertainty associated with edge detection, a variance filter was applied on the original image and the limits of the variance were detected. Fig. 4.32 shows the processing results for a thick-walled capillary with a nominal inner diameter of 500 μm. The obtained diameter was equal to 502.0 μm with a relative uncertainty of 1 %.

For the gravimetric measurements, the capillaries were weighed empty, then filled with ultra pure water. For each capillary, the measurements were repeated at least 3 times and the associated uncertainty was determined from the resolution of the balance and the standard deviation of the different measurement values.

The methods mentioned above are simple to implement but they only provide an average value of the inside diameter. The latter which is assumed to have a constant value along the capillary and at its ends. The uniformity of the internal diameter inside the capillary can however be questioned, since the manufacturers give the nominal diameters with relative uncertainties up to 10 %. As the flow depends on the square of the inner diameter and since our system was designed to measure flow rate fluctuations, it is essential to measure the diameter locally, at the positions where flow velocity is measured.

The measurement technique we chose to explore is fluorescence confocal microscopy. Besides the fact of being simple to implement, this method allows to visualise the hollow

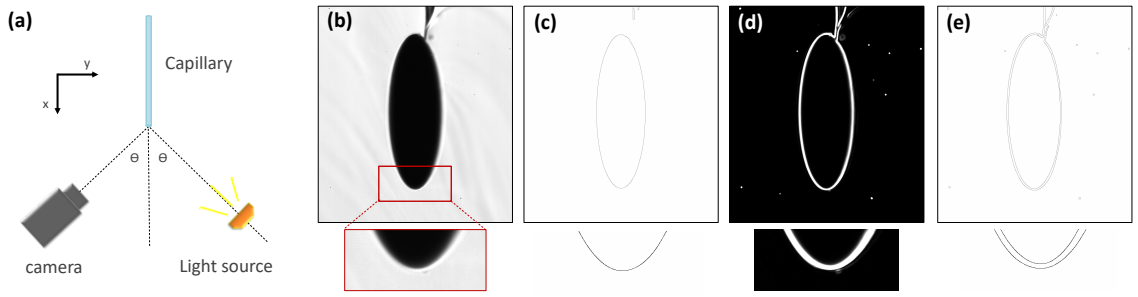

Figure 4.32: Measurement of the inner diameter at the capillary's entrance using a high resolution camera. (a) Experimental setup consisting mainly of a camera, light source and the capillary tube. (b) Initial acquired image of the capillary's end. (c) Initial image after edge detection. (d) Initial image after the application of a variance filter. (e) Variance image after edge detection.

volume of the capillary in a non-destructive way. The approach followed to measure the inner dimater from confocal images is explained in the following section.

4.3.2 Measurement of the Inner Diameter by Confocal Microscopy

Introduction

Confocal microscopy is a fluorescence imaging technique that utilizes a laser point source to scan a sample and a pinhole to eliminate out-of-focus light, for a 3d visualization of the sample. Instead of illuminating the fluorescent sample entirely, laser light beams are focused by an objective lens into a focal spot within it. The Fluorescent light emitted by the excited spot and the laser reflected light are then recollected by the objective lens and passed through a dichroic mirror (light splitter), which separates the laser light away from the detector. A pinhole is used to eliminate out-of-focus light, *i.e.* the light reflected by other focal planes. This allows only the light coming from the desired focal plane to enter the detector (Fig. 4.33). By scanning the specimen in a raster pattern, images of one single optical plane are created. 3D objects can be visualized by scanning several optical planes and stacking them using a suitable microscopy deconvolution software [113].

Experimental Setup

The measurements were carried out using a LEICA DMi 8 inverted fluorescence microscope with a 25x objective that works with water as an immersion liquid (Fig. 4.34). The inner diameters (ID) were measured for thin-walled capillary tubes from VitroCom Inc. The capillaries were made of clear fused quartz (GE type 214, manufacturer's inner diameters d=200 μm,500 μm) with a refractive index of n=1.459 at γ=587.6 nm. Nile Red powder (Sigma-Aldrich 2485-100MG) was diluted in Dimethyl sulfoxide (DMSO from VWR, n=1.477 at γ= 587.6 nm) with a concentration of 0.01 g/L. The capillaries were initially cleaned using isopropanol then filled, by capillarity, with the previously prepared solution. A volume of glycerol (Sigma-Aldrich, n=1.467 at γ=763.8 nm) was deposited in the centre of a coverslip (24x40 mm, thickness 170 μm, Menzel-Gläser 1.5H). The capillary tube was then placed horizontally at the middle of the coverslip. It was necessary that the glycerol covered the

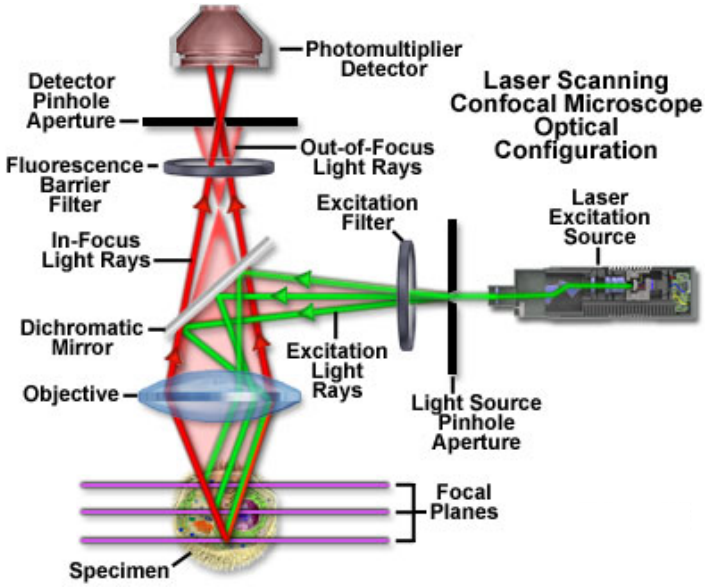

Figure 4.33: Experiment setup and Working principle of confocal microscopy [74].

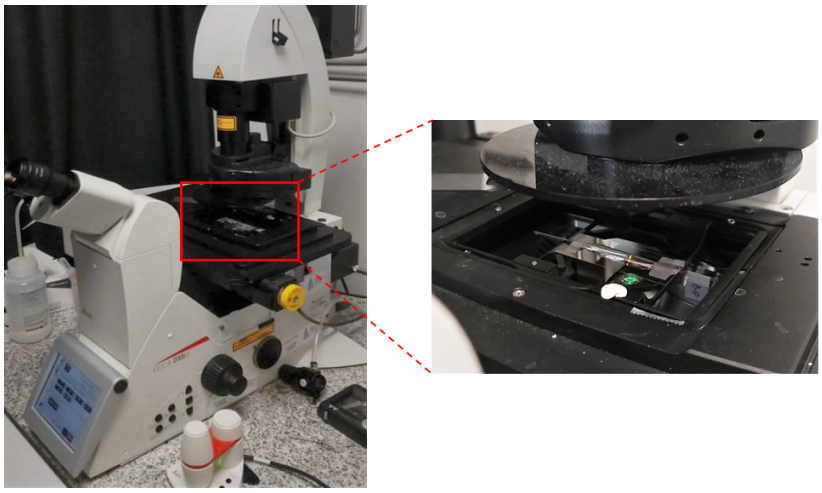

Figure 4.34: Photograph of the measurement setup. (left) general view of the Leica DMi8 microscope. (Right) Zoom into the setup including the filled capillary on a coverslip, covered by glycerol.

capillary's height completely and had a flat surface near the tube. This was achieved either by placing a glass slide on top of the capillary or by putting enough glycerol which, by the effect of gravity, flattened far from the edges. Double-sided tape was used to fix the tube on the coverslip (Fig. 4.35). Covering the capillary with glycerol and filling it with DMSO (that was necessary to dissolve the Nile Red dye), ensured to reduce the distortions caused by the light's refraction at the different air/glass and liquid/glass interfaces, since these liquids had similar refractive indices as the capillary's glass. A drop of water was deposited on the lens of the objective and the coverslip placed on the support, perpendicularly to the objective's axis, in contact with the drop.

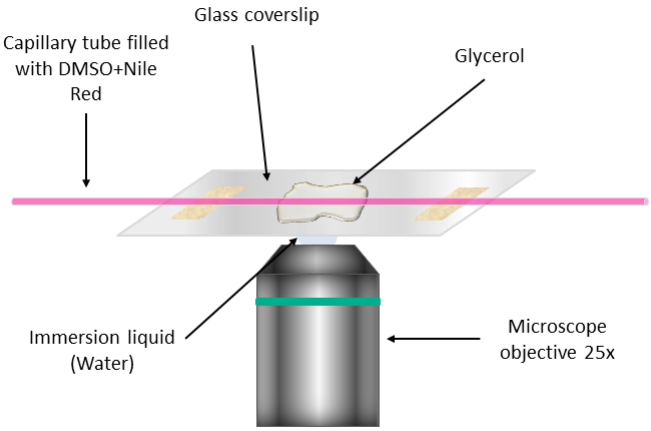

Figure 4.35: Schematic illustration of the capillary's arrangement on the coverslip.

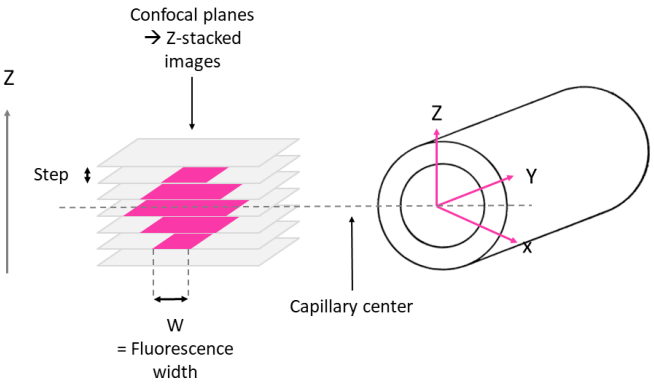

Figure 4.36: Schematic illustration showing the change in the fluorescent signal in a z-stack.

Working Principle

As the capillary is filled with a fluorescent component, exposing it to a light with a wavelength that is equal to the excitation wavelength of Nile Red will cause the liquid to emit light at its emission wavelength. This emitted light can be captured over all the confocal planes traversing horizontally the inside of the capillary. As the light is emitted only from the solution, it is possible to visualize the inside of the capillary in order to determine its inner diameter locally. The excitation and emission wavelengths were 480 nm and 575 nm, respectively.

Z-stacked confocal images across the capillary's height were acquired with a given z-step. The fluorescent signal on each image represents the horizontal cross section of a cylinder at a given height, as shown in Fig. 4.36. Starting from the bottom of the capillary, the width of the signal increases to reach its maximum at the center, then decreases until it disappears at the top. The widths of the fluorescent signal were measured by image processing and, assuming the cross section of the capillary to be circular, we determined its inner diameter from the radius of the fitting circle. Only a part of the capillary fits inside the microscope's field of view thus, In order to measure the inner diameter at different positions the capillary must be moved on the y axis.

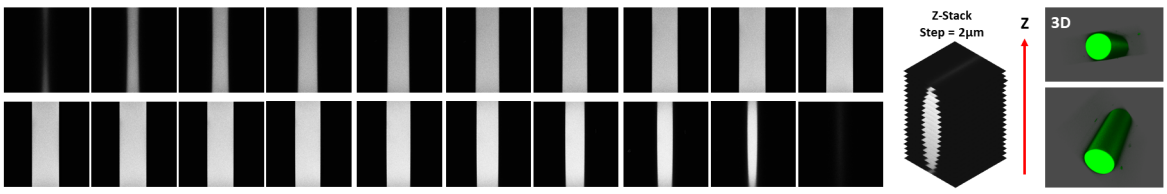

Figure 4.37: grayscale (8 bit) confocal images for a capillary with a nominal inner diameter of 200 μm, acquired from top to bottom with a z-step of 2 μm. On the right is a 3D view of the z-stack.

Fig. 4.37 shows the obtained grayscale (8 bit) images for a capillary with a nominal inner diameter of 200 μm, acquired from top to bottom with a step of 2 μm. In order to measure the inner diameter, the confocal images were processed using a homemade Python program. Images near the bottom and top of the capillary were not taken, as the fluorescent signal was very weak and nonuniform. The rest of images were all processed identically inside a loop, as follows. First, a region of interest (ROI) was selected using coordinates that were manually determined from the image with the largest width to ensure that the signal was always included in the cropped image. Then, a Gaussian blur filter with a kernel of size 5x5, was applied on the ROI in order to reduce noise. After that, the pixel levels were averaged vertically so as to have uniform columns. This was achieved by replacing all the pixels of a column by their mean intensity. Next, the edges of the fluorescent signal were detected using Canny edge detection method [30]. Given that the pixel intensities were uniform vertically, the two edges were represented only by their horizontal coordinates, x_1 and x_2. The width of the signal was then determined as:

$$w = |x_1 - x_2| \tag{4.48}$$

The estimation of the uncertainty associated with edge detection was carried out using the same method as in Section 4.1. Mainly, we evaluated the maximum range where each edge can be located, by applying a variance filter. The limits of the variance intervals were determined by edge detection. The combinations of the coordinates of the variance ranges and the initially detected edges were used to compute the possible signal widths (Fig.4.39). The final width was taken as the mean of all values w_i :

$$w = \frac{\sum_{i=1}^{N} w_i}{N} \tag{4.49}$$

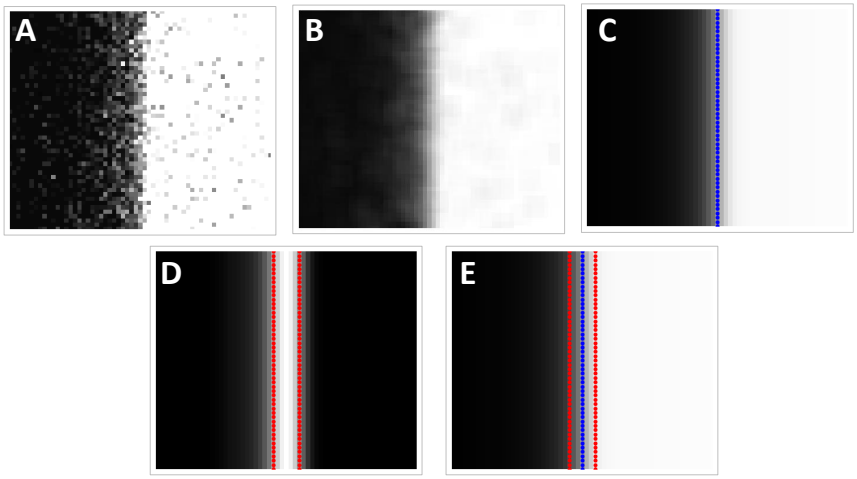

Figure 4.38: Image processing results on a part of one edge of the fluorescent signal. (A) Original image. (B) Smoothed image with a Gaussian blur filter. (C) Vertical averaging of the pixel intensities and detected edge (blue). (D) Application of a variance filter and the associated detected edges (red). (E) Averaged image with all previously detected edges (red and blue)

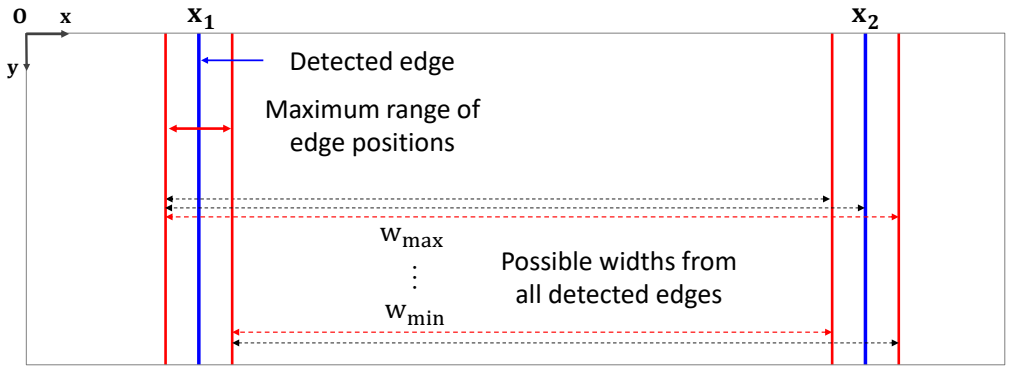

Figure 4.39: Schematic illustration of the measured widths of the fluorescent signal. $w_{\min}$ and $w_{\max}$ are the minimum and maximum widths the signal can have, respectively.

The inner diameter was determined by performing a circular regression on the half widths of the fluorescent signals and the associated z positions:

$$(x - x_c)^2 + (z - z_c)^2 = \frac{d^2}{4}, \tag{4.50}$$

where (x_c, z_c) are the coordinates of the circle's center. The latter was fixed at the origin of the x axis and the widths centred at x=0, in such a way that two x coordinates ($w/2$ and $-w/2$), were associated to the same z position (Fig. 4.40).

In this section, we described the experimental setup and working principle of the method developed. The image processing algorithm presented is described by a flowchart in Fig. 4.42. In the next section, we present the uncertainty budget which is used to estimate the total measurement uncertainty that is associated with the inner diameter.

Traceability and Uncertainty Budget

This section is devoted to the uncertainty budget of the confocal method developed and its traceability to the S.I. of Units. The sources of uncertainty include the measurement of the

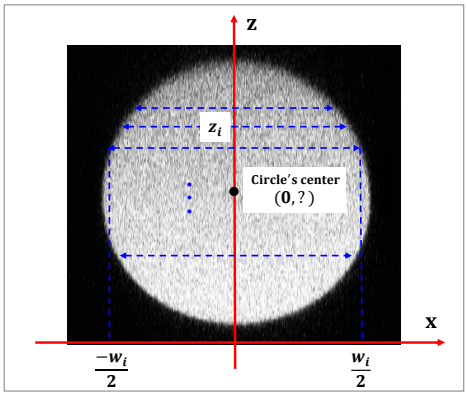

Figure 4.40: Schematic illustration showing the data points used to perform the circular fit used to determined the mean local inner dimater of the capillary. The fitted points are displayed on a confocal image of the capillary's cross section.

signal's widths by edge detection, the microscope's steps along the z axis and the residuals of the circular fit.

The expression of the total measurement uncertainty is obtained by combining the different uncertainty components:

$$u(d) = \sqrt{\left(\frac{\partial d}{\partial x}\right)^2 u^2(x) + \left(\frac{\partial d}{\partial z}\right)^2 u^2(z) + u_{\text{fit}}^2}, \tag{4.51}$$

where $u(x)$ is the uncertainty associated with the measurement of the signal's width along the x axis, $u(z)$ is the z-steps uncertainty which is taken as the resolution of the microscope's stage on the z axis and (u_{fit}) is the residuals of the circular fit performed on the measured widths with respect to the z-steps. The partial derivatives of d with respect to x and z are the sensitivity coefficients:

$$\frac{\partial d}{\partial x} = \frac{x - x_c}{\sqrt{(x - x_c)^2 + (z - z_c)^2}} = \frac{2(x - x_c)}{d} \tag{4.52}$$

$$\frac{\partial d}{\partial z} = \frac{x - x_c}{\sqrt{(x - x_c)^2 + (z - z_c)^2}} = \frac{2(z - z_c)}{d} \tag{4.53}$$

We choose to maximize the total uncertainty by taking the maximum differences $(x - x_c)$ and $(z - z_c)$ which are equal to $d/2$. In this case, the sensitivity coefficients are equal to 1 and the total uncertainty is written as:

$$u(d) = \sqrt{u^2(x) + u^2(z) + u_{\text{fit}}^2} \tag{4.54}$$

The uncertainty associated with the measurement of the fluorescent widths by image processing is expressed by Equation (4.55). This uncertainty results from the calibration of the microscope in order to determine the pixel size u_{pixel}, edge detection of the signal's widths u_{edges} and the limitations in the measurement of the widths due to the resolution of the microscope $u_{\text{resolution}}$:

$$u(x) = \sqrt{u_{\text{edges}}^2 + u_{\text{resolution}}^2 + u_{\text{pixel}}^2} \tag{4.55}$$

The microscope's calibration allows to convert the measured signal widths to metric units, from the pixel size. This calibration was carried out following the same method as in Section 4.1, *i.e.* using calibrated transfer standards that ensure the traceability of the measured widths to dimensional units. The corresponding uncertainty is given by Equation (4.16) that we remind here:

$$u_{\text{pixel}} = \sqrt{u_{\text{OM}}^2 + u_{\text{p-edges}}^2 + u_{\text{DT}}^2 + u_{\text{distortion}}^2}, \tag{4.56}$$

where u_{OM} and u_{DT} are the uncertainties associated with the calibration of the objective micrometer and distortion target, respectively, $u_{\text{p-edges}}$ is associated with the image processing algorithm used to determine the pixel size and $u_{\text{distortion}}$ is the standard deviation of the pixel sizes over the microscope's field of view.

The uncertainty associated with edge detection of the signal widths is deduced from the extreme signal widths, w_{min} and w_{max}, considering a uniform distribution. The extreme widths were measured in the image of the capillary's centre, *i.e.* for the largest fluorescent strip:

$$u_{\text{edges}} = \frac{w_{max} - w_{min}}{2\sqrt{3}} \tag{4.57}$$

The $u_{\text{resolution}}$ was determined from the pixel size p, considering a uniform distribution:

$$u_{\text{resolution}} = \frac{p}{2\sqrt{3}} \tag{4.58}$$

The mean inner diameter was determined assuming a circular cross section for the capillary. The uncertainty due to this assumption was evaluated from the fit residuals:

$$u_{\text{fit}} = 2\sqrt{\frac{\sum_{i=1}^{N}\left(R_i - R_{mean}\right)^2}{d_f}} = 2\sqrt{\frac{\sum_{i=1}^{N}\left(R_i - R_{mean}\right)^2}{N-2}}, \tag{4.59}$$

where R_i are the measured radii, R_{mean} the predicted radius of the fitting circle and $d_f = N - 2$ is the degrees of freedom for N measured radii.

In this section, we described in detail the different uncertainty component associated with the measurement of the inner diameter using confocal microscopy. In the following section, we present the measurement results and their associated uncertainties.

Results and Discussion

The measurement were carried out for 10 capillaries with nominal inner diameters of 200 μm and 500 μm and at z-steps of 2 μ and 5 μ, respectively. The results obtained and the associated uncertainties are presented in Table 4.1. The values of the different uncertainty components are also provided in the same table. As the fluorescent signal decreases quickly far from the capillary's centre, only the widths measured in images near the centre were processed.

The relative errors, which are obtained by comparing the measured diameters with the nominal ones, do not exceed 2 %. The estimated relative expanded uncertainties (k=2) do not exceed 4 % which is two times lower than the uncertainties provided by the manufacturers. The greatest uncertainty component results from the image analysis algorithm used to determine the widths of the fluorescent signals.

These measurements are also compatible with the ones carried out using the same experimental setup, but in a light transmission mode. (Fig. 4.41) shows the image processing steps to determined the inner diameter from transmission images. Using this method with the ninth capillary in the table, for example, gave an inner diameter of 195.8 μm with a relative expanded uncertainty of about 2 %. The measurement error by comparison with the value measured using confocal microscopy, *i.e.* 197.0 μm, is less than 0.7 %.

Table 4.1: Results of the inner diameter measurements using confocal microscopy.

Nominal ID (μm)	Tolerance degree given by manufacturer (%)	Capillary N◦	ID measured by confocal Microscopy (μm)	u_x (k=1) (μm)	u_z (k=1) (μm)	u_{fit} (k=1) (μm)	Total Uncertainty (k=1) (μm)	Relative Expanded Uncertainty (k=2) (%)	Relative Error (%)
500	10	1	493,7	3,1	0,01	0,9	3,2	1,3	1,3
		2	493,3	3,1	0,01	1,4	3,4	1,4	1,4
		3	496,8	3,6	0,01	1,1	3,7	1,5	0,6
		4	490,9	4,0	0,01	1,1	4,2	1,7	1,9
		5	492,6	4,0	0,01	1,2	4,2	1,7	1,5
		6	495,3	4,5	0,01	1,2	4,7	1,9	0,9
200		1	197,7	3,5	0,01	0,5	3,6	3,6	1,2
		2	197,8	3,5	0,01	1,2	3,7	3,8	1,1
		3	197,0	3,5	0,01	0,6	3,6	3,6	1,5
		4	199,0	3,5	0,01	0,9	3,7	3,7	0,5

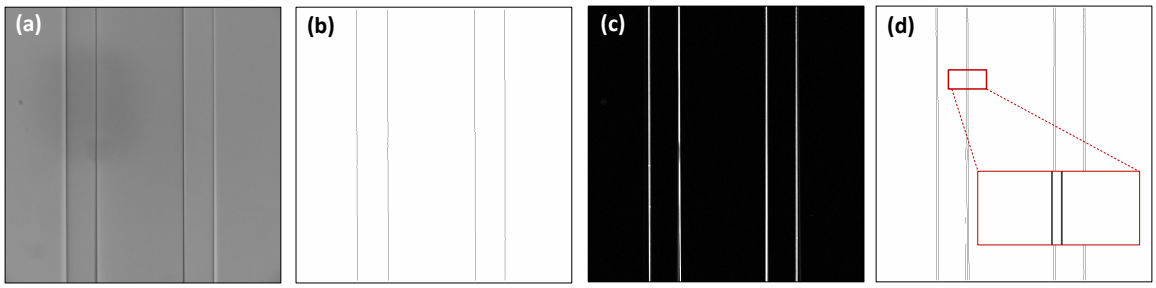

Figure 4.41: Measurement of the inner diameter using optical microscopy in transmission mode. (a): image at the center of the capillary. (b): initial image after edge detection. (c): initial image after the application of a variance filter. (d): variance image after edge detection.

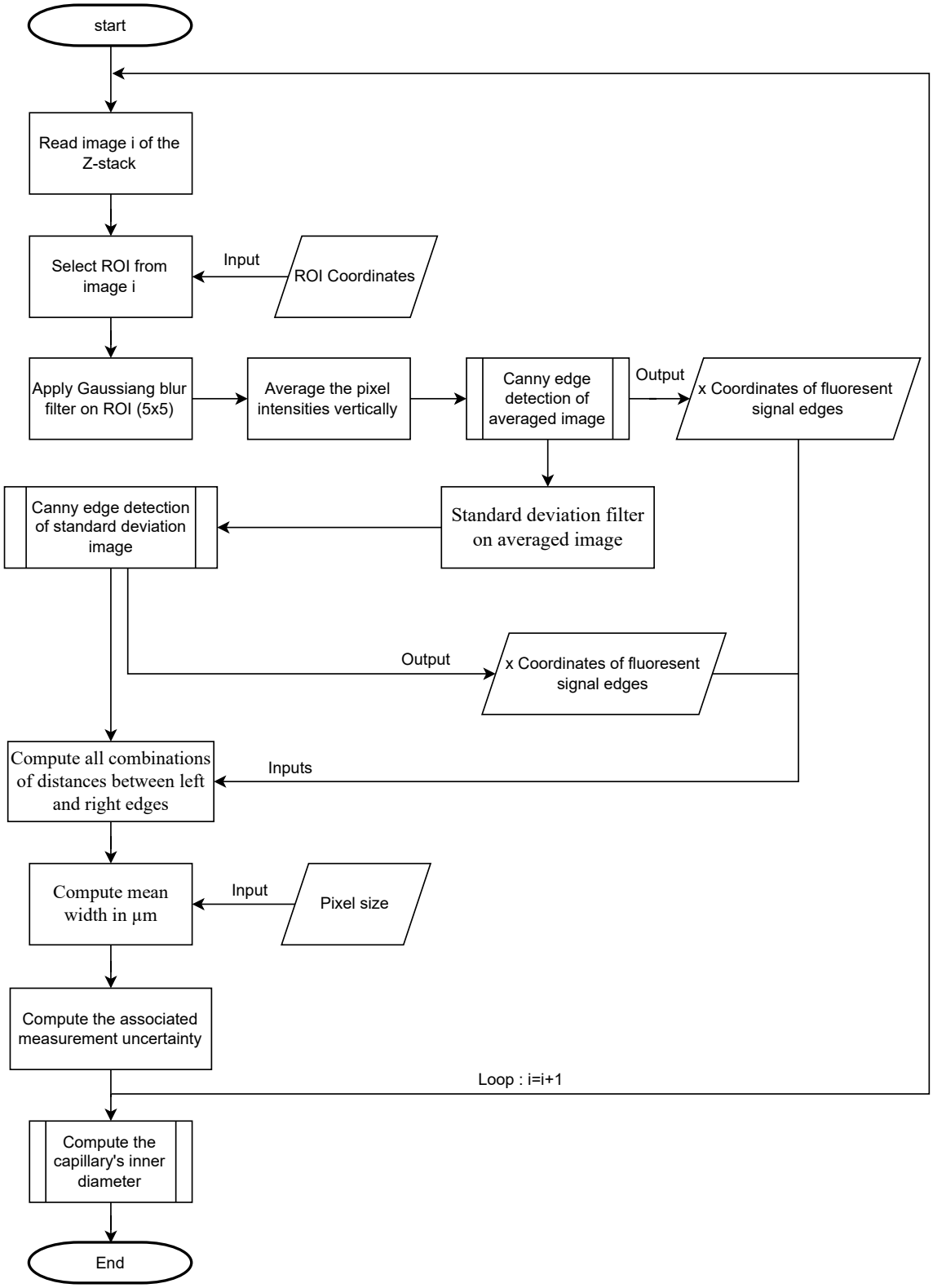

Figure 4.42: Image processing algorithm for the measurement of the capillary's inner diameter, using confocal microscopy.

Chapter 5

Preliminary Results

In the previous chapter, we presented the uncertainty budget and the methods used to ensure the traceability to the S.I. of Units of the interface tracking system. We showed that this metrological property is ensured when all the quantities on which the flow rate depends, are traceable themselves. On the one hand, the interface displacements were linked to the dimensional primary standard through the calibration of the camera, using calibrated transfer standards. On the other hand, The traceability of the timestamps was ensured by the calibration of the signal generator against an atomic clock, itself calibrated with comparison to the national French standard for frequencies. At the end of the chapter, we discussed a new method based on confocal microscopy, used to measure the inner diameter of capillary tubes, non-destructively and in a traceable way.

In this chapter, we move on to the first flow measurement results, which served as a first evaluation of the system's performances. In the first section, we discuss the stick-slip phenomenon and how it affected flow rates' stability, after which we propose a simple method to reduce its effect. A brief explanation of the physical origin of this phenomenon is also provided. In the second and last section, we present the results obtained for the calibration of a Coriolis flow meter from 20 to 5000 nL/min, using our measurement system.

5.1 Stick-Slip Effect

The first nano-flow measurements were carried out using uncoated capillary tubes. The coating was made for two main reasons. The first is to avoid having small droplets that are left behind when the interface is moved back. Receding the meniscus is necessary to keep it sufficiently far from the tube's end where evaporation is more important. These

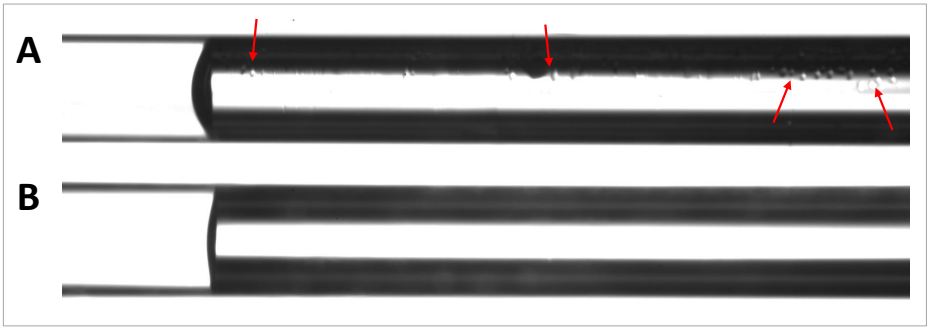

Figure 5.1: Static Water/air interface inside a capillary with an inner diameter of 500 μm (a) without and (b) with the glass repellency coating.

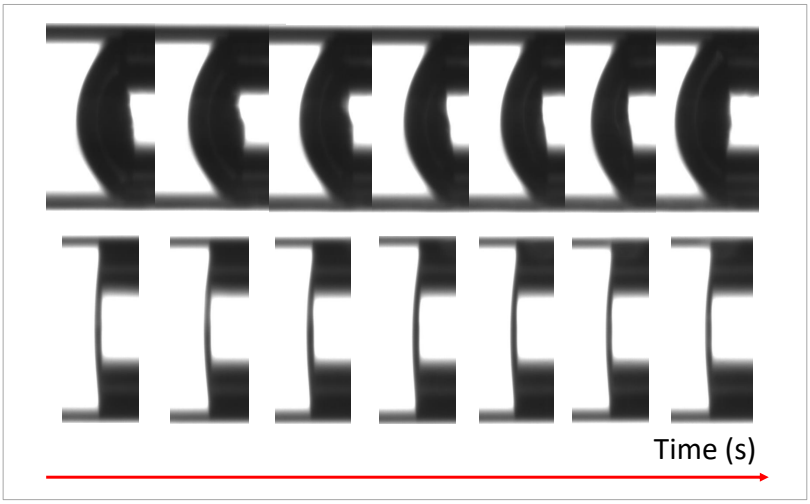

Figure 5.2: Images of a moving meniscus over time, inside an uncoated (top) and coated (bottom) capillary tubes, with an inner diameter of 500 μm.

small droplets (Fig. 5.1(a)), if not completely evaporated during the measurement, merge each time with the interface, creating larger displacements. In addition, they appear in the images causing changes in the background of the interface. As discussed in Section 3.2, the background needs to be the same no matter the position of the interface in the capillary, otherwise the template matching is affected by the differences in pixel intensities between successive images.

Fig. 5.2 shows images of an interface moving inside an uncoated (top) and coated (bottom) capillary. As can be seen, the contact angle is larger and the meniscus more stable over time in the case of the coated capillary. As was discussed in Section 3.2, a constant shape of the meniscus between the successive images leads to better matching results.

The second reason for which the inner surfaces were treated, is the pinning of the meniscus which was observed in images as well as in flow rate values. Visually from image sequences, the motion of the meniscus appears to be discrete as it sticks at given positions while its curvature decreases until it reaches a maximum, beyond which the meniscus slips. The pinning and depinning, *i.e.* stick and slip of the meniscus results in a step-like curve of the measured positions (Fig. 5.3(left)). In case a treated capillary is used, the motion of the meniscus is more continuous which results in a smooth curve (Fig. 5.3 (right)). The stick-slip effect appears in the flow rate curves as peeks that can be 50 times higher than the generated flow rate (Fig. 5.4 (left)). Such peeks were not observed in the case of treated capillaries (Fig. 5.4 (right)). As a matter of fact, this phenomenon produces flow rate fluctuations that originate from our measurement system and which should not be confused with the ones generated by the device to be calibrated. If the fluctuations that come from different sources are not decorrelated, the calibration results can be misinterpreted, leading to an erroneous characterization of the device under test.

The stick-slip effect is caused by the roughness and chemical heterogeneities of a surface. This was pointed by J. W. Gibbs who concluded that surface defects can cause the pinning of a contact line, leading to contact angle hysteresis [62]. The effect of roughness on the contact angle was first studied by Wenzel [170] who derived geometrically an equation giving the equilibrium contact angle of a droplet deposited on a solid and conforming to its roughness, as a function of the roughness factor of the solid. Cassie and Baxter [34, 33] on the other hand, studied the situation where the droplet does not conform to the surface but rather stays on top of the surface defect with air trapped below. This situation can happen when

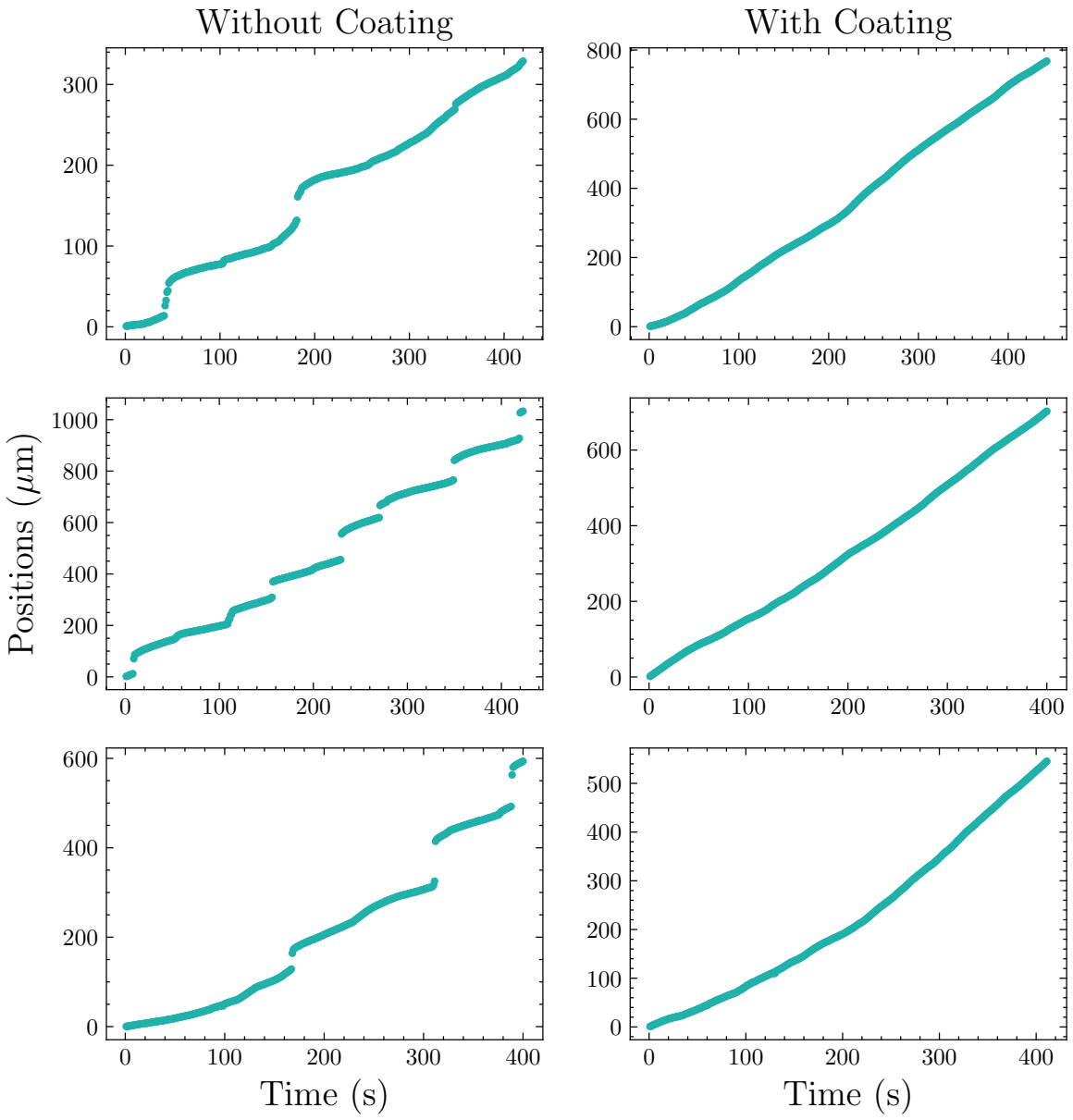

Figure 5.3: Interface positions over time for non-coated (left) and a coated (right) capillary tube.

the liquid is deposited on a hydrophobic surface [122].

As the inner surface of the capillaries cannot be perfectly smooth and chemically homogeneous, the meniscus experiences a contact angle hysteresis, thus a stick-slip motion. In order to reduce this effect, the capillaries were coated with a glass repellency treatment from Aculon, which make them acquire hydrophobic and oleophobic properties. The coating procedure is explained in Section 3.3.1. The coating's working principle is based on Aculon's proprietary "self-assembled monolayer of phosphonates" (SAMP) method. This procedure is used to provide a large range of materials with different surface properties such as: hydrophobicity, oleophobicity, adhesion, etc. Fig. 5.5 shows the structure of the coating monolayer which is made of phosphonate molecules. A phosphonate consists of a phosphonic acid "the reactive head group" which is connected through a stable phosphorous bond to a carbon based tail, known as the "functional tail group". The head group bonds with the

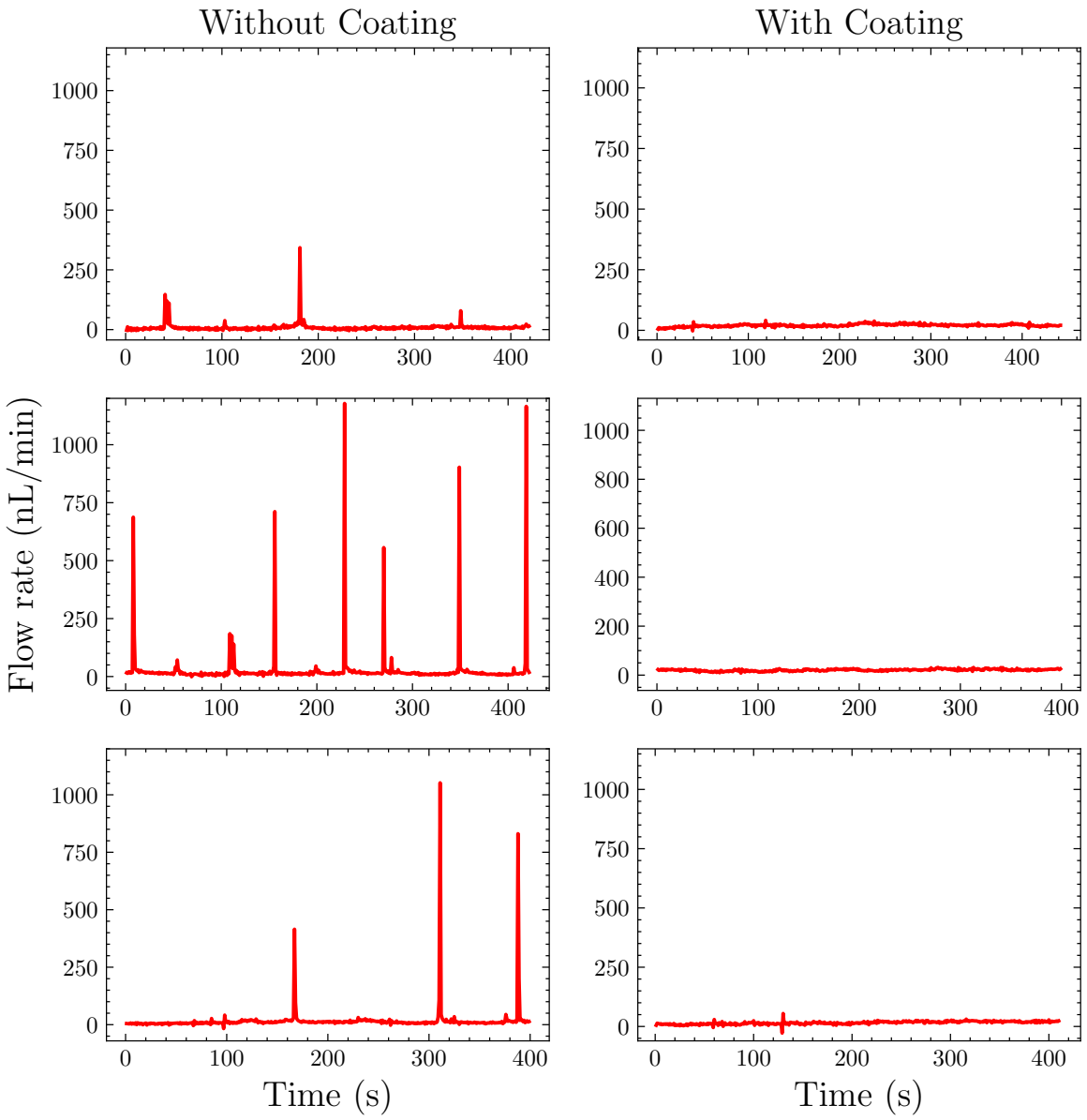

Figure 5.4: Flow rates over time for non-coated (left) and a coated (right) capillary tube.

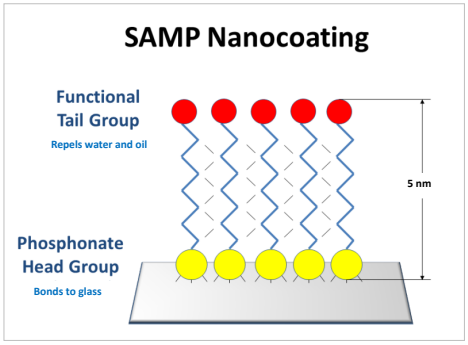

Figure 5.5: Schematic illustration showing the self-assembled monolayer of phosphonates (SAMP) [139].

surface to be treated through strong and highly stable covalent bonds. The functional tails are directed to the top and, depending on their chemical composition, provide the surface with specific properties [28, 139].

The coating of the internal surfaces of the capillaries with a hydrophobic and oleophobic solution, ensures their chemical uniformity but above all facilitates their cleaning. The repellent solution prevents dust and other residues that act as rough spots, from attaching to the glass. As a result, cleaning the capillaries using only pure water, removes the residues and significantly reduces meniscus pinning [3].

5.2 Calibration of a Coriolis Flow Meter

In the previous section, we showed how the coating of the capillaries improved the stability of the measured flow rates and the performances of the template matching algorithm. In this section, we present the results of a flow meter's calibration using the coated capillaries.

The first calibrated device was a BL100 Coriolis mass flow meter from Bronkhorst. This flow meter consists of a micro chip, containing a rectangular shaped tube, connected electrically through a printed circuit board. The chip is placed inside a stainless steel holder to facilitate its connection to the system. Its flow range covers 10 mg/h to 2g/h (About 167 nL/min to 33 μL/min) [146]. The accuracy curve of the BL100 flow meter within its flow range is given Fig. 5.7. The calibration was performed for flow rates going from 20 nL/min to 5000 nL/min. Table 5.1 and Fig. 5.8 show the obtained comparison results, *i.e.* the relative measurement errors of the calibrated flow meter when compared to the flow rates measurements obtained by our interface tracking system.

The preliminary results for the first calibration performed using our primary system are satisfactory. As can be observed in the graph of Fig. 5.8, the relative errors and the associated expanded uncertainties increase significantly for the lowest flow rates. This is in agreement with the errors and accuracy curve provided by the manufacturer (Fig. 5.7). The agreement between the comparison measurements is also observed in flow rate fluctuations. Instead of comparing the mean values of flow rates over the measurement time, we calculate the instantaneous flow rates and superimpose them with the flow meter's values that were recorded at a frequency of 10 values/s. For our measurement system, the frequency of the calculated values range from 5 to 50 values/s depending on the flow rate. The results are shown in Fig. 5.9. The fluctuations measured by our system at the lowest flow rate, *i.e.* 20 nL/min are lower than those of the flow meter. We observe an increase in these fluctuations

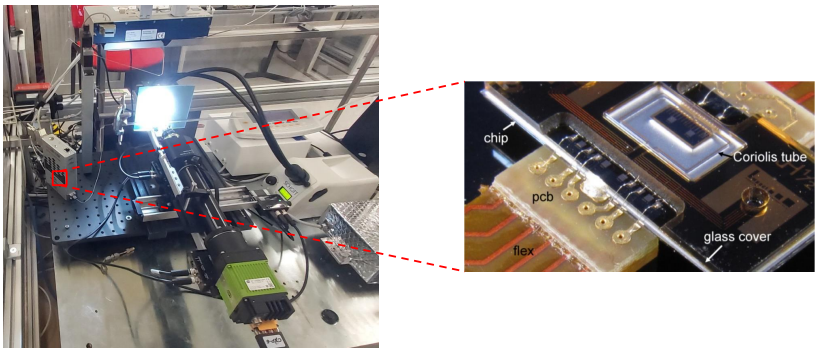

Figure 5.6: Experimental setup used for the calibration of BL100 flow meter with respect to interface tracking method and a zoom into Coriolis chip found inside the stainless steel holder [146].

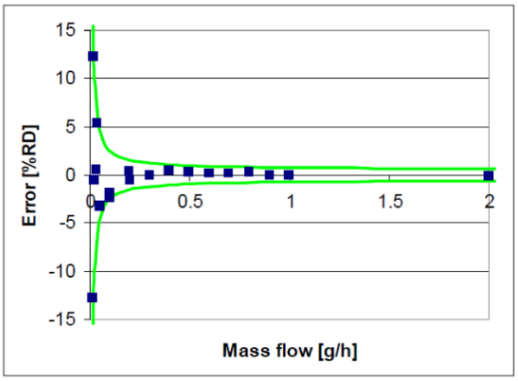

Figure 5.7: Relative measurement errors associated with water mass flow rates measured by the BL100 flow meter in comparison with the gravimetric method. The green curve represents a zero stability of 2 mg/h and a reading uncertainty of 0.5% [146].

with increasing flow rates. This can be explained by the use of a capillary with an inadequate inner diameter. In fact, the same capillary was used for all the generated flow rates, resulting in flow velocities ranging from 2 μL/s to values as high as 424 μL/s. High flow velocities lead to a less stable meniscus and significantly short measurement times.

Target Q_V (nL/min)	**Measurement time (s)**	**Q_V BL 100 (nl/min)**	**Q_V reference (nl/min)**	**Error (%)**	**Mean error (%)**	**u($K=2$) (%)**	**Mean u($K=2$) (%)**
20	131	29,21	30,97	5,7	21	1,9	23
	280	21,66	31,36	30,9		0,5	
	413	21,50	23,19	7,3		4,1	
	444	14,91	20,30	26,6		6,2	
	402	13,71	18,98	27,8		6,1	
	412	11,83	15,86	25,4		8,9	
100	429	112,54	117,63	4,3	6	2,6	9
	508	104,61	110,94	5,7		1,6	
	452	107,25	108,69	1,3		2,1	
	416	98,17	103,77	5,4		17,5	
	402	101,96	90,36	12,8		3,8	
	403	98,34	106,48	7,6		3,7	
500	116	533,00	491,62	-8,4	-7	1,5	2
	123	532,86	499,36	-6,7		0,8	
	124	533,59	498,01	-7,1		0,8	
1000	49	1272,91	1190,34	-6,9	-6	1,0	2
	51	1294,56	1215,50	-6,5		0,9	
	54	1194,99	1136,49	-5,1		2,5	
5000	13	5002,87	4707,79	-6,3	-5	2,4	3
	10	4817,60	4614,80	-4,4		1,4	
	13	4823,51	4598,95	-4,9		0,8	
	12	4088,81	5133,16	20,3		7,6	
	19	3234,73	3116,55	-3,8		6,7	
	22	2715,16	2635,73	-3,0		5,6	

Table 5.1: Results of the calibration of BL100 flow meter against interface tracking method, from 20 nL/min to 5000 nL/min. The volumetric flow rates Q_V measured by BL100 and interface tracking system are given with the corresponding relative errors and relative expanded uncertainties. The given flow rates are mean values calculated over the specified measurement time and the target flow rates are the ones generated by the syringe-pump. The mean relative error/uncertainties take into account the standards deviation of the single relative errors/uncertainties.

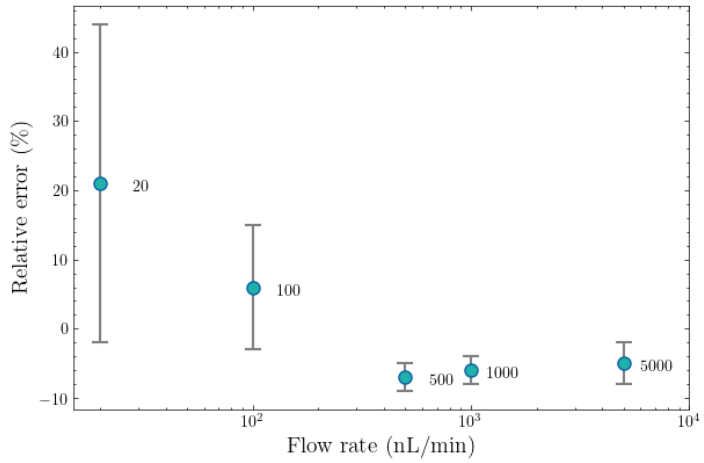

Figure 5.8: Relative measurement errors and the associated expanded relative uncertainties (k=2) obtained through the calibration of BL100 flow meter with respect to interface tracking primary system.

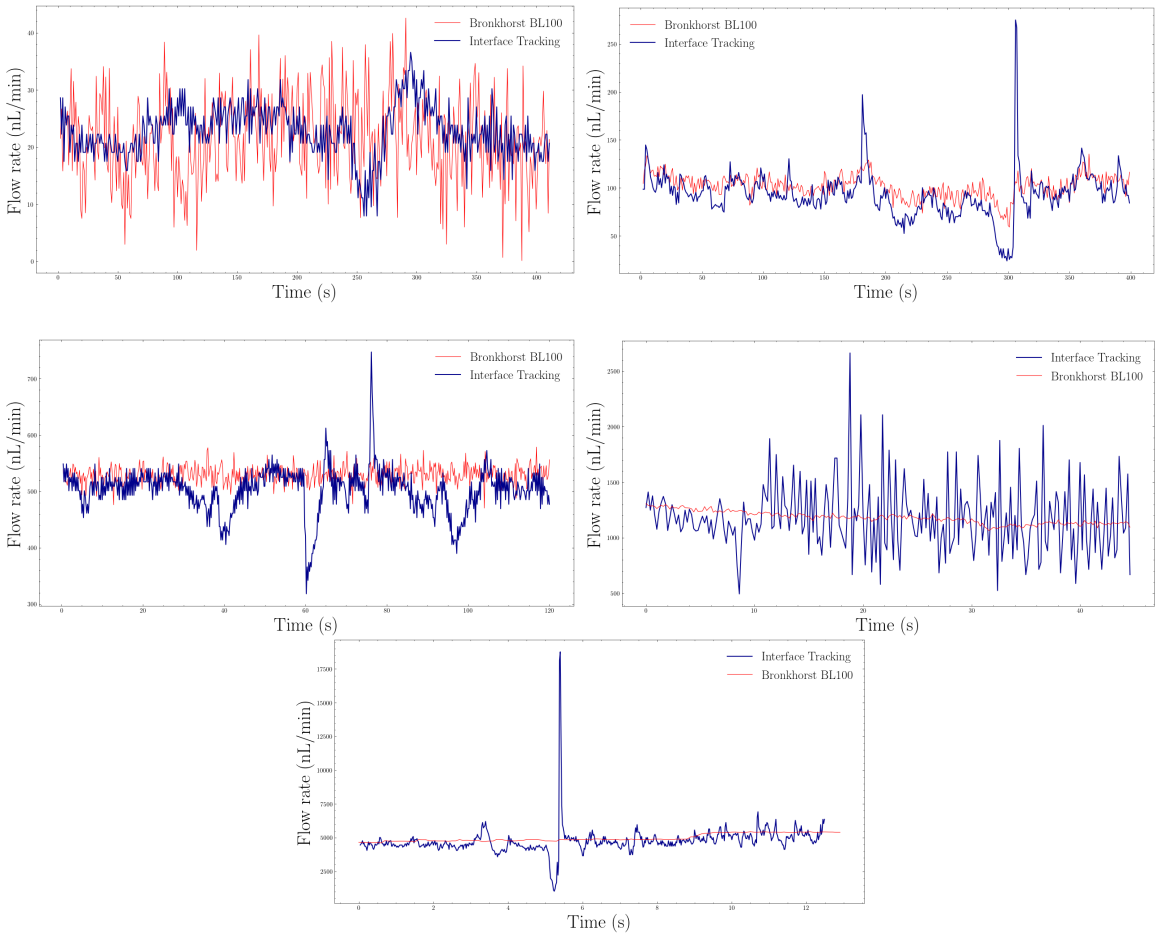

Figure 5.9: Flow rate fluctuations measured by BL100 flow meter and interface tracking system, for generated flow rate of 20, 100, 500, 1000 and 5000 nL/min, at 5, 5, 5, 10 and 50 fps, respectively.

In Section 3.3.2, we explain how to choose the proper parameters in order to improve measurement conditions. The peeks occurring after decreasing flow rates correspond to a pinning and depinning of the interface. In most cases the peeks occur at the same position in the capillary, which leads us to associate them with a coating defect, non-renewed old coating or persistent dust. Nevertheless, they occur less often and with lower amplitudes.

Chapter 6

Validation of the System by Interlaboratory Comparison

In the previous chapter, we presented the first calibration results using the interface tracking system. Particular attention was paid to meniscus pinning which affects the measured flow rates by introducing fluctuations and instabilities in the shape of the meniscus.

This chapter is devoted to the interlaboratory comparison that was carried out within the framework of the MeDD II project. The objective of this comparison was to validate externally, at European level, our primary system and those developed by the 8 participating laboratories. Following this procedure was necessary from a metrological point of view, since there were no primary standards for flow rates below 1.6 μL/min with which the systems could be compared. The comparison protocol is described in the first section, after which we present the results obtained.

6.1 Comparison Protocol

The comparison was carried out following the standard procedure defined in ISO/IEC 17043:2010 and described briefly in Section 1.4. The procedure consisted in the calibration, by each laboratory, of three transfer standards: two thermal mass flow meters and one syringe-pump (Fig. 6.1). Table 6.2 shows the participating laboratories and the measurement techniques they used. The calibrations were carried out for flow rates ranging from 5 nL/min to 1500 nL/min, following the procedure presented in the section 3.3. The references of the tested transfer standards and the flow rates at which they were calibrated are specified in Table. 6.1.

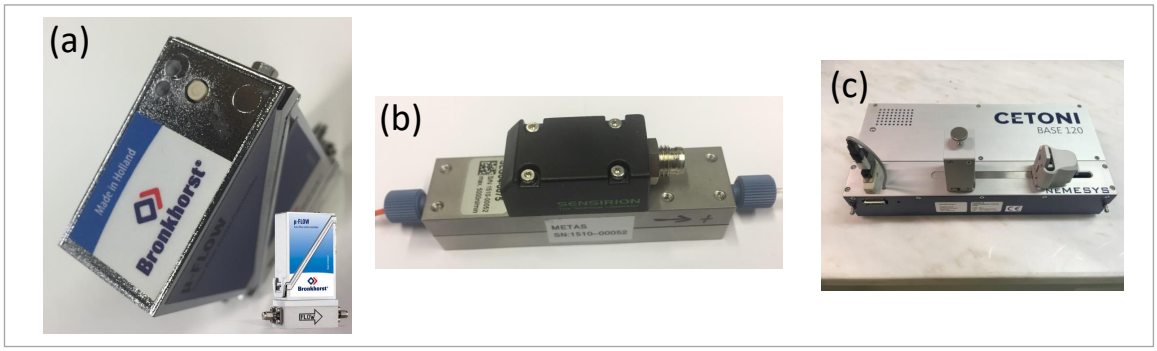

Figure 6.1: Photographs of the calibrated transfer standards. (a): Bronkhorst L01-20D flow meter. (b): Sensirion SLG64-0075 flow meter. (c): Cetoni syringe-pump [104].

Table 6.1: List of the calibrated transfer standards and the flow rates at which they were calibrated.

Flow Rate (nL/min)	5	10	20	50	70	100	500	1000	1500
Bronkhorst L01-20D flow meter	☒	☒	☑	☑	☑	☑	☑	☑	☑
Sensirion SLG64-0075 flow meter	☒	☒	☑	☑	☑	☑	☑	☑	☑
Cetoni syringe-pump	☑	☑	☑	☑	☒	☑	☒	☒	☒

6.2 Results and Discussion

The results of the three transfer standards' calibration by our interface tracking system, *i.e.* the measurement errors and associated uncertainties, are presented in Tables 6.3 to 6.5. The calibration results of all participating laboratories are given in the graphs of Fig. 6.2 (the corresponding data points are provided in Tables B.1 to B.3 in Appendix B.

These results were sent to the leading laboratory who was in charge of the analysis and reporting of the comparison results. The first thing in the analysis was to compute the weighted mean value at each flow rate. This parameter takes into account the relative measurement errors and uncertainties of all laboratories:

$$x_{REF} = \frac{\sum_{i=1}^{n} x_i/u^2(x_i)}{\sqrt{\sum_{i=1}^{n} 1/u^2(x_i)}}, \tag{6.1}$$

where n is the number of all participating laboratories, x_i is the relative error of the laboratory i at the given flow rate and $u(x_i)$ is the measurement expanded uncertainty associated with x_i.

Table 6.2: List of the interlaboratory comparison's participants and their measurement method, with a brief description of the main specifications of each method.

No	Participant	Method	Specifications
1	CETIAT (France)	Interface tracking	Based on template matching
2	THL (Germany)	Front tracking	Based on edge detection of the front
3	NEL/UoS (United Kingdom)	Micro-PIV	Performed in a microfluidics chip with serpentine channels
4	HS (Germany)	Micro-PIV	Based on digital holography
5	IPQ (Portugal)	Interferometry	High accuracy measurement of the distances travelled by the syringe-pump's piston
6	RISE (Sweden)	Gravimetry	Flow generation using a pressure vessel in a temperature-controlled bath
7	METAS (Switzerland)	Gravimetry	The collecting beaker is placed in an evaporation trap and water flows from a needle to the beaker through a glass filter and adsorbing foam to avoid droplet formation
8	DTI (Denmark)	Gravimetry	The water is covered with oil to reduce evaporation and the entire setup is placed in an isolation chamber for temperature stability
9	BHT (Netherlands)	Gravimetry	Generation of a stable flow using a flow controller that controls a piezoelectric valve and the tube is immersed in the water in beaker

The uncertainty associated with the weighted mean, which is known as the weighted uncertainty, is given by:

$$u(x_{REF}) = \frac{1}{\sqrt{\sum_{i=1}^{n} 1/u^2(x_i)}} \tag{6.2}$$

A chi-square goodness of fit test was then performed in order to check the consistency of the calibration results. The test consisted in computing the observed chi-square value χ^2_{obs} and compare it with the critical value given by the appropriate chi-square distribution. The chi-square value to be tested is written as:

$$\chi^2_{obs} = \sum_{i=1}^{n} \frac{(x_i - x_{REF})^2}{u^2(x_i)} \tag{6.3}$$

The consistency test was carried out using the function CHIIV(probability, degrees of freedom) in Microsoft Excel. The check was passed and the weighted mean x_{REF} accepted when $\chi^2_{obs} < \chi^2_{\nu}$, *i.e.* $p - value > 0.05$, where $\nu = n - 1$ is the degree of freedom. In the case where $\chi^2_{obs} >= \chi^2_{\nu}$ the results of the laboratory that contributes the most to the observed chi-square value was excluded from the evaluation at the given flow rate and the consistency test was repeated. After the chi-square test the equivalence between the remaining results was quantified using the degree of equivalence E_n defined in Section 1.4 and reminded here:

$$E_{n_i} = \frac{x_i - x_{REF}}{\sqrt{u(x_i)^2 + u(drift) - u(x_{REF})^2}}, \tag{6.4}$$

with $u(drift)$ the uncertainty associated with the drift of the calibrated device, given by $u(\text{drift}) = \frac{\Delta\varepsilon}{\sqrt{3}}$

Table 6.3: Results of the Bronkhorst (L01-20D) flow meter's calibration using the interface tracking system, at the static regime.

Target Q_V **(nL/min)**	**Reference mean** Q_V **(nL/min)**	**L01-20D mean** Q_V **(nL/min)**	**L01-20D zero (nL/min)**	**Time (s)**	**error (%)**	**Mean error (%)**	**u**($K = 2$) **(%)**	**Mean u**($K = 2$) **(%)**
20	24,1	21,1	-2,1	987	-12,5	-7,3	1,93	9,89
	22,0	21,0	-3,0	1078	-4,6		4,15	
	20,4	19,4	-1,6	1138	-4,7		1,35	
50	51,6	49,0	2,0	1173	-5,0	-5,2	0,45	1,18
	52,1	49,1	1,8	1145	-5,8		0,45	
	52,1	49,6	1,6	1147	-4,8		0,21	
70	72,7	69,2	1,5	816	-4,9	-3,3	0,19	2,91
	70,3	68,9	2,4	850	-2,0		0,26	
	70,6	68,4	2,8	842	-3,1		0,32	
100	105,0	100,5	1,2	564	-4,2	-4,6	0,34	1,03
	104,9	100,1	1,5	563	-4,5		0,15	
	105,6	100,1	1,8	560	-5,2		0,21	
500	496,8	490,5	-0,4	357	-1,3	-1,0	0,23	0,60
	494,9	490,2	-1,0	351	-0,9		0,26	
	494,3	490,6	-1,1	356	-0,7		0,29	
1000	986,0	980,2	-2,2	194	-0,6	-0,5	0,13	0,61
	990,8	983,0	-3,1	192	-0,8		0,14	
	984,5	982,5	-3,3	191	-0,2		0,14	
1500	1486,7	1483,0	-1,6	128	-0,2	-0,2	0,13	0,15
	1485,4	1482,8	-2,1	126	-0,2		0,13	
	1485,9	1482,6	-2,1	127	-0,2		0,14	

The value of $\Delta\varepsilon$ represents the maximum deviation of the device under test at a given flow rate, between two different calibration dates. The reproducibility tests for the two flow meters were performed by METAS. The Bronkhorst L01 meter was calibrated at three different dates : 09/12/2020, 11/12/2020 and 15/07/2020. The largest measured deviation was 0.71 % at 20 nL/min, leading to a relative expanded uncertainty of 0.41 % . The Sensirion SLG64-0075 was calibrated on the 28/08/2020, 07/01/2021 and 14/09/2021. Its maximum deviation was obtained at 20 nL/min with a value of 0.82 %, thus an expanded uncertainty of 0.47 %. As for the Cetoni syringe-pump, no sensible deviation was observed. Therefore, no drift uncertainty was included in the calculation of the E_n value. The chi-square values for the three transfer standards and at each calibration flow rate, are given in Tables B.4, B.5 and B.6 (Appendix B).

The degrees of equivalence for each laboratory are given in Tables 6.6, 6.7 and 6.8, where the x-box symbol is for the flow rate measurements that were not carried out by the laboratory concerned, the grey cells are for the flow rates at which a laboratory was excluded after failing the chi-square test, the orange cells are the flow rates at which a laboratory can validate its system if the $1<E_n1.2$ value is justified and the red cells represent the flow rates that are not validated by the laboratory as the equivalence condition is not satisfied.

The measurement errors obtained represent the deviation of the flow rates measured by the calibrated devices from the reference flow rates, *i.e.* the ones measured by the different primary systems. As shown by the results, these errors are very similar for the different laboratories, especially for flow rates greater than 100 nL/min. In general, taking into account the measurement uncertainties, the calibration results of the different laboratories are in good agreement.

The differences in the measurement uncertainties from one laboratory to another were

Table 6.4: Results of the Sensirion (SLG64-0075) flow meter's calibration using the interface tracking system, at the static regime.

Target Q_V **(nL/min)**	**Mean Reference** Q_V **(nL/min)**	**Mean SLG64-0075** Q_V **(nL/min)**	**SLG64-0075 zero (nL/min)**	**Time (s)**	**Error (%)**	**Mean error (%)**	**u**$(K=2)$ **(%)**	**Mean u**$(K=2)$ **(%)**
20	28,1	20,2	-4,7	849	-28,3	-14,0	0,73	27,52
	22,7	19,8	-5,2	1034	-13,0		0,61	
	19,9	19,7	-5,5	1190	-0,8		0,61	
50	52,1	50,5	-4,8	1133	-3,1	1,9	0,81	9,84
	48,9	50,0	-5,7	1205	2,2		0,75	
	47,8	51,0	-6,3	1237	6,7		0,59	
70	66,7	71,7	-7,2	892	7,5	7,3	0,43	0,92
	66,5	71,1	-6,5	890	6,8		0,57	
	66,7	71,6	-7,0	888	7,5		0,46	
100	101,8	101,6	-6,0	584	-0,1	2,6	0,42	4,82
	97,8	101,4	-6,4	610	3,7		0,28	
	97,4	101,5	-6,6	611	4,3		0,50	
500	499,2	512,3	-3,7	357	2,6	1,8	1,56	2,01
	505,4	512,7	-5,0	351	1,4		1,13	
	506,4	513,0	-4,8	356	1,3		0,91	
1000	1031,1	1028,4	-5,1	194	-0,3	0,1	0,67	1,06
	1028,6	1028,0	-4,5	192	-0,1		0,64	
	1022,3	1027,8	-4,3	191	0,5		0,65	
1500	1534,7	1544,0	-4,4	128	0,6	0,7	1,33	1,29
	1532,9	1543,6	-4,7	126	0,7		1,33	
	1531,7	1542,3	-4,5	127	0,7		1,13	

expected as different methods were employed, involving different uncertainty sources and most importantly, different measurement times. As the sensitivity coefficients are inversely proportional to time, the longer the measurement time, the lower the uncertainty (Equation (4.10)). The maximum measurement time for our system was 45 min at 5 nL/min, with at least one flow rate value per second. At this flow rate, some laboratories had a measurement time up to two hours, which explains the observed differences.

The high uncertainties of our system below 20 nL/min can be justified by the flow rate fluctuations which are taken into account as a source of uncertainty. These fluctuations mainly represent the instabilities of the flow generator, *i.e.* the syringe pump. Nevertheless, they must be taken into account, as the calibration uncertainty must include the entire calibration system, *i.e.* the flow generator and the measurement system. In addition, some of these fluctuations may be caused by the measurement system itself due to occasional stick-slip, for example.

In order to reduce the flow rate fluctuations, we suggest to use a pressure controller as a flow generator, instead of the syringe pump. By including a valve in the system to increase the hydraulic resistance, stable high pressures can be generated leading to stable flow rates.

Calibrations of the two flow meters were also carried out at the dynamic regime. A flow profile was generated with flow rates varying from 30 nL/min to 100 nL/min with steps of 30 s (Fig. 6.5). The results obtained are shown in Tables 6.9 and 6.10. The measurement errors were determined by comparing the mean flow rate measured by the flow meter, with the one measured by our system. For mean flow rates of about 60 nL/min, these errors does not exceed 8 % and the associated uncertainties vary between 5 % and 8 %.

Fig. 6.3, 6.4, 6.6 and 6.7 illustrate the flow rate fluctuations measured by the flow meter

Table 6.5: Results of the Cetoni syringe pump's calibration using the interface tracking system, at the static regime.

Target Q_V **(nL/min)**	**Mean Reference** Q_V **(nL/min)**	**Mean Cetoni** Q_V **(nL/min)**	**Time (s)**	**Error (%)**	**Mean error (%)**	**u**$(K=2)$ **(%)**	**Mean u**$(K=2)$ **(%)**
5	3.0	4.999	1525	67.1	28.5	3.45	51.73
	4.4	4.999	1395	14.7		4.51	
	4.3	4.999	1440	15.2		3.15	
	4.3	4.999	1490	16.8		2.30	
10	11.6	9.998	884	-14.2	-7.5	1.94	11.35
	11.1	9.998	915	-10.0		1.35	
	10.4	9.998	1016	-3.5		2.46	
	10.2	9.998	1040	-2.4		2.79	
20	21.4	19.980	456	-6.4	-1.2	1.64	14.21
	21.4	19.980	465	-6.8		1.62	
	18.7	19.980	516	6.6		4.89	
	19.6	19.980	512	1.8		5.73	
50	50.2	50.006	750	-0.5	-0.1	0.18	0.64
	50.1	50.006	750	-0.2		0.33	
	50.0	50.006	745	0.1		0.24	
	49.9	50.006	760	0.2		0.18	
70	69.8	69.986	535	0.3	0.5	0.25	0.66
	69.3	69.986	533	0.9		0.17	
	69.8	69.986	535	0.3		0.24	
	69.7	69.986	540	0.5		0.24	
100	100.8	100.013	379	-0.7	-0.5	0.15	0.70
	100.5	100.013	377	-0.5		0.19	
	100.9	100.013	378	-0.8		0.28	
	100.1	100.013	381	-0.1		0.19	

(red) and our system (red), at the static and dynamic regimes. The shift between the last curve of Fig. 6.6 is due to recording error in the starting measurement time, as the latter is not yet automated.

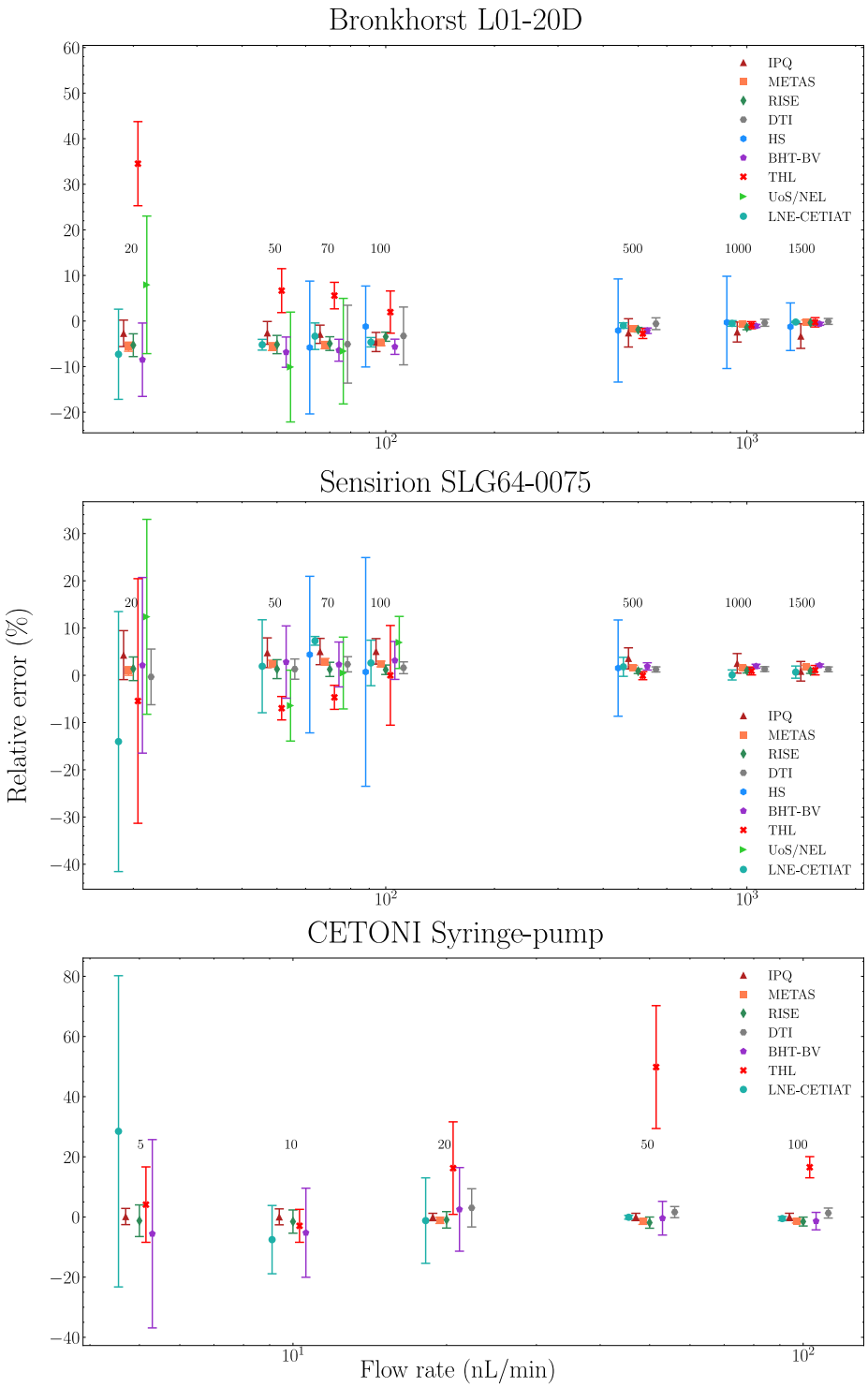

Figure 6.2: Relative measurement errors and the associated uncertainties obtained by the calibration of the three transfer standards, in the context of the interlaboratory comparison. The flow rates are displayed on a logarithmic scale and the errors at a given flow rate are shifted on the x axis, for clarity.

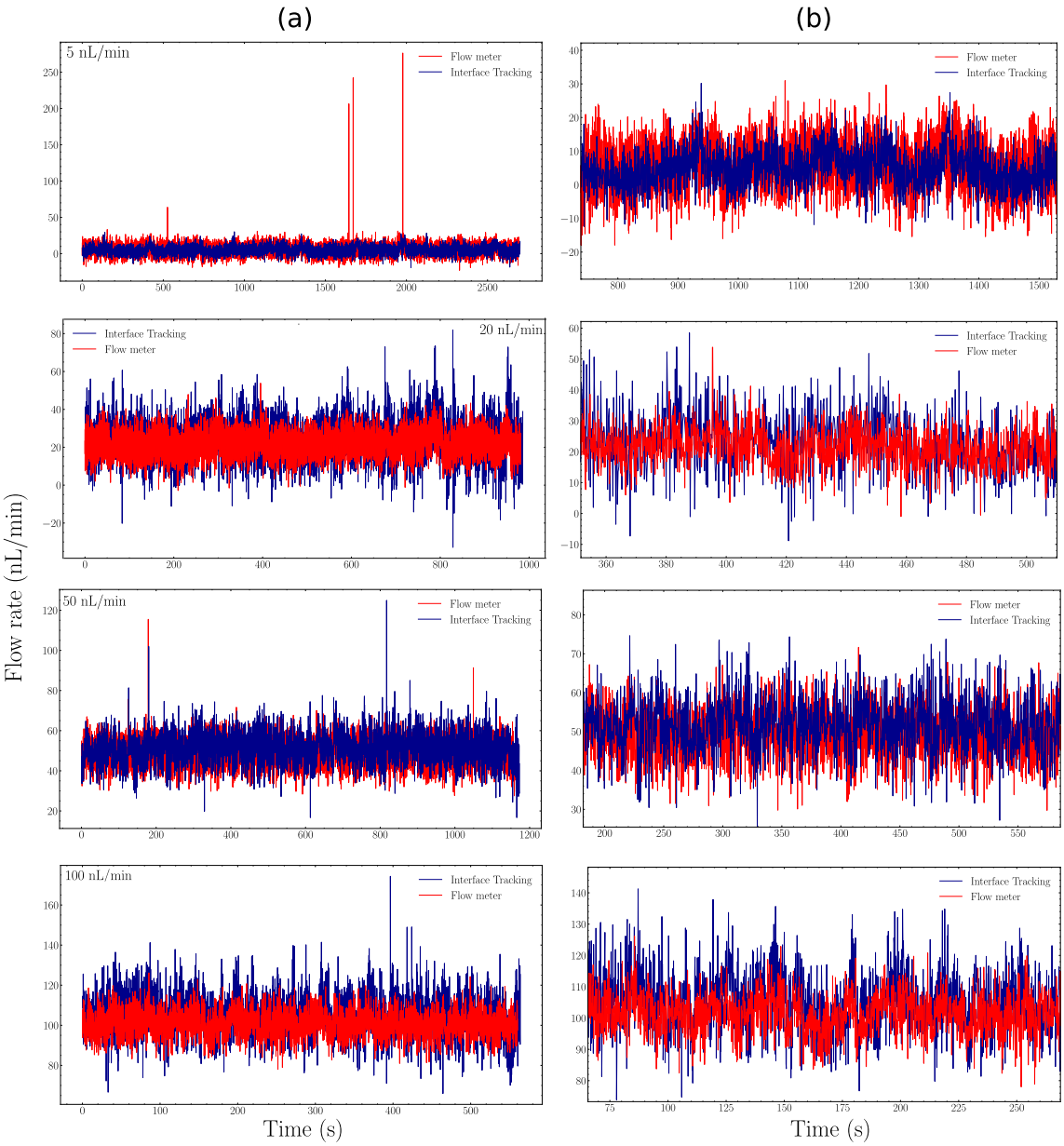

Figure 6.3: Graphs of the dynamic flow rates measured by the Bronkhorst L01-20D flow meter (red) and the interface tracking system (blue) at the target flow rates: 5nL/min (2 fps), 20 nL/min (4 fps), 50nL/min (4 fps) and 100 nL/min (8 fps) (a), with a zoom on each graph (b).

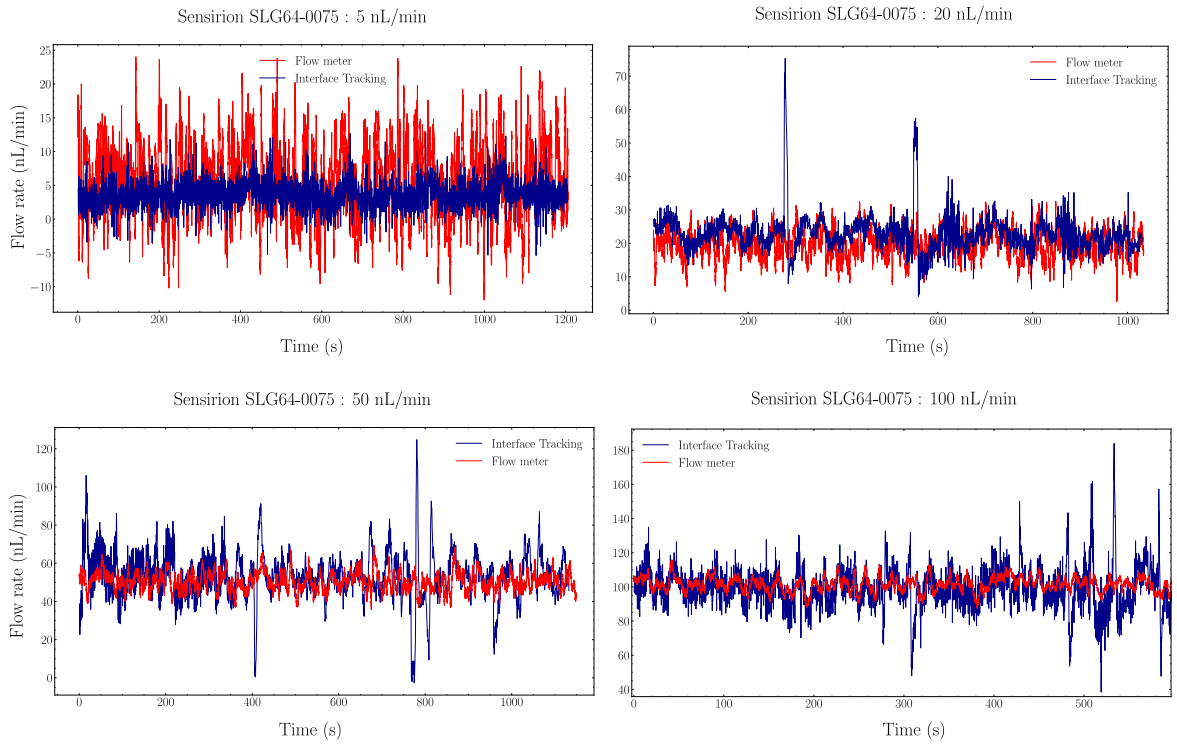

Figure 6.4: Graphs of the dynamic flow rates measured by the Sensirion SLG64-0075 flow meter (red) and the interface tracking system (blue) at the target flow rates: 5nL/min (2 fps), 20 nL/min (2 fps), 50nL/min (2 fps) and 100 nL/min (5 fps).

Table 6.6: Degrees of equivalence E_n of each participating laboratory for the calibration of the Bronkhorst L01-20D flow meter.

Flow rate (nL/min)	**Degree of equivalence E_n**								
	IPQ	CETIAT	METAS	RISE	DTI	HS	THL	Uos/ NEL	BHT
1500	1.11	0.18	0.06	0.14	0.27	0.18	0.02	⊠	0.65
1000	0.65	0.59	0.47	0.74	0.67	0.06	0.04	⊠	0.27
500	0.28	1.06	0.17	0.35	0.84	0.03	0.93	⊠	0.63
100	0.05	0.19	0.34	1.04	0.19	0.37	1.39	⊠	0.63
70	1.06	0.58	0.46	0.02	0.01	0.06	-	0.14	0.61
50	1.11	0.11	0.40	0.08	⊠	⊠	-	0.40	0.46
20	0.94	0.20	0.48	0.01	⊠	⊠	-	-	0.40

Table 6.7: Degrees of equivalence E_n of each participating laboratory for the calibration of the Cetoni syringe pump.

Flow rate (nL/min)	**Degree of equivalence E_n**								
	IPQ	CETIAT	METAS	RISE	DTI	HS	THL	Uos/ NEL	BHT
100	0.64	0.31	1.00	0.57	1.25	⊠	-	⊠	0.23
50	0.37	0.70	1.31	0.82	1.13	⊠	-	⊠	0.001
20	0.64	0.04	0.70	0.13	0.58	⊠	-	⊠	0.22
10	0.64	0.58	⊠	0.13	⊠	⊠	0.36	⊠	0.28
5	0.13	-	⊠	0.26	⊠	⊠	0.34	⊠	0.18

Table 6.8: Degrees of equivalence E_n of each participating laboratory for the calibration of the Sensirion SLG64-0075 flow meter.

Flow rate (nL/min)	Degree of equivalence E_n								
	IPQ	CETIAT	METAS	RISE	DTI	HS	THL	Uos/ NEL	BHT
1500	0.39	0.74	0.12	1.16	0.62	⊠	0.54	⊠	0.83
1000	0.51	1.21	0.40	0.70	0.21	⊠	0.58	⊠	0.79
500	1.03	0.27	0.61	0.59	0.01	0.03	1.42	⊠	0.73
100	1.08	0.10	0.41	0.96	0.43	0.06	0.20	0.87	0.25
70	0.86	-	0.37	0.95	0.20	0.10	-	0.28	0.07
50	0.81	0.03	0.31	0.49	0.45	⊠	-	-	0.07
20	0.63	-	0.22	0.14	0.24	⊠	0.25	0.55	0.06

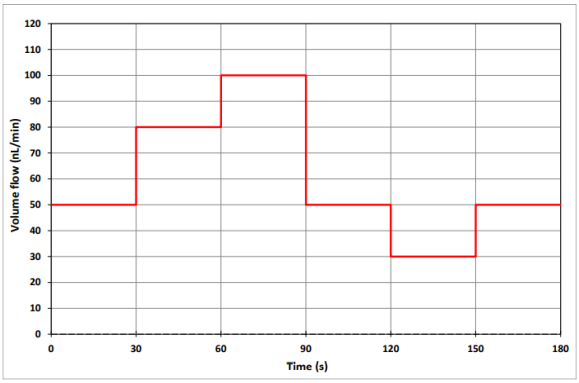

Figure 6.5: Flow profile generated for flow meters' calibration at the dynamic regime.

Table 6.9: Results of the Bronkhorst (L01-20D) flow meter's calibration using the interface tracking system, at the dynamic regime.

Profile N°	L01-20D mean flow rate (nL/min)	Reference mean flow rate (nL/min)	Error (%)	Expanded uncertainty ($k = 2$) (%)
1	56.6	61.1	-7.4	8.04
2	61.3	63.8	-4.0	6.22
3	61.1	64.9	-5.9	7.68
4	55.0	56.6	-2.8	7.95

Table 6.10: Results of the Sensirion (SLG64-0075) flow meter's calibration using the interface tracking system, at the dynamic regime.

Profile N°	SLG64-0075 mean flow rate (nL/min)	Reference mean flow rate (nL/min)	Error (%)	Expanded uncertainty ($k = 2$) (%)
1	61.6	63.6	-3.1	5.28
2	59.2	61.0	-2.9	6.29
3	62.1	61.8	0.5	6.40
4	60.3	60.3	-0.1	5.89

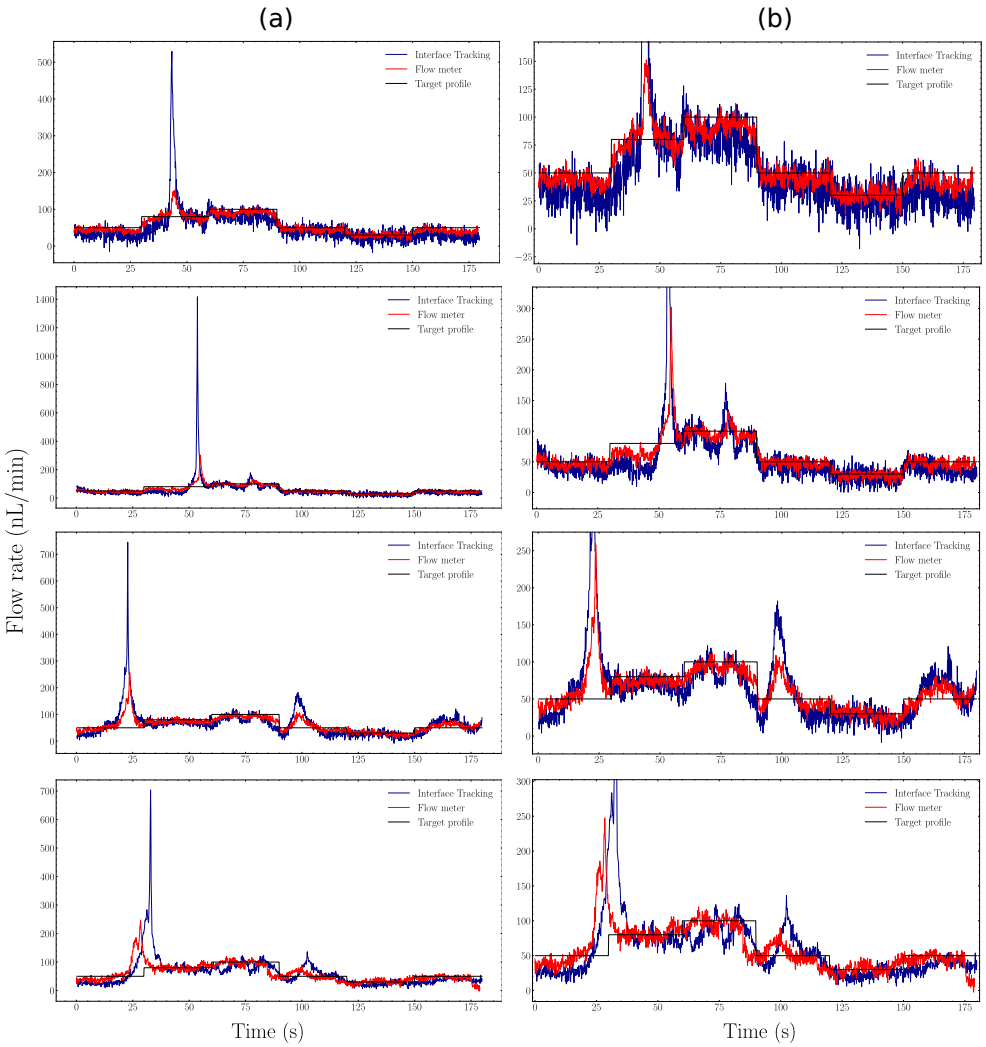

Figure 6.6: Graphs of the flow rates measured by the Bronkhorst L01-20D flow meter (red) and the interface tracking system (blue), at the dynamic regime.

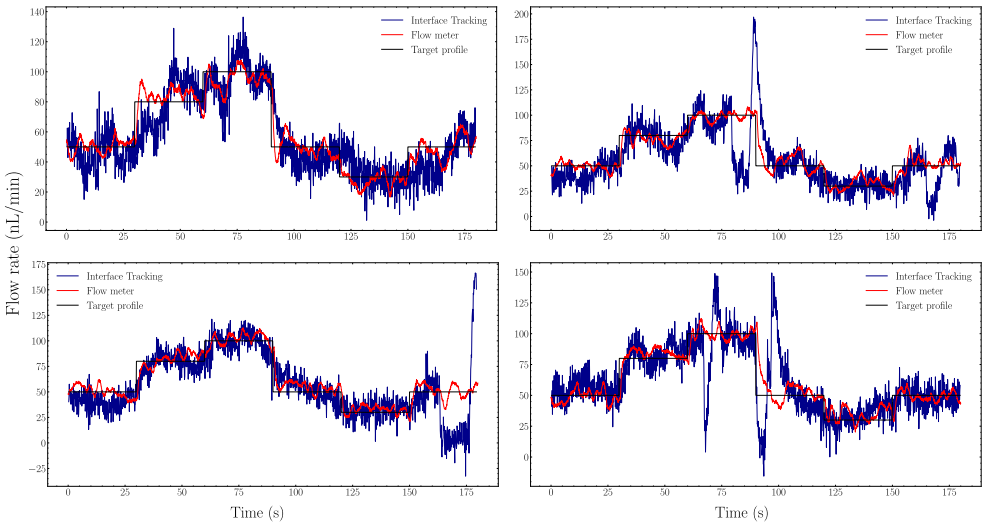

Figure 6.7: Graphs of the flow rates measured by the Sensirion SLG64-0075 flow meter (red) and the interface tracking system (blue), at the dynamic regime.

Chapter 7

Application and Perspectives

In the previous chapter, we presented the results of the interlaboratory comparison which was carried out in order to validate the primary systems developed by the different laboratories. Given the measurement uncertainties, the calibration results obtained are in good agreement, thus allowing a first metrological validation of our primary method.

In this chapter, we present a direct application of our system in the medical field. This application consisted in the calibration of an infusion pump, in order to evaluate its performance before use by patients. To conclude the chapter, we present a different configuration of the interface tracking system which allows the measurement of flow rates from the increasing volume of a pendant drop.

7.1 Calibration of Treprostinil Infusion Pump

As an example of a direct application of our primary system, we present here the calibration of a medical infusion pump from LenoMed Medical. In fact, the nano-flow measurement laboratory of CETIAT was solicited by the supplier Alphadiab, in order to evaluate the pump's metrological performances before commercialization. The pump is intended to deliver Treprostinil, a substance used to treat pulmonary arterial hypertension [12, 140]. Technically, this infusion device does not deliver the target flow rate continuously, instead it releases discrete amounts (infusions) separated by equal time intervals. The aim of the calibration is to investigate 3 different parameters: the time interval between infusions, the volume of each infusion and the number of infusions per hour for the given flow rate. By design, the pump is expected to release 4 infusions per hour with an interval of 10 min, at 200 nL/h. At 2000 nL/h and 35000 nL/h, the pump is expected to release 6 equal volume infusions per hour with a time interval of 10 min. The sum of the discrete volumes released during one hour should be equal to the target flow rate.

For our purposes, the calibration was carried out using insulin, instead of Treprostinil, as it has a similar viscosity but is more readily available. In order to be as close as possible to the conditions of use, the pump was connected to the capillary using its own catheter tubing with the metallic needle at the tip. The calibrated device operates like a standard syringe pump. The small syringe was filled completely with insulin then placed inside the pump to which the catheter tubing was connected. In order to avoid introducing bubbles in the system, the tubing was connected to the pump while empty. The other side of the tubing was connected to the capillary through the metallic needle. Glue was added around the needle to avoid any leakage (Fig. 7.1). The system was filled by producing several boluses with the volume of 0.03 mL. Once the tube was filled, a continuous low flow rate was generated in order to fill partially the capillary. The details for the different adjustments that needed to be done before starting measurements are explained in Section 3.3. The chosen parameters

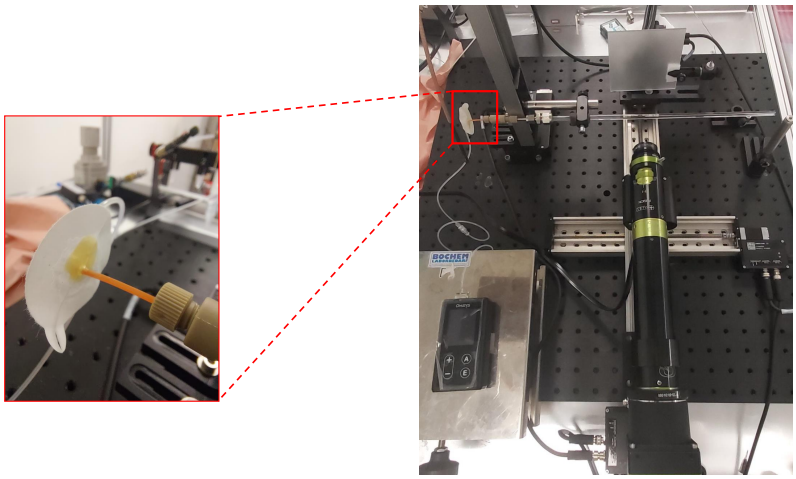

Figure 7.1: Photograph of the setup used for calibration of the infusion pump using the primary standard for nano-flow rates (right). View of the catheter's patch mounting on dedicated fittings. The needle coming out of the patch is glued to polymer tubing ensuring leak tightness (left).

for each flow rate are shown in Table 7.1.The measurements at each flow rate were repeated at least 3 times to evaluate the repeatability of the device. The time interval and mean flow rate between the infusions were calculated between the flow rate peeks. The released volume was obtained by multiplying the mean flow rate by the corresponding time interval.

The calibration results are shown in Tables 7.2, 7.3 and 7.4. Fig.7.2 shows the measured interface displacements and the flow rate over time. For all the measurements performed at 2000 nL/h and 35000 nL/h, 6 infusions are observed within one hour. Besides, the successive infusions occur periodically with time intervals equal or close to 10 min. This is in good agreement with the specifications given by the manufacturer regarding the number of infusions and the time that separates them. The volume of infusions on the other hand is not constant and varies in some cases by 50 %. Nevertheless, the total volume of all infusions together differs from the target volume by less than 10 %, for the highest flow rates. The lowest flow rate the pump should be able to generate is 200 nL/h. Contrary to the manufacturer's expectations, the calibrations carried out at this flow rate reveal that the pump releases only one infusion per hour instead of four. The measurements of the total volume released in one hour show differences of up to 50 % compared to the target value.

The results described above demonstrate the applicability of our primary system in the characterization of drug delivery devices. Furthermore, they show the interest of being able to measure dynamic flow rates, as in the case of the Treprostinil pump which generates

Table 7.1: Configuration of the interface tracking system for the calibration of the infusion pump.

Flow rate (nL/h)	**Flow rate (nL/min)**	**Capillary inner diameter (μm)**	**Camera zoom (%)**	**Pixel size (μm)**	**Horizontal field of view (μm)**	**Interface velocity (μm/s)**	**Frame rate (fps)**
200	3.33	1000	25	0.855	3502	0.07	0.5
2000	33.33	1000	25	0.855	3502	0.83	1
35000	583.33	3000	0	1.350	5530	1.02	1

Table 7.2: Measurement results at 35000 nL/h.

Infusion	Start (s)	end (s)	Time interval (min)	Flow rate (nL/min)	Volume (nL)
1	201	801	10.00	629.2	6292
2	801	1402	10.02	620.6	6216
3	1402	2002	10.00	514.1	5141
4	2002	2603	10.02	507.6	5084
5	2603	3203	10.00	472.3	4723
6	3203	3803	10.00	432.8	4328
Average			10.01	529.4	5297.3

very fluctuating flow rates. Finally, the discrepancies between the volume of infusions and the values declared by the manufacturer, whether small or large, highlight the importance of calibrating medical devices. The calibrations should be carried out against primary standards to ensure the best calibration accuracy possible and the traceability of the doses administered to the patients, and improve the patients' safety.

Table 7.3: Measurement results at 2000 nL/h. The flow rate and volume were not measured for the sixth point, as the measurement was stopped before the seventh infusion.

Infusion	Start (s)	end (s)	Time interval (min)	Flow rate (nL/min)	Volume (nL)
1	63	707	10.73	40.8	438
2	707	1300	9.88	40.1	396
3	1300	1887	9.78	35.2	345
4	1887	2500	10.22	29.9	306
5	2500	3102	10.03	33.6	337
6	3102	/	/	/	/
Average			10.13	35.9	364.3

Table 7.4: Measurement results at 200 nL/h.

Infusion	Start (s)	end (s)	Time interval (min)	Flow rate (nL/min)	Volume (nL)
1	579	4182	60.05	4.9	292.0

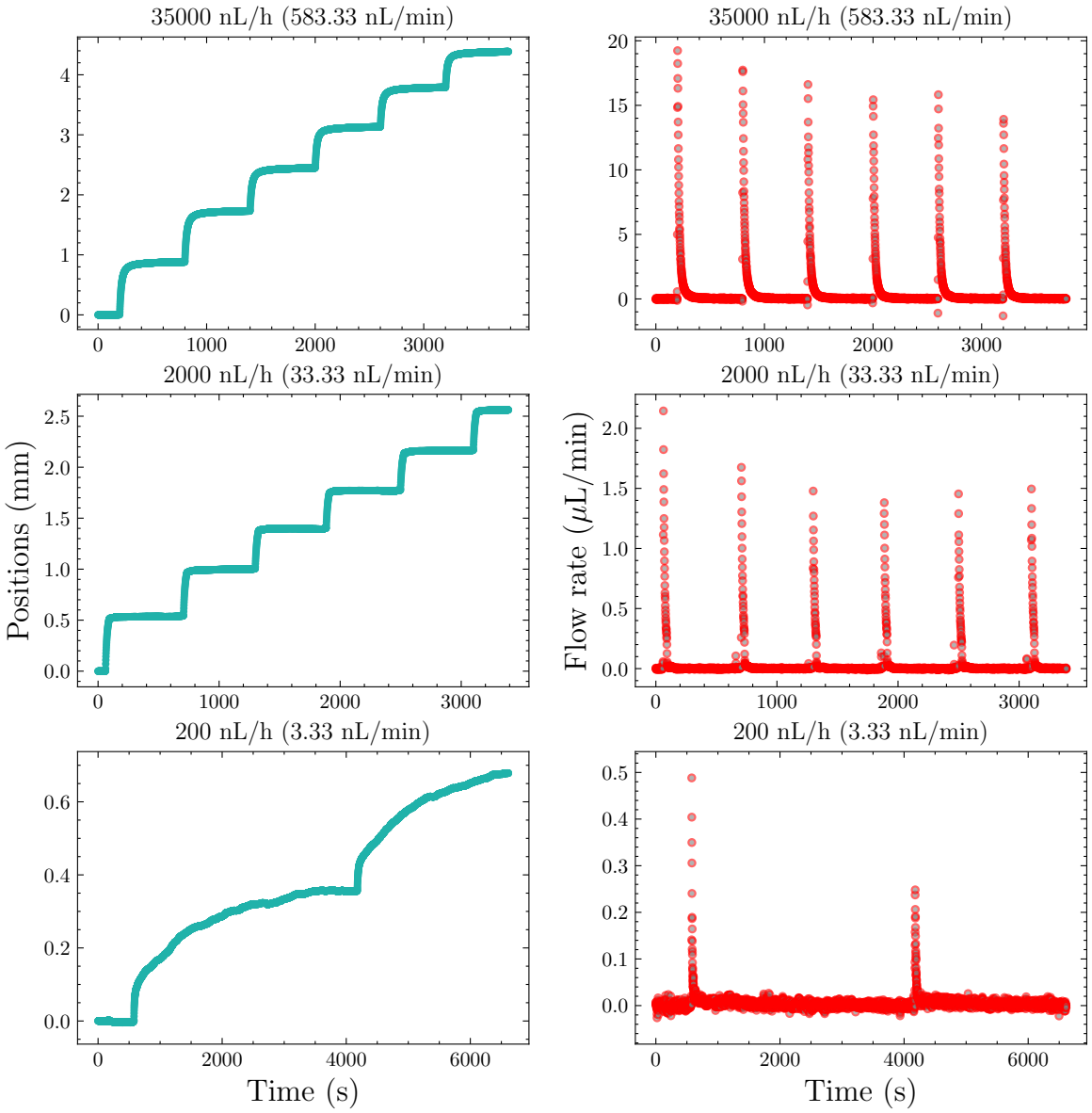

Figure 7.2: Interface positions over time (left) and dynamic flow rates (right) generated by the infusion pump and measured by the interface tracking system.

7.2 Pendant Drop Method

7.2.1 Description of the Method

The system developed for the measurement of flow rates using interface tracking method can also be used in a different configuration, for the same purpose. In fact, if the capillary tube is placed in a vertical position the flowing liquid forms a droplet when it reaches the end of the capillary. The pendant drop's volume increases until it reaches a maximum, after which it detaches from the capillary. The rate at which the droplet's volume increases is proportional to the generated flow rate.

Digital imaging of suspended liquid drops has been largely used for the accurate measurement of surface and interfacial tension. This is known as pendant drop tensiometry [48]. Mainly, this method consists on fitting the droplet's profile, in the acquired image, using the axisymmetric Young-Laplace equation. The best fit is then used to determine the droplet's

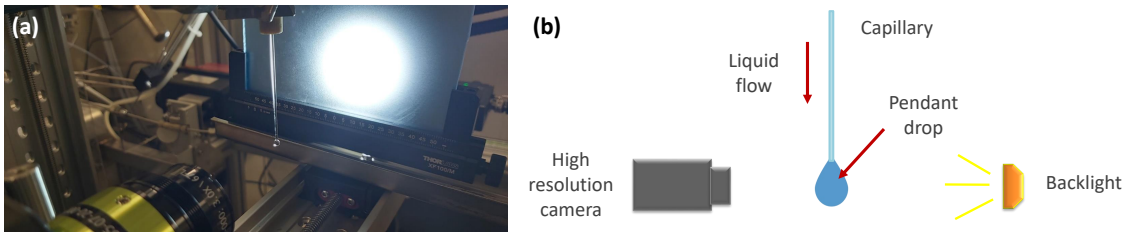

Figure 7.3: Photograph (a) and schematic illustration (b) of the experimental setup for the pendant drop method.

radius, volume and the liquid's surface tension [21, 65, 148]. J. D. Berry *et al.* [21] also mentioned the possibility of measuring the rate of evaporation by tracking the droplet's volume over time.

Following the same principle, we propose to use the pendant drop method to measure low flow rates. As mentioned above, the experimental setup is adapted from the interface tracking system by placing vertically the capillary tube (Fig.7.3). The capillaries used have a thin wall and are coated at their end with a hydrophobic glass repellency treatment from Aculon (Section 3.3.1), to prevent the droplet from rising by capillarity along the outer surface of the tube. This occurs particularly when the droplet's volume is very small, *i.e.* the capillary forces are more important than the droplet's weight. The flow rate is determined from the increase in the droplet's volume over time:

$$Q_{volumetric} = \dot{V}_{droplet}, \tag{7.1}$$

where $Q_{\text{volumetric}}$ is the volumetric flow rate and $\dot{V}_{\text{droplet}}$ is the time derivative of the droplet's volume.

Fig. 7.4 shows images of a pendant drop at 1.6 μL/min. The droplet's volume at a given instant is determined by slicing the whole volume into cylindrical subvolumes with a height of 1 pixel (Fig. 7.5) [157, 119]. By doing so, we assume that every subvolume is symmetrical around its vertical axis. However, we make no assumption regarding the total symmetry of the droplet. As a matter of fact, it is very hard to keep the droplet symmetrical during the entire measurement time, due to flow rate fluctuations, potential vibrations in the system and possible deviations from the vertical axis. Therefore, instead of considering a rotational symmetry for the whole droplet, we consider only the symmetry of the separate subvolumes. This implies that every horizontal slice in the volume is circular and has its own axis of symmetry without any constraints on the general shape of the droplet. This hypothesis makes the fitting of the droplet's profile more complicated. Nevertheless, it allows to have

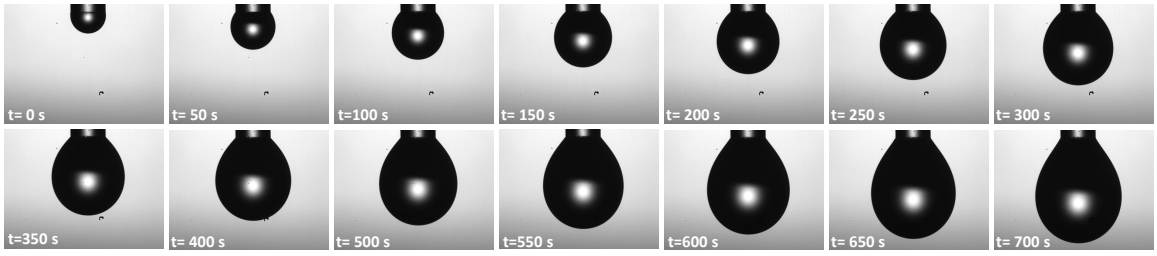

Figure 7.4: Image sequence of a drop pending from a capillary with an inner diameter of 1 mm, at a generated flow rate of 1.6 μL/min. The time interval between the successive images is 50 s.

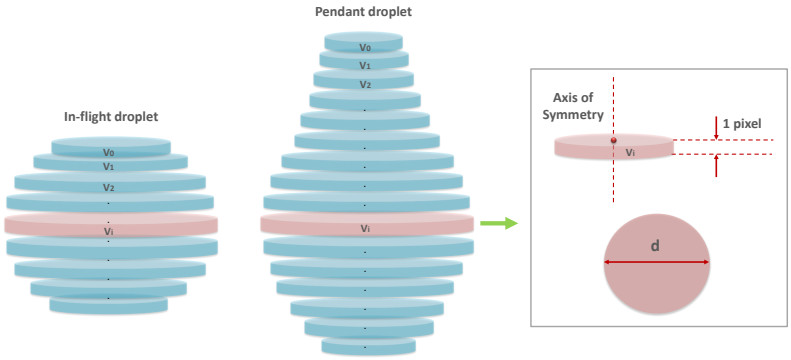

Figure 7.5: Schematic illustration showing the method used to measure the droplet's volume.

more accurate values when the measurement conditions are not ideal. The total volume of the droplet results from the addition of all the cylindrical subvolumes:

$$V_{droplet} = \sum_{i=1} V_i = \sum_{i=1} \frac{\pi}{4} d_i^2 . h, \tag{7.2}$$

where V_{droplet} is the total volume of the droplet, V_i the volume of the i^{th} cylinder, d_i the diameter of the i^{th} cylinder and h the height of a cylinder which is equal to 1 pixel. The image processing procedure used to fit the droplet's profile, determine the diameter of each cylinder and deduce the flow rate is explained in the following subsection.

7.2.2 Image Processing Algorithm

The measurement of the flow rate from an image sequence of the growing droplet is carried out using a home made software based on a script written in Python language and a GUI written in TKinter (Fig. 7.6). The GUI was mainly created to enter input parameters such as the path of images, frame rate and pixel size. It also enables to perform operations on images, in real time, in order to extract more information. Once all the input parameters are specified and the program launched, the images are processed automatically within a loop, at the end of which the results are displayed and saved. It is worth mentioning that this software also allows to measure the volume of an in-flight drop which can be used in drop-on-demand inkjet printing [133, 147, 77], for example.

The steps for the measurement of the flow rate are the following. First, the image with the largest drop is selected and the path to the rest of the images specified as an input value. Then, a region of interest (ROI) is selected in such a way that a part of the tube's end is included. Defining the ROI from the image with the largest droplet ensures that the droplet is always smaller than the ROI. As the boundary between the tube and droplet is not well defined in images and in order to avoid additional uncertainty sources, the starting position of the droplet is determined by image processing from each image. This is achieved by measuring the widths of the tube starting from the top of the image and going down with an increment of 1 pixel. As the tube's outer diameter is relatively constant, its boundary with the droplet is taken as the position at which the measured widths start to increase continuously. The widths are measured as the distances between the left and right edges of the tube/droplet which are detected using Canny method (Appendix A). In order to reduce the measurement time, it is possible to draw a horizontal line, across the tube and sufficiently above the boundary, that defines the starting point at which the widths are measured. After

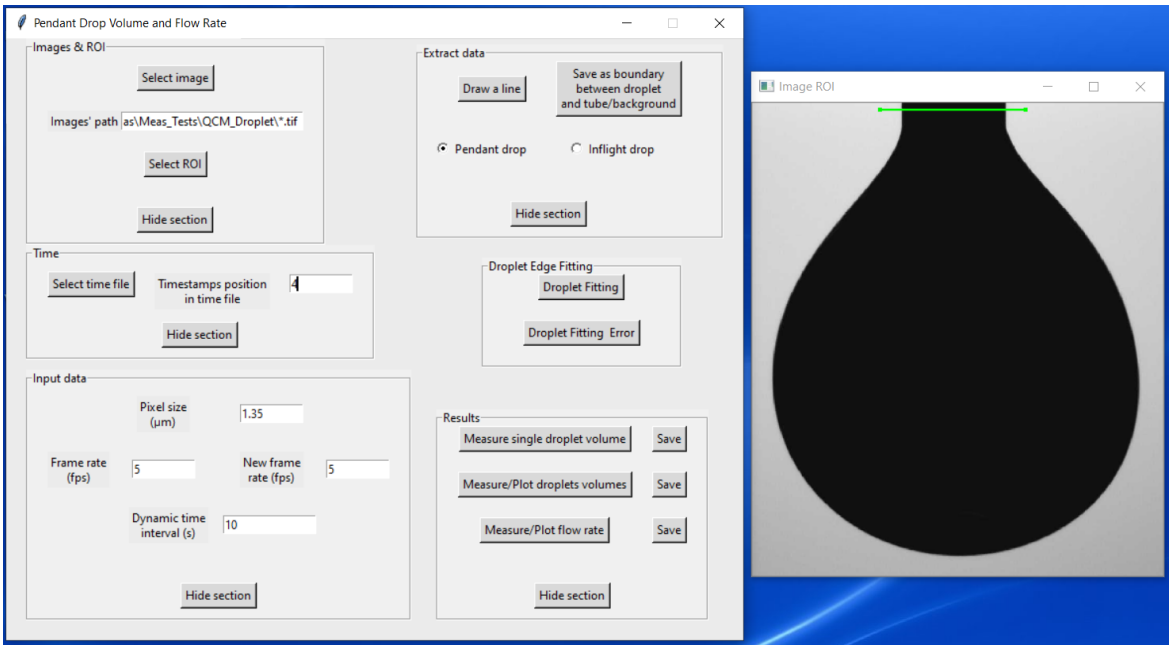

Figure 7.6: Image of the GUI of the pendant drop software.

specifying the input parameters, the measurement can be started. Within a general loop, the first image is opened and a ROI selected using the initial saved coordinates. A Gaussian blur filter is applied on the ROI image in order to reduce the noise. The droplet's edges are detected using Canny edge detection method which results in a binary image with a black background and white edges. The coordinates of these are separated into 6 parts (3 on each side of the drop) and fitted with a polynomial function. The choice to fit each part of edges separately was made for the simple reason that it is hard to fit the whole profile of a non-symmetrical droplet, as this requires the use of high-order, implicitly defined functions. In order to obtain a continuous fitting, the points that lie near the boundary of two given parts were taken into account in the fitting of these two parts. Fig. 7.7 shows the results of edge detection and the associated fitting profile. The latter is used to determine the diameter of each cylindrical subvolume which is taken as the difference between the right and left edges. The total volume of the droplet at the given instant is obtained by adding all the subvolumes

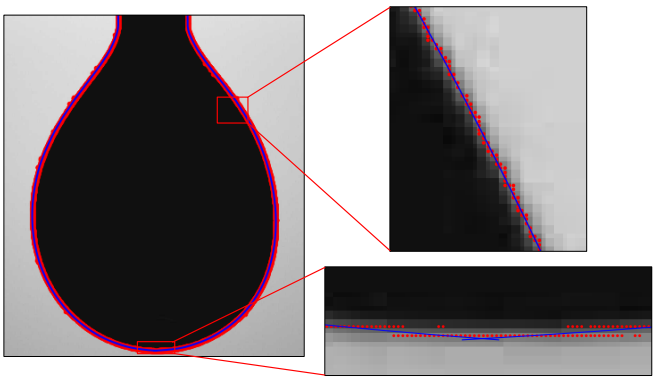

Figure 7.7: Image of the pendant drop on which are displayed the detected edges (red) and the corresponding fitting profile (blue). The right side images represent a zoom into two different regions of the droplets' edges.

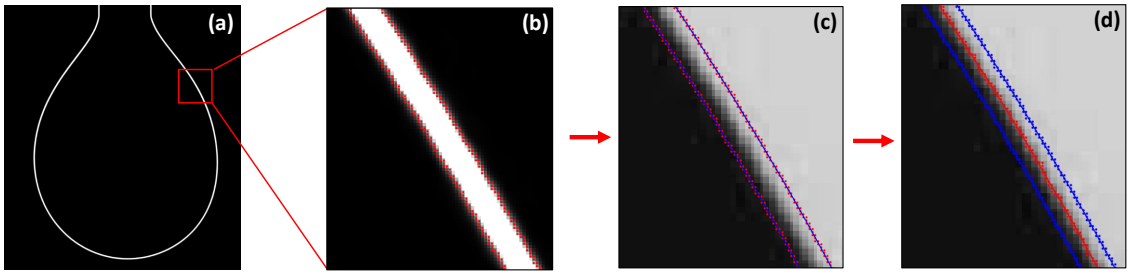

Figure 7.8: Image of the pendant drop after the application of the variance filter (a) with a zoom into a part of the droplet's borders : (b) is the variance strip on the sides of which are displayed the detected edges (red), (c) shows the same region in the original image on which are displayed the variance edges (red) and their corresponding fitting profile (blue). (d) shows the same region with all the previously detected edges and the corresponding polynomial fits.

that are deduced from the measured diameters.

As the transition between the background and the droplet is not immediate, is it important to quantify the uncertainty associated with edge detection, *i.e.* with the measurement of the subvolumes' diameters. Following the same methodology as for the measurement of the pixel size using a calibration target or the measurement of the capillary's inner diameter from the fluorescent signal (Sections 4.1 and 4.3.2), we estimate the largest interval of positions where the droplet's edge can be located. To do this, a variance filter is applied on the initial ROI image and the edges of the obtained variance regions are detected. These edges represent the limits of the interval we wish to determine. By fitting the inner and outer edges separately, we obtain two droplet profiles that represent the smallest and largest possible volumes for the droplet at the given instant. The difference between these extreme volumes is used to estimate the maximum measurement uncertainty due to edge detection, as shown in the next subsection. Obtained results for the aforementioned operations are shown in Fig. 7.8. After all the volumes are measured the mean flow rate is determined by performing a linear regression on the volumes with respect to time. The described algorithm is summarized in the flowchart presented in Fig. 7.9.

7.2.3 Uncertainty Budget

The measurement uncertainty associated with the flow rate results mainly from the measurement of the droplet volumes and the corresponding timestamps. Evaporation rate of the droplet in air is included in the budget as an uncertainty source. The total uncertainty is given by:

$$u(Q_V) = \sqrt{\left(\frac{\partial Q_V}{\partial V}\right)^2 u^2(V) + \left(\frac{\partial Q_V}{\partial t}\right)^2 u^2(t) + u^2_{\text{evap}}}, \tag{7.3}$$

where $u(V)$ and $u(t)$ are the measurement uncertainties associated with the droplet's volume and timestamp, respectively. u_{evap} is the evaporation rate of the droplet. The Sensitivity coefficients C_V and C_t are given by the following equations:

$$\frac{\partial Q_V}{\partial V} = C_V = \frac{1}{t} \tag{7.4}$$

$$\frac{\partial Q_V}{\partial t} = C_t = \frac{-V}{t^2} \tag{7.5}$$

The uncertainty $u(t)$ is associated with the determination of image timestamps from the acquisition frequency, taking into account exposure time and potential delays between the signals sent and the instant at which images are acquired. A detailed explanation of this component is provided in Section 4.1.5. The uncertainty associated with the measurement of the droplet's volume is given by Equation (7.6). It results from the detection of the droplet edges u_{edges}, the limitation due to camera resolution $u_{\text{resolution}}$ and the calibration of the camera u_{pixel}. The latter results from the determination of the pixel size and the quantification of the optical distortions, as explained in details in Section 4.1.

$$u(V) = \sqrt{u_{\text{edges}}^2 + u_{\text{blur}}^2 + u_{\text{resolution}}^2 + u_{\text{pixel}}^2} \tag{7.6}$$

As explained in the previous subsection, the uncertainty of the droplet's volume due to edge detection is taken as the difference between the maximum and minimum volumes the droplet can have at a given instant. Assuming the volumes to follow a uniform statistical distribution, the uncertainty writes as:

$$u_{\text{edges}} = \frac{V_{max} - V_{min}}{2\sqrt{3}} \tag{7.7}$$

The component u_{blur} is caused by the motion blur, *i.e.* the change in the droplet's volume during exposure time. It is determined by multiplying the mean measured flow rate Q_V by exposure time t_{exposure} as follows (assuming a uniform statistical distribution during the exposure time):

$$u_{\text{blur}} = \frac{Q_V . t_{\text{exposure}}}{2\sqrt{3}} \tag{7.8}$$

The uncertainty due to camera resolution is written as a function of the pixel size p, considering a uniform distribution:

$$u_{\text{resolution}} = \frac{p}{2\sqrt{3}} \tag{7.9}$$

7.2.4 Discussion of the Pendant Drop Method

The choice of the capillary's inner diameter is very important in flow rate measurements using interface tracking method. As shown in Chapter 3, low flow rates require using small diameter capillaries in order to obtain measurable displacements. In the same way, at low flow rates, the change in the droplet's volume can be very small. Naturally, the smallest diameter the droplet can have is of the order of the capillary's diameter. This implies that larger capillary diameters lead to larger droplets, but smaller and in some cases non-measurable volume changes. The adequate capillary diameters were determined, depending on the flow rate, using an approximate calculation. For simplicity reasons, the droplet is assumed to be spherical. From our observations using different capillary tubes, the droplet's largest diameter for an intermediate volume is about 2 to 3 times the size of the tip. This is used to determine roughly the change in the droplet's diameter, at a given flow rate and for different capillary diameters. In Table 7.5 we give examples of the expected changes in the droplet's diameter at two different flow rates and for three different capillary diameters.

Table 7.5: Expected changes in the droplet's diameter at different flow rates and capillary diameters

Capillary outer diameter (μm)	**250**	**500**	**1000**
Droplet diameter at an intermediate volume (μm)	625	1250	2500
Droplet volume (nL)	128	1023	8181
Generated flow rate (nL/min)		20	
Droplet diameter after 30 s	641	1254	2501
Change in diameter (μm)	16	4	1
Change in diameter (%)	2,5	0,3	0,0
Generated flow rate (nL/min)		1000	
Droplet diameter after 30 s	1062	1427	2550
Change in diameter (μm)	437	177	50
Change in diameter (%)	70,0	14,2	2,0

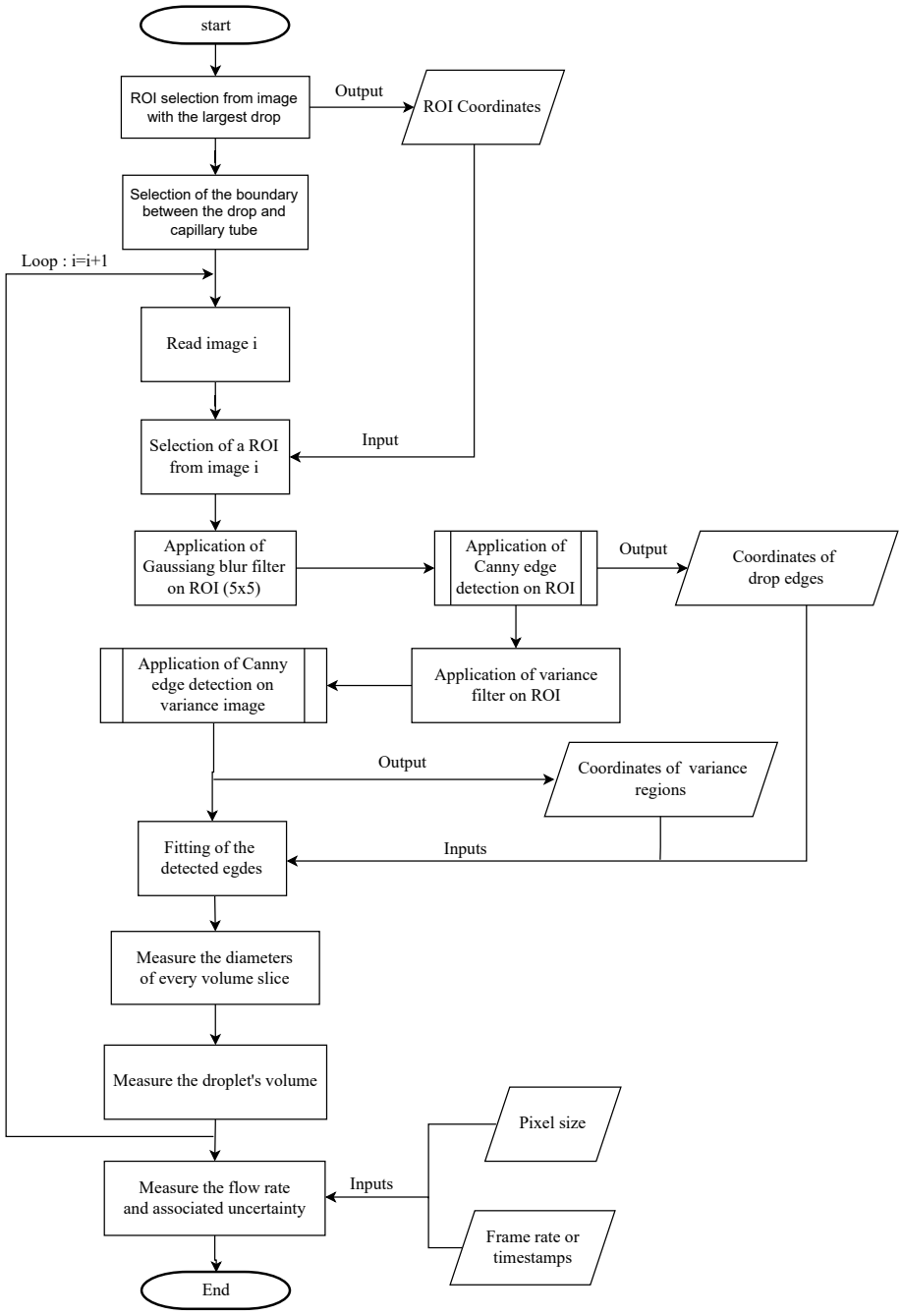

Figure 7.9: Image processing procedure for the measurement of the flow rate using the pendant drop method.

Conclusion

Before the MeDD II project, the metrological traceability of liquid flow meters and generators operating at nano-flows was not guaranteed, for lack of primary standards. As a result, drug delivery devices such as infusion and syringe pumps could not be calibrated in a traceable way, leading to an increased risk of dosing errors. These errors can endanger patients. The danger is particularly acute when it comes to drugs used in intensive care, which must be administered in small and controlled quantities.

Responding to this need for primary standards was the main objective of this thesis. This goal has been successfully achieved thanks to the development of our interface tracking system. This primary, non-intrusive system covers flow rates 1000 times lower than the limit reached by the previously-existing primary standard.

Our interface tracking system is based on a robust algorithm for measuring the displacements of the advancing meniscus. In order to ensure the traceability of the measured displacements, a procedure for camera and timestamps' calibration was established. The flow rates' traceability depends also on that of the capillary's inner diameter. The latter was ensured either by camera calibration, when end-on microscopy was used, or by calibration of the weighing scale, when gravimetry was used. Naturally, these two methods only give an average value of the inner diameter. However, the flow rate measured at a given position along the capillary, depends on the diameter at that position. In order to overcome this limitation and ensure a better measurement accuracy of flow fluctuations, we developed a new method based on confocal fluorescence microscopy. The traceability of this non-destructive method was ensured by the calibration of the confocal microscope using transfer standards. Inner diameters of 200 μm and 500 μm have been measured with a relative expanded uncertainty lower than 4 % (k=2).

Our measurement system enables flow rate measurements down to 5 nL/min, with at least one flow rate value per second. The ability to measure flow rate fluctuations was exploited in the calibration of a *Treprostinil* infusion pump. This calibration represents a direct application of our system and the first nano-flow calibration service proposed by CETIAT.

The external validation of our system was achieved by an interlaboratory comparison which gathered laboratories from nine different countries in Europe. Through the comparison, the metrological capabilities of our system have been proven in a flow rate range of 10 nL/min to 1500 nL/min, with relative expanded uncertainties (k=2) of 12 % to 0.15 %, respectively. These measurement and calibration capabilities (CMCs) were peer-reviewed and validated by CIPM Mutual Recognition Arrangement approval process, and are publicly available in BIPM's key comparison database (KCDB) [58]. The validation of the CMCs represents international recognition of our system as the French national primary standard for liquid nano-flow rates.

Despite the validity of our method, certain improvements could be made. As was explained in the thesis, the measurements were carried out only when the interface was in the camera's field of view. As a result, the measurement time was limited, especially for flow

rates of the order of 1 µL/min. In order to solve this problem, translation stages were used to move the camera with the interface. The flow rate was then determined from the interface displacements taking into account the camera's displacements. However, a calibration of the translation stage revealed large discrepancies between the nominal steps and the distances traveled in the image. Besides, when the capillary was not perfectly perpendicular to the camera's axis, the interface always got out of focus, after a given distance. Nevertheless, we believe that using higher-resolution translation stages and mounts that ensure a better alignment, can help overcome this limitation.

Flow rate fluctuations produced by the flow generator represent one of the largest uncertainty components of our calibration system. In order to ensure more stable flow rates and better uncertainties, we believe that the syringe pump should be replaced by a pressure controller with a valve integrated into the system. The valve will serve to increase the hydraulic resistance, allowing low flow rates to be generated by applying high thus, stable pressures.

As a perspective, we have shown that the interface tracking system can be used in a different configuration in which the flow rate is determined from the increasing volume of a pendant drop. Despite the development of software associated with this method and the quantification of its uncertainty sources, it still needs to be validated. This validation will be carried out in the future through interlaboratory comparisons.

Appendix A

Edge Detection

Canny Edge Detection

Canny Edge Detection is a popular edge detection method that was developed by John F. Canny in 1986 [30]. As part of the image processing program used for camera calibration, edges were detected using the function cv2.Canny(image,threshold1,threshold2) from Python's OpenCV library [102]. This function took as input parameters the image to be processed and the two threshold values, threshold1 and threshold2, that were obtained by Otsu's method [112]. The cv2.canny algorithm consists of the following steps:

1. Image smoothing: Reduce image noise by applying a Gaussian blur filter, *i.e.* by convolving a Gaussian kernel of a given size with the image. Fig. A.1 shows examples of Gaussian kernels with different sizes.

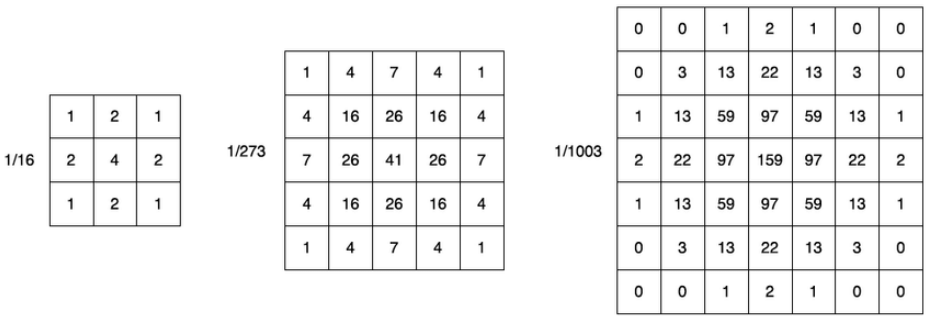

Figure A.1: Gaussian kernels with sizes 3x3, 5x5 and 7x7

2. Finding intensity gradient of the image: Apply a Sobel filter on the blurred image in both horizontal and vertical directions to get first derivative in horizontal direction (Gx) and vertical direction (Gy). The Sobel filter [143] consists in convolving the original image with the Sobel kernels G_x and G_y of size 3x3 to calculate approximations of the derivatives in the horizontal and vertical directions (Fig. A.2).

-1	0	+1
-2	0	+2
-1	0	+1

Gx

+1	+2	+1
0	0	0
-1	-2	-1

Gy

Figure A.2: Sobel kernels used to calculate image gradients along x (left) and y (right)

From the previously calculated gradients, the edge gradient G and direction for each pixel can be found as follows:

$$G = \sqrt{G_x^2 + G_y^2} \tag{A.1}$$

$$\Theta = tan^{-1}\left(\frac{G_x}{G_y}\right) \tag{A.2}$$

The direction of the gradient is always perpendicular to the edge. The angle Θ is rounded in a way that only 4 directions are possible: the vertical, horizontal and the two diagonal ones.

3. Remove non-maximum pixels: Given the gradient magnitudes and the associated directions, all the pixels that may not constitute an edge are removed. At every pixel position the gradient's magnitude is checked if it is a local maximum relative to the neighboring pixels in the direction of gradient, as explained in Fig. A.3.

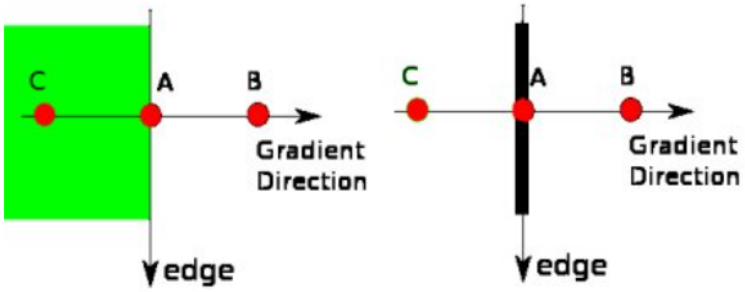

Figure A.3: Schematic illustration showing the determination of local gradient maxima as part of Canny edge detection method [102].

Pixel A is on the vertical edge to which the gradient direction is normal. Pixels B and C are in the gradient direction. The gradient at the position A is compared to the one at B and C to see if it forms a local maximum. If so, the value is preserved for the next step, otherwise, it is suppressed, *i.e.* put to 0. This results in a binary image with thin edges.

4. Hysteresis Thresholding: In this part is decided which edges are true edges and which are not. Two threshold values, minVal and maxVal, are defined. The edges with gradient magnitudes greater than maxVal are sure to be true edges and those with gradients less than minVal are sure to be non-edges, so suppressed. The pixels with

gradients ranging between the two thresholds are classified true edges or non-edges based on their connectivity. Only the pixels connected to "sure-edge's" ones are kept and considered to be part of true edge as explained below (Fig. A.4).

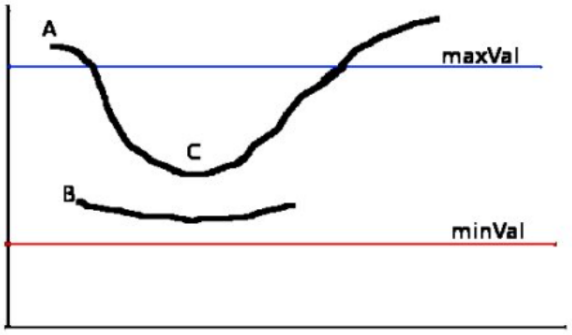

Figure A.4: Image gradient values' thresholding for Canny edge detection [102].

Pixel A is considered as true edge since its gradient value is greater than maxVal. Pixel C, with a gradient value above minVal but below maxVal, is also considered as a valid edge since it is connected to the true edge A. Pixel B, however, although being above minVal, *i.e.* in same region as pixel C, is discarded due to the fact that it is not connected to any "sure-edge". The threshold values minVal and maxVal are then, very important to detect the edges correctly. In this step, the small pixels noises are also removed considering that edges are long lines.

Otsu's method This method is used to perform automatic image thresholding [112]. The corresponding algorithm returns a single threshold value that separates image pixels into foreground and background classes. The threshold is determined by minimizing the weighted intra-class intensity variance $\sigma_w^2(t)$, or equivalently, by maximizing inter-class variance $\sigma_b^2(t)$. The weighted variance is expressed as:

$$\sigma_w^2(t) = w_0(t)\sigma_0^2(t) + w_0(t)\sigma_0^2(t) \tag{A.3}$$

where $w_0(t)$, $w_1(t)$ are the probabilities of the two classes separated by a threshold t, which value is within the range of 0 to 255, and $\sigma_0^2(t)$, $\sigma_1^2(t)$ are variances of these two classes. The class probability $w_{0,1}(t)$ is computed from the L bins of the pixel intensities histogram as follows:

$$w_0(t) = \sum_{i=0}^{t-1} p(i) \tag{A.4}$$

$$w_1(t) = \sum_{i=t}^{L} p(i) \tag{A.5}$$

Where $p(i)$ is the occurence probability of a pixel intensity i and is given by:

$$p(i) = \frac{n_i}{n}. \tag{A.6}$$

n being the total number of pixels in the image and n_i the number of pixels with intensity i.

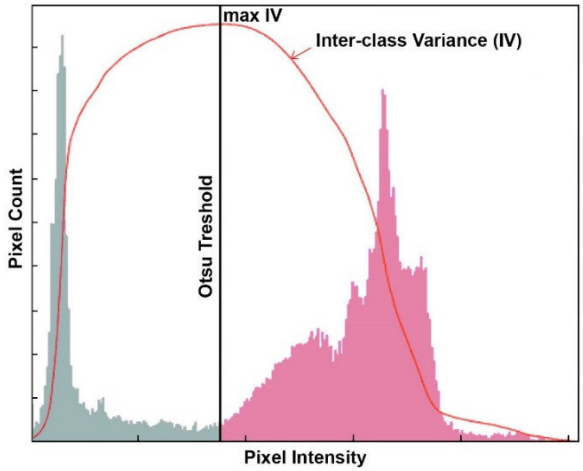

Figure A.5: Histogram of pixel intensities and the associated inter-class variance from which Otsu's threshold is determined [151].

Minimizing the intra-class variance is equivalent to maximizing inter-class variance $\sigma_b^2(t)$ which is written, in terms of the class probabilities $w_{0,1}(t)$, class intensity means $\mu_{0,1}(t)$ and the general intensity mean μ_T, as: :

$$\sigma_b^2(t) = \sigma_T^2 - \sigma_w^2(t) = w_0(t)(\mu_0(t) - \mu_T)^2 + w_1(t)(\mu_1(t) - \mu_T)^2 = w_0(t)w_1(t)[\mu_0(t) - \mu_1(t)]^2 \tag{A.7}$$

where:

$$\mu_0(t) = \frac{\sum_{i=0}^{t-1} ip(i)}{w_0(t)} \tag{A.8}$$

$$\mu_0(t) = \frac{\sum_{i=t}^{L-1} ip(i)}{w_1(t)} \tag{A.9}$$

$$\mu_T = \sum_{i=0}^{L-1} ip(i) \tag{A.10}$$

The algorithm for this method can be summarized in the following steps:

1. Compute the probability for each pixel intensity from the image's histogram.
2. Compute the initial class probabilities $w_{0,1}(0)$, class means $\mu_{0,1}(0)$ and the intra-class variance $\sigma_b^2(0)$ for the threshold $t = 0$.
3. For each threshold t in the range of 1 to 255, update the values of $w_{0,1}(t)$ and $\mu_{0,1}(t)$, and compute the new $\sigma_b^2(t)$.
4. The desired threshold t is the one that maximizes $\sigma_b^2(t)$.

The threshold values for Canny edge detection method (Section 4.1) were determined using the function cv2.threshold(src,thresh,maxval,type from OpenCV library, to which we pass as inputs the gradient image, the minimum and maximum pixel intensities in the image and the thresholding type cv2.THRESH_BINARY+cv2.THRESH_OTSU) that is based on Otsu's method. This function return one threshold value that we take as threshold2 in cv2.Canny(image,threshold1, threshold2), *i.e.* the function used to detect edges using Canny method. The value of threshold1 is taken as half the threshold computed by Otsu's method.

Standard deviation filter

The standard deviation filter applied on images in Section 4.1 was obtained by passing to the function ndimage.generic_filter(input, function, size=n) the image to be processed as input, the Numpy function np.std as function and the size of the window of pixels in which the standard deviation is calculated as n. This generic filter, from the Python library SciPy [136], iterates over all the pixel positions in the image and calls the function at each position. The standard deviation of the pixel intensities I inside a window of size w, *i.e.* with a total number w^2 elements is written as:

$$\sigma = \sqrt{\frac{\sum_{i=1}^{w^2} \left(I_i - \bar{I}\right)^2}{w^2}} \tag{A.11}$$

where $\bar{I}$ is the mean pixel intensity inside the window and is given by:

$$\bar{I} = \frac{\sum_{i=1}^{w^2} I_i}{w^2} \tag{A.12}$$

Normal test

In order to test the distribution of the pixel sizes determined from camera calibration, we used D'Agostino-Pearson's method that combines skew and kurtosis to produce an omnibus test of normality [46, 45]. The function used is scipy.stats.normaltest(a, axis=0, nan_policy='propagate') from SciPy [137] which tests the null hypothesis that a sample comes from a normal distribution.

Appendix B

Results of the Interlaboratory Comparison

In this appendix we give the results of the interlaboratory comparison obtained by the participant laboratories. These results include the measurement errors and the associated uncertainties obtained by the calibration of two flow meters (Bronkhorst and Sensirion) and a syringe pump (Cetoni) (Tables B.1, B.2 and B.3). The chi-squared values and degrees of equivalence that served for the validation or exclusion of the participant laboratories are given in Tables 6.6, 6.8 and 6.7.

Table B.1: measurement errors and the associated uncertainties, obtained by the calibration of the mass flow meter Bronkhorst L01-20D.

Target Q_V (nL/min)		**1500**	**1000**	**500**	**100**	**70**	**50**	**20**
CETIAT	Error (%)	-0.22	-0.53	-0.99	-4.65	-3.33	-5.20	-7.29
	u(K=2) (%)	0.15	0.61	0.60	1.03	2.91	1.18	9.89
IPQ	Error (%)	-3.30	-2.40	-2.60	-4.60	-2.90	-2.60	-2.70
	u(K=2) (%)	2.70	2.20	3.10	2.10	2.00	2.50	2.90
METAS	Error (%)	-0.26	-0.65	-1.60	-4.69	-5.28	-5.61	-5.63
	u(K=2) (%)	0.48	0.51	0.58	0.71	0.80	0.86	1.00
RISE	Error (%)	-0.38	-1.40	-1.91	-3.44	-4.95	-5.16	-5.30
	u(K=2) (%)	0.50	0.50	0.50	1.00	1.50	2.00	2.50
DTI	Error (%)	-0.09	-0.38	-0.59	-3.27	-5.08	⊠	⊠
	u(K=2) (%)	0.65	0.77	1.29	6.34	8.54	⊠	⊠
HS	Error (%)	-1.25	-0.30	-2.08	-1.20	-5.81	⊠	⊠
	u(K=2) (%)	5.22	10.12	11.31	8.88	14.57	⊠	⊠
BHT	Error (%)	-0.62	-1.08	-2.13	-5.65	-6.41	-6.83	-8.49
	u(K=2) (%)	0.32	0.34	0.60	1.67	2.40	3.32	8.05
THL	Error (%)	-0.28	-0.91	-2.75	1.96	5.58	6.67	34.52
	u(K=2) (%)	1.02	0.78	1.09	4.63	2.91	4.82	9.23
Uos/NEL	Error (%)	⊠	⊠	⊠	⊠	-6.61	-10.09	7.94
	u(K=2) (%)	⊠	⊠	⊠	⊠	11.58	12.05	15.09

Table B.2: measurement errors and the associated uncertainties, obtained by the calibration of the mass flow meter Sensirion SLG64-0075.

Target Q_V (nL/min)		**1500**	**1000**	**500**	**100**	**70**	**50**	**20**
CETIAT	Error (%)	0.67	0.07	1.79	2.61	7.29	1.91	-14.03
	u(K=2) (%)	1.29	1.06	2.01	4.82	0.92	9.84	27.52
IPQ	Error (%)	0.85	2.53	3.58	5.06	5.03	4.78	4.27
	u(K=2) (%)	2.07	2.07	2.23	2.70	2.78	3.14	5.18
METAS	Error (%)	1.74	1.69	1.63	2.39	2.87	2.44	0.91
	u(K=2) (%)	0.38	0.40	0.48	0.60	0.69	0.75	0.92
RISE	Error (%)	0.90	0.99	0.87	1.17	1.25	1.30	1.38
	u(K=2) (%)	0.50	0.50	0.50	1.00	1.50	2.00	2.50
DTI	Error (%)	1.26	1.31	1.24	1.59	2.33	1.31	-0.34
	u(K=2) (%)	0.51	0.51	0.54	1.25	1.61	2.14	5.89
HS	Error (%)	⊠	⊠	1.52	0.71	4.38	⊠	⊠
	u(K=2) (%)	⊠	⊠	10.19	24.21	16.57	⊠	⊠
BHT	Error (%)	2.10	1.92	1.88	3.14	2.19	2.80	2.11
	u(K=2) (%)	0.28	0.42	0.77	4.01	4.75	7.65	18.59
THL	Error (%)	1.08	0.91	-0.08	-0.01	-4.67	-6.97	-5.44
	u(K=2) (%)	1.00	0.84	0.85	10.55	2.54	2.48	25.89
Uos/NEL	Error (%)	⊠	⊠	⊠	6.95	0.48	-6.42	12.38
	u(K=2) (%)	⊠	⊠	⊠	5.51	7.60	7.50	20.63

Table B.3: measurement errors and the associated uncertainties, obtained by the calibration of the Cetoni syring pump.

Target Q_V (nL/min)		**100**	**50**	**20**	**10**	**5**
CETIAT	Error (%)	-0.53	-0.09	-1.21	-7.35	28.48
	u(K=2) (%)	0.70	0.64	14.21	11.35	51.73
IPQ	Error (%)	0.02	0.01	0.00	0.04	0.15
	u(K=2) (%)	1.21	1.21	1.22	2.65	2.69
METAS	Error (%)	-1.29	-1.51	-1.11	⊠	⊠
	u(K=2) (%)	0.72	0.95	1.04	⊠	⊠
RISE	Error (%)	-1.52	-1.88	-0.95	-1.53	-1.25
	u(K=2) (%)	1.48	1.86	2.73	3.86	5.26
DTI	Error (%)	1.30	1.62	3.03	⊠	⊠
	u(K=2) (%)	1.66	1.85	6.35	⊠	⊠
HS	Error (%)	⊠	⊠	⊠	⊠	⊠
	u(K=2) (%)	⊠	⊠	⊠	⊠	⊠
BHT	Error (%)	-1.37	-0.41	2.52	-5.24	-5.57
	u(K=2) (%)	2.9	5.6	13.9	14.8	31.3
THL	Error (%)	16.54	49.83	16.24	-2.94	4.11
	u(K=2) (%)	3.52	20.42	15.38	5.47	12.53
Uos/NEL	Error (%)	⊠	⊠	⊠	⊠	⊠
	u(K=2) (%)	⊠	⊠	⊠	⊠	⊠

Table B.4: Chi-squared values and degrees of equivalence obtained by each laboratory, for the calibration Bronkhorst flow meter.

Flow rate (nL/min)	**Population size n-1**	**Observed chi-squared** χ^2_{obs}	**Calculated threshold** $\chi^2(n-1)$	**Weighted mean error REF2**	**Weighted uncertainty UREF2**
1500	7	3.99	14.07	-0.29	0.12
1000	7	2.34	14.07	-0.94	0.21
500	7	3.50	14.07	-1.71	0.27
100	7	12.31	14.07	-4.46	0.47
70	7	4.29	14.07	-4.98	0.62
50	5	5.68	11.07	-5.31	0.62
20	4	4.07	9.49	-5.32	0.87

Table B.5: Chi-squared values and degrees of equivalence, obtained by each laboratory for the calibration of Sensirion flow meter.

Flow rate (nL/min)	**Population size n-1**	**Observed chi-squared** χ^2_{obs}	**Calculated threshold** $\chi^2(n-1)$	**Weighted mean error REF2**	**Weighted uncertainty UREF2**
1500	6	3.66	12.59	1.67	0.18
1000	6	3.84	12.59	1.45	0.21
500	7	5.79	14.09	1.25	0.25
100	8	9.45	15.51	2.14	0.46
70	6	4.29	12.59	2.64	0.57
50	5	3.00	11.07	2.25	0.65
20	6	10.33	12.59	1.04	0.84

Table B.6: Chi-squared values and degrees of equivalence obtained by each laboratory for the calibration of Cetoni syringe pump.

Flow rate (nL/min)	**Population size n-1**	**Observed chi-squared** χ^2_{obs}	**Calculated threshold** $\chi^2(n-1)$	**Weighted mean error REF2**	**Weighted uncertainty UREF2**
100	5	3.97	11.07	-0.71	0.42
50	5	4.95	11.07	-0.41	0.45
20	5	3.40	11.07	-0.61	0.75
10	4	5.99	9.49	-1.09	1.98
5	3	2.64	7.81	-0.03	2.35

Bibliography

[1] *2021 Product Performance Report: Performance Report Neuromodulation*. Tech. rep. Medtronic, 2022.

[2] Ronald J Adrian and Jerry Westerweel. *Particle image velocimetry*. 30. Cambridge university press, 2011.

[3] M Ahrens et al. "Design and uncertainty assessment of a setup for calibration of microfluidic devices down to 5 nL min- 1". In: *Measurement Science and Technology* 25.1 (2013), p. 015301.

[4] Martin Ahrens et al. "An experimental setup for traceable measurement and calibration of liquid flow rates down to 5 nl/min". In: *Biomedical Engineering/Biomedizinische Technik* 60.4 (2015), pp. 337–345.

[5] Ji-Yong An et al. "Quantitative analysis of artificial sweeteners by capillary electrophoresis with a dual-capillary design of molecularly imprinted solid-phase extractor". In: *Bulletin of the Korean Chemical Society* 39.11 (2018), pp. 1315–1319.

[6] Taras Andrukh et al. "Meniscus formation in a capillary and the role of contact line friction". In: *Soft Matter* 10.4 (2014), pp. 609–615.

[7] Rutherford Aris. "On the dispersion of a solute in a fluid flowing through a tube". In: *Proceedings of the Royal Society of London. Series A. Mathematical and Physical Sciences* 235.1200 (1956), pp. 67–77.

[8] Ryan T Armstrong and Steffen Berg. "Interfacial velocities and capillary pressure gradients during Haines jumps". In: *Physical Review E* 88.4 (2013), p. 043010.

[9] Roger C Baker. *Flow measurement handbook*. Vol. 99. Cambridge University Press Cambridge, 2000.

[10] Roger C Baker. *Flow measurement handbook: industrial designs, operating principles, performance, and applications*. Cambridge University Press, 2016.

[11] Carmen Bambach. *Les plus beaux croquis de Léonard de Vinci*. URL: `https://www.nationalgeographic.fr/photography/2019/04/les-plus-beaux-croquis-de-leonard-de-vinci?image=carmen-bambach-leonardo-q-a-heart-anatomy`.

[12] Robyn J Barst et al. "Long-term outcome in pulmonary arterial hypertension patients treated with subcutaneous treprostinil". In: *European Respiratory Journal* 28.6 (2006), pp. 1195–1203.

[13] E Batista et al. "New EMPIR project–Metrology for drug delivery". In: *Flow Measurement and Instrumentation* 72 (2020), p. 101716.

[14] Elsa Batista et al. "Development of an experimental setup for micro flow measurement using the front tracking method". In: *Measurement: Sensors* 18 (2021), p. 100152.

[15] Elsa Batista et al. "Development of an experimental setup for microflow measurement using interferometry". In: *Flow Measurement and Instrumentation* 75 (2020), p. 101789.

[16] Elsa Batista et al. "Experimental testing for metrological traceability and accuracy of liquid microflows and microfluidics". In: *Flow Measurement and Instrumentation* 71 (2020), p. 101691.

[17] WE Baucum. *Evaluation of a Coriolis mass flow meter for pulverized coal flows*. Tech. rep. Tennessee Univ., Tullahoma (USA). Space Inst., 1979.

[18] K Beissner. "On a measure of consistency in comparison measurements". In: *Metrologia* 39.1 (2002), p. 59.

[19] Michael S Bello, Roberta Rezzonico, and Pier Giorgio Righetti. "Use of Taylor-Aris dispersion for measurement of a solute diffusion coefficient in thin capillaries". In: *Science* 266.5186 (1994), pp. 773–776.

[20] Daniel Bernoulli. "Hydrodynamica". In: *Dulsecker. Consultable en ligne http://imgbase-scd-ulp. u-strasbg. fr/displayimage. php* 1738 (1738).

[21] Joseph D Berry et al. "Measurement of surface and interfacial tension using pendant drop tensiometry". In: *Journal of colloid and interface science* 454 (2015), pp. 226–237.

[22] IEC BIPM et al. "International vocabulary of metrology—Basic and general concepts and associated terms (VIM), JCGM 200: 2012". In: *This 3rd edition is also published as ISO Guide* 99 (2012).

[23] Hugo Bissig, Martin Tschannen, and Marc de Huu. "Micro-flow facility for traceability in steady and pulsating flow". In: *Flow Measurement and Instrumentation* 44 (2015), pp. 34–42.

[24] Hugo Bissig et al. *Final Publishable JRP Report: HLT07 MeDD*. Tech. rep. 2016.

[25] Hugo Bissig et al. "Primary standards for measuring flow rates from 100 nl/min to 1 ml/min–gravimetric principle". In: *Biomedical Engineering/Biomedizinische Technik* 60.4 (2015), pp. 301–316.

[26] Walt Boyes. *Instrumentation reference book*. Butterworth-Heinemann, 2009.

[27] Glenn Brown. "Henry Darcy's Perfection of the Pitot Tube". In: (June 2003), pp. 14–23. DOI: 10.1061/40683(2003)3.

[28] Eric L Bruner. "Surfaces Matter". In: *MRS Online Proceedings Library (OPL)* 1209 (2009).

[29] Robert Bud and Deborah Warner. *Instruments of science: An historical encyclopedia*. Routledge, 1997.

[30] John Canny. "A computational approach to edge detection". In: *IEEE Transactions on pattern analysis and machine intelligence* 6 (1986), pp. 679–698.

[31] Fritjof Capra. *Learning from Leonardo: Decoding the notebooks of a genius*. Berrett-Koehler Publishers, 2013.

[32] Furio Cascetta. "Short history of the flowmetering". In: *Isa Transactions* 34.3 (1995), pp. 229–243.

[33] ABD Cassie. "Contact angles". In: *Discussions of the Faraday society* 3 (1948), pp. 11–16.

[34] ABD Cassie and SJToTFS Baxter. "Wettability of porous surfaces". In: *Transactions of the Faraday society* 40 (1944), pp. 546–551.

[35] Benedetto Castelli. *Delia misura dell'acque correnti*. Francesco Caualli, 1639.

[36] Haijin Chen et al. “Ultrasensitive gas refractometer using capillary-based Mach–Zehnder interferometer”. In: *Sensors* 20.4 (2020), p. 1191.

[37] JP Chervet, M Ursem, and JP Salzmann. “Instrumental requirements for nanoscale liquid chromatography”. In: *Analytical chemistry* 68.9 (1996), pp. 1507–1512.

[38] Kyung-Hyun Choi et al. *Electrohydrodynamic inkjet-micro pattern fabrication for printed electronics applications*. INTECH Open Access Publisher, 2011.

[39] CT Collet, John C Hughes, and Francis C Morey. “Measurement of the internal diameters of metallic capillary tubes”. In: *J. Res. Nat. Bur. Stand* 45 (1950), pp. 283–288.

[40] Robert T Collins, Michael T Harris, and Osman A Basaran. “Breakup of electrified jets”. In: *Journal of Fluid Mechanics* 588 (2007), pp. 75–129.

[41] Gaspard Gustave Coriolis. *Mémoire sur les équations du mouvement relatif des systèmes de corps*. Bachelier, 1835.

[42] Alessandro Cosci et al. “Confocal reflectance microscopy for determination of microbubble resonator thickness”. In: *Optics Express* 23.13 (2015), pp. 16693–16701.

[43] Ana Letıcia Rodrigues Costa, Andresa Gomes, and Rosiane Lopes Cunha. “Studies of droplets formation regime and actual flow rate of liquid-liquid flows in flow-focusing microfluidic devices”. In: *Experimental Thermal and Fluid Science* 85 (2017), pp. 167–175.

[44] Christopher T Culbertson and James W Jorgenson. “Flow counterbalanced capillary electrophoresis”. In: *Analytical chemistry* 66.7 (1994), pp. 955–962.

[45] Ralph d’agostino and Egon S Pearson. “Tests for departure from normality. Empirical results for the distributions of b 2 and b”. In: *Biometrika* 60.3 (1973), pp. 613–622.

[46] Ralph B d’Agostino. “An omnibus test of normality for moderate and large size samples”. In: *Biometrika* 58.2 (1971), pp. 341–348.

[47] Giovanni D’Orazio, Silvia Rocchi, and Salvatore Fanali. “Nano-liquid chromatography coupled with mass spectrometry: Separation of sulfonamides employing non-porous core–shell particles”. In: *Journal of Chromatography A* 1255 (2012), pp. 277–285.

[48] Pierre-Gilles De Gennes, Françoise Brochard-Wyart, David Quéré, et al. *Capillarity and wetting phenomena: drops, bubbles, pearls, waves*. Vol. 315. Springer, 2004.

[49] Mario Di Fidio and Claudio Gandolfi. “Flow velocity measurement in Italy between Renaissance and Risorgimento”. In: *Journal of Hydraulic Research* 49.5 (2011), pp. 578–585.

[50] Toan Dinh, Nam-Trung Nguyen, and Dzung Viet Dao. *Thermoelectrical Effect in SiC for High-Temperature MEMS Sensors*. Springer, 2018.

[51] Daniel M Dohmeier and James W Jorgenson. “Evaluation of etched borosilicate glass capillary columns in reversed phase open tubular liquid chromatography”. In: *Journal of Microcolumn Separations* 3.4 (1991), pp. 311–317.

[52] Chiara Fanali et al. “Nano-liquid chromatographic separations”. In: *Handbook of Advanced Chromatography/Mass Spectrometry Techniques*. Elsevier, 2017, pp. 309–363.

[53] Michael Faraday. “VI. The Bakerian lecture.-Experimental researches in electricity.-Second series”. In: *Philosophical Transactions of the Royal Society of London* 122 (1832), pp. 163–194.

[54] Caio Fernandes et al. “Measuring inner diameter of capillary tubes”. In: *Journal of Physics: Conference Series*. Vol. 1826. 1. IOP Publishing. 2021, p. 012018.

[55] Willard J Fisher. "The Calibration of Capillary Tubes". In: *Physical Review (Series I)* 23.3 (1906), p. 249.

[56] Ogheard Florestan, Margot Sandy, and Savary Julien. "Recent improvements of the French liquid micro-flow reference facility". In: *Measurement Science and Technology* 29.2 (2018), p. 024007.

[57] Jacob Fraden. *Handbook of modern sensors: physics, designs, and applications*. 1998.

[58] *France, LNE-CETIAT (Centre Technique des Industries Aérauliques et Thermiques)*. URL: `https://www.bipm.org/kcdb/cmc/quick-search?keywords=Optical+Interface+tracking`.

[59] Arjan Fraters et al. "Meniscus oscillations driven by flow focusing lead to bubble pinch-off and entrainment in a piezoacoustic inkjet nozzle". In: *Physical review applied* 16.4 (2021), p. 044052.

[60] Mariana Roberto Gama, Carol H Collins, and Carla BG Bottoli. "Nano-liquid chromatography in pharmaceutical and biomedical research". In: *Journal of Chromatographic Science* 51.7 (2013), pp. 694–703.

[61] A Mohamad Ghazi and Stephen Shuttleworth. "Trace element determination of single fluid inclusions by laser ablation ICP-MS: applications for halites from sedimentary basins". In: *Analyst* 125.1 (2000), pp. 205–210.

[62] Josiah Willard Gibbs. *The scientific papers of JW Gibbs*. Dover, 1961.

[63] Leah A Godwin et al. "Passively operated microfluidic device for stimulation and secretion sampling of single pancreatic islets". In: *Analytical chemistry* 83.18 (2011), pp. 7166–7172.

[64] Mira T Guo et al. "Droplet microfluidics for high-throughput biological assays". In: *Lab on a Chip* 12.12 (2012), pp. 2146–2155.

[65] FK Hansen and G Rødsrud. "Surface tension by pendant drop: I. A fast standard instrument using computer image analysis". In: *Journal of colloid and interface science* 141.1 (1991), pp. 1–9.

[66] HappyApple. *Nilometer Wikipedia, The Free Encyclopedia*. 2006. URL: `https://en.wikipedia.org/wiki/Venturi_effect`.

[67] William D Harkins and FE Brown. "The determination of surface tension (free surface energy), and the weight of falling drops: the surface tension of water and benzene by the capillary height method." In: *Journal of the American Chemical Society* 41.4 (1919), pp. 499–524.

[68] Clemens Herschel. "The Venturi Water Meter: An Instrument Making use of a New Method of Gauging Water, Applicable to the Cases of Very Large Tubes, and of a Small Value Only, of the Liquid to be Gauged". In: *Transactions of the American Society of Civil Engineers* 17.2 (1887), pp. 228–258.

[69] MB Hisham et al. "Template matching using sum of squared difference and normalized cross correlation". In: *2015 IEEE student conference on research and development (SCOReD)*. IEEE. 2015, pp. 100–104.

[70] Nelly Hobeika et al. "Help from a hindrance: Using astigmatism in round capillaries to study contact angles and wetting layers". In: *Langmuir* 33.21 (2017), pp. 5179–5187.

[71] Yiping Hong and Fujun Wang. "Flow rate effect on droplet control in a co-flowing microfluidic device". In: *Microfluidics and Nanofluidics* 3.3 (2007), pp. 341–346.

[72] *Hot Wire Anemometer*. URL: https://circuitglobe.com/hot-wire-anemometer.html.

[73] *Hydrophobic Coating Technology*. URL: https://www.aculon.com/hydrophobic/.

[74] *Introduction to Confocal Microscopy*. URL: https://www.olympus-lifescience.com/en/microscope-resource/primer/techniques/confocal/confocalintro/.

[75] *Mesure de débit des liquides dans les conduites fermées – Méthode par pesée*. Standard. Geneva: International Organization for Standardization, Mar. 1991.

[76] *Conformity assessment — General requirements for proficiency testing*. Standard. Geneva: International Organization for Standardization, Mar. 2010.

[77] Loıc Jacot-Descombes et al. "Fabrication of epoxy spherical microstructures by controlled drop-on-demand inkjet printing". In: *Journal of Micromechanics and Microengineering* 22.7 (2012), p. 074012.

[78] Gareth James et al. *An introduction to statistical learning*. Vol. 112. Springer, 2013.

[79] JCGM JCGM. "100: 2008 (GUM 1995 with minor corrections) Evaluation of measurement data-Guide to the expression of uncertainty in measurement". In: *Joint Committee for Guides in Metrology* 19 (2008).

[80] Ken-ichiro Kamei et al. "Integrated heart/cancer on a chip to reproduce the side effects of anti-cancer drugs in vitro". In: *RSC advances* 7.58 (2017), pp. 36777–36786.

[81] Louis Vessot King. "XII. On the convection of heat from small cylinders in a stream of fluid: Determination of the convection constants of small platinum wires with applications to hot-wire anemometry". In: *Philosophical transactions of the royal society of London. series A, containing papers of a mathematical or physical character* 214.509-522 (1914), pp. 373–432.

[82] Laurance A Knecht, Edward J Guthrie, and James W Jorgenson. "On-column electrochemical detector with a single graphite fiber electrode for open-tubular liquid chromatography". In: *Analytical Chemistry* 56.3 (1984), pp. 479–482.

[83] Jörg Kohr and Heinz Engelhardt. "Characterization of quartz capillaries for capillary electrophoresis". In: *Journal of Chromatography A* 652.2 (1993), pp. 309–316.

[84] Aristotle G Koutsiaris, Dimitris S Mathioulakis, and Sokrates Tsangaris. "Microscope PIV for velocity-field measurement of particle suspensions flowing inside glass capillaries". In: *Measurement Science and Technology* 10.11 (1999), p. 1037.

[85] Jonathan TW Kuo, Lawrence Yu, and Ellis Meng. "Micromachined thermal flow sensors—A review". In: *Micromachines* 3.3 (2012), pp. 550–573.

[86] Soonmu Kwon et al. "Precise measurement of inner diameter of mono-capillary optic using X-ray imaging technique". In: *Journal of X-ray Science and Technology* 26.2 (2018), pp. 263–272.

[87] Le plombier du désert. *Histoire du métier de plombier Wikipedia, The Free Encyclopedia*. 2016. URL: https://fr.wikipedia.org/wiki/Histoire_du_m%5C%C3%5C%A9tier_de_plombier.

[88] Philip J Lee, Paul J Hung, and Luke P Lee. "An artificial liver sinusoid with a microfluidic endothelial-like barrier for primary hepatocyte culture". In: *Biotechnology and bioengineering* 97.5 (2007), pp. 1340–1346.

[89] Yung-Sheng Lin et al. "A microfluidic chip using phenol formaldehyde resin for uniform-sized polycaprolactone and chitosan microparticle generation". In: *Molecules* 18.6 (2013), pp. 6521–6531.

[90] *Linear stages*. URL: https://www.zaber.com/products/linear-stages.

[91] MS Longuet-Higgins and GER Deacon. "The electrical and magnetic effects of tidal streams". In: *Geophysical Journal International* 5 (1949), pp. 285–307.

[92] Awwa Meter Manual. "Chapter I—Early History of Water Measurement and the Development of Meters". In: *Journal (American Water Works Association)* 51.6 (1959), pp. 791–799.

[93] Benjamin Marie et al. "Novel proteins from the calcifying shell matrix of the Pacific oyster Crassostrea gigas". In: *Marine biotechnology* 13.6 (2011), pp. 1159–1168.

[94] Edme Mariotte and Philippe de La Hire. *Traité du mouvement des eaux et des autres corps fluides*. Chez Claude-Jombert, 1718.

[95] *Medfusion®4000 Wireless Syringe Infusion Pump and PharmGuard®Infusion Management Software - US Brochure*. URL: https://www.smiths-medical.com/fr-fr/resources/medfusion-4000-wireless-syringe-infusion-pump-and-pharmguard---us-brochure.

[96] Matthias Mehling and Savaş Tay. "Microfluidic cell culture". In: *Current opinion in Biotechnology* 25 (2014), pp. 95–102.

[97] Allan A Mills. "Newton's water clocks and the fluid mechanics of clepsydrae". In: *Notes and Records of the Royal Society of London* 37.1 (1982), pp. 35–61.

[98] *MiniMed 630G System User Guide*. English. Medtronic. March 20, 2018.

[99] K Mishima and T Hibiki. "Some characteristics of air-water two-phase flow in small diameter vertical tubes". In: *International journal of multiphase flow* 22.4 (1996), pp. 703–712.

[100] Louis Mitchell. "Meters for Measuring Cold Water". In: *Journal (American Water Works Association)* 25.7 (1933), pp. 956–964.

[101] Nhlakanipho Mkhize and Harish Bhaskaran. "Electrohydrodynamic jet printing: Introductory concepts and considerations". In: *Small Science* 2.2 (2022), p. 2100073.

[102] Alexander Mordvintsev and K Abid. "Opencv-python tutorials documentation". In: *Obtenido de https://media. readthedocs. org/pdf/opencv-python-tutroals/latest/opencv-python-tutroals. pdf* (2014).

[103] J Morgan et al. *A1.3.5: Report on the results from the inter-comparison of the primary standards and improved measurement facilities for flow rates from 5 nL/min to 1500 nL/min (with uncertainty targets of 1 % (k=2) for steady flow and 2 % (k=2) for fast changing flow): EURAMET 18HLT08 MeDDII*. Tech. rep. 2021.

[104] J Morgan et al. *Calibration methods for measuring the response or delay time of drug delivery devices using Newtonian liquids for flow rates from 5 nL/min to 100 nL/min: EURAMET 18HLT08 MeDDII*. Tech. rep. 2021.

[105] Raquel Nogueira. "Metrological traceability of measurement results in pharmaceutical and chemical sciences: selection and use of certified reference materials". In: *Journal of the Brazilian Chemical Society* 26 (2015), pp. 209–217.

[106] *Object Detection*. URL: https://docs.opencv.org/4.x/df/dfb/group__imgproc__object.html#ga586ebfb0a7fb604b35a23d85391329be.

[107] *Objective Micrometer: Horizontal Scale (Transmitted type, Reflected type)*. URL: https://www.shibuya-opt.co.jp/eng/stage.html.

[108] F Ogheard, S Margot, and J Savary. "Experimental study of buoyancy and surface tension effects of an immersed capillary gravimetric micro-flow facility". In: *Conf. Proc. FLOMEKO 2016*. 2016.

[109] Olaf Tauch. *Nilometer Wikipedia, The Free Encyclopedia*. 2011. URL: https://en.wikipedia.org/wiki/Nilometer.

[110] M Serdar Onses et al. "Mechanisms, capabilities, and applications of high-resolution electrohydrodynamic jet printing". In: *Small* 11.34 (2015), pp. 4237–4266.

[111] *Optem Fusion*. URL: https://www.qioptiq-shop.com/en/Precision-Optics/Micro-Imaging/Optem-Fusion/.

[112] Nobuyuki Otsu. "A threshold selection method from gray-level histograms". In: *IEEE transactions on systems, man, and cybernetics* 9.1 (1979), pp. 62–66.

[113] Stephen W Paddock et al. *Confocal microscopy: methods and protocols*. Vol. 122. Springer, 1999.

[114] Evangelos Papadopoulos. "Heron of Alexandria (c. 10–85 AD)". In: *Distinguished figures in mechanism and machine science*. Springer, 2007, pp. 217–245.

[115] J Pfahler. "Gas and Liquid Flow in small Channels, Micromechanical sensors, Actuators, and Ssystems". In: *ASME*. Vol. 32. 1991, pp. 49–60.

[116] Henri Pitot. "Description d'une machine pour mesurer la vitesse des eaux courantes et le sillage des vaisseaux". In: *Mémoires de L'Académie* 1732 (1732).

[117] Tom H Platenkamp et al. "Low flow liquid calibration setup". In: *Micromachines* 6.4 (2015), pp. 473–486.

[118] *Pompes a insuline externes portables et programmables*. Tech. rep. Haute Autorité de Santé, 2021.

[119] Etienne Portuguez et al. "Evolution of a water pendant droplet: Effect of temperature and relative humidity". In: *Natural Science* 9.01 (2017), p. 1.

[120] *Principles and features of electromagnetic flow meters*. URL: https://www.keyence.com/ss/products/process/flowknowledge/types/electromagnetic.jsp.

[121] *Publishable Summary for 18HLT08 MeDDII Metrology for Drug Delivery Overview*. Tech. rep. 2021.

[122] David Quéré. "Wetting and roughness". In: *Annual review of materials research* 38.1 (2008), pp. 71–99.

[123] *R1L3S3PR - Positive Reflective Grid Distortion Target*. URL: https://www.thorlabs.com/thorproduct.cfm?partnumber=R1L3S3PR.

[124] M Raffel, Ch Willert, and J Kompenhans. "Aprticle Image Velocimetry: A practical guide". In: *Verlag, Berlin* (1998).

[125] G Rajita and Nirupama Mandal. "Review on transit time ultrasonic flowmeter". In: *2016 2nd International Conference on Control, Instrumentation, Energy & Communication (CIEC)*. IEEE. 2016, pp. 88–92.

[126] Gyan Rana et al. "Hydrodynamics of a confined meniscus in a square capillary tube at low capillary numbers". In: *Frontiers in Heat Pipes (FHP)* 5.1 (2014).

[127] Jay Ribeiro. *What are Positive Displacement Flowmeters?* URL: https://www.flomec.com.au/blogs/articles/what-are-positive-displacement-flowmeters.

[128] M Richter, P Woias, and D Weiβ. "Microchannels for applications in liquid dosing and flow-rate measurement". In: *Sensors and Actuators A: Physical* 62.1-3 (1997), pp. 480–483.

[129] Laurent Rieux, Evert-Jan Sneekes, and Remco Swart. "Nano LC: principles, evolution, and state-of-the-art of the technique". In: *LC-GC North America* 29.10 (2011), pp. 926–933.

[130] C Robbe et al. "Quantification of the uncertainties of high-speed camera measurements". In: *International Journal of Metrology and Quality Engineering* 5.2 (2014), p. 201.

[131] *Rotameter Working and Types*. URL: `https://chemicalengineeringworld.com/rotameter-working-and-types/`.

[132] S Satomura. "Ultrasonic blood rheograph". In: *Proceedings of the Third International Conference on Medical Electronics, 1960*. 1960, pp. 254–258.

[133] Rachel E Saunders, Julie E Gough, and Brian Derby. "Delivery of human fibroblast cells by piezoelectric drop-on-demand inkjet printing". In: *Biomaterials* 29.2 (2008), pp. 193–203.

[134] Joerg Schroeter et al. "Characterisation of medical microfluidic systems regarding fast changing flow rates using optical front tracking methods". In: *Medical Engineering & Physics* 48 (2017), pp. 39–48.

[135] Hugo Schultze. "Die innere Reibung von Argon und ihre Änderung mit der Temperatur". In: *Annalen der Physik* 310.5 (1901), pp. 140–165.

[136] *SciPy Reference Guide, Release 1.8.0*. English. SciPy community.

[137] *scipy.stats.normaltest*. URL: `https://docs.scipy.org/doc/scipy/reference/generated/scipy.stats.normaltest.html`.

[138] Jozef Šesták, Dana Moravcová, and Vladislav Kahle. "Instrument platforms for nano liquid chromatography". In: *Journal of Chromatography a* 1421 (2015), pp. 2–17.

[139] Chrys Shea, Ray Whittier, and Eric Hanson. "Development, Testing and Implementation of SAMP-Based Stencil Nano Coatings". In: *IPC proceedings* ().

[140] Gerald Simonneau et al. "Continuous subcutaneous infusion of treprostinil, a prostacyclin analogue, in patients with pulmonary arterial hypertension: a double-blind, randomized, placebo-controlled trial". In: *American journal of respiratory and critical care medicine* 165.6 (2002), pp. 800–804.

[141] Marcus OD Sjödin, Jonas Bergquist, and Magnus Wetterhall. "Mining ventricular cerebrospinal fluid from patients with traumatic brain injury using hexapeptide ligand libraries to search for trauma biomarkers". In: *Journal of Chromatography B* 878.22 (2010), pp. 2003–2012.

[142] Robert Walter Sloley. "Primitive methods of measuring time: with special reference to egypt". In: *The Journal of Egyptian Archaeology* (1931), pp. 166–178.

[143] Irwin Sobel, Gary Feldman, et al. "A 3x3 isotropic gradient operator for image processing". In: *a talk at the Stanford Artificial Project in* (1968), pp. 271–272.

[144] Xavier Casadevall i Solvas and Andrew DeMello. "Droplet microfluidics: recent developments and future applications". In: *Chemical Communications* 47.7 (2011), pp. 1936–1942.

[145] Timothy W Sowers et al. "Capillary driven flow of polydimethylsiloxane in open rectangular microchannels". In: *Soft Matter* 12.26 (2016), pp. 5818–5823.

[146] Wouter Sparreboom et al. “Compact mass flow meter based on a micro Coriolis flow sensor”. In: *Micromachines* 4.1 (2013), pp. 22–33.

[147] Hendrik JJ Staat et al. “Ultrafast imaging method to measure surface tension and viscosity of inkjet-printed droplets in flight”. In: *Experiments in fluids* 58.1 (2017), pp. 1–8.

[148] Clyde E Stauffer. “The measurement of surface tension by the pendant drop technique”. In: *The journal of physical chemistry* 69.6 (1965), pp. 1933–1938.

[149] Xuefei Sun et al. “Controlled dispensing and mixing of pico-to nanoliter volumes using on-demand droplet-based microfluidics”. In: *Microfluidics and nanofluidics* 15.1 (2013), pp. 117–126.

[150] JF Swindells, JR Coe Jr, and TB Godfrey. “Absolute viscosity of water at 20 C”. In: *Journal of Research of the National Bureau of Standard* 48.1 (1952).

[151] Maciej Szeląg. “Evaluation of cracking patterns in cement composites—From basics to advances: A review”. In: *Materials* 13.11 (2020), p. 2490.

[152] Sara Taglialagamba. “Hydraulics in Renaissance Science”. In: (2021).

[153] Ahmadreza Takhreh. *Principes et bases des instruments de précision : Partie VIII - Echangeurs de fluides (2)*. URL: https://nicsaco.com/articles/86/Flow-Transducers-types-Obstruction-Non-Intrusive.

[154] M Tanaka et al. “Recommended table for the density of water between 0 C and 40 C based on recent experimental reports”. In: *Metrologia* 38.4 (2001), p. 301.

[155] James Thomson. “Fundamental principles of diaphragm meters”. In: *INTERNATIONAL SCHOOL OF HYDROCARBON MEASUREMENT* (1995), pp. 28–32.

[156] *Thorlabs: Produits*. URL: https://www.thorlabs.com/navigation.cfm.

[157] Kerstin Thurow, Thomas Krueger, and Norbert Stoll. “An Optical Approach for the Determination of Droplet Volumes in Nanodispensing”. In: *Journal of automated methods management in chemistry* 2009 (Jan. 2009), p. 198732. DOI: 10.1155/2009/198732.

[158] Emanuele Trucco and Alessandro Verri. *Introductory techniques for 3-D computer vision*. Vol. 201. Prentice Hall Englewood Cliffs, 1998.

[159] *Turbine Flowmeter Design Requirement in Process Industry*. URL: https://paktechpoint.com/turbine-flowmeter-design-requirement/.

[160] *Ultrasonic measurement techniques*. URL: https://www.u-f-m.nl/ultrasonic-flow-measurement/?lang=en.

[161] Wolfram Urbanek, Jay N Zemel, and HH Bau. “An investigation of the temperature dependence of Poiseuille numbers in microchannel flow”. In: *Journal of Micromechanics and microengineering* 3.4 (1993), p. 206.

[162] *Using Coherence Scanning Interferometry to Measure High-Slope Parts*. URL: https://www.azom.com/article.aspx?ArticleID=13792.

[163] Giovanni Battista Venturi. *Recherches expérimentales sur le principe de la communication latérale du mouuement dans les fluides, appliqué à l’explication de différens phénomènes hydrauliques. Par... JB Venturi.*. chez Houel et Ducros, 1797.

[164] A Venugopal, Amit Agrawal, and SV Prabhu. “Review on vortex flowmeter—Designer perspective”. In: *Sensors and Actuators A: Physical* 170.1-2 (2011), pp. 8–23.

[165] Ludolf Von Mackensen. *Neue Ergebnisse zur ägyptischen Zeitmessung: die Inbetriebnahme und Berechnung der ältesten erhaltenen Wasseruhr*. Callwey, 1978.

[166] Maarten Vraanes. "Thermal Mass Flow Sensors for Gas and Liquid Applications". In: (2017).

[167] WA Wakeham, A Nagashima, and JV Sengers. "Measurement of the transport properties of fluids. Experimental Thermodynamics". In: *London: Blackwell Scientific Publications* 3 (1991), p. 14.

[168] Zhao Wang et al. "Improvements in micro-CT method for characterizing x-ray monocapillary optics". In: *Optics Communications* 504 (2022), p. 127474.

[169] John G Webster and Halit Eren. *Measurement, Instrumentation, and Sensors Handbook: Two-Volume Set*. CRC press, 2018.

[170] Robert N Wenzel. "Surface roughness and contact angle." In: *The Journal of Physical Chemistry* 53.9 (1949), pp. 1466–1467.

[171] *What is metrology ?: To measure is to compare*. URL: `https://metrologie-francaise.lne.fr/en/metrology/what-is-metrology`.

[172] *What Is Pitot tube? Construction, Working Principle of Pitot tube*. URL: `https://www.mecholic.com/2017/05/pitot-tube-construction-working-principle.html`.

[173] Christian E Willert and Morteza Gharib. "Digital particle image velocimetry". In: *Experiments in fluids* 10.4 (1991), pp. 181–193.

[174] Zhenhua Wu et al. "Absolute quantification of DNA methylation using microfluidic chip-based digital PCR". In: *Biosensors and Bioelectronics* 96 (2017), pp. 339–344.

[175] Shuang Zhang et al. "Characterizing the inner surface of parabolic monocapillary with contrast-enhanced micro-CT technology and ray-tracing computing method". In: *Optics Communications* 475 (2020), p. 126182.

[176] Xiaoyun Zhang et al. "Application of confocal X-ray fluorescence based on capillary X-ray optics in nondestructively measuring the inner diameter of monocapillary optics". In: *Optics Communications* 436 (2019), pp. 38–41.

[177] Xiaoyun Zhang et al. "Measurement of the inner diameter of monocapillary with confocal x-ray scattering technology based on capillary x-ray optics". In: *Applied Optics* 58.5 (2019), pp. 1291–1295.

[178] BV Zhmud, F Tiberg, and K Hallstensson. "Dynamics of capillary rise". In: *Journal of colloid and interface science* 228.2 (2000), pp. 263–269.

[179] Kedi Zhou et al. "Small But Powerful Optically: Glass Microcapillaries for Studying Complex Fluids or Biological Systems with Submicrolitre Samples under Harsh Conditions". In: *Instrumentation, Mesure, Métrologie* 19.3 (2020), pp. 221–227.

[180] Kevin Y Zhu et al. "Microfluidic chip based nano liquid chromatography coupled to tandem mass spectrometry for the determination of abused drugs and metabolites in human hair". In: *Analytical and Bioanalytical Chemistry* 402.9 (2012), pp. 2805–2815.

[181] Pingan Zhu, Xin Tang, and Liqiu Wang. "Droplet generation in co-flow microfluidic channels with vibration". In: *Microfluidics and Nanofluidics* 20.3 (2016), pp. 1–10.

RÉSUMÉ

La traçabilité métrologique des mesures de débit liquide est assurée par une chaîne ininterrompue d'étalonnages par comparaisons à des étalons primaires et secondaires. Cependant, pour des débits inférieurs à quelques microlitres par minute, la traçabilité n'était pas assurée par manque de références nationales. Dans le cadre de cette these, qui fait partie du projet europeen « Metrology for Drug Delivery II », nous avons développé un système primaire optique et non-intrusive pour la mesure de nano-débits de liquides. Ce systeme est basé sur la mesure du deplacement d'une interface liquide/air à l'intérieur d'un tube capillaire, méthod que nous appelons "interface tracking". Afin d'assurer la traçabilité des mesures de débit, une procédure d'étalonnage de caméras et une méthode de mesure du diamètre interne des capillaires ont été etablies. Pour chaque methode developpée un bilan detaillant les différentes sources d'incertitude a été réalisé. Ce système permet d'étalonner des générateurs de débit et débitmètres tels que les dispositifs médicaux, les capteurs de débit, les régulateurs de pression et les pousse-seringues. Ces appareils sont utilisés, par exemple, dans des applications médicales et microfluidiques. Le système développé permet également la mesure des fluctuations de débit, ce qui le rend adapté à l'evaluation de la stabilité et du temps de réponse d'un dispositif. Dans le cadre de la validation externe du système, le CETIAT a participé à une comparaison interlaboratoire qui a consisté en l'étalonnage de différents débitmètres et d'un pousse-seringue, de 5 nL/min à 1500 nL/min, c.à.d. à des débit 1000 fois plus faibles que la limite atteinte par l'étalon primaire précedent. Les résultats de la comparaison montrent des incertitudes relatives étendues allant de 12 % pour 10 nL/min à 0,15 % pour 1500 nl/min. Ces capacités de mesure et d'étalonnage (CMCs) ont été examinées et validées par le processus d'approbation du BIPM (Bureau International des Poids et Mesures). Cette validation représente une reconnaissance internationale de notre système en tant qu'étalon national français pour les nano-débits de liquides.

MOTS CLÉS

Interface tracking, nano-débits de liquides, étalon primaire

ABSTRACT

The metrological traceability of liquid flow rate measurements is ensured by an uninterrupted chain of calibrations against national primary and transfer standards. However, for flow rates that fall below a few microliters per minute, traceability becomes difficult due to the lack of references at this scale. In this work, and as part of the «Metrology for Drug Delivery II» European joint research project, we developed a primary system for the measurement of low liquid flow rates based on the optical tracking of a liquid/air interface moving inside a glass capillary tube. A quantification of the physical phenomena occurring at the interface and an assessment of the different uncertainty components were carried out. In order to ensure the traceability of flow rate measurements, a camera calibration procedure has been established and a method for measuring the inner diameter of capillary tubes has been developed. The system allows the calibration of liquid flow generating and measurement devices such as drug delivery systems, flow sensors, pressure controllers and syringe pumps. These devices are used for e.g. medical and microfluidics applications. Our system also enables the study of flow rate fluctuations and thus, a complete characterization of flow generating devices. As part of the external validation of the system, CETIAT participated in an interlaboratory comparison which consists in the calibration of different flow meters and a flow generator, from 5 nL/min to 1500 nL/min, for both static and dynamic flows. The results of the comparison show a measurement-expanded relative uncertainty ranging from 12 % at 10 nL/min to 0.15 % at 1500 nl/min. These measurement and calibration capabilities (CMCs) were peer-reviewed and validated by BIPM's (International Bureau of Weights and Measures) approval process. This validation represents international recognition of our system as the French national primary standard for liquid nano-flow rates.

KEYWORDS

Interface tracking, nano-flow rates, primary standard